MAGNETIC RESONANCE IMAGING OF ENHANCED OIL RECOVERY PROCESSES IN POROUS ROCKS

by

Armin Afrough

Bachelor of Science, Petroleum University of Technology, 2011

A Dissertation Submitted in Partial Fulfillment
of the Requirements for the Degree of

Doctor of Philosophy

in the Graduate Academic Unit of Chemical Engineering

Supervisors:	Laura Romero-Zerón, Ph.D., Chemical Engineering Bruce J. Balcom, Ph.D., Physics and Chemistry
Examining Board:	Felipe Chibante, Ph.D., Chemical Engineering Brian Lowry, Ph. D., Chemical Engineering Igor Mastikhin, Ph. D., Physics
External Examiner:	Martin Hürlimann, Ph.D. Schlumberger-Doll Research,1 Hampshire St. Cambridge MA 02139

This dissertation is accepted by the
Dean of Graduate Studies

THE UNIVERSITY OF NEW BRUNSWICK

April, 2019

©Armin Afrough, 2019

ABSTRACT

Magnetic resonance imaging methods were employed to investigate fluid/pore surface interactions in enhanced oil recovery processes. The spin echo – single point imaging method was utilized to image fluid content and transverse relaxation time constant distribution along core plugs in water-shock and CO_2 flooding experiments. Physical parameters dependent on the wetted pore surface area were reported in each experiment.

In the water-shock experiments, the permeability spatial profile was calculated for fines migration in Berea core plugs. CO_2 flooding of decane-saturated core plugs was performed under miscible and immiscible conditions. Under miscible conditions, the density of decane in the bound fluid layer was reduced with drainage by CO_2. However, in the immiscible drainage of decane by CO_2, the surface area wetted by decane did not decrease until the residual decane saturation was reached. It is hypothesized that decane forms non-continuous wetting films on the pore surface below the residual oil saturation during the drainage process. Partial derivatives of decane saturation were acquired with a smoothing spline interpolation and processed to compute saturation wave velocity, dispersion coefficient, and the advection-dispersion kernel. It was possible to observe leading and trailing shocks in the CO_2 displacement of decane in a Berea core plug.

Finally, building on the analysis of transverse relaxation time constant T_2 distributions in rocks, it was recognized that non-ground eigenstates contribute to the relaxation of homogeneous magnetization of rocks in magnetic resonance relaxation experiments. This

significant finding makes possible to calculate the confinement size of porous materials using magnetic resonance relaxation methods without any calibration. Several examples demonstrate the validity of this finding.

ACKNOWLEDGEMENTS

I was supported by many individuals and organizations for five years. First and foremost, I gratefully acknowledge Prof. Bruce J. Balcom for the knowledge and wisdom he shared during my studentship. His teachings, words of encouragement, scientific approach, and our discussions were invaluable in this research. I learned from his way of travelling, macro-management, concern for safety and the environment, and the way he handles his relationships. I would also like to thank Prof. Laura Romero-Zerón for her guidance. Prof. Romero-Zerón significantly improved the quality of this research. She is really understanding, and I am happy that I was co-supervised by her. Dr. Ezatallah Kazemzadeh introduced me to magnetic resonance imaging of rocks in 2007. I really appreciate him for encouraging me to pursue this subject. I still remember him telling me that "who knows, maybe you end up doing MRI" and "with Dr. Balcom". I am also grateful to my mother, Fariba, for motivating me and providing the necessary resources for me to study computer programming in my youth. Without her encouragement, I would have not been able to handle the large data sets analyzed in this research in Windows, Mac and Linux environments, either on personal or high-performance computers.

I would also like to express my gratitude to UNB MRI Centre members particularly Jennie McPhail, Mojtaba Shakerian, Sam Zamiri, Rodney MacGregor, Dr. Sarah Vashaee, Dr. Ming Li, Dr. Bryce MacMillan, Dr. Florin Marica, Brian Titus, Prof. Benedict Newling. Dr. Frédéric G. Goora, Razieh Enjilela, Shahla Ahmadi, Dr. Dan Xiao, Prof. Igor Mastikin, and Dr. Yuechao Zhao. Jennie made my life much easier by handling most of my

paperwork and providing me tips to survive and enjoy my graduate studentship. Mojtaba, and particularly Sam, helped me in running several of my experiments. Yuechao, Ming, Mojtaba, Florin, Brian, and Rod helped me design or implement the high-pressure flow system. Numerous conversations with Fred, Sarah, Ben, Florin, and Bryce improved my understanding of signal processing, magnetic resonance imaging, magnetic fields, and relaxation in porous media. I especially thank Bryce for introducing me to the subject of "exchange" in chemical systems or in porous materials during the first year of my studies. Writing the term-paper "Exchange in Nuclear Magnetic Resonance: Chemical Systems and Porous Materials" for the Magnetic Resonance Imaging course in 2014 was the first step in truly understanding magnetic resonance relaxation in porous materials. Igor, Ben, and Dan provided me with invaluable comments during MRI research group meetings. I also appreciate all the help from Karen Annett, and especially Sylvia Demerson, from the Department of Chemical Engineering at UNB, during my PhD studies.

Several people significantly changed my life in Fredericton: Mojtaba Shakerian and Nojan Attari, and Kellie Chippett. Mojtaba and Nojan were much more than friends to me and I will miss them a lot. Kellie and I spent two of our best years together; we traveled all over Canada together, learned from each other and shared good memories. She is an inspiration.

UNB Libraries, in particular Pamela Smith and Beverly Benedict from the Science and Forestry Library, and the Document Delivery section of library services are acknowledged for their exceptional assistance. I would also like to thank Profs. Steven Ross, and Zong-Chao Yan for teaching me quantum mechanics. The research I did on non-ground modes

in magnetic resonance relaxation could have not been done without what I learned from these two great professors.

During my studentship, I was financially supported by graduate research scholarships provided by the UNB MRI Research Centre led by Prof. Balcom. I also earned a Master's Advanced Studies Scholarship from the Association of Professional Engineers and Geoscientists of New Brunswick, a Science, Technology, Engineering, and Mathematics Doctoral Award from the New Brunswick Innovation Fund, and the Gerald I. Goobie Chemical Engineering Scholarship from UNB School of Graduate Studies. I worked at the Chemical Engineering Department in the capacity of a teaching assistant, mainly for Prof. Mladen Eić, but also for Profs. Laura Romero-Zeron, Felipe Chibante, Brian Lowry, and Francis Lang. This was an excellent opportunity for me to learn professionalism and diligence in work from Prof. Eić. I would also like to thank ConocoPhillips, Saudi Aramco, Atlantic Innovation Fund, Green Imaging Technologies, and NSERC of Canada for their financial contributions to the UNB MRI Research Centre during my studies.

Table of Contents

ABSTRACT ii

ACKNOWLEDGEMENTS iv

Table of Contents vii

List of Tables xiii

List of Figures xv

List of Symbols, Nomenclature or Abbreviations xxx

Chapter 1 – Introduction 1

1.1 Research Objectives 2

1.1.1 Fines Migration 3

1.1.2 CO_2 Flooding 4

1.2 Research Organization 5

1.2.1 Fines Migration 7

1.2.2 CO_2 Flooding 7

1.2.3 Non-Ground Eigenvalues in Magnetic Resonance Relaxation of Porous Media 8

1.3 References 10

Chapter 2 – Magnetic Resonance in Porous Rocks 11

2.1 Chemical Reaction Analogy for Magnetic Resonance Relaxation in Porous Media 11

2.1.1 Chemical Reaction in Diffusing Systems – Slab Geometry 11

2.1.2 Magnetic Resonance Relaxation versus Chemical Reaction 22

2.1.3 MR Relaxation in Slab Geometry – Special Cases 24

2.2 Magnetic Resonance in Porous Rocks 27

2.2.1 Transverse Relaxation in Porous Rocks 28

2.2.2 Bulk Relaxation 29

2.2.3 Surface Relaxation 29

2.2.4 Diffusion Induced Relaxation 30

2.2.5 Surface Relaxation: Two Different View Points 31

2.3 Magnetic Resonance Imaging 34

2.3.1 Data Processing 36

2.4 References 39

Chapter 3 – Instruments, Materials, and Experimental Methods 41

3.1 Instruments 41

3.1.1 System Components 45

3.1.2 Flow system 59

3.1.3 Connection Standards 61

3.2 Fluids 62

3.3 Material Selection 65

3.3.1 Metallic Parts 66

3.3.2 Polymeric Materials 68

3.4 Pressurizing and Depressurizing the Apparatus 70

3.5 References 78

Chapter 4 – Magnetic Resonance Imaging of Fines Migration in Berea Sandstone 81

4.1 Introduction 82

4.2 Materials and Methods 85

4.2.1 Sampling 86

4.2.2 Instrumentation 86

4.2.3 Experimental Procedures and Measurements 88

4.3 Results and Discussion 90

4.4 Conclusions 108

4.5 References 109

Chapter 5 – Magnetic Resonance Imaging of CO_2 Flooding in Berea Sandstone: Partial Derivatives of Fluid Saturation 113

5.1 Introduction 113

5.2 Mathematical and Experimental Methods 118

5.2.1 Numerical Differentiation 118

5.2.2 Advection-Dispersion Equation and Partial Derivatives of Saturation 120

5.2.3 Core-Plug Samples and Materials 124

5.2.4 Instrumentation 125

5.2.5 Experimental Methodology 127

5.2.6 Miscible and Immiscible Drainage of Decane 127

5.2.7 Immiscible Flooding of Heavy Oil 128

5.2.8 Imaging Parameters 128

5.3 Results and Discussion 130

5.3.1 Displacement of Heavy Oil by CO_2 130

5.3.2 Displacement of Decane by CO_2 131

5.3.3 Limitations of the Current Study and Future Work. 147

5.4 Conclusions 149

5.5 Appendix—Thermodynamics of Decane/CO_2 Mixtures 150

5.6 References 154

Chapter 6 – Magnetic Resonance Imaging of High-Pressure Carbon Dioxide Displacement: Fluid Behavior and Fluid/Surface Interaction 162

6.1 Introduction 163

6.2 Materials and Methods 169

6.2.1 Core Plug Samples and Materials 170

6.2.2 Instrumentation 171

6.2.3 Experimental Methodology 172

6.2.4 Immiscible Flooding of Heavy Oil 174

6.2.5 Imaging Methods 175

6.2.6 Imaging Parameters 176

6.2.7 Validity and Reliability 177

6.3 Results and Discussion 178

6.3.1 Fluid Saturation Measurement 178

6.3.2 T_2 Distribution Measurement 179

6.3.3 Displacement Mechanisms 191

6.3.4 Miscible CO_2 Flooding of Decane 192

6.3.5 Immiscible CO_2 Flooding of Decane 196

6.3.6 Extraction of Light Components from Heavy Oil 201

6.4 Conclusions 205

6.5 References 208

Chapter 7 – Non-Ground Eigenstates in Magnetic Resonance Relaxation of Porous Media: Absolute Measurement of Pore Size 215

7.1 Introduction 216

7.2 Methods and Materials 220

7.3 Results and Discussion 226

7.4 Non-Ground Eigenvalues in 1D Data 232

7.5 Conclusion 234

7.6 References 234

Chapter 8 – Conclusions and Future Work 238

8.1 Conclusions 238

8.2 Recommendations for Future Work 242

8.2.1 Fines migration 242

8.2.2 CO_2 Flooding 244

8.2.3 Non-Ground Eigenstates in Magnetic Resonance of Porous Media 244

8.3 References 245

Appendix A – Exponential Capillary Pressure Functions in Sedimentary Rocks 246

Appendix B – Fast Measurement of 180° RF Pulse Length 262

Curriculum Vitae

List of Tables

Table 2-1 Summary of the reaction-diffusion problem that defines the concentration evolution function $c_\alpha(x,t)$…… 15

Table 2-2 The solution to the reaction-diffusion problem summarized in Table 2-1… 21

Table 2-3 Analogous parameters in a chemical reaction and in MR relaxation mathematical models…… 22

Table 2-4 The magnetization evolution in a slab geometry for longitudinal MR relaxation. ……. 23

Table 3-1 Mechanical and electrical properties of SS 316 and Hastelloy-C276. From Shakerian et al. (2017)…… 67

Table 4-1 Physical properties of core plug samples A and B……. 87

Table 4-2 Semi-quantitative mineral composition of the Berea core plug and collected fines as percentages for Sample A…… 104

Table 5-1 Physical properties of core plug samples. These rock samples are all homogeneous Berea sandstones from the Kipton formation.…… 124

Table 5-2 Physical properties of pore-filling fluids at 40 °C and ambient pressure (except for CO_2)…… 124

Table 5-3 Summary of the experiments performed in this research. INVREC is an abbreviation for inversion recovery magnetic resonance method used to measure T_1 distributions…… 129

List of Figures

Figure 2-1. The reaction $\alpha \rightarrow \beta$ is occurring homogeneously in the space between $x = +a/2$ and $x = -a/2$, with the disappearance rate of $R_\alpha(x,t) = k_{HG}c_\alpha(x,t)$. α also produces β in a heterogeneous reaction on the surfaces $x = +a/2$ and $x = -a/2$, where the flux of species α to the surface is $N_\alpha(+a/2\,,t) = k_{HT}c_\alpha(a/2\,,t)$ and $N_\alpha(+a/2\,,t) = k_{HT}c_\alpha(a/2\,,t)$. The arrows demonstrate diffusion of species α to the surface for reaction and diffusion of the product β from surface to the bulk of the fluid…… 12

Figure 3-1. The generalized flow system utilized in experiments performed in this research. The diagram is color coded based on fluids the tubing lines carry: orange for nitrogen, red for decane, blue for water and brine, purple for carbon dioxide, pink for glycerol/water mixture, and gray for Fluorinert. Brown tubing lines can carry a mixture of fluids……. 42

Figure 3-2. Flow system and instruments employed in CO_2 flooding experiments. The 2 MHz (a) and 8.5 MHz (b) MRI magnets, the Teledyne ISCO (c), Quizix (d), and Shimadzu (e) pumps, the valve panel (f), the CO_2 (g) and N_2 (h) cylinders, CO_2 meter (i), and oscilloscopes (j) are visible in this picture…… 43

Figure 3-3. The flow system. The Teledyne ISCO (a) and Shimadzu (b) pumps, an Ashcroft K1 pressure transducer (c), an analog Swagelok pressure gauge (d), the valve panel (e), the CO_2 (f) and N_2 (g) cylinders, thermometer (h), coiled tubing (i), MRI magnet (j), and the CO_2 meter (k) are visible in this picture…… 44

Figure 3-4. The valve panel. Up to four 3-way ball valves can be installed on the valve panel to facilitate fluid flow to the core holder or the waste container…… 47

Figure 3-5. Transfer vessel (Phoenix Instruments, Splendora, TX) and its stand. The transfer vessel facilitates isolation and displacement of a fluid without contaminating the pump cylinders with any fluid other than water……. 48

Figure 3-6. Close-up of the back-pressure regulators installed behind the magnet. The KPB back-pressure regulator (a), with its inlet (b), outlet (c), and stand (d), is on the top. The Equilibar back-pressure regulator (e), with its inlet (f), outlet (g), and reference port (h), is at bottom right. Swagelok SS-2F-2 filter (i), thermocouple (j), Ashcroft K1 pressure transducer (k), and Swagelok SS-ORS2 needle valve (l) are also shown in the picture.. 51

Figure 3-7. Close-up of the 'Christmas tree', the tubing and fittings leading to the top of the core holder installed inside the magnet. Tubing lines connecting movable instruments were formed into coils, two turns approximately 6" in diameter, for enhanced safety. One such coil, in the tubing connecting the nitrogen cylinder to the Equilibar back pressure regulator behind the magnet, is visible in this picture (a). Swagelok SS-2C-1/3 check valve (b), Swagelok SS-ORS2 needle valve (c), Swagelok analog pressure gauge ('d' for pore pressure and 'f' for confining fluid), Ashcroft K1 pressure transducer (e), thermocouples ('i' for CO_2 flow and 'g' for confining fluid), and the brass ball valve (h) for draining the confining fluid are visible in this picture…… 56

Figure 4-1. Comparing T_2 spectra of the core inlet and outlet, average of a 6.25 mm section starting 10 mm away from the ends of the core. The T_2 spectra of the inlet (dashed line) and outlet (solid line) coincide before core flooding, as shown in the insets. After core flooding, the T_2 spectra of the core inlet (dashed line) and outlet (solid line) are shifted to longer and shorter T_2 times respectively, as shown in the main figure. The changes are ascribed to fines detachment at the inlet and blockage at the outlet of the core respectively…… 93

Figure 4-2. T_2 maps of the core plugs before and after flooding in grayscale. Water content values from zero to 550 in arbitrary units are linearly mapped black to white. The homogeneity of the Berea core plugs is apparent from their even T_2 map before core flooding (Left, 'a' and 'c'). The shift of T_2 distribution after flooding suggests structural change in the pore space (Right, 'b' and 'd'). Fines migration leads to longer T_2 components, larger pores, in the entrance (bottom of Sample A and top of Sample B). Shorter T_2 in the outlet end region (top of Sample A and bottom of sample B) is the result of fines filtration…… 94

Figure 4-3. Pseudo pore size distributions at different positions along the core Sample A. Gray and black lines represent T_2 distributions before and after flooding respectively. The disappearance of short T_2 components, zero to ten milliseconds, is noticeable in this plot. The reason for this disappearance is not clear, but it may be ascribed to the confined water associated with authigenic clay plates covering rock grains; the structure of which change after exposure to deionized water…… 95

Figure 4-4. Logarithmic mean transverse relaxation time along the Berea core plugs before (square markers, solid line) and after (circle markers, dashed line) deionized water flooding. The mean T_2 profile along the core shows a distinctive declining pattern after flooding. The filtration of detached clay particles within the core leads to reduced pore size distributions along the core. Position is represented by the volume element (voxel) number starting from the inlet of the cores…… 96

Figure 4-5. The ratio of porosities of volume elements in the core plugs Sample A (solid line) and B (dashed line) before and after flooding as a function of voxel number from the inlet end of the cores. Each voxel is a slab of the core 6.25 mm thick. The porosity ratio is more than one for all the measured points and decreases with distance from the inlet end. Porosity trend in Sample B is within the uncertainty range, while Sample A shows a clear declining trend along the core. Position is represented by the volume element (voxel) number starting from the inlet end of the cores…… 101

Figure 4-6. Permeability ratio along the core plug. Fines migration in the core plug causes reduced permeability as a result of pore throat plugging and reduced connectivity. Position is represented by the volume element (voxel) number starting from the inlet of the cores……. 102

Figure 4-7. Surface area ratio profile of the sample inferred from T_2 distributions. Position is represented by the volume element (voxel) number starting from the inlet of the cores. Surface area increases with distance from the inlet of the core. Migration of clay particles

which have high surface to volume ratio leads to higher surface area close to the outlet of the core plug…… 107

Figure 5-1. Immiscible CO_2 flooding of heavy oil in Berea at residual D_2O water saturation, at 6 MPa and 40°C; (a) Oil saturation S and (b) logarithmic mean T_2, T_{2LM} from 1D SE-SPI method. Changes in T_{2LM} suggest extraction of more light components from the top of the core than the bottom. The constant T_{2LM} region at the left side of (b) demonstrates the time period before CO_2 entered the core plug.…….. 132

Figure 5-2. Decane saturation distribution in immiscible CO_2 flooding. Two-dimensional center slices are from 3D π EPI MRI images. Images are at times (a) 0.08, (b) 0.66, (c) 1.22, and (d) 1.78 days. The sample was initially fully saturated at $t = 0.08$ days and approaches residual saturation at $t = 1.78$ days.…… 134

Figure 5-3. Miscible flooding of decane by CO_2 at 9 MPa and 40°C; (a) decane saturation S and (b) $\partial S/\partial y$, (c) $\partial S/\partial t$, and (d) $\partial^2 S/\partial y^2$ as a function of position y and time t from 1D SE-SPI. CO_2 injection almost completely displaced decane at the end of the experiment at $t > 1$ days. Slanted lines in the partial derivatives of saturation reveal the propagation of leading (left line) and trailing (right line) shocks.…….…… 135

Figure 5-4. Immiscible flooding of decane by CO_2 at 6 MPa and 40°C; (a) decane saturation S and (b) $\partial S/\partial y$, (c) $\partial S/\partial t$, and (d) $\partial^2 S/\partial y^2$ as a function of position y and time t from 1D SE-SPI. The trailing shock, a slanted line, leaves an approximate residual decane saturation of $S = 0.25$.…….…… 136

Figure 5-5. (a) Miscible 9 MPa, and (b) immiscible 6 MPa, both at 40°C, flooding of decane-saturated Berea core plugs with CO_2; correlation of partial derivatives of saturation. With a saturation-independent D_L, in (a) partial derivatives have a linear correlation. No such correlation exists for (b) due to the saturation dependent D_{Lc} …… 141

Figure 5-6. Miscible flooding of decane by CO_2 at 9 MPa and 40°C; (a) saturation S profiles ○ and their analytical fits —. Profiles from top to bottom at $t = 0.19, 0.24, 0.32, 0.36, 0.39$, and 0.44 days (b) $(\partial y/\partial S)^2$ versus time t. Data points ● are calculated from experimental data with a linear function. The dispersion coefficient was calculated from $(\partial y/\partial S)^2 = 4\pi D_L(t - t_0)$ to be $D_L = 5.9 \times 10^{-9}$ m^2/s…… 140

Figure 5-7. Wave velocity $v_s = (\partial y/\partial t)_S$ as a function of saturation for (a) Miscible 9 MPa, and (b) immiscible 6 MPa, both at 40°C, flooding of decane-saturated Berea core plugs with CO_2. Each data point estimates v_s for individual core plug sections at discrete times. The solid line marks the median; dashed lines mark 95% confidence bounds; and the horizontal bar is the intrinsic CO_2 velocity. Flow is downward. The generally increasing trend of velocity with saturation is due to the velocity constraint. Local extrema, indicating self-sharpening fronts, demonstrate shocks in agreement with the entropy condition… 143

Figure 5-8. The evolution of the fundamental solution of the advection-dispersion equation as a function of position in miscible (a) and immiscible (b) displacement of decane-saturated Berea core plugs with CO_2. (i) to (iv) in (a) represent $t = 0.19, 0.59, 0.83$, and 0.91 days; (i) to (iv) in (b) represent $t = 1.07, 1.20, 1.35$, and 1.67 days. The integration

of the saturation wave demonstrates the fraction of the saturation wave visible in the core plug window, (b) and (d). Self-sharpening kernel functions in (c) demonstrate the development of shockwaves…….. 148

Figure 5-9. Pressure-composition $P - z_{C_{10}}$ relationship for CO_2/decane mixtures at 40°C: from the PR-EOS ─ and from experimental equilibrium data ● in (a) Full range of $z_{C_{10}}$ and (b) the dew-point region. The experimental datasets are referenced in the text and were performed at temperatures in the range of 37°C to 50°C. The solid horizontal line at $P = 6$ MPa demonstrates the vapor-liquid tie line.…… 150

Figure 5-10. Molar volume for the contribution --- of decane and CO_2 ($z_{C_{10}} V_{C_{10}}$ and $z_{CO_2} V_{CO_2}$) to the ideal solution volume V^{id} ─, the real mixture volume V ─, experimental data ●, and excess molar volume V^E … at $P = 6$ MPa (a), and 9 MPa (b). Excess molar volume indicates nonidealities in the volume change of mixing. Data from the literature referenced in the text…..…… 151

Figure 5-11. Saturation, measured by MRI methods, as a function of total decane molar composition $z_{C_{10}}$ at P = 6 MPa --- and 9 MPa ─. The unit-slope is a guideline. There is an evident deviation from a linear relationship between saturation and composition. At $P = 6$ MPa, CO_2/decane mixtures form two phases in the range of $0 < z_{C_{10}} < 0.41$ which corresponds to $0 < S < 0.72$.…… 154

Figure 6-1. Decane saturation S as a function of position y and time t for (a) miscible and (b) immiscible displacement of decane by CO_2. The core plug center marks the $y = 0$ position and y increases in the axial upward direction. x and z directions form the radial plane of the core plug and gravity is in the $-y$ direction. CO_2 was injected from the top of the core plugs. Grayscale values from black to white represent saturation values from zero to one. Hydrodynamic dispersion effects are observed as saturation contour lines in the transition zone of the miscible flooding (a). Immiscible displacement is dominated by capillary dispersion with capillary end effects at late time data (b). 3D π EPI measurements confirmed 1D decane saturation values in (b)…… 181

Figure 6-2. T_2 maps of miscible flooding at four discrete time points at (a) 0.10 days, (b) 0.31 days, (c) 0.74 days, and (d) 1.14 days. Incremental saturation is shown as a function of position and T_2 in each T_2 map. The incremental saturation values from zero to 0.1 are mapped from black to white. Fading T_2 distributions show decane saturations close to zero at times 0.74 days and 1.14 days. T_{2LM} is superimposed on the T_2 map as a solid white line. The summation of incremental saturation over all T_2 values in each pixel position is equal to the decane saturation of the respective core plug pixel…… 185

Figure 6-3. T_2 maps of immiscible flooding at four time points (a) 0.00 day, (b) 1.13 days, (c) 1.50 days, and (d) 1.97 days. Incremental saturation is shown as a function of position and T_2 in each T_2 map. The incremental saturation values from zero to 0.1 are mapped from black to white. Fading T_2 distributions show decane saturations close to zero at times 1.50 days and 1.97s day. T_{2LM} is superimposed on the T_2 map as a solid white line. The plotting

and processing parameters with these T_2 maps are the same as those for the miscible injection case, Figure 5-2…… 186

Figure 6-4. T_2 maps of heavy oil at six time points during the CO_2 flooding (a) 0.00 day, (b) 1.41 days, (c) 1.86 days, (d) 2.02 days, (e) 3.11 days, and (f) 7.03 days. Incremental saturation is shown as a function of position and T_2 in each T_2 map. The incremental saturation values from zero to 0.1 are mapped from black to white. T_{2LM} is superimposed on the T_2 map as a solid white line. T_2 first shifted to longer times and then shifted back to short T_2 times. The plotting and processing parameters of these T_2 maps are the same as those for the miscible and immiscible injection cases, Figure 5-2 and 5-3…… 187

Figure 6-5. (a) Decane saturation S and (b) logarithmic mean transverse relaxation time T_{2LM} as functions of position y and time t for miscible displacement of decane. CO_2 was injected from the top of the core plug. Grayscale values from black to white represent S values from zero to one and T_{2LM} values from 0 ms to 60 ms respectively. Hydrodynamic dispersion is the dominant phenomenon in this miscible flooding process…… 188

Figure 6-6. (a) Decane saturation S and (b) logarithmic mean transverse relaxation time T_{2LM} as functions of position y and time t for immiscible displacement of decane. CO_2 was injected from the top of the core plug. Colors from black to white represent S values from zero to one and T_{2LM} values from 0 ms to 70 ms respectively. At a capillary number of 2.6×10^{-7}, the displacement is in quasi-static drainage mode and is dominated by interfacial forces. 3D π EPI measurements confirmed 1D decane saturation values in (a)……. 189

Figure 6-7. (a) Oil saturation S and (b) logarithmic mean transverse relaxation time T_{2LM} as functions of position y and time t for CO_2 displacement of heavy oil. CO_2 was injected from the top of the core plug. Grayscale values from black to white represent S values from zero to one and T_{2LM} values from zero to 30 ms, respectively. Changes in T_{2LM} suggest extraction of more light components from the top of the core than the bottom. T_{2LM} also suggests viscosity change along the core plug during the experiment. The short T_{2LM} region at left in (b) is due to heavy oil unexposed to CO_2 during the first 36 hours of the experiment……. 190

Figure 6-8. The $T_{2LM} - S$ cross plot for (●) miscible drainage of decane by CO_2, (○) immiscible drainage of decane by CO_2, and (■) displacement of heavy oil by CO_2. Saturation and logarithmic mean transverse magnetization T_{2LM} data from SE-SPI method were measured at all sections 1 mm thick along the axis of core plugs. This cross plot doesn't show much difference between the miscible and immiscible cases early in the flooding process. However, the slope and residual saturation of these two processes are different indicating a major difference between miscible and immiscible flooding. CO_2 flooding of heavy oil is shown as a triangle in the cross plot. Uncertainty in the immiscible flooding data is higher than that of the miscible case. This is the result of more noise in MRI measurements which propagates through T_{2LM} calculations…… 197

Figure 6-9. (a) $1/T_{2LM}$ versus $1/S$ for miscible CO_2 displacement of decane in Berea. $S - T_{2LM}$ pairs measured for each core plug pixel employing SE-SPI are shown as circles. A smoothing spline was fitted to the binned data points (solid line). The spline was

employed for calculating the derivative $d(1/T_{2LM})/d(1/S) = (\rho_s/\rho_B) \cdot \left(\delta\hat{S}_p/\tilde{V}_p T_{2s}\right)$ (b). $d(1/T_{2LM})/d(1/S)$ is directly proportional to ρ_s and demonstrates changes in the density of decane molecules at the pore surface as a function of saturation……. 198

Figure 6-10. $1/T_{2LM}$ versus $1/S$ for immiscible CO_2 displacement of decane in Berea. $S - T_{2LM}$ pairs measured for each core plug pixel employing SE-SPI are shown as circles. The core plug had an average residual decane saturation of 0.25 ($1/S = 4$). A smoothing spline was fitted to the binned data points (solid line). The spline was employed for calculating the derivative $d(1/T_{2LM})/d(1/S) = \left(S_p/\hat{S}_p\right) \times \left(\delta\hat{S}_p/\tilde{V}_p T_{2s}\right)$ (b). $d(1/T_{2LM})/d(1/S)$ is directly proportional to S_p and demonstrates changes in the pore surface area wetted by decane as a function of saturation…… 202

Figure 6-11. $1/T_{2LM}$ versus $1/S$ for CO_2 displacement of heavy oil in Berea. $T_{2LM} - S$ pairs measured for core plug pixels employing SE-SPI are shown as discrete data points. Initially, there was an inhomogeneous oil concentration with the same T_{2LM} along the core plug, due to capillary end effect, as shown in region 'a'. Oil T_{2LM} increased and oil saturation decreased with CO_2 entering the core plug, as shown in region 'b'. Oil T_{2LM} was then reduced and oil saturation was reduced further after a few days, as shown in region 'c'. The increase in T_{2LM}, in region 'b', is attributed to the increased mobility of heavy oil in contact with CO_2. The reduction in concentration and T_{2LM} of heavy crude oil, as shown in region 'c', is ascribed to the vaporization of light components from the heavy crude oil. The significant difference between this figure and Figure 5-9 and Figure 5-10 demonstrates

the contrast between the mechanisms involved in the displacement of decane and heavy oil by CO_2, in the absence and presence of water phase, respectively…… 207

Figure 7-1. Backscattered electron scanning microscopy images of resin-impregnated Berea sandstone (left) and Indiana limestone (right) with polished surfaces. Resin-filled pore space is black; in the sandstone sample, quartz is medium gray, feldspar is light gray, and clay is dark gray. Virtually all of the limestone is composed of calcite……. 224

Figure 7-2. Two-dimensional relaxation correlation functions $I(T_{1,p}, T_{2,q})$ for brine-saturated Berea sandstone (top) and Indiana limestone (bottom) at $B_0 = 0.05$ T and regularization parameters of $\alpha = 1000$, 10, and 0.1. Intensity range of 10^{-4} to 10^{-2} is mapped to purple (black) to yellow (white), respectively, using a logarithmic scale to reveal small eigenvalues. Only ground eigenvalues are visible at $\alpha = 1000$. Non-ground eigenvalues emerge at $\alpha = 10$ and 0.1. Wide ground-state peaks split at small regularization parameters (Borgia, Brown, and Fantazzini, 1998). $P00$, $P11$, and $P22$ are the first three eigenvalues of magnetization relaxation in Berea sandstone. In the case of Indiana limestone Spq and Lpq respectively represents eigenvalues of small and large pores. $N0q$ mark signal that demonstrates bulk-like features in the T_1 domain…… 230

Figure 7-3. Volumetric probability of pore diameter from scanning electron microscopy (---) and X-ray micro-tomography (—) for Berea sandstone (left) and Indiana limestone (right). The pore size from magnetic resonance relaxation by a direct search algorithm is shown as a gray rectangle. A pore diameter of 22.1 μm was computed for Berea sandstone

and pore diameters of the large and small pores in Indian limestone were estimated to be 39.6 μm and 10.0 μm. The width of the rectangle shows the estimated size by varying the input parameters and the heights demonstrate relative pore size population…… 231

Figure 7-4. T_2 distribution of Berea sandstone and its estimated ground and non-ground eigenvalues. The T_2 distribution (–) was measured using the CPMG method with an inter-echo spacing of 300 μs. Varying l and ρ_2 and using a planar geometry for solving eigenvalues of the relaxation-diffusion equation lead to estimated (– –) contributions to the T_2 distribution by the dominant ground eigenvalues and a smaller non-ground eigenvalue peak…… 233

Figure A-1. A typical oil/water drainage capillary pressure as a function of the wetting phase saturation in a semi-log plot. The exponential capillary pressure function of $\log_{10} P_c/\text{kPa} = -1.344\, S_w + 2.191$ fits experimental data ● in the saturation range of $(0.23, 0.75)$, shown by the vertical lines, with $R^2 = 0.993$. Deviation from this exponential function is because of film flow + and macropores □ at low and high saturations, respectively. The Brooks-Corey capillary pressure function … of $P_c/\text{kPa} = 11.75\, S_w^{-1.389}$ were obtained by a descriptive fit to experimental data ● and +. It appears that the line … fits data well, however, the deviation of data from the fitted line … in the range of $(0.23, 0.75)$ demonstrates an obvious trend that is far from random. Data from Cano Barrita (2008)……. 254

Figure A-2. Seventeen experimental datasets of drainage capillary pressure by centrifuge methods shown by ●. Colored lines represent descriptive fits of exponential capillary pressure functions in the range of their validity to sandstone ─ and carbonate --- samples. (a) is the $P_c - S_w$ relationship in a semi-log graph and (b) is the same data in the log-log form. All $P_c - S_w$ data at low wetting phase saturations collapse to power-law relationships, one for sandstones and one for carbonates shown by gray lines, representing the conditions at which film flow dominates. The exponential capillary pressure function fits experimental data down to a saturation on the power-law line…… 255

Figure A-3. Air/water capillary pressure for carbonate sample E13. Data from a porous plate experiment ■ and a centrifuge capillary pressure measurement of rotation speeds 2800 ●, 4000 ×, 5600 +, 7900 ○, and 15000 * revolutions per minute agree each other. Two exponential capillary pressure functions of $\log_{10} P_c/\text{kPa} = -1.213\, S_w + 2.751$ (─) and $\log_{10} P_c/\text{kPa} = -3.248\, S_w + 3.922$ (---) fit the experimental data in the saturation ranges of $(0.57, 0.94)$ and $(0.27, 0.55)$ with $R^2 = 0.90$ and 0.93, respectively. Deviation from the exponential function (…) is likely because of film flow at low saturations. Data from Baldwin and Yamanashi (1991)…… 257

Figure B-1. FID signal magnitude as a function of RF pulse length in an experiment to measure the 90° and 180° RF pulse lengths. FID measurements are shown as gray circles on top of a theoretical fit…… 264

Figure B-2. The signed FID signal intensity as a function of RF pulse length in an experiment to measure the 90° and 180° RF pulse lengths. FID measurements are shown as gray circles on top of a sine function fitted to the data……. 265

Figure B-3. The first term of the Taylor series expansion of the sine function at $\theta = \pi$ is a linear function. Four FID points are measured around $\theta = \pi$, two shorter and two longer than π. The linear function fitted to these four experimental points shows the 180° RF pulse length at its intersection with zero signal intensity…… 266

List of Symbols, Nomenclature or Abbreviations

1D	One-dimensional
2D	Two-dimensional
3D	Three-dimensional
A	Cross sectional area
A_n	Fractional contribution of each eigenstate to net magnetization
a	Proportionality constant
B	Bulk (subscript)
B_0	Static magnetic field of MRI instrument
B_1	RF magnetic field
BRD	A T_2 inversion method by Butler Reeds Dawson (*SIAM J. Numer. Anal.* **18** (3): 381-397)
BT	Brownstein-Tarr number defined as $\rho a/2D$
b	Bulk (subscript)
C	Molar concentration of decane in a core plug section
C_{in}	Initial molar concentration of decane in a core plug section
CAD	Canadian dollar
CPMG	Carr-Purcell-Meiboom-Gill, a magnetic resonance measurement method
CT	Computed tomography
c_α	Volumetric concentration of reactant α

$c_{\alpha 0}$	Initial volumetric concentration of reactant α
cc	Cubic centimeter
cm	Centimeter
D	Diffusion (subscript)
D	Self-diffusivity; or fractal dimension
D_m	Mass diffusivity
D_L	Longitudinal dispersion coefficient
D_{Lc}	Longitudinal capillary dispersion coefficient
D_2O	Heavy water
DAQ	Data acquisition
DHK	Double half *k*-space
dB	Decibel
E	Error measure functional; or overall flooding efficiency
E_D	Microscopic efficiency
E_V	Macroscopic efficiency
ECTFE	Ethylene chlorotrifluoro-ethylene
EOR	Enhanced oil recovery
ETFE	Ethylene tetrafluoro-ethylene
F	The combined effect of error and roughness measures balanced by a smoothing parameter
FEP	Fluorinated ethylene propylene
FID	Free induction decay

FLASH	Fast low angle shot, an MRI measurement method
f	Frequency
G	Gauss, a unit of magnetic field
G	The fundamental solution of the advection-dispersion equation
G_i	Internal magnetic field gradient in the pore space
H	Enthalpy
^{1}H	Hydrogen nucleus
I_n	Fractional contribution of each eigenstate n to total magnetization
I_{0i}	Initial amplitude of an electric signal
INVREC	Inversion recovery, a magnetic resonance method
k	Thermal conductivity; permeability
k_{HG}	Homogeneous reaction constant
k_{HT}	Heterogeneous reaction constant
k_r	The ratio of final to initial permeability; or effective permeability
kHz	kilohertz
kW	kilowatt
L	Length of core plug
M	Total nuclear magnetization
M_0	The initial magnetization of material
M_+	Total nuclear magnetization in the transverse plane
M_x	Total nuclear magnetization in the x-direction

M_y	Total nuclear magnetization in the y-direction
M_z	Total nuclear magnetization in the z-direction
MHz	megahertz
MMP	Minimum miscibility pressure
MPa	megapascal
MR	Magnetic resonance
MRI	Magnetic resonance imaging
m	Magnetic moment per unit volume along some specified direction
mD	millidarcy
min	Minute
mm	millimeter
ms	millisecond
NMR	Nuclear magnetic resonance
NPT	National Pipe Thread
N_α	Flux of species α
n	Echo number
n_α	Total molar amount of species α in a defined geometry
n-	Normal (prefix)
no.	Number
P	Pressure, or saturation pressure
P_c	Capillary pressure

P_b	Bubbling pressure, as defined by the Brooks-Corey equation
PCTFE	Poly chlorotrifluoroethylene
PDE	Partial differential equations
Pe	Peclet number
PEEK	Polyether ether ketone
PFA	Perfluoro alkoxy alkanes
PTFE	Poly tetrafluoroethylene
PVDF	Poly vinylidenefluoride
pixel	Picture element
q	Volumetric flow rate
R	Roughness measure functional
R_α	Homogeneous rate of reaction
RF	Radiofrequency
r	Pore diameter; or position vector
r	Ratio (subscript)
S	Siemens, the unit of electric conductance
S	Molar oil saturation; or any surface area
S^*	Molar oil saturation at the extremum of excess molar volume
S_{nwr}	Residual non-wetting phase saturation
S_p	Wetted surface area
S_{pr}	The ratio of final to initial pore surface area

S_w	Effective wetting-phase saturation
S_{we}	Effective saturation as defined by Brooks-Corey equation
S_{wr}	Residual wetting-phase saturation
SAE	Society of Automotive Engineers
SDR	Schlumberger-Doll Research Center
SE-SPI	Spin echo - single point imaging method
SEMS	Spin echo multi slice imaging method
SNR	Signal-to-noise ratio
SPRITE	Single point ramped imaging with T_1 enhancement
SS	Stainless steel
s	Surface (subscript)
T	Tesla
T	Temperature, or absolute temperature; or any time decay constant
T_1	Longitudinal relaxation time constant
T_2	Transverse relaxation time constant
T_{2b}	Transverse relaxation time constant of the pore-filling fluid in bulk
T_{2s}	Transverse relaxation time constant of the bound fluid
T_{2LM}	Logarithmic mean of transverse relaxation time distribution
T_{2LMr}	The ratio of final to initial T_{2LM}
T_2^*	Apparent transverse relaxation time constant

T_C	Critical temperature
t	Measurement time
t_E	Echo time
UNB	University of New Brunswick
u	Intrinsic fluid velocity
V	Volt
V	Pore volume, or fluid molar volume
V_r	The ratio of final to initial pore volume
V_p	Pore fluid volume
$\widetilde{V_p}$	Pore volume
V^E	Excess molar volume
V^{id}	Ideal molar volume
$V_{\mathrm{CO_2}}$	Contribution of CO_2 to ideal molar volume
$V_{\mathrm{C_{10}}}$	Contribution of C_{10} to ideal molar volume
Viton	Vinylidene fluoride-hexafluoropropylene copolymer
v	Macroscopic mean advection velocity
v_S	Wave velocity
voxel	Volume element
wt%	Weight percent
x	Space coordinates (*x* and *z* are in the radial plane)
$x_{\mathrm{CO_2}}$	CO_2 mole fraction in the liquid phase

Y	Yield strength
y	Space coordinates (in the axial direction, positive upwards)
y_{CO_2}	CO_2 mole fraction in the vapor phase
y_0	$L/2$; position of the top face of a core plug
z	Space coordinates (*x* and *z* are in the radial plane)
α	Smoothing parameter in spline interpolation
	Reactant in a hypothetical unitary reaction of $\alpha \rightarrow \beta$
β	Product in a hypothetical unitary reaction of $\alpha \rightarrow \beta$
γ	Gyromagnetic ratio
δ	The thickness of the bound layer
$\partial\Omega$	The outer surface of geometry Ω
ζ	Experimental independent variable; could be a vector
η	Oil viscosity; or experimental dependent variable; could be a vector
θ	The phase of magnetization vector in the rotating frame of reference
λ	Phase mobility; or pore-size-distribution index
μ	Viscosity
μs	microsecond
ξ_n	A dimensionless representative of eigenvalue n of reaction-diffusion on pore surfaces
π	The ratio of a circle's circumference to its diameter
π EPI	π echo planar imaging

ρ	Surface relaxivity constant
ρ_B	Bulk molar density of decane
ρ_P	Proton density
ρ_{PS}	Smoothed proton density
ρ_{PS}^{BK}	Smoothed background proton density
ρ_{PS}^{SA}	Smoothed saturated proton density
ρ_s	Molar density of decane in the bound layer
σ	Electrical conductivity
τ	Half of the spacing between the 180° RF pulses in CPMG and SE-SPI methods; or tortuosity factor in porous media, or any time constant
τ_0	The spacing between the 90° RF pulse and the first 180° pulse in SE-SPI method
τ_i	An exponential decay constant
ϕ	Porosity
ϕ_r	The ratio of final to initial porosity
Ω	The volume defining a specific geometry
$\mathcal{D}$	Differential operator
$x_{\mathrm{C_{10}}}$	Molar liquid composition of C_{10}
$x_{\mathrm{CO_2}}$	Molar liquid composition of CO_2
$y_{\mathrm{C_{10}}}$	Molar vapor composition of C_{10}

y_{CO_2}	Molar vapor composition of CO_2
$z_{C_{10}}$	Total molar composition of C_{10}
$z^*_{C_{10}}$	Total molar composition of C_{10} at the extremum of excess molar volume
z_{CO_2}	Total molar composition of CO_2

Chapter 1 – Introduction

Worldwide, fossil fuels remain as the primary source of energy. In 2014, oil accounted for 31% of the world's energy consumption (International Energy Agency 2016). In addition to further oil exploration, increased extraction from currently producing oil reservoirs is an economically viable option to meet global energy demand. Enhanced Oil Recovery (EOR) methods boost oil production from petroleum reservoirs previously producing under natural drive and secondary oil recovery processes (i.e. water flooding). Fluids injected into reservoirs displace oil toward producing wells. The overall efficiency of any secondary and EOR process can be considered as the product of microscopic and macroscopic displacement efficiencies.

$$E = E_D E_V \tag{1-1}$$

where E is the overall efficiency, E_D is the microscopic efficiency, and E_V is the macroscopic efficiency. E_V is the fraction of the reservoir volume contacted by the displacing fluid. E_D is a measure of the effectiveness of the oil mobilization at the pore level in locations contacted by the displacing fluid. The microscopic efficiency of oil displacement by the displacing fluid largely determines the success or failure of any EOR process (Green and Willhite 1998). Microscopic efficiency is measured in the laboratory in terms of the residual oil saturation after injecting the displacing fluid. EOR fluids are designed to alter the viscous/capillary force ratio or phase behavior to enhance the mobilization of the hydrocarbon phase. Typical fluids employed in EOR processes include:

low-salinity water, hydrocarbon gases, polymer solutions, surfactant solutions, alkaline agents, air, CO_2, nitrogen, and many others. The introduction of foreign fluids into a petroleum reservoir may strongly influence the solid-fluid and fluid-fluid interfaces. Studying these effects is an inherent part of every EOR project. Laboratory and pilot projects determine the success of proposed EOR projects. Favorable physicochemical interactions between the displacing fluid and oil include decreasing the interfacial tension between the fluids, miscibility between the fluids, reducing oil viscosity, and oil volume expansion (Green and Willhite 1998). However, undesired fluid-fluid and solid-fluid interactions can cause negative effects on the reservoir productivity, such as asphaltene precipitation, migration of clay particles, and scale formation (Krueger, 1986). Magnetic Resonance Imaging (MRI) offers great potential to the experimental evaluation of EOR processes due to the non-intrusiveness of MRI, allowing measuring physical properties of rocks and fluid saturations as a function of position and time.

1.1 Research Objectives

The main objective of this research is to evaluate the interactions between the displacing fluid, porous rocks, and their pore-filling fluids for petroleum engineering applications utilizing MRI methods. The Spin Echo-Single Point Imaging (SE-SPI) MRI method provides quantitative information about fluids saturation and fluid distribution in rocks. The following sections describe two cases of physicochemical interactions during waterflooding as a secondary recovery process and during miscible and immiscible CO_2 flooding as the EOR processes that were evaluated in this research.

1.1.1 Fines Migration

Waterflooding is the most common secondary oil recovery process applied worldwide. Incompatible aqueous phase chemistry and/or high flow rate water injection may mobilize fines within reservoir rocks. Fines are micaceous particles, thin sheets, with large surface area. Permeability impairment associated with fines migration is one of the major problems that occurs in production and injection wells in oil fields, particularly during waterflooding. Accumulation of clay particles near the wellbore region obstructs pore throats and ultimately results in reduced reservoir productivity.

Limitations and complexity of theoretical models have led companies to rely on laboratory methods to prevent potential fines migration problems, particularly concerning to the rock sensitivity to the water injection rate. Fines migration is a classic example of fluid-solid interactions in petroleum engineering (Sahimi et al. 1990) which significantly changes the pore surface area. The transverse relaxation time T_2 is an MR parameter which is inversely correlated to the pore surface area. SE-SPI, an MRI method which measures the T_2 distribution, can measure the changes in petrophysical properties, including porosity, pore surface area ratio, and permeability. These petrophysical properties were measured or estimated in core plugs undergoing fines migration induced by water-shock experiments. The methodology used in this work significantly reduces the number of experiments necessary to study fines migration in waterflooding projects. In addition, by easily demonstrating the conditions under which fines migration occurs, it may be possible to avoid frequent acidizing jobs in the oilfield.

1.1.2 CO_2 Flooding

Carbon dioxide from a variety of sources, such as natural CO_2 reservoirs, synthetic fuel power plant emissions, and gas processing plants, has been injected into petroleum reservoirs for EOR for several decades (Beckwith 2011). Intense contemporary interest in carbon sequestration for mitigating climate change also requires a better understanding of the phenomena associated with CO_2 flooding. Capillary trapping and mineral dissolution/formation are two important phenomena associated with interactions of CO_2 with the formation rock. Moreover, the thermodynamics of the CO_2/oil system is of more importance as it determines the success of the CO_2 flooding. The phase behavior of the CO_2/oil system has profound effects on the mechanisms of oil recovery by CO_2. Miscible CO_2 injection leads to near perfect microscopic recoveries if enough volume of the miscible phase is injected and the oil composition is favorable (Green and Willhite 1998). However, immiscible CO_2 flooding leaves oil as isolated blobs in the pore volume or as thin layers on the pore surface (Berg et al. 2013).

In this work, a model oil, decane, in Berea sandstone was used to study fluid/surface interactions during miscible and immiscible CO_2 flooding experiments employing MRI methods. CO_2 flooding of heavy oil in Berea also demonstrated *in situ* change in the properties of the heavy oil in contact with CO_2.

The SE-SPI method measured the quantitative change in the wetted surface area in immiscible drainage of decane by CO_2. The MRI methods also measured the interaction

between the displaced phase and the pore surface in terms of the density of decane on the pore surface for miscible drainage. CO_2 flooding of oil saturated rocks demonstrates the capabilities of MRI methods in revealing mechanisms of miscible and immiscible oil recovery.

This study improves our understanding of rock-fluid interaction in EOR by waterflooding and CO_2 flooding. It also provides new analytical methods to petroleum laboratories and research and development centers.

The last part of this research draws information from the fine details of relaxation spectra in the fines migration and CO_2 flooding studies. Furthermore, this work demonstrates that it is possible to experimentally observe non-ground eigenvalues in magnetic resonance relaxation measurements. Up to three eigenvalues of the diffusion-relaxation equation, with a distinct pattern, are observed in a simple magnetic resonance relaxation experiment on a brine-saturated Berea sandstone sample. This finding makes it possible to directly measure pore size in petroleum or aquifers wells using magnetic resonance well logging tools. Previously, such measurements had to be calibrated against laboratory data.

1.2 Research Organization

This dissertation follows the Thesis Journal Format and is organized in eight chapters as follows. Chapter 2 provides background knowledge about quantitative MRI measurements in porous materials and the effect of fluid/surface interaction on such measurements. The

analogy between magnetic resonance relaxation in porous media and heterogeneous reactions on catalyst pellets is discussed.

Chapter 3 describes practical aspects of the research methodology and the experimental set-up such as high-pressure flow system design.

Chapter 4 proposes a new method for the quantitative characterization of fines migration employing MRI. The proposed method measures surface area, porosity, and permeability in situ as a function of position in core plugs undergoing fines migration induced by water-shock.

Chapter 5 deals with the core-scale analyses of miscible and immiscible CO_2 flooding in Berea sandstone. Dispersion coefficient, wave velocity, and advection-dispersion kernels were computed from the partial derivatives of saturation with respect to time and position.

Chapter 6 investigates displacement mechanisms in miscible and immiscible CO_2 flooding processes. Fluid/surface interactions during miscible and immiscible CO_2 flooding of decane-saturated Berea core plugs were studied quantitatively. The in-situ extraction (mass transfer) of light components from the heavy oil phase to the gas phase (CO_2) was demonstrated during immiscible CO_2 flooding.

Chapter 7 demonstrates that non-ground eigenvalues contribute to the relaxation of homogeneous magnetization in porous media and provide procedures for calculating pore size from simple relaxation experiments.

Chapter 8 concludes the thesis, summarizes its contributions, and outlines future work.

The results of this research are reported in Chapters 4-7 for fines migration and CO_2 flooding experiments, and pore size measurements corresponding to papers that have been already published or submitted for publication. Several members of the UNB MRI Centre and the Chemical Engineering Department at UNB have contributed to these papers as coauthors. The contribution of the author and coauthors is described as follows.

1.2.1 Fines Migration

Armin Afrough, the first author of this paper, performed the identification of the research problem, experimental design, experimental measurements, and the MRI data analysis of experimental data. Mohammad S. Zamiri conducted acquisition of the data and all permeability calculations from pressure gauge readings. Profs. Bruce J. Balcom and Laura Romero-Zerón advised the author on designing the MRI experiments and petrophysical analysis, respectively. The manuscript was written by the author with the assistance of Profs. Bruce J. Balcom and Laura Romero-Zerón. Dr. Ven Reddy performed the XRD analysis. Anonymous reviewers commented on the paper which significantly improved the technical content of the paper.

1.2.2 CO_2 Flooding

Dr. Bruce J. Balcom identified the overall research problem and designed a high-level experimental plan. The first author, Armin Afrough, generated the detailed experimental design, conducted the majority of the experiments, performed the analysis of all the data,

and wrote the paper. Dr. Bruce J. Balcom, Dr. Laura Romero-Zerón, Mojtaba Shakerian, Mohammad S. Zamiri, Rodney McGregor, Dr. Florin Marica, Dr. Bryce MacMillan, Ming Li, Dr. Ben Newling, Dr. Igor Mastikhin, Dr. Sarah Vashaee, and Dr. Yuechao Zhao provided additional technical advice, including MRI data analysis. Caleb Bell assisted the first author with the Aspen Properties thermodynamics software and thermodynamics analysis. Finally, Dr. Bruce J. Balcom, Dr. Laura Romero-Zerón, and Dr. Benedict Newling edited the manuscript.

1.2.3 Non-Ground Eigenvalues in Magnetic Resonance Relaxation of Porous Media

The first author, Armin Afrough, identified the problem and designed the experimental plan and conducted the analysis of all the experimental data with advice from Prof. Balcom. Dr. Sarah Vashaee and Prof. Laura Romero-Zerón improved the quality of this work through discussions and insights. The author wrote the manuscript with assistance and advice from Prof. Balcom. Prof. Zong-Chao Yan provided suggestions on improving the quality of the manuscript. Steven R. Cogswell instructed the author on performing scanning electron microscopy and X-ray microtomography and performed most of the microscopy imaging.

Four journal papers were generated from this research that have been published and submitted to the SPE Journal and Physical Review Applied: (1) Magnetic Resonance Imaging of Fines Migration in Berea Sandstone (Chapter 4), (2) Magnetic Resonance Imaging of CO_2 Flooding in Berea Sandstone: Partial Derivatives of Fluid Saturation

(Chapter 5), (3) Magnetic Resonance Imaging of High Pressure Carbon Dioxide Displacement – Fluid Behavior and Fluid-Surface Interaction (Chapter 6), and (4) Non-Ground Eigenstates in Magnetic Resonance Relaxation of Porous Media – Absolute Measurement of Pore Size (Chapter 7).

Two manuscripts (Chapters 4 and 6) have been already published by the SPE Journal. Manuscript (2), Chapter 6, is revised and resubmitted to the SPE Journal and is currently undergoing the peer review process. Manuscript (4), Chapter 7, is accepted for publication in the journal Physical Review Applied. Those who contributed to this research are either acknowledged as co-authors or are mentioned in the acknowledgement section of the manuscripts.

Research on exponential capillary pressure functions in rocks has been an ongoing work of the first author, Armin Afrough, before graduate studies, who after joining UNB, has further developed this area of research using experimental MRI data to verify its applicability. The “Exponential Capillary Pressure Functions in Sedimentary Rocks” is published in the Society of Core Analysts proceedings and is provided in Appendix A of this dissertation.

Finally, Appendix B describes a fast method to determine 180° RF pulse lengths using four free induction decay measurements. The method described in Appendix B improves the quantitative analysis of MRI images by frequent measurement of the actual 180° RF pulse lengths.

1.3 References

Beckwith, R. 2011. Carbon Capture and Storage: A Mixed Review. *J. Petrol. Technol.* 63 (5): 42-45. SPE-0511-0042-JPT. http://dx.doi.org/10.2118/0511-0042-JPT.

Berg, S., Ott, H., Klapp, S. A., et al. 2013. Real-Time 3D Imaging of Haines Jumps in Porous Media Flow. *P. Natl. Acad. Sci. USA* 110 (10): 3755-3759. http://dx.doi.org/10.1073/pnas.1221373110.

Green, D. W., Willhite, G. P. 1998. *Enhanced Oil Recovery*. Richardson: Society of Petroleum Engineers.

International Energy Agency. 2016. World Energy Trends: An Overview In *Excerpt From World Energy Balances (new release, 2016 edition)*. 3-19.

Krueger, R. F. 1986. Overview of Formation Damage and Well Productivity in Oilfield Operations. *J. Petrol. Technol.* 38 (2): 131-152.

Sahimi, M., Gavalas, G. R., Tsotsis, T. T. 1990. Statistical and Continuum Models of Fluid-Solid Reactions in Porous Media. *Chem. Eng. Sci.* 45: 1443-1502. http://dx.doi.org/10.1016/0009-2509(90)80001-U.

Chapter 2 – Magnetic Resonance in Porous Rocks

This chapter provides concise background information of the effect of fluid/surface interactions on magnetic resonance (MR) measurements, quantitative magnetic resonance imaging (MRI), and describes the data analysis methods employed in this research. An introduction to the basics of MR and MRI as applied in petroleum and chemical engineering could respectively be found in Coates et al. (1999) and Stapf and Han (2006).

2.1 Chemical Reaction Analogy for Magnetic Resonance Relaxation in Porous Media

Diffusion in reacting systems is common in chemical engineering applications. Catalytic reactors and reaction-absorption of gases in agitated tanks are two such examples. Likewise, during MR relaxation measurements in porous media, molecular diffusion plays an important role. This section summarizes the analogy between chemical reaction and MR relaxation, particularly in porous media. MR relaxation measurements in porous media have gained currency in petroleum well logging (Coates et al. 1999) and laboratory petrophysical core analysis (Mitchell et al. 2013). The following subsection demonstrates the similarities between diffusion in porous media systems and diffusion in catalytic reaction systems.

2.1.1 Chemical Reaction in Diffusing Systems – Slab Geometry

Chemical reactions occur both in bulk fluids and on solid surfaces. These two reactions are called homogeneous and heterogeneous chemical reactions, respectively. In mass balance equations, homogeneous reactions appear as source, or sink, terms. However,

heterogeneous reactions appear as boundary conditions of mass balance equations. Heterogeneous reactions usually occur at the surface of solid catalysts which reduce the activation energy of the reaction.

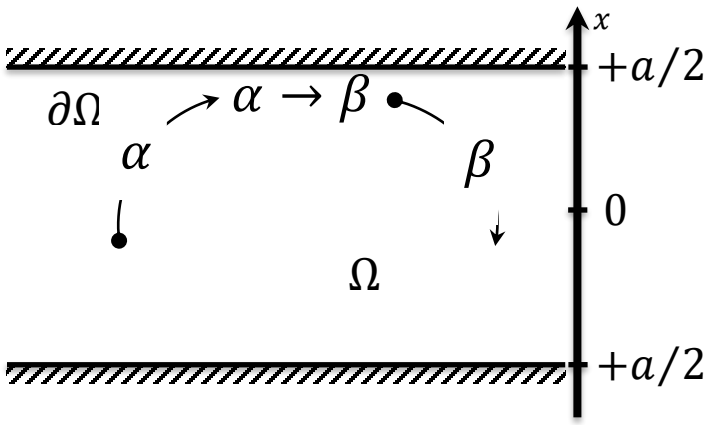

Figure 2-1 The reaction $\alpha \rightarrow \beta$ is occurring homogeneously in the space between $x = +a/2$ and $x = -a/2$, with the disappearance rate of $R_\alpha(x,t) = k_{HG}c_\alpha(x,t)$. α also produces β in a heterogeneous reaction on the surfaces $x = +a/2$ and $x = -a/2$, where the flux of species α to the surface is $N_\alpha(+a/2\,,t) = k_{HT}c_\alpha(a/2\,,t)$ and $N_\alpha(+a/2\,,t) = k_{HT}c_\alpha(a/2\,,t)$.

Consider the chemical reaction

$$\alpha \rightarrow \beta \tag{2-1}$$

in a fluid occupying a slab geometry, as shown in Figure 2-1. The reaction occurs in the spacing between the flat surfaces, as a homogeneous chemical reaction in domain Ω. The

reaction, Equation (2-1), could be enhanced on the surfaces as a heterogeneous chemical reaction in subdomain $\partial\Omega$. It is desired to evaluate the concentration evolution $c_\alpha(x,t)$ and chemical amount $n_\alpha(t)$ of species α, in moles, where

$$n_\alpha(t) = \int_\Omega c_\alpha(x,t)dv. \tag{2-2}$$

If species α and β have the same physical properties, there will be no reaction-induced bulk flow in domain Ω since the number of moles are conserved in the chemical reaction. The molar flux $N_\alpha(x,t)$ is expressed as

$$N_\alpha(x,t) = -D_{\alpha\beta}\frac{\partial c_\alpha(x,t)}{\partial x} \tag{2-3}$$

where $D_{\alpha\beta}$ is the mass diffusivity of α in the fluid. The continuity equation

$$\frac{\partial c_\alpha(x,t)}{\partial t} + \frac{\partial N_\alpha(x,t)}{\partial x} = R_\alpha(x,t) \tag{2-4}$$

describes the concentration evolution in which $R_\alpha(x,t)$, with units of mol m^{-3} s^{-1}, is a sink term that quantifies the rate of disappearance of α in unit volume in the bulk of fluid. $\alpha \rightarrow \beta$ is a first-order chemical reaction with

$$R_\alpha(x,t) = k_{HG}c_\alpha(x,t), \tag{2-5}$$

where k_{HG}, with units of s^{-1}, is the reaction rate constant. In contrast, for the heterogeneous reaction which may be faster, or slower, than that of the bulk, the kinetics of reaction are related to the flux of species α at the surfaces as

$$N_\alpha(+a/2\,,t) = k_{HT}c_\alpha(+a/2\,,t), \tag{2-6}$$

and

$$N_\alpha(-a/2\,,t) = k_{HT}c_\alpha(-a/2\,,t). \tag{2-7}$$

The heterogeneous reaction rate constant k_{HT} has units of m s^{-1}, contrary to k_{HG} that has units of s^{-1}. Assuming a concentration-independent diffusivity $D_{\alpha\beta}$, substituting N_α and R_α, from Equations (2-3) and (2-5), into Equation (2-4) leads to

$$\frac{\partial c_\alpha(x,t)}{\partial t} - D_{\alpha\beta}\frac{\partial^2 c_\alpha(x,t)}{\partial x^2} = -k_{HG}c_\alpha(x,t). \tag{2-8}$$

The partial differential equation (PDE) Equation (2-8) is complete with boundary conditions, Equations (2-6) and (2-7), and the initial condition

$$c_\alpha(x,0) = c_{\alpha 0}. \tag{2-9}$$

Please note that because of symmetry along the x-axis, it can be assumed that

$$N(0,t) = -D_{\alpha\beta}\frac{\partial c_\alpha(0,t)}{\partial x} = 0. \tag{2-10}$$

Table 2-1 Summary of the reaction-diffusion problem that defines the concentration evolution function $c_\alpha(x,t)$.

Partial Differential Equation	$\frac{\partial c_\alpha(x,t)}{\partial t} - D_{\alpha\beta}\frac{\partial^2 c_\alpha(x,t)}{\partial x^2} = -k_{HG}c_\alpha(x,t)$
Initial Condition	$c_\alpha(x,0) = c_{\alpha 0}$
Boundary Condition 1	$N_\alpha(+a/2\,,t) = k_{HT}c_\alpha(+a/2\,,t)$
Boundary Condition 2	$N_\alpha(-a/2\,,t) = k_{HT}c_\alpha(-a/2\,,t)$

For the sake of simplicity, we first attempt the solution of the homogeneous version of Equation (2-8), that is

$$\frac{\partial c_\alpha(x,t)}{\partial t} - D_{\alpha\beta}\frac{\partial^2 c_\alpha(x,t)}{\partial x^2} = 0. \tag{2-11}$$

Equation (2-11) can be easily solved by separation of variables employing

$$c_\alpha(x,t) = F(x)G(t) \tag{2-12}$$

that simplifies the homogeneous PDE, Equation (2-11), to

$$F(x)\frac{dG(t)}{dt} - D_{\alpha\beta}G(t)\frac{d^2F(x)}{dx^2} = 0. \tag{2-13}$$

Equation (2-13) can be separated into two independent ordinary differential equations (ODE) with independent variables t and x:

$$\frac{1}{G(t)}\frac{dG(t)}{dt} = D_{\alpha\beta}\frac{1}{F(x)}\frac{d^2F(x)}{dx^2} = -\lambda^2. \tag{2-14}$$

Please note that there are no partial derivatives in Equation (2-14) and the values of $-\lambda^2$, except negative real numbers, lead to unrealistic solutions. It is very easy to solve for $G(t)$ in Equation (2-14) by employing the derivative of the natural logarithm function and a simple integration which results in

$$G(t) = G(t_0)e^{-\lambda^2(t-t_0)} \tag{2-15}$$

which is

$$G(t) = G(0)e^{-\lambda^2 t} \tag{2-16}$$

for $t_0 = 0$. λ^2 has units of s^{-1} and corresponds to an exponential decay time T, where

$$\lambda^2 = \frac{1}{T}. \tag{2-17}$$

The ODE for $F(x)$ can be expressed as

$$\frac{d^2F(x)}{dx^2} = -\frac{1}{D_{\alpha\beta}T}F(x) \tag{2-18}$$

that for negative real values of $-\lambda^2$ has the general solution of

$$F(x) = P \sin \frac{x}{\sqrt{D_{\alpha\beta} T}} + Q \cos \frac{x}{\sqrt{D_{\alpha\beta} T}}. \tag{2-19}$$

Substituting $F(x)$ and $G(t)$, from Equations (2-16) and (2-19), into Equation (2-12) leads to

$$c_\alpha(x,t) = \left[P \sin\left(\frac{x}{\sqrt{D_{\alpha\beta} T}}\right) + Q \cos\left(\frac{x}{\sqrt{D_{\alpha\beta} T}}\right) \right] \cdot G(0) e^{-t/T} \tag{2-20}$$

that should meet the boundary and initial conditions, as summarized in Table 2-1. The boundary conditions, Equations (2-6) and (2-7), result in

$$P \equiv \phi \tag{2-21}$$

which simplifies Equation (2-20) to

$$c_\alpha(x,t) = Q \cos\left(\frac{x}{\sqrt{D_{\alpha\beta} T}}\right) \cdot G(0) e^{-t/T}. \tag{2-22}$$

Equation (2-22) cannot satisfy the initial condition, Equation (2-9), in its current form. However, a linear combination of terms like Equation (2-22), can approximate the initial condition by a Fourier cosine series. The general solution of the PDE summarized in Table 2-1 can be expressed as

$$c_\alpha(x,t) = c_{\alpha 0} \sum_n A_n \cos\left(\frac{x}{\sqrt{D_{\alpha\beta} T_m}}\right) e^{-t/T_n}. \tag{2-23}$$

This solution is also called the normal mode analysis (Brownstein and Tarr, 1979) of the PDE described in Table 2-1. Equation (2-23) is made of orthogonal cosine terms that decay

with time. Finishing the normal mode analysis solution of the PDE requires the calculation of values of A_n and T_n.

First, we solve for T_ns by employing the boundary condition, Equation (2-6), at $x = a/2$:

$$-D_{\alpha\beta}\frac{\partial c_\alpha(a/2,t)}{\partial x} = k_{HT}c_\alpha(a/2\,,t). \tag{2-24}$$

Equation (2-24) in its expanded form becomes

$$D_{\alpha\beta}c_{\alpha 0}\sum_n \frac{A_n}{\sqrt{D_{\alpha\beta}T_n}}\sin\left(\frac{a/2}{\sqrt{D_{\alpha\beta}T_n}}\right)e^{-t/T_n} = k_{HT}c_{\alpha 0}\sum_n A_n\cos\left(\frac{a/2}{\sqrt{D_{\alpha\beta}T_n}}\right)e^{-t/T_n} \tag{2-25}$$

which after grouping terms can be simplified to

$$c_{\alpha 0}\sum_n A_n\left[\frac{D_{\alpha\beta}}{\sqrt{D_{\alpha\beta}T_n}}\sin\left(\frac{a/2}{\sqrt{D_{\alpha\beta}T_n}}\right) - k_{HT}\cos\left(\frac{a/2}{\sqrt{D_{\alpha\beta}T_n}}\right)\right]e^{-t/T_n} = 0. \tag{2-26}$$

Since the sine and cosine terms in Equation (2-26) are orthogonal, each term in the square brackets should be zero, that leads to

$$\tan\left(\frac{a/2}{\sqrt{D_{\alpha\beta}T_n}}\right) = k_{HT}\sqrt{\frac{T_n}{D_{\alpha\beta}}}. \tag{2-27}$$

If the dimensionless argument of tan in Equation (2-27) is assigned to ξ_n, where

$$\xi_n = \frac{a/2}{\sqrt{D_{\alpha\beta}T_n}}, \text{ or } T_n = \frac{a^2}{4\,D_{\alpha\beta}\xi_n^2}, \tag{2-28}$$

Equation (2-27) simplifies to

$$\xi_n \tan(\xi_n) = \frac{k_{HT}(a/2)}{D_{\alpha\beta}}, \tag{2-29}$$

from which T_ns are calculated.

We now consider A_ns. The molar amount $n_\alpha(t)$ of species α in the slab geometry can be evaluated as a function of time by integration of $c_\alpha(x,t)$ over the slab volume,

$$\begin{aligned} n_\alpha(t) &= \int_{-\frac{a}{2}}^{+\frac{a}{2}} c_\alpha(x,t)\, S dx \qquad (2\text{-}30) \\ &= c_{\alpha 0} S \sum_n 2\, A_n \sqrt{D_{\alpha\beta} T_n} \sin\left(\frac{a/2}{\sqrt{D_{\alpha\beta} T_n}}\right) e^{-t/T_n} \\ &= n_{\alpha 0} \sum_n A_n \xi_n^{-1} \sin(\xi_n)\, e^{-t/T_n}, \end{aligned}$$

where $n_{\alpha 0} = c_{\alpha 0} S a$.

The square molar amount $n_\alpha^2(t)$ would be

$$\begin{aligned} n_\alpha^2(t) &= Sa \int_{-\frac{a}{2}}^{+\frac{a}{2}} c_\alpha^2(x,t)\, S dx \qquad (2\text{-}31) \\ &= c_{\alpha 0}^2 S^2 a \int_{-\frac{a}{2}}^{+\frac{a}{2}} \left[\sum_n A_n \cos\left(\frac{x}{\sqrt{D_{\alpha\beta} T_n}}\right) e^{-t/T_n}\right]^2 dx \\ &= \frac{n_{\alpha 0}^2}{a} \int_{-\frac{a}{2}}^{+\frac{a}{2}} \sum_n A_n^2 \cos^2\left(\frac{x}{\sqrt{D_{\alpha\beta} T_n}}\right) e^{-2t/T_n}\, dx \\ &= \frac{n_{\alpha 0}^2}{a} \sum_n A_n^2 \left[\int_{-\frac{a}{2}}^{+\frac{a}{2}} \cos^2\left(\frac{x}{\sqrt{D_{\alpha\beta} T_n}}\right) dx\right] e^{-2t/T_n} \end{aligned}$$

$$= \frac{n_{\alpha 0}^2}{a} \sum_n \frac{A_n^2}{2} \left[\sqrt{D_{\alpha\beta} T_n} \ \sin\left(2 \frac{a/2}{\sqrt{D_{\alpha\beta} T_n}} \right) + a \right] e^{-2t/T_n}$$

$$= \frac{n_{\alpha 0}^2}{4} \sum_n A_n^2 \left[\frac{\sqrt{D_{\alpha\beta} T_n}}{a/2} \ \sin\left(2 \frac{a/2}{\sqrt{D_{\alpha\beta} T_n}} \right) + 2 \right] e^{-2t/T_n}$$

$$= \frac{n_{\alpha 0}^2}{4} \sum_n A_n^2 [\sin(2\xi_n)/\xi_n \ + 2] e^{-2t/T_n}.$$

Therefore, the squared molar amount at $t = 0$, $n_\alpha^2(0)$, would be

$$n_\alpha^2(0) = n_{\alpha 0}^2 = \frac{1}{4} n_{\alpha 0}^2 \sum_n A_n^2 [\sin(2\xi_n)/\xi_n + 2], \tag{2-32}$$

which is also equal to

$$n_\alpha^2(0) = n_{\alpha 0} \cdot n_{\alpha 0} \sum_n A_n \sin(\xi_n)/\xi_n, \tag{2-33}$$

$$= \ n_{\alpha 0}^2 \cdot \sum_n A_n \sin(\xi_n)/\xi_n.$$

Subtracting Equation (2-33) from Equation (2-32) leads to

$$0 = n_{\alpha 0}^2 \sum_n \frac{1}{4} A_n^2 [\sin(2\xi_n)/\xi_n + 2] - A_n \sin(\xi_n)/\xi_n \tag{2-34}$$

$$= n_{\alpha 0}^2 \cdot \sum_n A_n \left\{ \frac{A_n}{4} [\sin(2\xi_n)/\xi_n + 2] - \sin(\xi_n)/\xi_n \right\}$$

that requires A_n to meet

$$A_n = \frac{4 \sin(\xi_n)/\xi_n}{2 + \sin(2\xi_n)/\xi_n}. \tag{2-35}$$

Equation (2-35), alongside Equations (2-27) and (2-23), completes the solution to the PDE summarized in Table 2-1. Particular solutions of Equation (2-8) could be obtained by assuming

$$c_\alpha(x,t) = F(x)G(t)H(t) \tag{2-36}$$

where $H(t)$ will be found to be

$$H(t) = e^{-t/k_{HG}}. \tag{2-37}$$

Table 2-2 provides the complete solution to the PDE summarized in Table 2-1.

Table 2-2 The solution to the reaction-diffusion problem summarized in Table 2-1.

Concentration Evolution	$c_\alpha(x,t) = c_{\alpha 0}\sum_n A_n \cos\left(\xi_n \frac{x}{a/2}\right) e^{-t/T_n - t/k_{HG}}$
Amount of Substance	$n_\alpha(t) = n_{\alpha 0}\sum_n A_n \xi_n^{-1} \sin(2\xi_n)\, e^{-t/T_n - t/k_{HG}}$
Decay Time Constants	$\xi_n \tan(\xi_n) = k_{HT}(a/2)/D_{\alpha\beta}$
	$T_n = \frac{a^2}{4\, D_{\alpha\beta}\xi_n^2}$
Constants	$A_n = \frac{4\ \sin(\xi_n)/\xi_n}{2 + \sin(2\xi_n)/\xi_n}$

The approach undertaken in this section is similar to those used in studies of transport phenomena (Bird, Stewart, Lightfoot 1966, pp. 529-537)

2.1.2 Magnetic Resonance Relaxation versus Chemical Reaction

MR relaxation of fluids in porous materials could be modeled using the same mathematical analysis presented in the previous subsection by assuming a simplified hypothetical reaction such as: excited → relaxed.

The concentration of excited nuclei, in contrast to chemical systems, is expressed as magnetic moment per unit volume $m(x,t)$ along some specified direction; while the amount of magnetization is expressed as the total nuclear magnetization $M(t)$ of the sample. In such an analogy, the bulk relaxation rate $1/T_{1b}$ and MR surface relaxivity ρ of the nuclear magnetization is analogous to the homogeneous and heterogeneous chemical reaction rate constants k_{HG} and k_{HT}, respectively. Table 2-3 demonstrates the analogy between different parameters in the chemical reaction and MR relaxation mathematical models. Table 2-4 transforms the notation used in the previous section to describe MR longitudinal relaxation for a slab geometry. Please note that both problems are equivalent, and the longitudinal magnetization is normalized in the range of 0 to 1 instead of -1 to 1.

Table 2-3 Analogous parameters in a chemical reaction and in MR relaxation mathematical models.

Description	Chemical Reaction	MR Relaxation
Density	$c_{\alpha 0}(x,t)$	$m(x,t)$
Amount	$n_{\alpha}(t)$	$M(t)$
Homogeneous Rate Constant	k_{HG}	$1/T_{1b}$
Heterogeneous Rate Constant	k_{HT}	ρ_1
Diffusivity	$D_{\alpha\beta}$	D

Table 2-4 The magnetization evolution in a slab geometry for longitudinal MR relaxation.

Problem		
Partial Differential Equation	$\frac{\partial m(x,t)}{\partial t} - D\frac{\partial^2 m(x,t)}{\partial x^2} = -\frac{m(x,t)}{T_{1b}}$	(2-38)
Initial Condition	$m(x,0) = m_0$	(2-39)
Boundary Condition 1	$-D\frac{\partial m(+a/2\,,t)}{\partial x} = \rho_1 m(+a/2\,,t)$	(2-40)
Boundary Condition 2	$-D\frac{\partial m(-a/2\,,t)}{\partial x} = \rho_1 m(-a/2\,,t)$	(2-41)
Solution		
Magnetization Evolution	$m(x,t) = m_0 \sum_n A_n \cos\left(\xi_n \frac{x}{a/2}\right) e^{-t/\tau_{1n}}$	(2-42)
Total Magnetization	$M(t) = M_0 \sum_n I_n e^{-t/\tau_{1n}}$	(2-43)
Decay Time Constants	$\xi_n \tan(\xi_n) = \rho_1(a/2)/D$	(2-44)
	$T_{1n} = \frac{a^2}{4\,D\xi_n^2}$	(2-45)
	$\frac{1}{\tau_{1n}} = \frac{1}{T_{1n}} + \frac{1}{T_{1b}}$	(2-46)
Constants	$A_n = \frac{4\ \sin(\xi_n)/\xi_n}{2 + \sin(2\xi_n)/\xi_n}$	(2-47)
	$I_n = \frac{4\ \sin^2(\xi_n)}{\xi_n(2\xi_n + \sin(2\xi_n))}$	(2-48)

2.1.3 MR Relaxation in Slab Geometry – Special Cases

In this section, we review the properties of magnetization evolution and total magnetization in MR relaxation in a slab geometry for a few special cases. The Brownstein-Tarr dimensionless number

$$\mathrm{BT}_1 = \frac{\rho_1(a/2)}{D}$$

lies at the core of the properties of the magnetization evolution and total magnetization function through Equation (2-44) that determines ξ_n. BT_1 is named in this work after K. R. Brownstein and C. E. Tarr who investigated the importance of diffusion in relaxation in porous media (Brownstein and Tarr, 1979). The dimensionless number analogous to BT_1 is the Damköhler number of the second kind which is the ratio of reaction to diffusion rate in diffusion-reaction systems (Bird, Stewart, and Lightfoot 2002).

Case I – $\mathrm{BT}_1 \ll 1$, diffusion rate is much faster than surface relaxation rate

In this case, employing the Taylor series expansion of $\tan$ at $\xi_n = 0$ for small values of ξ_n, Equation (2-44) simplifies to

$$\xi_0^2 \cong \frac{\rho_1(a/2)}{D} \tag{2-49}$$

which using $T_{10} = a^2/4\,D\xi_0^2$ results in

$$T_{10} = a/2\rho_1. \tag{2-50}$$

For $n > 0$, Equation (2-44) simplifies to $\tan(\xi_n) \cong 0$ with solutions of $\xi_n = n\pi$ for which the corresponding time constants are

$$T_{1n} = \frac{a^2}{4\, n^2 \pi^2 D}. \tag{2-51}$$

The first term of the summation in Equations (2-42) and (2-43) dominate, $A_0 \cong I_0 \cong 1$, and the magnetization profile in the x-direction case is almost constant in this case:

$$m(x,t) = m_0 \cos\left(\xi_0 \frac{x}{a/2}\right) e^{-t/\tau_{10}} \approx m_0 e^{-t/\tau_{10}}, \text{ and} \tag{2-52}$$

$$M(t) = M_0 e^{-t/\tau_{10}}, \tag{2-53}$$

where

$$\frac{1}{\tau_{10}} = \frac{1}{T_{10}} + \frac{1}{T_{1b}}. \tag{2-54}$$

Please note that rewriting Equation (2-54) using Equation (2-50) leads to

$$\frac{1}{\tau_{10}} = \frac{\rho_1}{a/2} + \frac{1}{T_{1b}} \tag{2-55}$$

which is the simplified case of

$$\frac{1}{\tau_{10}} = \rho_1 \frac{2S}{Sa} + \frac{1}{T_{1b}} = \rho_1 \frac{S_p}{V_p} + \frac{1}{T_{1b}} \tag{2-56}$$

that is the well-known relationship for relaxation in porous media in the fast-exchange regime (Coates et al. 1999, p. 65), where S_p and V_p are the pore surface area and pore volume, respectively.

Case II – $\mathrm{BT}_1 \gg 10$, diffusion rate is much slower than surface relaxation rate

In this case, we can assume $\xi_n \tan(\xi_n) = +\infty$ the solutions of which are

$$\xi_n = \pi\left(n + \tfrac{1}{2}\right). \tag{2-57}$$

The transverse relaxation time constants would then be

$$T_{1n} = \frac{a^2}{4\,D\pi^2\left(n+\frac{1}{2}\right)^2}. \tag{2-58}$$

The magnetization evolution function and total magnetization of the systems in this case are:

$$m(x,t) = m_0 \textstyle\sum_n A_n \cos\left(\pi\left(n + \frac{1}{2}\right)\frac{x}{a/2}\right) e^{-t/\tau_{1n}}, \text{ and} \tag{2-59}$$

$$M(t) = M_0 \textstyle\sum_n I_n e^{-t/\tau_{1n}}, \tag{2-60}$$

where

$$A_n = \frac{2\ \mathrm{sinc}\left(\pi\left(n+\frac{1}{2}\right)\right)}{1+\mathrm{sinc}\left(2\pi\left(n+\frac{1}{2}\right)\right)}, \text{ and} \tag{2-61}$$

$$I_n = 2\ \mathrm{sinc}^2\left(\pi\left(n+\tfrac{1}{2}\right)\right). \tag{2-62}$$

Therefore, it is shown here that the mathematical problems of reaction-diffusion and relaxation-diffusion in the slab geometry are equivalent. This analogy can be also generalized to any geometry.

In magnetic resonance relaxation of rocks at common magnetic field strengths in laboratories, BT_1 is neither in the fast-exchange regime nor in the slow exchange regime. The value of BT_1 commonly lies in the range of 0.1 to 10 which makes possible the observation of non-ground modes that allow the calculation of pore size from simple magnetic resonance relaxation experiments. This phenomenon is utilized in Chapter 7 for the computation of pore size in experiments starting with an initial homogeneous magnetization.

In the next section, equations like Equation (2-56) will be derived for transverse relaxation without the complications caused by diffusion, by assuming that the bulk fluid in the pore is in fast exchange with the interfacial fluid.

2.2 Magnetic Resonance in Porous Rocks

The subject of MR in porous rocks in the context of nuclear magnetic resonance (NMR) logging is well established (Coates et al. 1999). Each MR experiment involves a spectrometer registering a time-varying electric signal received by a radio frequency (RF) coil. In porous materials, the MR signal is normally in the form of $I_{i0}\exp(-t/\tau_i)$ or a

summation of such terms in which I_{i0} is an initial amplitude, τ_i is an exponential decay constant, and t is the evolution time after manipulating magnetization employing an RF pulse.

MR experiments can be designed to extract ^{1}H density, the longitudinal relaxation time constant T_1, the transverse relaxation time constant T_2, the effective transverse relaxation time constant T_2^*, or diffusivity D from the initial amplitude or decay constant of the signal or a series of signals. Properties of fluids (Hürlimann et al. 2009) and porous media (Kleinberg 1999) can be measured or inferred from these MR properties. For example, fluid content is proportional to the ^{1}H density and pore surface-to-volume ratio is correlated with $1/T_2$.

2.2.1 Transverse Relaxation in Porous Rocks

The transverse relaxation time constant T_2 is one of the primary MR parameters of interest to petroleum engineers. T_2 has the potential to provide information such as pore size distribution, permeability, oil saturation, oil viscosity, and irreducible water saturation (Coates et al. 1999).

The transverse relaxation rate $1/T_2$ in porous rocks is primarily affected by three processes: (1) bulk fluid relaxation, (2) surface relaxation, and (3) diffusion in magnetic field gradients. The three relaxation processes in porous rocks act in parallel and their rates add to determine the total transverse relaxation rate,

$$\left(\frac{1}{T_2}\right)_{total} = \left(\frac{1}{T_2}\right)_B + \left(\frac{1}{T_2}\right)_S + \left(\frac{1}{T_2}\right)_D \quad (2\text{-}63)$$

where $(1/T_2)_B$ is the bulk contribution, $(1/T_2)_S$ is the surface contribution, and $(1/T_2)_D$ is the contribution of diffusion in internal magnetic field gradients (Kleinberg 1999).

2.2.2 Bulk Relaxation

The term bulk relaxation is applied to the relaxation measured in a fluid when surface and magnetic gradient effects are eliminated (Kenyon 1997). It can be measured by employing the Carr-Purcell-Meiboom-Gill (CPMG) method with a uniform sample in a homogeneous magnetic field. The bulk transverse relaxation time constant depends on the dynamics of the fluid, which is affected by chemical composition, temperature, and pressure. The bulk transverse relaxation time constant of dead oils (crude oils with almost no remaining dissolved gas) is a function of their viscosity and temperature (Coates et al. 1999),

$$T_{2bulk} = 0.00713\ \frac{T}{\eta}, \quad (2\text{-}64)$$

where T is the absolute temperature in Kelvin, and η is fluid viscosity in mPa.s. This relationship is employed in Chapter 6 to report on the viscosity change during the process of extraction of light fluid components from heavy oil.

2.2.3 Surface Relaxation

Surface defects and paramagnetic ions such as iron and manganese significantly enhance transverse relaxation at the pore surface (Kleinberg 1999). Surface relaxation mechanisms

include homonuclear dipole-dipole coupling, cross-relaxation by other nuclear spins, relaxation by paramagnetic ions, and relaxation by free electrons (Kleinberg 1999).

The surface relaxation rate is usually faster than that of the bulk fluid. Therefore, if fluid diffusion within a pore is much faster than the relaxation rate at the pore surface, all fluid molecules relax at the pore surface. This condition is called the fast diffusion limit (Coates et al. 1999). It is possible to measure the pore surface-to-volume ratio employing the CPMG method through the transverse relaxation rate,

$$\frac{1}{T_{2surface}} = \rho_2 \left(\frac{S}{V}\right)_{pore}, \tag{2-65}$$

where ρ_2 is the surface relaxivity and $(S/V)_{pore}$ is the pore surface-to-volume ratio.

2.2.4 Diffusion Induced Relaxation

Magnetic fields induce internal magnetic field gradients in the pore space of rocks (Hürlimann 1998), due to the magnetic susceptibility mismatch between the rock matrix and pore fluids. This effect scales with static magnetic field strength. Diffusion of fluid molecules in a region of variable magnetic field increases the average transverse relaxation rate by

$$\frac{1}{T_{2\text{diffusion}}} = D\frac{(\gamma G_i t_E)^2}{12} \tag{2-66}$$

where D is the molecular self-diffusivity of the bulk fluid, γ is the gyromagnetic ratio, G_i is the internal magnetic field gradient in the pore space, and t_E is the echo time.

Employing a low static magnetic field and a short echo time ensure that the contribution of diffusion-induced transverse relaxation is negligible. It is assumed that this condition was met in all MRI measurements in this research. The SE-SPI experiments were performed with an echo time of 1.8 ms at static magnetic fields of 0.2 T or 0.05 T. It has been reported that internal magnetic field gradients in porous rocks become important beyond 0.24 T (Mitchell and Fordham 2014). Studying liquids with moderate molecular diffusivity D further reduces the contribution of the third term in Equation (2-63).

Substituting Equations (2-65) and (2-66) in Equation (2-63) yields

$$\frac{1}{T_2} = \frac{1}{T_{2bulk}} + \rho_2 \left(\frac{S}{V}\right)_{pore} + D\frac{(\gamma G t_E)^2}{12}. \tag{2-67}$$

This is the average transverse relaxation rate equation in porous rocks as commonly applied in MR logging and core analysis.

2.2.5 Surface Relaxation: Two Different View Points

There are two models in the literature that consider the effect of surface relaxation on the average transverse relaxation of exchanging systems: (1) diffusion in a medium with surface-like sinks, and (2) the two-population bound/bulk fluid system.

Brownstein and Tarr (1979) developed the mathematical foundation for the effect of diffusion on the average transverse relaxation rate in a system with surface- and volume-like sinks. Only the molecular diffusivity of the bulk fluid is used in their model to show

that the multi-exponential nature of the relaxation is a consequence of geometry of the medium. From their model, they found (1) the length-scale at which surface effects become important, (2) the characteristic size of the medium, and (3) the ratio of active volume to total fluid volume. This model is not typically employed in the petroleum industry because of its mathematical complexity.

The two-population surface/bulk fluid system assumes that there are two volume elements within a single pore: surface fluid and bulk fluid. The surface fluid has different physical properties, particularly a short transverse relaxation time constant, T_{2s}. The surface fluid forms a layer of thickness δ on wetted surface S in a pore of volume V. The rest of the pore contains bulk fluid which has bulk physical properties and relaxes at rate $1/T_{2b}$. The surface and bulk fluids are assumed to exchange rapidly. Therefore, the relaxation rate of these two populations add to yield a weighted average transverse relaxation rate,

$$\frac{1}{T_2} = \left(1 - \frac{\delta S_p}{V_p}\right)\frac{1}{T_{2b}} + \frac{\delta S_p}{V_p}\frac{1}{T_{2s}}. \tag{2-68}$$

Low magnetic fields induce minimal internal magnetic field gradients in the pore space (Hürlimann 1998). Equation (2-68) is derived assuming that internal magnetic field gradients are insignificant.

Under different experimental conditions, it is possible that one or more of the terms in Equation (2-67) become insignificant. If the diffusion rate D/r^2, where r is the pore radius, is greater than the surface relaxation rate $1/T_{2s}$, the second term in the right side of

Equation (2-67) dominates the average relaxation rate (Kenyon 1997). For liquids in Berea sandstone, at low static magnetic fields, the condition for fast-diffusion regime holds as follows (Coates et al. 1999):

$$\frac{1}{T_2} = \frac{\delta S_p}{V_p}\frac{1}{T_{2s}}. \tag{2-69}$$

Therefore, it is possible to extract information about the surface-to-volume ratio of pores in the fast-diffusion regime. A pore departs the fast diffusion regime when the pore size becomes large or the surface relaxation time constant or self-diffusion decreases (Kenyon 1997). For example, the self-diffusivity of heavy oil is not sufficiently high for all its protons to relax at the pore surface. Therefore, for heavy oil in a Berea core plug, at low magnetic fields, bulk processes are the main contributor to the transverse relaxation mechanisms (Coates et al. 1999). Thus,

$$\frac{1}{T_2} = \frac{1}{T_{2b}}, \tag{2-70}$$

where T_{2b} is the bulk heavy oil transverse relaxation time constant.

Equations (2-69) and (2-70) form the basis of the quantitative MRI methods employed in Chapters 4 and 6 of this research. Equation (2-69) provides the surface area in contact with fluids, while Equation (2-70) gives the bulk fluid relaxation time for heavy oils. It is possible to predict a variety of petrophysical properties and fluid characteristics from these

two MR parameters. Quantities such as pore size, permeability, and viscosity are commonly deduced from MR measurements.

The author has developed models like Equation (2-69) to account for two-phase/two-component and single-phase/two-component decane/CO_2 mixtures in Berea core plugs as described in Chapter 6. These models provided

(1) quantitative data on the pore surface area wetted by the decane-rich phase of a Berea core plug saturated by a decane/CO_2 mixture, and

(2) quantitative data about the density of decane molecules in the bound fluid layer of single phase decane/CO_2 mixture saturating Berea core plugs.

The bound/bulk fluid model is the model commonly used in petroleum engineering and therefore it was also employed in this work for analyzing the experimental data. The Brownstein-Tarr solution was employed only in Chapter 7 to analyze the experimental data.

2.3 Magnetic Resonance Imaging

Nuclear magnetic resonance (NMR) logs measure MR properties, such as proton density (^{1}H content), T_1, T_2, and D, as a function of reservoir depth in oil wells. Spatial resolution is achieved by displacing the NMR logging instrument vertically in the well. In contrast to NMR logging, laboratory MRI instruments measure MR properties of 3D objects by the application of external magnetic field gradients (Nishimura 2010). External magnetic field

gradients change the static magnetic field of the laboratory MRI instruments linearly in the x, y, and z directions. It is possible to switch external magnetic field gradients and apply RF excitation pulses in many ways to acquire MR images of objects. The chronological order by which the switching external magnetic field gradients and RF pulses are applied is called a pulse sequence. There are a variety of tailored pulse sequences that measure MR parameters (Brown et al. 2014). Mitchel et al. (2013) have reviewed MRI methods for petrophysical studies of reservoir core and core plug samples.

MRI methods determine the MR properties of rocks in one, two, or three dimensions and save them as arrays in computer systems. MR images are arrays containing MR parameters as a function of position. One-dimensional MRI images are vectors, 2D MRI images are matrices, and 3D images are three dimensional arrays, a stack of matrices. In addition, it is possible to acquire time resolved images which add an additional dimension to the measurement array.

For visualization purposes, MRI images can show MR properties in grayscale or color using color maps. However, if quantitative MRI methods are applied, it is possible to employ these MRI data arrays in petrophysical calculations. The Single Point Ramped Imaging with T_1-Enhancement (SPRITE) and T_2-mapping SE-SPI methods are pure phase-encoding MRI methods with quantitative capabilities that are designed for core laboratory measurements. The SPRITE and SE-SPI methods can measure fluid content and the T_2 distribution in core plugs within quantitative uncertainties of conventional laboratory

methods (Muir and Balcom 2012; and Mitchel et al. 2013). These two methods are particularly useful in core flooding applications to measure fluid content and the T_2 distribution as a function of time and position within a core plug.

In most core flooding applications, the variation of petrophysical properties of interest are along the axis of the core plug, rather than the radial direction. This is because the periphery of the core plug is a no-flow boundary and the length of the core plug is usually longer than its diameter in such experiments. The SPRITE and SE-SPI methods are often employed to image core plugs in one dimension only. This saves time and increases the signal-to-noise (SNR) ratio. SNR, experiment time, and the dominance of phenomena only in the axial direction are three factors that motivate performing quantitative MRI measurements mainly in one dimension.

2.3.1 Data Processing

Petrophysical or fluid phase properties, such as saturation, porosity, permeability, and viscosity, have applications in verifying models of fluid transport in porous rocks developed as the solution of PDE with different boundary conditions. Usually, experimental measurements for such verifications are limited to bulk properties. The 1D double half k-space (DHK) SPRITE method can provide quantitative porosity and saturation profiles along a core plug. In addition, T_2-mapping SE-SPI can report quantitatively on the viscosity of the hydrocarbon phase, permeability, and wetted pore surface area along a core plug. These two methods have the potential to verify a variety of

mechanisms and mathematical models describing displacement processes in porous rocks. The objective of this work was not the validation of petrophysical models of fluid flow based on PDE equations of time and position. However, this work provides spatially and temporally resolved properties for such investigations. Chapter 5 studies the evolution of the advection-dispersion PDE kernel in miscible and immiscible displacement of decane by CO_2 in Berea sandstone as an example.

The 1D DHK SPRITE method (Muir and Balcom 2012) measures proton density as a function of position along a core plug. Each 1D DHK SPRITE profile is a vector containing numbers which are proportional to the number of moles of hydrogen atoms present in a volume element (voxel) within the core plug. This vector can be converted to a porosity profile or saturation profile along the core plug employing different mathematical operations. Calibration measurements using pore-filling fluids and imaging before starting the process are necessary for calculations that respectively provide porosity or saturation profiles.

T_2-mapping SE-SPI measures T_2-weighted profiles, as vectors, along the core plug. The T_2-weighted profiles are usually pruned to reduce the number of profiles. The pruning results in reduced computation time in time-consuming T_2 inversion algorithms or curve-fitting procedures. Ultimately, performing T_2 inversion or exponential curve fitting on the profiles calculates the T_2 distribution for each voxel within a core plug. The T_2 distribution for each voxel can further be converted into a single mean value (Nechifor et al. 2014),

most commonly the logarithmic mean T_2 (Borgia et al. 1997). The logarithmic mean T_2, $T_{2\mathrm{LM}}$, is the best average method as it has shown a better agreement in petrophysical correlations than other averaging methods. Other petrophysical properties can be acquired from the petrophysical correlations with porosity, saturation, and $T_{2\mathrm{LM}}$. This vector calculation is easy, robust and can be reduced to an average to provide bulk properties of core plugs.

An extensive function library was developed in this research in the MATLAB programming language to read MR and MRI data and image files, perform phase correction, remove background signal, filter images, perform Fourier transformation, perform image registration, perform uncertainty calculation, and store and visualize data. Petrophysical properties have been evaluated utilizing this function library and reported for three cases in this research:

(1) Porosity and permeability ratio before and after fines migration in a Berea core plug as a function of position,

(2) Molar saturation of decane, wetted pore surface area for the immiscible CO_2 flooding of decane, the density of decane molecules on the pore surface in miscible flooding of decane by CO_2, partial derivatives of saturation with respect to position and time, wave velocity, dispersion coefficient, and advection-dispersion kernel.

(3) Pore size in natural rocks from $T_1 - T_2$ experiments.

Fines migration experiments are discussed in Chapter 4, CO_2 flooding of oil saturated core plugs is discussed in Chapters 5 and 6, and measurement of pore size in rocks is discussed in Chapter 7.

2.4 References

Bird, R. B., Stewart, W. E., Lightfoot, E. N. 1966. *Transport Phenomena*. New York: Wiley.

Borgia, G. C., Brown, R. J. S., and Fantazzini, P. 1997. Different "Average" Nuclear Magnetic Resonance Relaxation Times for Correlation with Fluid-Flow Permeability and Irreducible Water Saturation in Water-Saturated Sandstones. *J. Appl. Phys.* 82 (9): 4197-4204. http://dx.doi.org/10.1063/1.366222.

Brown, R. W., Cheng, T. C. N., Haacke, E. M., Thompson, M. R., Venkatesan, R. 2003. *Magnetic Resonance Imaging: Physical Principles and Sequence Design, 2nd Ed.* New York: Wiley-Blackwell.

Brownstein, K. R., Tarr, C. E. Importance of Classical Diffusion in NMR Studies of Water in Biological Cells. *Phys. Rev. A* 19 (6): 2446-2453. http://dx.doi.org/10.1103/PhysRevA.19.2446.

Coates, G. R., Xiao, L., and Prammer, M. G. 1999. *NMR Logging: Principles and Applications*. Houston: Halliburton Energy Services.

Hürlimann, M. D. 1998. Effective Gradients in Porous Media due to Susceptibility Differences. *J. Magn. Reson.* 131 (2): 232-240. http://dx.doi.org/10.1006/jmre.1998.1364.

Hürlimann, M. D., Freed, D. E., Zielinski, L. J., et al. 2009. Hydrocarbon Composition from NMR Diffusion and Relaxation Data. *Petrophysics* 50 (2): 116-129. SPWLA-1997-v38n2a1.

Kleinberg, R. L. 1999. Nuclear Magnetic Resonance. In *Methods in the Physics of Porous Media*, ed. Wong, P., Chap. 9, 337-385. San Diego: Academic Press. http://dx.doi.org/10.1016/S0076-695X(08)60420-2.

Kenyon, W. E. 1997. Petrophysical Principles of Applications of NMR Logging. *Log Analyst* 38 (2): 21-40.

Mitchell, J., Fordham, E. J. Contributed review: Nuclear magnetic resonance core analysis at 0.3 T. *Rev. Sci. Instrum.* 85 (11): 111502. http://dx.doi.org/10.1063/1.4902093.

Mitchell, J., Chandrasekera, T. C., Holland, D. J., et al. 2013. Magnetic Resonance Imaging in Laboratory Petrophysical Core Analysis. *Phys. Rep.* 526 (3): 165-225. http://dx.doi.org/10.1016/j.physrep.2013.01.003.

Muir, C. E. and Balcom, B. J. 2012. Pure Phase Encode Magnetic Resonance Imaging of Fluids in Porous Media. In *Annual Reports on NMR Spectroscopy*, Vol. 77, ed. Webb, G.A., Chap. 2, 81-113.Burlington: Academic Press. http://dx.doi.org/10.1016/B978-0-12-397020-6.00002-7.

Nechifor, R. E., Romanenko, K., Marica, F. et al. 2014. Spatially Resolved Measurements of Mean Spin-Spin Relaxation Time Constants. *J. Magn. Reson.* 239: 16-22. http://dx.doi.org/10.1016/j.jmr.2013.11.012.

Nishimura, D. G. 2010. *Principles of Magnetic Resonance Imaging*. Palo Alto: Stanford University.

Stapf, S., Han, S. -I. 2006. *NMR Imaging in Chemical Engineering*. Berlin: Wiley-VCH.

Chapter 3 – Instruments, Materials, and Experimental Methods

The objective of this chapter is to document the assembly and operation of core flooding apparatus compatible with magnetic resonance (MR) measurements. This chapter elaborates on the technical aspects of this work that was not covered in Chapters 4 - 6. The instruments, flow system, materials, material selection, and procedures for the pressurizing and depressurizing of the apparatus are described below.

3.1 Instruments

The samples under study in this research are core plugs that are cylindrical porous rocks of 38 mm diameter and lengths ranging from 40 to 70 mm. Fluids are driven into the core plugs to displace the original fluids saturating the core plugs. Therefore, a core displacement flow system was employed to inject the fluids into the core plugs. Each fluid was injected into the flow system using a pump connected to a plumbing system that included tubing lines, unions, tees, crosses, needle valves, check valves, relief valves, back pressure regulators, and 3-way ball valves.

Experiments, including CO_2 flooding of decane, CO_2 flooding of heavy oil, and fines migration, utilized similar flow systems with minor differences. A generalized flow system that unifies the important features of these flow systems is shown in the simplified diagram of Figure 3-1. The experimental setup for the CO_2 flooding of decane-saturated core plugs is shown in Figure 3-2. The core flooding displacement tests were conducted at elevated

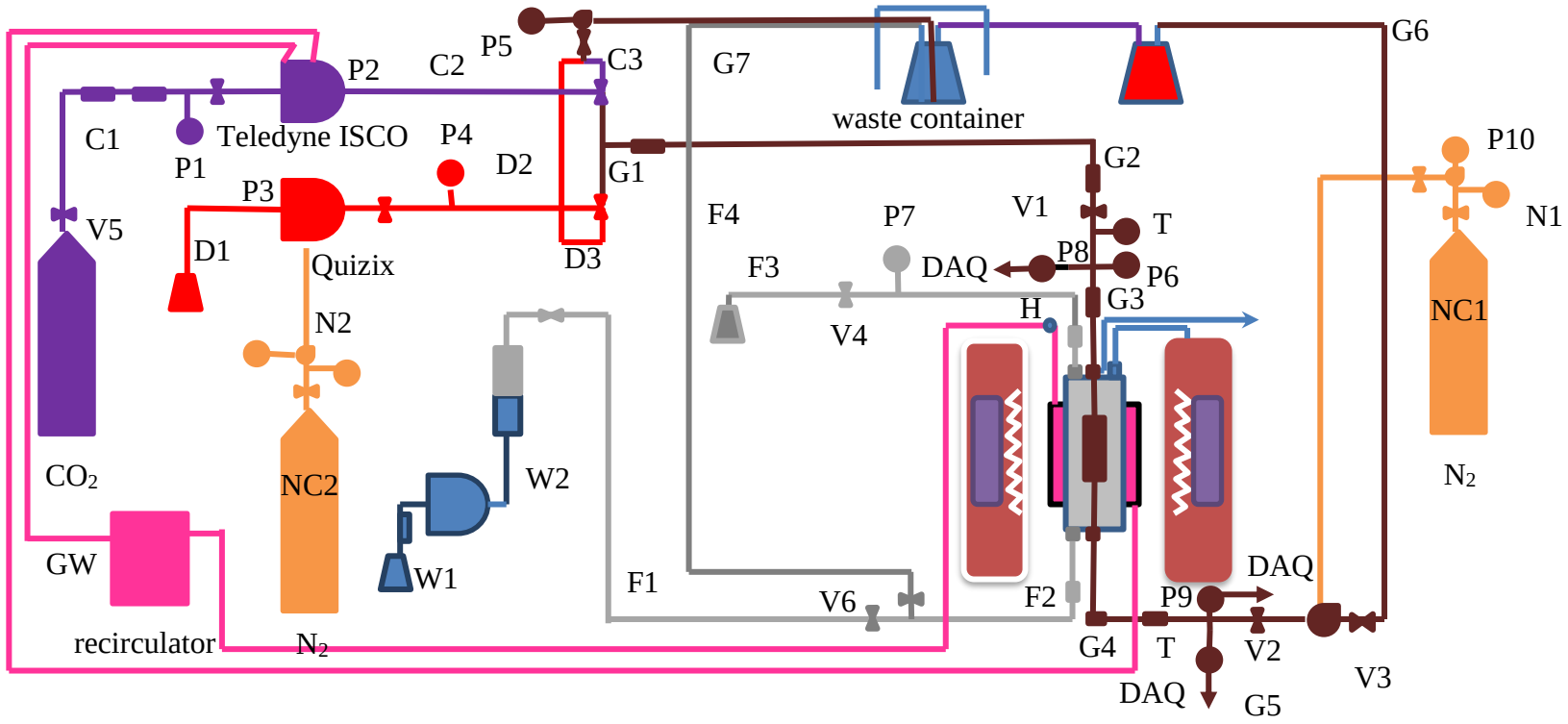

Figure 3-1 The generalized flow system utilized in experiments performed in this research. The diagram is color coded based on fluids the tubing lines carry: orange for nitrogen, red for decane, blue for water and brine, purple for carbon dioxide, pink for glycerol/water mixture, and gray for Fluorinert. Brown tubing lines can carry a mixture of fluids.

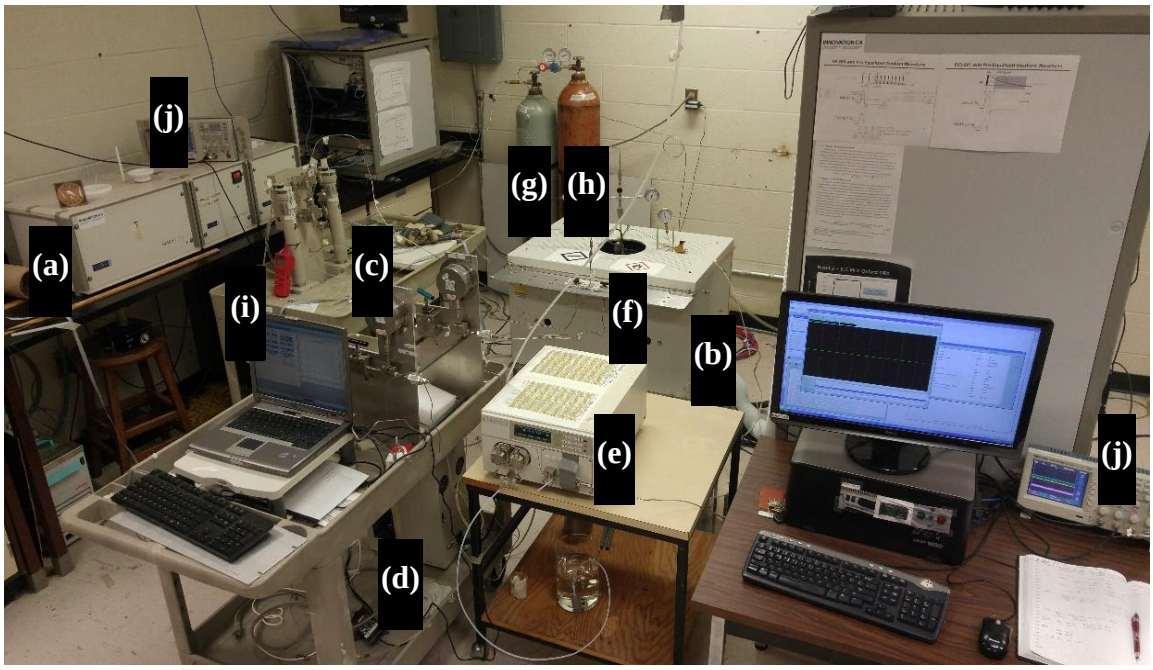

Figure 3-2 Flow system and instruments employed in CO_2 flooding experiments. The 2 MHz (a) and 8.5 MHz (b) MRI magnets, the Teledyne ISCO (c), Quizix (d), and Shimadzu (e) pumps, the valve panel (f), the CO_2 (g) and N_2 (h) cylinders, CO_2 meter (i), and oscilloscopes (j) are visible in this picture.

pressures, therefore, a robust flow system was designed to apply the correct boundary conditions to the core plug for each fluid displacement experiment.

A variety of instruments, including pumps, data acquisition (DAQ) devices, pressure transducers, thermocouples, magnetic resonance imaging (MRI) systems, and an oscilloscope, were employed in these flow experiments. Some of these instruments are

discernible in Figure 3-2 and 3-3. The technical details of the flow system and instruments employed in this research are presented below.

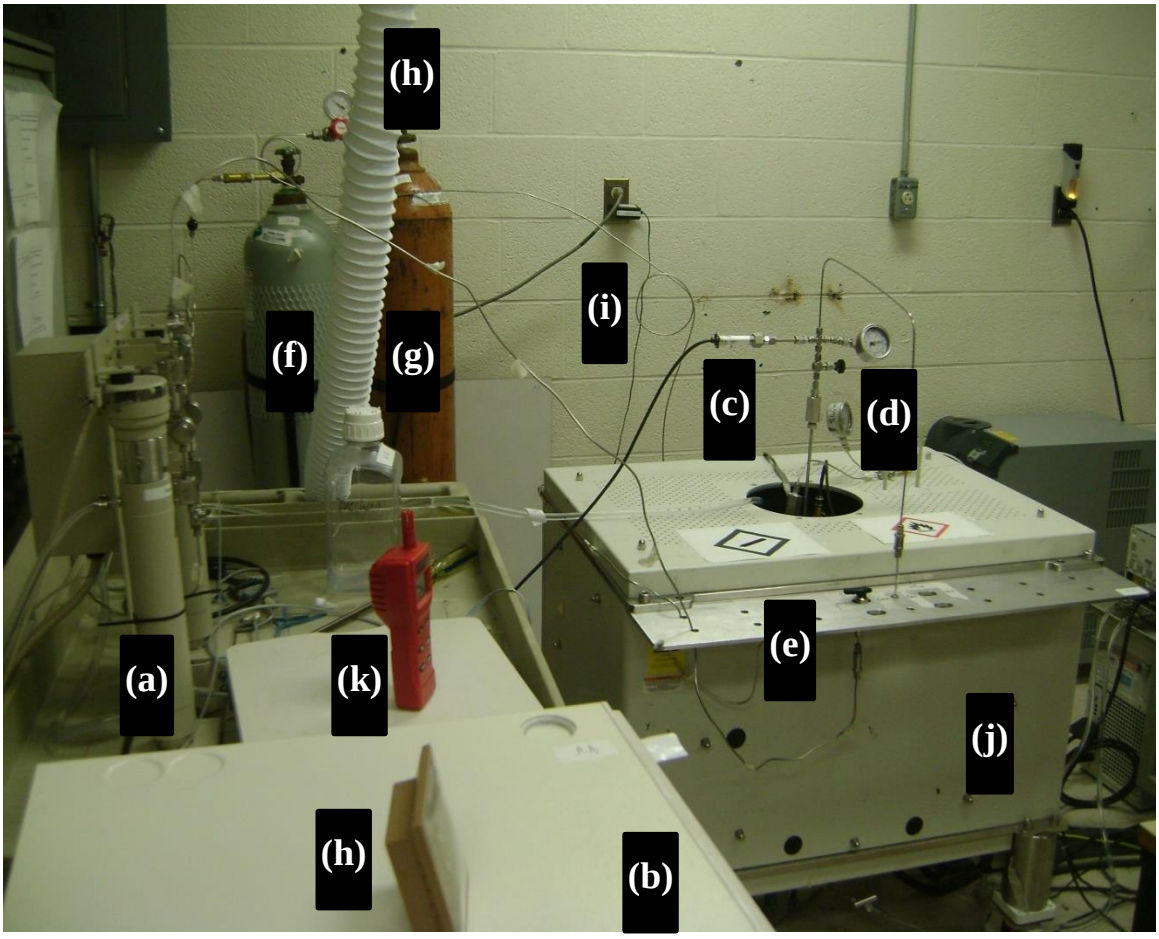

Figure 3-3 The flow system. The Teledyne ISCO (a) and Shimadzu (b) pumps, an Ashcroft K1 pressure transducer (c), an analog Swagelok pressure gauge (d), the valve panel (e), the CO_2 (f) and N_2 (g) cylinders, thermometer (h), coiled tubing (i), MRI magnet (j), and the CO_2 meter (k) are visible in this picture.

3.1.1 System Components

Supercritical CO_2, at pressures exceeding 7 MPa and in volumes as large as a standard 38 mm diameter core plug, is a major challenge to MR measurements. The current study employed MS-5000, a new high-pressure non-magnetic metallic core holder that was designed by Mojtaba Shakerian and built in-house (Shakerian et al. 2017; Li et al. 2016). This core holder has a working pressure of 35 MPa and working temperature of 170 °C. In this study, the core holder was employed at 40°C and pressures up to 20 MPa. This core holder was made of Hastelloy-C276 (Haynes International Inc., IN, USA), which is non-magnetic and has low electrical conductivity (Shakerian et al. 2017) to reduce eddy currents induced by switching magnetic field gradients (Goora et al. 2014). This core holder also features an integrated solenoid radiofrequency (RF) probe. The incorporation of the RF probe inside the vessel enhances the Signal-to-Noise Ratio (SNR) according to the principle of reciprocity (Hoult and Richards 1976). This core holder was placed inside the Maran DRX-HF MRI magnet (Figure 3-3j) for high pressure experiments.

Two MRI systems were utilized in this study: (1) 2.21 MHz Oxford Maran Ultra, and (2) 8.5 MHz Oxford Maran DRX-HF, both from Oxford Instruments (Abingdon, UK). The Oxford Maran Ultra (Figure 3-2a) was utilized during the low-pressure fines migration experiment. The Oxford Maran Ultra is a vertical bore permanent magnet with an internal bore diameter of 51 mm operating at a ^{1}H frequency of 2.21 MHz. This unit includes an RF probe and RF amplifier, a Crown Macro-Tech 5002VZ gradient amplifier. This unit has only one magnetic field gradient, in the *y*-direction, with a maximum strength of 41.5

G/cm. The DRX-HF system has a vertical bore permanent magnet, shown as ‘b’ in Figure 3-2, operating at a ^{1}H frequency of 8.5 MHz. This unit includes a 1 KW BT01000-AlphaS RF amplifier (TOMCO Technologies, Sydney, Australia) and a shielded three-axis magnetic field gradient coil set driven by three Techron 7782 (Techron, Elkhart, IN) gradient amplifiers providing maximum magnetic field gradients of 26 G/cm, 24 G/cm, and 33 G/cm in the *x*, *y*, and *z*-directions, respectively.

A valve panel, as shown in Figure 3-4, was connected to the top of the MRI magnet to facilitate fluid flow from the pumps to the core holder. Three dual-cylinder pumps manufactured by different vendors were employed in this work: (1) Teledyne ISCO 100DX, (2) Quizix 6000-SS, and (3) Shimadzu LC-8A. A Teledyne ISCO 100DX (Teledyne ISCO, Lincoln, NE) pump equipped with heating jackets was utilized for injecting CO_2. The Teledyne ISCO and Quizix pumps are equipped with integrated DAQ systems with analog and digital input/output ports. However, the DAQ system for the Teledyne ISCO pump (shown as ‘c’ and ‘a’ in Figure 3-2 and Figure 3-3, respectively) can only show readings on a computer screen and cannot record pressure and flow rate data due to limited software features. New software in the LabVIEW (National Instruments, Austin, TX) environment should be developed so that pressure and flow rate readings from the Teledyne ISCO pump can be recorded.

Two Quizix 6000-SS (Chandler Engineering, Tulsa, OK) pumps were utilized for pumping the aqueous and oleic phases. Li (2009) has discussed important features and operational

procedures for this pump. Care was taken to ensure that the pumps did not contain air in their cylinders before starting the experiments. Two Shimadzu LC-8A (Shimadzu, Kyoto, Japan) pumps, Figure 3-2e, were employed for pumping the water phase into the core plugs or the transfer vessels.

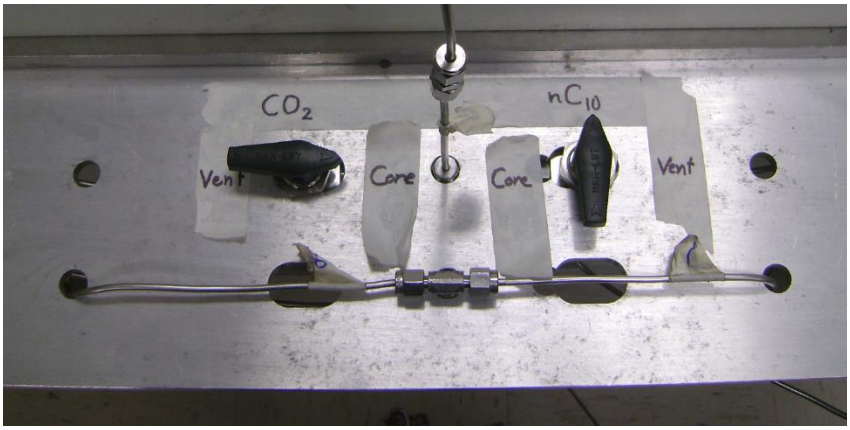

Figure 3-4 The valve panel. Up to four 3-way ball valves can be installed on the valve panel to facilitate fluid flow to the core holder or the waste container.

The transfer vessel (Figure 3-5) employed in this study was manufactured by Phoenix Instruments (Splendora, TX) from stainless steel 316 with a capacity of 250 cc and a working pressure of 69 MPa. 250 cc of Fluorinert (3M, St. Paul, MN) was charged in the transfer vessel for each of the CO_2 flooding experiments. Fluorinert is heavier than water and is immiscible with hydrocarbon oils and water; therefore it is easy to identify or separate it from other phases in case of leakage. The following procedure was employed for preparing the transfer vessel.

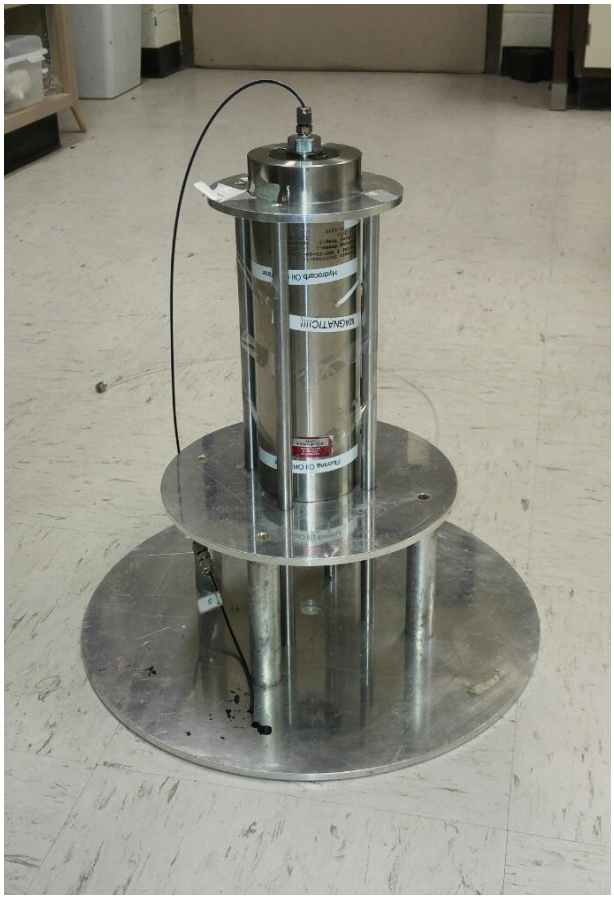

Figure 3-5 Transfer vessel (Phoenix Instruments, Splendora, TX) and its stand. The transfer vessel facilitates isolation and displacement of a fluid without contaminating the pump cylinders with any fluid other than water.

(1) Place the transfer vessel in its stand.

(2) Pour deaerated water in the transfer vessel and fasten the threaded cap covering the same side.

(3) Water should fill the 1/8” Swagelok port connector of the threaded cap. Plug the port connector using a 1/8” Swagelok plug (SS-200-P).

(4) Turn the transfer vessel upside down and place it back in the stand.

(5) Inject water in a 1/8” tubing line with a Swagelok nut and ferrule set (SS-200-NFSET) on its end. Displace and discard a volume equivalent to the capacity of four pump cylinders to ensure that air is not trapped in the pump.

(6) Turn the transfer vessel, together with the stand, upside down, so that the bottom of the stand is on top.

(7) Put the pump on a low injection rate, 0.1 cc/min for example. Replace the plug from the water side of the transfer vessel with the tubing carrying water from the pump. Make sure that air is not trapped on this side of the transfer vessel.

(8) Turn the transfer vessel, together with the stand, and position them upright.

(9) Continue with steps (10) - (12), if there is not enough space on the top side of the transfer vessel to contain 250 cc of Fluorinert. Otherwise, skip to step (13).

(10) Connect the top side of the transfer vessel to a nitrogen gas cylinder and exert a pressure of 0.3 MPa on its piston.

(11) Put the pump on the retract mode and start the pump to increase the volume of the nitrogen-filled side. Stop the pump when there is ~250 cc space in the nitrogen side.

(12) Slowly reduce the pressure of the nitrogen side by loosening the tubing nut and disconnect the nitrogen cylinder from the transfer vessel.

(13) Unfasten the top threaded cap of the transfer vessel and pour Fluorinert into the transfer vessel. Fasten the threaded cap on top of the transfer vessel.

(14) Connect a valve and tubing line on top of the transfer vessel.

Two nitrogen gas cylinders were employed in the flow system for (i) the air-operated valves of the Quizix pump, and (ii) providing a reference pressure to the EB1HP1 back pressure regulator (Equilibar, Fletcher, NC). The Quizix pump has a port for a nitrogen source at a pressure of 0.40 to 0.55 MPa. Air pressure is used in switching the pump's valves. Nitrogen was provided from two gas cylinders equipped with Matheson 3040 Series high pressure delivery regulators (Matheson Tri-Gas, Basking Ridge, NJ) that can deliver gas at pressures up to 17 MPa.

The Equilibar EB1HP1 back-pressure regulator sets the pressure at the exit stream of the core holder. This maintains the outlet pressure of the core holder and thereby controls the phase behavior of fluids within the core plug. The Equilibar back-pressure regulator, as shown in Figure 3-6, has three ports: inlet, outlet, and reference. The inlet fluid exits the instrument from the outlet port, if its pressure exceeds that of the reference. A nitrogen cylinder with its pressure controlled by a Matheson pressure regulator was connected to the reference port. Pressure data recorded during measurements indicated that the Equilibar back-pressure regulator opens and closes frequently to vent fluids to the outlet port to

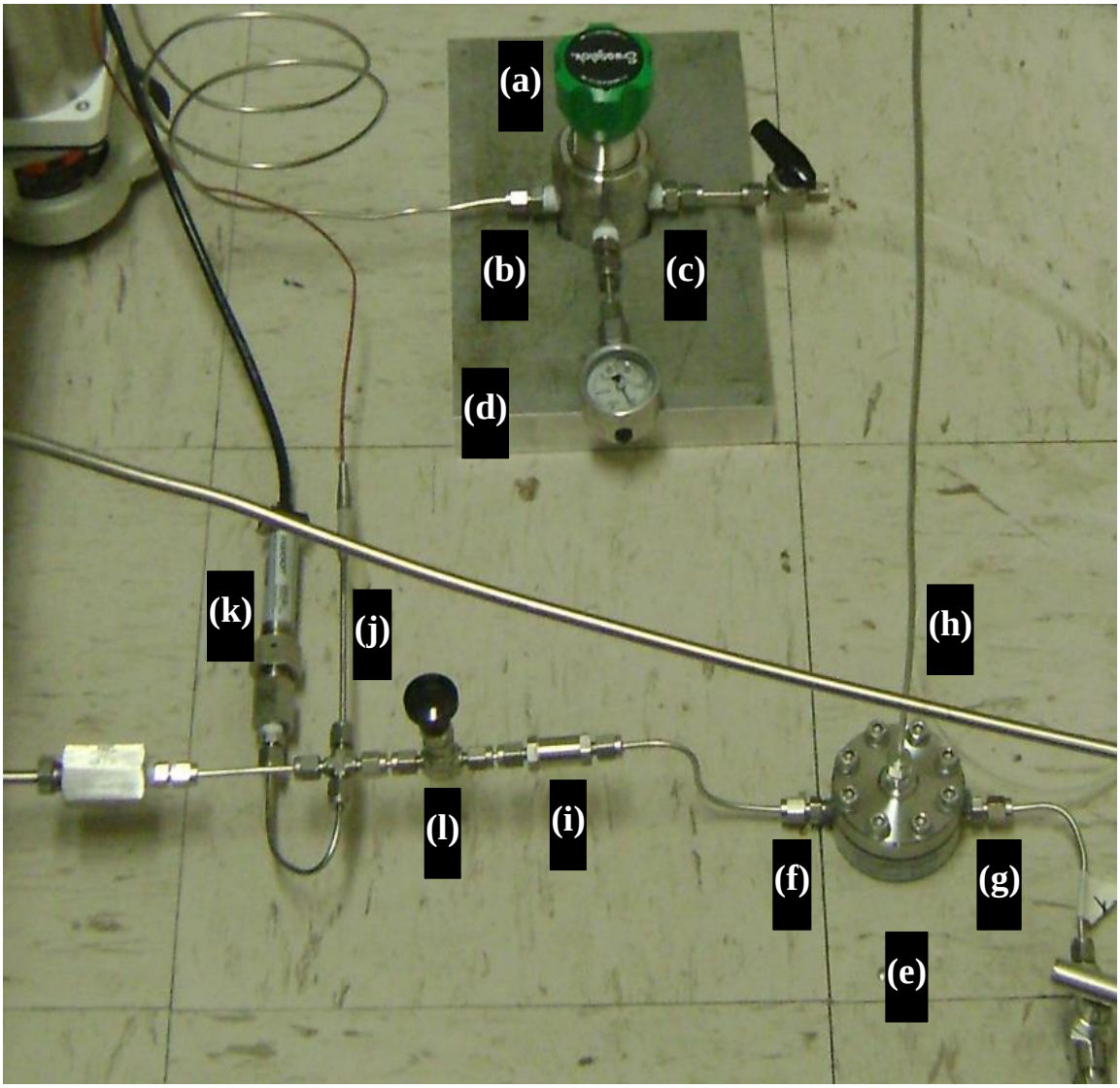

Figure 3-6 Close-up of the back-pressure regulators installed behind the magnet. The KPB back pressure regulator (a), with its inlet (b), outlet (c), and stand (d), is on the top. The Equilibar back-pressure regulator (e), with its inlet (f), outlet (g), and reference port (h), is at bottom right. Swagelok SS-2F-2 filter (i), thermocouple (j), Ashcroft K1 pressure transducer (k), and Swagelok SS-ORS2 needle valve (l) are also shown in the picture.

maintain the inlet pressure of the back-pressure regulator. The frequent switching of the regulator causes minor fluctuations in the upstream pressure at the outlet of the back-pressure regulator. Two measures were undertaken to mitigate this problem: (i) installing a PTFE/Glass diaphragm with Kalrez O-rings, and (ii) installing a half-open needle valve (Figure 3-6l, Swagelok SS-ORS2) after the back-pressure regulator. Commonly used diaphragms in back-pressure regulators, made of stainless steel, polyimide, or PTFE, result in poor pressure control or develop holes at the diaphragm-to-orifice seals. In contrast, PTFE/glass composite diaphragms provide a stable pressure control with longer operational life.

Sudden pressure reduction can damage O-rings and elastomers when dissolved gases expand rapidly. Such processes are referred to as rapid gas decompression. Kalrez O-rings have excellent resistance in rapid gas decompression applications (Legros et al. 2017), such as the high-pressure CO_2 experiments performed in this research. Installing a half-open needle valve, after the back-pressure regulator, reduces the CO_2 pressure in two steps and provides a slow depressurization to reduce rapid gas decompression and damage to the O-ring and the diaphragm (Mann and Jennings 2017). This setting is shown in Figure 3-6.

KPB1N0D412P20000, a KPB series (Swagelok, Solon, OH) back pressure regulator was employed to reduce the pressure of the vent streams before directing them to a waste container. Figure 3-6 shows the back-pressure regulators employed in this research. The KPB back pressure regulator uses a spring load as the reference pressure. The inclusion of

this back-pressure regulator, as a precaution, improves the safety of the flow system as high-pressure fluids vented to the waste container could be hazardous. The vent streams are connected to two 3-way ball valves. In addition to safety features, the vent streams ensure that there is no air in the fluid stream entering the core plug during the experiment.

The waste container contains two liters of water in which three tubing lines are submerged. These three tubing lines come from (1) the KPB back-pressure regulator, (2) the Equilibar back-pressure regulator, and (3) a relief valve (Swagelok SS-4R3A) connected to the confining space of the core holder. The waste container was made of a clear plastic to facilitate differentiating between different liquid phases such as Fluorinert and decane and gas phase. The waste container had an overhead flexible air suction duct to remove any excess of CO_2 not dissolved in the water phase of the waste container. The flexible air suction duct was connected to a suction ceiling port in the laboratory.

An Amprobe CO_2-100 handheld carbon dioxide meter, as shown in Figure 3-3k, measured the concentration of CO_2 in the ambient environment. Exposure to CO_2 concentrations exceeding 2000 ppm leads to difficulty in breathing and other health problems (Satish et al 2012). CO_2 could leak into the environment because of poor sealing in different components of the flow system. CO_2 leaks were mainly observed from the NPT connections or Valco connections of the Teledyne ISCO pump. Based on experience in this research, vibration can induce leakage in Valco connections. The CO_2 meter

functioned as a safety monitor, but also helped detect minor leaks, in surveying the flow system.

CO_2 has a critical temperature of 31.10 °C (Smith et al. 2004). Filled CO_2 cylinders exist at the vapor-liquid equilibrium at the saturation pressure corresponding to ambient temperature. For a two-phase CO_2 system, at constant pressure, temperature, and CO_2 cylinder volume the number of moles of CO_2 in the cylinder, and the mass ratio between vapor to liquid defines the state of the system. Therefore, at an ambient temperature of 20°C and corresponding pressure of 5.72 MPa (Lemmon 2013), saturated-liquid CO_2 vaporizes and saturated-vapor volume increases with the withdrawal of saturated-liquid CO_2 from the cylinder.

In a typical CO_2 cylinder, saturated-vapor CO_2 exits the main valve of the gas cylinder and a pressure regulator sets a lower output pressure. However, with specialized cylinders, saturated-liquid CO_2 can also be delivered at the main valve of a CO_2 cylinder. A dip tube CO_2 cylinder has a siphon tube inserted deep below the vapor-liquid interface in the cylinder and takes only saturated-liquid CO_2 from the main valve of the cylinder. No pressure regulator is required for a dip tube CO_2 cylinder. A dip tube CO_2 cylinder (99.7%, Air Liquide Canada Inc., Montreal, QC) was employed to provide the saturated-liquid CO_2 required in this study; which requires much less compression, compared to the same volume of vapor CO_2, to produce a specific amount of supercritical CO_2.

The CO_2 cylinder, marked with ‘f’ in Figure 3-3, fed the Teledyne ISCO pump with liquid CO_2. The main valve of the cylinder can be blocked with dry ice, due to a transient pressure loss. CO_2 temperature is reduced with decreasing pressure at constant enthalpy. Therefore, inadvertently high CO_2 flow rates, corresponding to high pressure losses, can cause low temperatures in flow lines, and especially valves and fittings. To ensure the safety of the flow system, saturated-liquid CO_2 flow rates were maintained under 5 cc/min and an additional needle valve (Swagelok SS-ORS2) was employed on the CO_2 supply line in case the cylinder valve failed to close completely. Placing a filter (Swagelok SS-2F-2) and a check valve (Swagelok SS-2C-1/3) after the CO_2 cylinder ensured that no particulates could enter the flow system and high-pressure fluids from the flow system would not invade the CO_2 cylinder due to an instrumentation failure.

The experimental design required flow of different fluids at different stages of experiments. The pressure difference between fluid sources can cause back flow after opening valves to new fluids. Check valves circumvented this problem. Check valves, however, have their limitations. The difference between the outlet and inlet pressures of the check valve should not exceed the maximum backpressure. In such a case, backpressure could dislodge the the check valve O-ring and fluids could flow from the outlet to the inlet port. This occurred once when depressurization of the flow system was not performed appropriately. Installing a backup ring, to support the O-ring, can avoid this problem in case the check valves are not handled properly. Check valves also require a pressure difference of 0.002 MPa to open

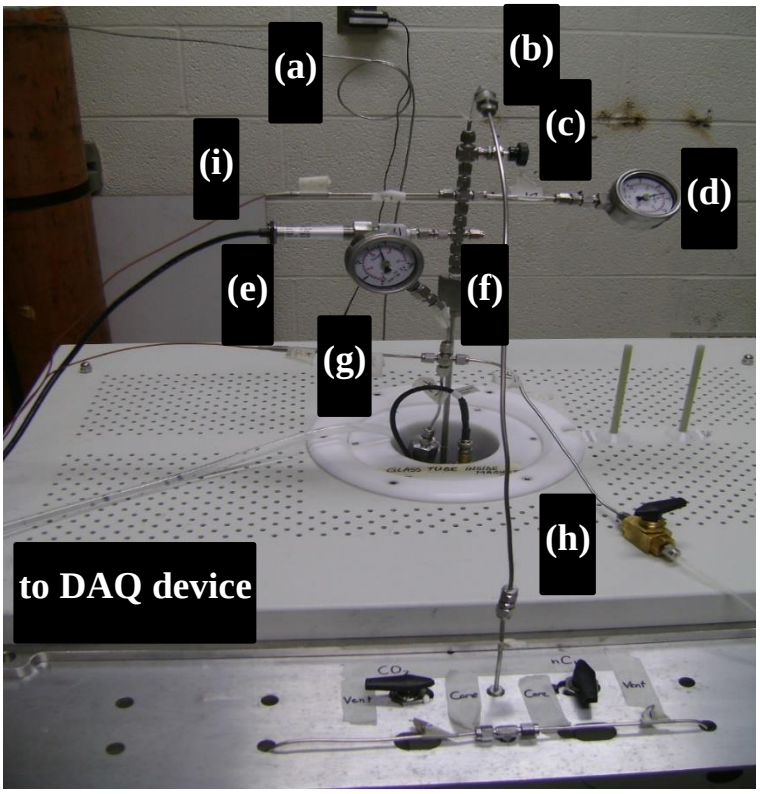

Figure 3-7 Close-up of the 'Christmas tree', the tubing and fittings leading to the top of the core holder installed inside the magnet. Tubing lines connecting movable instruments were formed into coils, two turns approximately 6" in diameter, for enhanced safety. One such coil, in the tubing connecting the nitrogen cylinder to the Equilibar back pressure regulator behind the magnet, is visible in this picture (a). Swagelok SS-2C-1/3 check valve (b), Swagelok SS-ORS2 needle valve (c), Swagelok analog pressure gauge ('d' for pore pressure and 'f' for confining fluid), Ashcroft K1 pressure transducer (e), thermocouples ('i' for CO_2 flow and 'g' for confining fluid), and the brass ball valve (h) for draining the confining fluid are visible in this picture.

for the type employed (Swagelok SS-2C-1/3) in this research. This avoids continuous flow of fluids into the core plug for very small flow rates.

Particulates should be filtered from the inlet streams of the pumps, core holder, and the back-pressure regulators. Fine particles may disrupt the operation of the pumps, clog the nozzles of the back-pressure regulators, and plug pore throats in the core plug. Various filters were placed in different flow lines of the flow system:

(1) CO_2 inlet to the Teledyne ISCO pump (in-line filter assembly 209-0161-64, Teledyne ISCO, Lincoln, NE),

(2) Suction filter (228-20031-00, Shimadzu, Kyoto, Japan) for the Shimadzu pump inlet, and

(3) SS-2F-2 Swagelok filters before the Equilibar and KPB back-pressure regulators, and the core holder.

All pumps had built-in digital pressure transducers. However, both analog and electronic pressure transducers were employed to read pressure at different points in the flow system. The points at which pressure readings are available are marked as P1 to P12 in Figure 3-1. Two analog pressure gauges showed the confining and pore-filling fluid pressures. The analog pressure gauges had four main applications:

(a) reading the pressure of the core holder in case of emergency or a power outage,

(b) reading the pressure of the core holder in case of data acquisition device malfunction,

(c) double checking pressures shown by the data acquisition devices, and

(d) monitoring the system pressure while the data acquisition device was shut down to limit electrical noise in MR/MRI measurements.

Pressure transducers were found to increase noise in MR measurements when in operation. It is advisable to turn off any pressure transducers and DAQ devices when acquiring MR/MRI data. This is especially important during imaging because of noise propagation in the numerical Fourier transform algorithm performed during MRI data processing.

Ashcroft K1 pressure transducers (Ashcroft, Stratford, CT) in conjunction with an OM-DAQ-USB-2401 USB data acquisition system (Omega Engineering Inc., Stamford, CT) were employed to record pressures at the inlet and outlet of the core holder. The Ashcroft K1 is a versatile pressure transducer employed in chemical industries. Female connections of the pressure transducers made cleaning their ports facile. The pressure transducers operated in the 1-5V range, easy to read utilizing a DAQ system such as OM-DAQ-USB-2401 (Omega Engineering Inc., Stamford, CT). TJ36-CAIN-18U-4 thermocouples (Omega Engineering Inc., Stamford, CT) were used in conjunction with the Omega DAQ to read room, core holder inlet and core holder outlet temperatures. The thermocouples were 1/8” probes that fit into a bored-through cross fitting (Swagelok SS-200-4 BT) with a nut and ferrules.

The Omega DAQ used for registering pressure and temperature was the most significant source of electrical noise during MR data acquisition. This was confirmed by switching the DAQ device on and off and distancing the unit from the magnet. The operation of the DAQ unit close to the magnet increased the noise amplitude eight fold. Therefore, it was necessary to turn off the Omega DAQ unit during MRI measurements and to maintain it at a significant distance from the magnet. The presence of the DAQ unit close to the magnet, even if it was not connected to any power source, increased noise amplitude by 33%.

3.1.2 Flow system

The flow lines of Figure 3-1 are color coded based on the fluids they carry. Flow lines marked as brown can carry a mixture of fluids. Needle valves, check valves, pumps, and back pressure regulators control the flow. Fluid pressure, temperature, and flow rate are read at different points throughout the flow system. These measurements are read or recorded employing either integrated DAQ systems, installed in pumps, or the external Omega DAQ device. More information on the pumps, the external DAQ device, and other instruments is provided previously in the sub-section ‘System Components’.

The six different fluids present in the flow system are color coded for

(1) Nitrogen (green)

(a) from nitrogen cylinder NC1 to the Equilibar back-pressure regulator reference port (N1), and

(b) from nitrogen cylinder NC2 to the Quizix pump (N2), as the 0.40-0.55 MPa high-pressure source for the air-operated valves;

(2) Decane (red)

(a) from the decane reservoir to the Quizix pump (D1),

(b) from the Quizix pump to the decane 3-way ball valve (D2), and

(c) from the 3-way ball valve to the KPB back-pressure regulator (D3);

(3) Water (blue)

(a) from the water reservoir to the Shimadzu pump (W1), and

(b) from the Shimadzu pump to the transfer vessel (W2).

(4) CO_2 (purple)

(a) from the CO_2 cylinder to the Teledyne ISCO pump (C1),

(b) from the Teledyne ISCO pump to the CO_2 3-way ball valve (C2), and

(c) from the CO_2 3-way ball valve to the KPB back-pressure regulator (C3);

(5) Glycerol/water (pink) mixture as a loop circulating between the core holder heat exchanger, the Teledyne ISCO pump, and the heating circulator (GW);

(6) and Fluorinert (gray)

(a) from the transfer vessel to needle valve (Swagelok SS-ORS2), V6 (F1),

(b) from needle valve V6 to the core holder confining space (F2),

(c) recycling reservoir (F3), and

(d) potentially from the relief valve to the waste container (F4).

Flow lines color coded as brown can carry different fluids. All liquids were deoxygenated through application of a vacuum and all flow lines were deaerated by CO_2, decane, or Fluorinert before starting the experiment.

3.1.3 Connection Standards

A complicated flow system, such as the one employed in this research, inevitably contains instruments and components from different companies. These instruments may have high pressure connections which use different sealing technologies. High pressure connections from five companies and standards were used in the construction of this flow system: (1) HiP (High Pressure Equipment Co, Erie, PA), for the core holder port connectors and pressure transducers, (2) Swagelok (Solon, OH), for the majority of the flow system, such as tubing lines, tees, crosses, needle valves, thermocouples, and analog pressure gauges, (3) Valco (Vici Valco Instruments, Houston, TX), for the Teledyne ISCO pump, (4) National Pipe Thread (NPT) standard, for the back pressure regulators, and a few HiP to Swagelok convertors, and (5) Shimadzu (Kyoto, Japan) for the Shimadzu LC-8A pump. Based on experience in this study, NPT connections are not recommended for high pressure

applications and were the cause of most leaks in this research. HiP is the most robust connection among these five technologies for high pressure fluid flow. However, it is very expensive – more than CAD$100 for an 1/4" HiP union. Swagelok products offer a leak-free flow system at pressures as high as 25 MPa for a moderate price and formed most of the flow system components employed in this research.

3.2 Fluids

The range of fluids affect the materials and seals selected for the flow system components. Seven different fluids were used in this study: (1) carbon dioxide, (2) nitrogen, (3) decane, (4) heavy oil, (5) Fluorinert, (6) glycerol/water mixture, and (7) water and brine. Nitrogen is employed at three points in the flow system or its preparation: (i) the reference port of the Equilibar back-pressure regulator, (ii) air-operated valves of the Quizix pump, and (iii) preparation of the transfer vessel. Nitrogen and CO_2 are both MR invisible at the ^1H Larmor frequency, as they have no ^1H in their molecular structure. Air was displaced from the flow lines as oxygen can affect the relaxation time constants of ^1H bearing fluids. CO_2 was employed in displacing air in the flow system and core plug because of its significant solubility in both aqueous and oleic liquids employed at high pressure.

The Joule-Thompson effect can affect the flow system in the CO_2 flooding of the decane phase. The enthalpy of a real gas is a strong function of its pressure and temperature. In gas flow through constrictions, such as pipes, fittings, valves, and porous materials, gas expands with no adequate heat transfer to offset the temperature change. This isenthalpic

process results in gas temperature change with pressure changes. Based on $(dT/dP)_H$, the gas temperature may rise or fall. CO_2 has a negative Joule-Thompson constant. Therefore, with decreasing CO_2 pressure, its temperature falls. This was observed as low temperatures in parts of the flow system, such as tees and valves, where CO_2 pressure is reduced locally. Previous investigators (Suekane et al. 2005; Zhao et al. 2011) used high CO_2 flow rates and reported different temperatures at the inlet and outlet gas streams in their CO_2/decane experiments, because of the Joule-Thompson effect. A low CO_2 flow rate, 0.04 cc/min, was used to ensure that the gas temperature was the same as the design temperature.

High pressure fluids, such as nitrogen, and particularly CO_2, can diffuse into polymeric components of instruments. However, this process is slow and reversible and the gas can be desorbed with reducing pressure. Pressure reduction should be performed slowly for polymeric materials that have been exposed to high pressure gases. Otherwise, the polymer structure deteriorates (Major and Lang 2010). Experiments performed on the Aflas and Viton core plug sleeves have shown that the exposure of these two materials to CO_2 increases their Free Induction Decay (FID) and Carr-Purcell-Meiboom-Gill (CPMG) MR signal intensities. We assume that the dissolved CO_2 enhances the mobility of ^1H present in the polymer structure. This observation translates into a varying background signal during the measurements. Precautions were taken to keep MRI measurements quantitative by exposing the core plug sleeve to high pressure CO_2 before commencing the experiment.

Decane, $CH_3(CH_2)_8CH_3$, is a hydrogen-rich alkane that was used as a model oil during the CO_2 displacement experiments. Decane can be first contact-miscible or immiscible with CO_2 in a narrow pressure and temperature range (Nagarajan and Robinson 1986). In addition, the CO_2/decane system is well studied and the physical properties of their mixture is available in the literature (Nagarajan and Robinson 1986; Orr 2007). The forces between decane molecules and CO_2 are simple enough for current equations of state to accurately predict their phase behavior (Tsuji et al. 2004). The simplicity of the CO_2/decane mixture also makes analyzing the decane/pore surface interaction by MR methods easier. The decane used in this study (≥95%, Sigma-Aldrich Co., St. Louis, MO) was degassed to remove all the oxygen dissolved in the liquid phase.

Phase behavior of the CO_2/decane mixture is sensitive to temperature and pressure, particularly near the critical points of the components and the mixtures (Danesh 1998). Studying the CO_2/decane mixture at 40°C in Berea sandstone required accurate temperature and pressure control. The CO_2/decane mixture at 40°C forms only a single phase above 8 MPa (Liu et al. 2015), irrespective of the mole fraction of CO_2. Therefore, at 40°C and pressures above 8 MPa, CO_2 and decane are miscible. The reported miscibility pressure of the CO_2/decane mixture was confirmed by a P-x_{CO2}-y_{CO2} phase diagram at the constant temperature of 40°C. The phase diagram was calculated employing Peng-Robinson equation of state in Aspen Properties software (Aspen Technology, Bedford, MA). Under miscible conditions, the injected CO_2 fluid forms a single phase with the pore-filling decane upon contact. No phase boundaries will form as the result of the contact.

This behavior is termed first contact miscibility in the petroleum engineering vocabulary (Green and Willhite 1998).

Water was used in the transfer vessel to displace the piston through hydraulic force. Water was deaerated so that it would dissolve any air remaining in the transfer vessel, pump cylinders, and, core plugs. In the fines migration and CO_2 flooding of heavy oil experiments, 3 wt% brines from H_2O and D_2O were prepared, both deaerated. The 50/50 water/glycerol heat transfer fluid was temperature regulated to 40°C with a Julabo F25 heating circulator (Julabo, Seelbach, Germany). The heat transfer fluid flowed on the periphery of the core holder shell and in the heating jacket of the pumps. The CO_2 tubing lines from the Teledyne ISCO pump to the core holder were not temperature regulated. However, regulating the temperature of the Teledyne ISCO pump kept the volumetric flow rate set on the pump the same as the volumetric CO_2 flow rate in the core holder.

Fluorinert liquids (3M, St. Paul, MN), particularly FC-43, were employed as the confining fluid. Fluorinert has dielectric properties that make it an important fluid in insulation applications (Anderson and Mudawar, 1989). Fluorinert is a perfluorinated compound with no ^{1}H content. The confining fluid space and its filling process can be imaged, if desired by, employing MRI methods at the ^{19}F frequency.

3.3 Material Selection

The instruments employed in this research are made of components manufactured from different materials. Proper material selection for components of each instrument makes

measurement at high pressure and a moderate static magnetic field possible. This subsection explains important materials wetted by fluids employed in this research.

3.3.1 Metallic Parts

Most of the metallic components employed in this research were made from SAE 316 stainless steel, or Hastelloy-C276. The SAE 316 stainless steel, SS 316, is a nickel-chromium molybdenum-alloyed steel (Cardarelli 2008). It is significantly resistant to pitting corrosion compared to other grades of steel (Cardarelli 2008). SS 316 is negligibly responsive to magnetic fields (Cardarelli 2008). Therefore, it is an economic choice for low magnetic field applications. SS 316 is a relatively poor conductor of both heat and electricity. This is an important factor in reducing induced eddy currents on metallic parts placed in an MRI system (Shakerian et al. 2017). Apparatus parts such as tubing lines, fittings, port connectors, and the body of back pressure regulators, valves, and filters were made of SS 316.

The vessel and closures of the core holder were machined from Hastelloy-C276 pipe and bar. Hastelloy C-276 has excellent corrosion resistance to strong oxidizing and reducing corrosives, acids, and chlorine-contaminated hydrocarbons (Cardarelli 2008). Like SS 316, Hastelloy-C276 is a nickel-chromium molybdenum-alloyed steel (Cardarelli 2008). However, it has lower heat and electrical conductivity and higher yield strength, as shown in Table 3-1. Hastelloy-C276 is resistant to corrosive fluids commonly employed in core laboratory experiments such as supercritical carbon dioxide, brine, and live oil (Cardarelli

2008). The low-conductivity of Hastelloy-C276 reduces eddy current effects (Shakerian et al. 2017). The metal core holder is also an RF shield at the frequencies employed for MRI measurements (Shakerian et al. 2017). Therefore, no signal is observed from the heat exchanger fluid on the exterior of the metallic vessel.

Table 3-1 Mechanical and electrical properties of SS 316 and Hastelloy-C276. From Shakerian et al. (2017).

Material	Electrical conductivity σ ($\times 10^6$ Sm^{-1})	Thermal conductivity k ($Wm^{-1}K^{-1}$)	Yield strength Y (MPa)
Copper	58.8	385	33.3
Aluminum	37.7	167	276
SS316	1.35	16.2	290
Hastelloy-C276	0.76	9.8	363

Some parts in the valves, pressure regulators, and filters were not manufactured from SS 316. These small parts, such as springs and seals, did not have a significant effect on the operation of the system at low to moderate magnetic field as they were not in the imaging space. The metallic materials employed for these parts include:

(1) Brass C360, for the port connector of the gas cylinders, their filter, and a needle valve,

(2) SS 302, for check valve springs (Swagelok SS-2C-1/3) and filters (Swagelok SS-2F-2),

(3) SS 304, for gland of the needle valves (Swagelok SS-ORS2),

(4) S17700, for the relief valve (Swagelok SS-4R3A) spring, and needle valve (Swagelok SS-ORS2) packing springs, and

(5) Elgiloy, for the piston seal spring in the KPB back pressure regulator.

3.3.2 Polymeric Materials

Polymeric materials play a vital role in high pressure seals and coating of metallic parts susceptible to reactive fluids, such as supercritical CO_2, oil, and brine. Inappropriate material selection for seals and coatings may cause safety hazards, damage to instruments, or unintended reactions in the high-pressure system. Major polymeric materials used in this research along with their application is included below.

(1) Polyether-ether-ketone (PEEK) is a semi-crystalline thermoplastic aromatic polymer. It has good chemical, heat, fire, and radiation resistance, toughness, rigidity, bearing strength, and processability (Massey 2003). PEEK has excellent chemical resistance to dry CO_2 and good chemical resistance to wet CO_2 (Massey 2003). PEEK was employed in four parts of the flow system.

(a) The body of the RF probe placed in the metallic core holder. PEEK has a high dielectric strength to withstand the high voltages generated during RF excitation. It also has a low background MR signal which is minimized at a free induction decay (FID) evolution time of 146 μs (Shakerian et al. 2017). The high tensile strength of PEEK also

increases the operating pressure of the core holder due to the contact pressure effect described by the Tresca theory (Shakerian et al. 2017).

(b) Fluid distributors on both ends of the core plug to recess the metallic fittings into the core holder closures. These parts are wetted by CO_2, wet or dry, brine, decane, and heavy oil in different experiments.

(c) Non-metallic tubing lines electrically insulating the pressure transducers from the core holder for improved SNR.

(d) KPB piston seal retainer.

(2) Fluoropolymers

Fluoropolymers are a class of paraffinic thermoplastic polymers where some or all hydrogen atoms have been replaced by fluorine atoms (Massey 2003). The result is either a fully fluorinated polymer such as poly-tetra-fluoro-ethylene (PTFE), fluorinated ethylene propylene (FEP), or perfluoro alkoxy alkanes (PFA), or a partially fluorinated polymer such as ethylene-chloro-tri-fluoro-ethylene (ECTFE), poly-chloro-tri-fluoro-ethylene (PCTFE), ethylene-tetra-fluoro-ethylene (ETFE), and poly-vinyli-dene-fluoride (PVDF) (Massey 2003). Fully fluorinated fluoropolymers are chemically more stable than partially fluorinated polymers and are significantly resistant to CO_2, brine, and live oil. Fluoropolymers were employed in different parts of the flow system as described below.

(a) PFA was used in the packings of the ORS2 needle valve (Swagelok SS-ORS2).

(b) PTFE was used as the coating of Viton O-rings in the relief valve, and in the piston seal in the KPB back pressure regulator, high pressure (5 MPa) tubing, and the shell of the core holder heat exchanger.

(c) PCTFE was used in the seal of the KPB back-pressure regulator

(3) Fluoroelastomer

Vinylidene-Fluoride-Hexafluoropropylene-Copolymer (Viton) is a well-known fluoroelastomer used in industrial applications (Massey 2003). Aflas and Viton sleeves, made of this elastomer, were used for sealing the plug periphery. O-rings in the transfer vessel, the core holder heat exchanger, and the Shimadzu pump were also made of Viton. Viton O-rings in the Equilibar back-pressure regulator were replaced with Kalrez (a perfluoroelastomer) O-rings for increased resistance to rapid gas decompression (Legros et al. 2017).

3.4 Pressurizing and Depressurizing the Apparatus

There are several safety and technical issues during the starting and ending of CO_2 core flooding experiments:

(1) The apparatus should be airtight starting from the high-pressure sources, including the high-pressure fluid cylinders and pumps down to the back-pressure regulators. Care was taken to ensure the airtightness of the system before starting the experiments. NPT connections at the Equilibar back-pressure regulator were the

principal leak points. These leaks were fixed with SWAK® Anaerobic Thread Sealant (Swagelok MS-PTS-6).

(2) Air present in all tubing lines, containers, valves, and the core holder should be displaced before starting the experiment. This can be done by either applying vacuum from the effluent line of the apparatus, or by removing the air using a driving and/or displacing fluid, like CO_2. Carbon dioxide, decane, and Fluorinert were employed to displace oil from the flow lines, fittings, valves, and filters. Deaerating the liquids before the experimental runs that even if there was some air in the dead spaces of the system, it would be dissolved in the liquid.

(3) Phase behavior of the CO_2/decane mixture strongly depends on temperature. Sufficient time, usually one day, was allotted for the core holder to reach the set temperature. This time also allowed the dissolution of any air or CO_2 into the decane phase.

(4) N_2 and particularly CO_2 diffuse into almost all plastics and elastomers in the system. Sudden exposure of these materials to high pressure CO_2 and N_2 poses no special problem to their integrity, if they can tolerate the stress. However, for safety, it is recommended to pressurize the system slowly. Based on experience, depressurization is ideally performed at 0.50 MPa/min. This rate ensures that the CO_2 and nitrogen dissolved in the plastics and elastomers have enough time to diffuse out.

(5) Check valves allow flow in one direction only. A nominal cracking pressure, the difference between the inlet and outlet pressure, of 0.002 MPa allows fluid flow from inlet to outlet. If the outlet pressure is more than the inlet pressure, no flow occurs from outlet to inlet. However, if the difference between the outlet and inlet exceeds 6.7 MPa, the check valve seals will be damaged, and the check valve will not work as intended. Care should be taken to ensure that the fluids at high-pressure are depressurized in all of the system, not only up to the check valves' downstream.

(6) Power or instrument failure can pose danger to the integrity of the flow system and personnel exposed to it. This is particularly important if the system temperature is lower than the room temperature, as with temperature increase, the pressure of the fluids in the system will increase and may exceed the operational pressure limits of the instruments. A few measures successfully reduced the risk of susceptibility of the apparatus to power and instrument failure.

(a) The main valve of the CO_2 cylinder was always closed, except for the recharging of the Teledyne ISCO pump.

(b) A relief valve set to 24 MPa was connected to the confining fluid connection at the bottom of the core holder.

(c) Analog pressure gauges were used for the core plug and confining fluid pressures in addition to pressure transducers.

(d) The CO_2 meter used for safety monitoring was battery powered.

(e) A notice was placed on the door of the room in which the apparatus was installed with instructions to follow in case of an emergency.

(f) The apparatus was operated at a pressure lower than its operating pressure.

(g) The apparatus was meticulously tested for air tightness before starting any experiments. This ensures that without operation of any pump the apparatus will contain the pressure of the system.

In case the pressure of the flow system increases, fluids would be either (i) contained in the flow system, or (ii) released into the waste container via the Equilibar back-pressure regulator or the relief valve.

(7) Supercritical CO_2 present in the apparatus occupies approximately 100 times more volume when its pressure is reduced. Sudden release of CO_2 to the environment poses a health hazard to personnel in the vicinity. A flexible air suction duct removed any effluent CO_2 outside the building.

The following procedure was followed in setting up the flow system and during the beginning of experiments.

(1) Place the core plug in the Aflas sleeve. Place the PEEK distributors with their connecting tubes in the sleeve. Apply a heat shrinkable tubing to the Aflas sleeve and place the combination in the MS-5000 core holder.

(2) Assemble the MS-5000 core holder and charge it with high pressure nitrogen to test its airtightness. Monitor, over several hours, the pressure to ensure it is stable.

(3) Fill the transfer vessel with deaerated water and Fluorinert (W1, W2, and F1).

(4) Install the valve panel (Figure 3-4) containing 3-way ball valves for CO_2 and decane (G1).

(5) Install the KPB back-pressure regulator, the waste container, and the flexible air suction duct. (G7)

(6) Connect the Nitrogen cylinder to the Quizix pump (N2).

(7) Connect the Quizix pump to the decane reservoir (D1).

(8) Connect the Quizix pump to the valve panel (D2).

(9) Connect the decane 3-way ball valve from the panel to the KPB back-pressure regulator (D3).

(10) Inject 60 cc of decane to the waste container to empty air in lines D1, D2, and D3 and fill them with decane at pressures up to 0.40 MPa.

(11) Connect the CO_2 cylinder to the Teledyne ISCO pump (C1).

(12) Connect the Teledyne ISCO pump to the valve panel (C2).

(13) Connect the CO_2 3-way ball valve to the KPB back-pressure regulator (C3).

(14) Inject 400 cc of liquid CO_2 to the waste container to empty air in the cylinders of the Teledyne ISCO pump, and flow lines C1, C2, and C3. Reduce the gas volume in the Teledyne ISCO pump cylinders to zero and open the outlet valves of both cylinders.

(15) Ensure that pressures at points P1, P2, P3, P4, and P5 agree.

(16) Install the core holder inside the MRI magnet (G2, and G3)

(17) Install the effluent stream tubing, connections, and the Equilibar back-pressure regulator (G4, G5, G6, F2, F3, and F4).

(18) Set the pressure regulator at point P10 to 0.79 MPa.

(19) Install the heat exchanger pipes and start the heat circulator to set the experiment temperature in the Teledyne ISCO pump and the core holder. Make sure that the outlet valves of the Teledyne ISCO pump are open for both cylinders.

(20) Open the needle valve on F3 half way and inject Fluorinert, the confining fluid, into the core holder. Increase the pressure of the system to 0.7 MPa.

(21) Image Fluorinert at the ^{19}F frequency to make sure that the core plug is centered in the gradient set and monitor the core holder filling process.

(22) Close the valves on Fluorinert line F3 and open valves on lines F1 and F2. Monitor pressure at P11 to ensure that the confining fluid does not leak.

(23) Fill both cylinders of the Teledyne ISCO pump with liquid CO_2.

(24) Open valve V1 slightly and start injecting CO_2 from the Teledyne ISCO pump to remove air from lines G1, G2, G3, G4, G5, and G6. Inject a total of 1000 cc of CO_2 to ensure that all air is removed.

(25) Install the Omega OM-DAQ-USB-2401 USB DAQ system for pressure transducers and thermocouples.

(26) Close valves V1 and V2 to monitor digital pressure readings to ensure that G2, G3, G4, and G5 are gas tight.

(27) Inject decane at low flow rates over long periods of time to remove CO_2 and measure permeability of the core plug.

(28) Tune the RF probe to the ^{1}H frequency and perform MRI measurements.

(29) Open valve V3 half way to mitigate pressure fluctuations at the Equilibar back-pressure regulator.

(30) Start injecting CO_2, record pressures, and perform MR measurements.

(31) The confining pressure will increase because of CO_2 diffusion into Fluorinert driven by osmotic pressure difference. Periodically reduce the confining fluid pressure by opening valve V4.

The following procedure was followed to depressurize the flow system at the end of the experiment:

(1) Inject high flow rate CO_2 to remove all remaining decane saturating the core plug and measure the background signal. Stop the pumps and close valve V5.

(2) Loosen the nitrogen cylinder connector slowly to reduce the reference pressure of the Equilibar back-pressure regulator, P10, down to 0.30 MPa at a rate of 0.002 MPa/min. At the same time reduce the confining fluid pressure by loosening a fitting at the outlet of the Shimadzu pump. The confining pressure should always be higher than the reference pressure at P10.

(3) Reduce the pressure of the KPB back-pressure regulator slowly to zero.

(4) Turn off the heat circulator. Return the water/glycerol heat exchanger fluid to the heat circulator by employing high pressure air applied from point H in the direction of both the core holder heat exchanger and the Teledyne ISCO pump. High pressure air drives all heat exchanger fluid remaining in the tubing back to the heat exchanger for reuse.

(5) Open valve V4. Close valve V4. Disconnect the tubing connected to V4 and connect the tubing to the left side of valve V6.

(6) Open both valves V4 and V6 to drain Fluorinert from the core holder. Apply high pressure air to remove remaining Fluorinert in the confining fluid space of the core holder by creeping flow.

(7) Slowly loosen the fitting connected to C1 to reduce its pressure.

(8) Dismantle the apparatus.

Chapters 4 to 6 describe the experiments performed using the experimental set-up described in the preceding sections.

3.5 References

Anderson, T. M., Mudawar, I. 1989. Microelectronic Cooling by Enhanced Pool Boiling of a Dielectric Fluorocarbon Liquid. *J. Heat. Transf.* 111 (3): 752-759.

Bitz, E. 2017. Personal Communication.

Cardarelli, F. 2008. *Materials Handbook: A Concise Desktop Reference, 2nd Ed*. London: Springer-Verlag. PP 59-157.

Cullick, A. S., Mathis, M. L., 1984. Densities and Viscosities of Mixtures of Carbon Dioxide and n-Decane from 310 to 403 K and 7 to 30 MPa. *J. Chem. Eng. Data* 29 (4): 393-396. http://dx.doi.org/0.1021/je00038a008.

Danesh, A. 1998. *PVT and Phase Behaviour of Petroleum Reservoir Fluids*. Amsterdam: Elsevier.

Goora, F. G., Colpitts, B. G., Balcom, B. J. 2014. Arbitrary Magnetic Field Gradient Waveform Correction Using an Impulse Response Based Pre-Equalization Technique. *J. Magn Reson.* 238: 70-76. http://dx.doi.org/10.1016/j.jmr.2013.11.003.

Green, D. W., Willhite, G. P. 1998. *Enhanced Oil Recovery*. Richardson: Society of Petroleum Engineers.

Hoult, D. I., Richards, R. E. 1976. The Signal-to-Noise Ratio of the Nuclear Magnetic Resonance Experiment. *J. Magn. Reson.* 24 (1): 71-85. http://dx.doi.org/10.1016/0022-2364(76)90233-X.

Legros, J. C., Mialdun, A., Strizhak, P., Shevtsova, V. 2017. Permeation of Supercritical CO_2 through Perfluoroelastomers. *J. Supercrit. Fluid* 126 (1): 1-13. http://dx.doi.org/10.1016/j.supflu.2017.02.022.

Lemmon, E. W. 1998. Thermophysical Properties of Fluids In *Handbook of Chemistry and Physics, 97th Ed.,* ed. Haynes, W.M., Chap. 6, 21-37. Boca Raton: Taylor & Francis.

Li, M., Xiao, D., Shakerian, M., Afrough, A., Goora, F., Marica, F., Romero-Zerón, L., and Balcom, B. J. 2016. Magnetic Resonance Imaging of Core Flooding in a Metal Core Holder. International Symposium of the Society of Core Analysts, Snowmass, Colorado, 21-26 August. SCA2016-019.

Li, L. 2009. *Quantitative MR/MRI Analysis of Fluids in Porous Media.* PhD Dissertation. University of New Brunswick.

Major, Z., Lang, R. W. 2010. Characterization of the Fracture Behavior of NBR and FKM Grade Elastomers for Oilfield Applications. *Eng. Fail. Anal.* 17 (3): 701-711. http://dx.doi.org/10.1016/j.engfailanal.2009.08.004.

Mann. J., Jennings, J. 2017. Application Bulletin: University of Sydney New Back Pressure Regulator Enables Carbon Sequestration Research. https://www.equilibar.com/PDF/Pressure-Regulator-Carbon-Sequestration-Research.pdf, Retrieved on 27/03/2017.

Massey, L. K. 2003. *Permeability Properties of Plastics and Elastomers: A Guide to Packaging and Barrier Materials, 2nd Ed*. Norwich: William Andrew Publishing.

Nagarajan, N., Robinson, R. L. 1986. Equilibrium Phase Compositions, Phase Densities, and Interfacial Tensions for CO_2 + Hydrocarbon Systems. 2. CO_2 + n-Decane. *J. Chem. Eng. Data* 31(2): 168-171. http://dx.doi.org/10.1021/je00044a012.

Orr, F. M. 2007. *Theory of Gas Injection Processes*. Holte: Tie-Line Publications. p. 15, 76.

Satish, U., Mendell, M. J., Shekhar, K., Hotchi, T., Sullivan, D., Streufert, S., Fisk, W. J. 2012. Is CO_2 an Indoor Pollutant? Direct Effects of Low-to-Moderate CO_2 Concentrations on Human Decision-Making Performance. *Environ. Health Persp.* 120 (12): 1671-1677. http://dx.doi.org/10.1289/ehp.1104789.

Shakerian, M., Marica, F., Afrough, A., Goora, F. G., Li, M., Vashaee, S., Balcom, B. J. 2017. A High-Pressure Metallic Core Holder for Magnetic Resonance Based on Hastelloy-C. *Rev. Sci. Instrum.* 88 (12): 123703. https://doi.org/10.1063/1.5013031.

Smith, J. M., Van Ness, H., Abbott, M. 2004. *Introduction to Chemical Engineering Thermodynamics, 7th Ed*. Boston: McGraw-Hill Education.

Suekane, T., Soukawa, S., Iwatani, S., and Tsushima, S., Hirari, S. 2005. Behavior of Supercritical CO_2 Injected into Porous Media Containing Water. *Energy* 30 (11-12): 2370-2382. http://dx.doi.org/10.1016/j.energy.2003.10.026.

Tsuji, T., Tanaka, S., Hiaki, T., Saito, R. 2004. Measurements of Bubble Point Pressure for CO_2 + Decane and CO_2 + Lubricating Oil. *Fluid Phase Equilibr*. 219 (1): 87-92. http://dx.doi.org/10.1016/j.fluid.2004.01.019.

Zhao, Y., Song, Y., Liu, Y., Liang, H., Dou, B. 2011. Visualization and Measurement of CO_2 Flooding in Porous Media Using MRI. *Ind. Eng. Chem. Res.* 50 (8): 4707-4715. http://dx.doi.org/10.1021/ie1013019.

Chapter 4 – Magnetic Resonance Imaging of Fines Migration in Berea Sandstone[1]

The theory of magnetic resonance relaxation in rocks and technical aspects of core flooding in MRI magnets is previously discussed in Chapters 2 and 3. In this chapter, a practical application of MRI core flooding is studied that can monitor changes induced in a rock due to filtration of fines. This chapter is largely based on a published paper[1].

Fines migration is a phenomenon of practical importance in the petroleum production and drilling industry. The movement of clay particles, induced by incompatible aqueous phase chemistry or high flow rate, obstructs pore throats downstream of the fluid flow leading to permeability reductions that can be as large as two orders of magnitude. Magnetic resonance imaging (MRI) methods based on Carr-Purcell-Meiboom-Gill (CPMG) can map T_2 distributions in porous rocks, hence showing the spatial variation of the pseudo pore size distribution.

In this work, the traditional water-shock experiment was used to mobilize clay particles in the aqueous phase flowing in Berea core plugs. Spin Echo - Single Point Imaging (SE-SPI), a phase encoding MRI method based on the CPMG method, was used to determine

[1] Largely based on: Afrough, A., Zamiri, M. S., Romero-Zerón, L., Balcom, B. J. 2017. Magnetic Resonance Imaging of Fines Migration in Berea Sandstone. *SPE J.* **22** (5): 1385-1392. SPE-186089-PA. https://doi.org/10.2118/186089-PA.

spatially resolved T_2 spectra of the samples, and therefore the pseudo pore size distributions.

The shift in the T_2 spectra of the core inlet and outlet showed opposite trends. The pore size distribution of the inlet and outlet, inferred from T_2 distributions, were shifted to larger and smaller values, respectively. Therefore, the average pore size was increased at the inlet of the core and reduced at the outlet of the core. This MRI method provides a new analytical approach to screen reservoirs for potential fines migration problems.

4.1 Introduction

Permeability impairment associated with fines migration is one of the major problems that occurs in production and injection wells in oilfields. Increased fines near the wellbore region obstruct pore throats and ultimately result in reduced reservoir productivity. The migrated fines, mainly kaolinite, illite, and chlorite clays in Berea sandstone, are part of the rock matrix not confined by the mechanical stress (Azari and Leimkuhler 1990). Incompatible aqueous phase chemistry and/or high shear stress can overcome the forces holding them to the rock matrix, resulting in their detachment. Other factors affecting the hydrodynamic detachment of fines from the matrix include particle size, particle elasticity, and gravity (Sharma et al. 1992).

Non-invasive spatial pore size measurements are still lacking for studying formation damage, reduced permeability as a side effect of drilling or production processes. In this work, spin echo-single point imaging (SE-SPI), a pure phase encoding Carr-Purcell-

Meiboom-Gill (CPMG) based magnetic resonance imaging (MRI) method, was utilized to spatially resolve the T_2 distribution yielding a pseudo pore size distribution in core plugs undergoing water-shock experiment.

Fluid saturated porous rocks have been studied by magnetic resonance (MR) techniques since 1964 and MRI technology was introduced to petroleum research labs in 1986 (Vinegar 1986). Magnetic susceptibility differences between the pore-filling fluid and rock grains lead to internal magnetic field gradients in the pore space. Diffusion of the pore-filling fluid in these gradients is an inherent problem in all MR measurements involving porous rocks (Hürlimann 1998). Phase encoding MRI methods provide quantitative maps, which are not affected by B_0 inhomogeneity, susceptibility effects, and chemical shift (Muir and Balcom 2012). In contrast to phase encoding, common frequency encoding methods are inherently affected by susceptibility. In addition, switched magnetic field gradients, which are not well characterized, can result in image artifacts in frequency encoding measurements.

MRI has been used in relatively few formation damage studies related to fines migration. Horsfield et al. (1989) obtained spin echo profiles of inverted magnetizations by frequency encoding to monitor T_1 and hence void ratio in a filter cake. The results of this experiment were in excellent agreement with the time rate of change in void ratio predicted by filtration theories. Fordham et al. (1991; 1993) studied the filtration of sodium montmorillonite suspension in an oolitic limestone and two sandstones using prefocused FLASH MRI

imaging. A polymeric core holder capable of handling pressures up to 0.6 MPa was used in their study. Spatial profiles of T_1 relaxation times, calculated from single exponential fits, were indicative of the depth of penetration of colloidal particles, predominantly montmorillonite.

Straley (1994; 1995) imaged spin echo profiles of inverted magnetization by phase encoding to monitor bentonite invasion of a Berea core. The shortest echo time was limited to 2 ms. Van der Zwaag et al. (1997) in a radial filtration experiment calculated relaxation time weighted porosity profiles from two-dimensional non-slice selective spin echo images. The experiment was undertaken with a Berea core sample and three different drilling muds. X-ray CT and bulk NMR were used to measure depth filtration and pseudo pore size distribution, respectively (Tran et al. 2010). The results were compared to simulations based on the size distribution of barite particles in the water-based drilling fluid. Al-Abduwani et al. (2005) measured concentration profiles of hematite particles filtered in a homogeneous siliceous porous medium using x-ray CT. SE-SPI was used by Al-Duailej et al. (2013) to measure the pseudo pore size distribution spatially resolved in seven carbonate cores stimulated with emulsified acids, some with chelating agents. In their static experiments, wormholes were drained because of problems with maintaining fluid in the samples. In none of these studies, except the study by Al-Duailej et al. (2013), the distribution of T_1 or T_2 were measured spatially.

In addition to the common MRI methods to investigate fines migration, a field tool has also been developed to potentially address the problem. The MRX, a new NMR logging tool developed by Schlumberger, has a permanent magnetic field gradient that works at distinct frequencies to probe different depths of investigation up to 150 mm. (Heaton et al. 2002; Minh 2011). The pseudo pore size distribution measured at four different radial locations can reveal fines invasion and washout. This has the potential to reduce drilling rig time by choosing the right sampling locations for wireline formation testers.

4.2 Materials and Methods

The spin echo class of MR methods can measure the transverse relaxation time or T_2, which has been related to pore size, surface to volume ratio, permeability, and capillary pressure (Coates et al. 1999). CPMG is the classic spin echo method widely used in NMR logging. It consists of a 90° radio frequency pulse followed by a train of 180° pulses that rotate the net magnetic moment of the sample hydrogen nuclei in the Larmor frequency rotating frame of reference. The spacing between the 90° and the first 180° pulse is half the echo time, τ, and the spacing between the 180° pulses is 2τ, the inter-echo spacing. Echoes of declining amplitude will form between the 180° pulses from the value of which the transverse relaxation time is extracted. The initial amplitude of this echo train is proportional to porosity and its time constant is T_2 which is proportional to the pore size in water saturated porous rocks. CPMG compensates for the effects of magnetic field inhomogeneity and corrects the effect of imperfect 180° pulses (Coates et al. 1999).

SE-SPI, a pure phase encoding CPMG based MRI method (Petrov et al. 2011), was utilized here to measure the spatially resolved T_2 distributions, i.e. pseudo pore size distribution, in two core plugs undergoing water-shock experiment. SE-SPI is the same as CPMG in applying radio frequency pulses and includes gradients between the 90° and the first 180° pulse to spatially resolve the T_2 spectra. The results show how the pseudo pore size distribution changes because of fines migration in the rock. The amount of water and the T_2 distribution are two independent properties measured by SE-SPI from which, porosity ϕ and logarithmic mean T_2, T_{2LM}, are calculated at each volume element of core plugs.

4.2.1 Sampling

Two Berea core plugs, Sample A and B, were drilled from blocks taken from the Kipton formation by Kocurek Industries (Caldwell, Texas, US). Physical properties of the core plugs are listed in Table 4-1. Berea is a standard rock type, well characterized by the petroleum research community. For the experiment, two injection liquids were used: brine and deionized water. Three weight percent sodium chloride brine was prepared from degassed deionized water. The deionized water and brine containers were both capped throughout the experiment.

4.2.2 Instrumentation

MRI measurements were performed with an Oxford Maran Ultra (Oxford Instruments, Abingdon, UK) vertical bore permanent magnet with internal bore diameter of 51 mm operating at ^{1}H frequency of 2.21 MHz. This unit includes a radiofrequency probe and

amplifier, and a Crown Macro-Tech 5002VZ gradient amplifier. The maximum gradient strength for this instrument was 41.5 G/cm. All MRI images were measured in one direction only. SE-SPI sequence with 16 elements in *k*-space was used for spatially resolved T_2 distribution profiles. The WinDXP software program (Oxford Instruments, Abingdon, UK) was used for extracting T_2 spectra from the exponentially decaying signal using the BRD algorithm. Programs developed in-house (UNB MRI Centre) written in the IDL environment (Exelis Visual Information Solutions, Boulder, Colorado, USA), and Matlab (Mathworks, Natick, Massachusetts, US) were used for post-processing and preparing plots.

A Quizix-6000-SS pump (Chandler Engineering, Tulsa, OK) was utilized for pumping aqueous fluids. Differential pressures and solution conductivity were measured using an Omegadyne DPG409 pressure gauge and Omegadyne PHH-80BMS pH/conductivity meter respectively (Omega Engineering Inc., Sunbury, Ohio, US).

Table 4-1 Physical properties of core plug samples A and B

Sample	**A**	**B**
Diameter, mm	38	38
Length, mm	49	52
Initial Porosity, fraction (Gravimetric)	NA	0.200
Initial Porosity, fraction (FID, Magnetic Resonance)	0.191	0.205
Initial Permeability, mD (Initial SE-SPI image)	7.1	1450
Final Permeability, mD (Final SE-SPI image)	3.2	49.8

4.2.3 Experimental Procedures and Measurements

The oven dried Berea core in an Aflas sleeve was held tight by two heat shrink tubing pieces applying 0.15 MPa to the periphery of the core. A set of flow lines connected the pump, core holder, differential pressure gauge and brought the effluent fluid to a glass container for monitoring pH and conductivity. Brine flowed through the core while the core was in the magnet vertically. Only after the effluent conductivity reached a plateau, the pumped fluid was changed to deionized water. A safety pressure setting of 0.10 MPa prevented the pore pressure going beyond the overburden pressure. The inlet pressure exceeded the safety pressure, indicative of permeability reduction in the core plug. Deionized water injection was restarted after each over-pressure incident. Sub-millimeter semi-transparent particles were observed in the clear PTFE outlet tubing.

The SE-SPI image was 16 voxels with a field of view of 100 mm. The 90° and 180° pulse durations were 28.35 μs and 56.70 μs respectively with a deadtime of 30 μs. A filter width of 125 kHz corresponding to a dwell time of 8 μs was used in all measurements. The receiver deadtime for this filter was 33 μs. The gradient ramp up time, encoding time, and ramp down were set to 100 μs, 200 μs, and 100 μs respectively. The first echo time was set to be 100 μs longer than the remaining echoes. The measurement was repeated 16 times which required 27 minutes. Echo trains of all voxels in the SE-SPI measurements were inverted to spectra using a fixed regularization parameter of 1 in the BRD algorithm (Butler et al. 1981). The experimental procedures followed for Sample A and B were slightly different, which is explained below.

Sample A was vacuum saturated in the core holder and 12 pore volumes of brine flowed through the core at constant flow rate and ramped flow rate mode while the core was vertically in the magnet. Flow direction was from *bottom to top*. The inlet pressure exceeded the safety pressure and injection was started again four times. Fine particles carried by the effluent stream were collected in the glass container for X-ray diffraction measurements. Sixteen time-domain points were sampled on 1152 echoes collected with an echo time of 1800 μs.

Sample B was saturated in a vacuum chamber and transferred to the core holder afterwards. Air present in all the flow lines leading to and leaving the core plug and differential pressure gauge was meticulously purged. Brine flowed into the core from *top to bottom* at eight flow rates ranging from 0.1 to 0.5 cc/min before the first and after the last step of deionized water injection. A total of 37 pore volumes of brine was injected at a series of constant flow rates not exceeding 0.5 cc/min into the core before starting deionized water injection at a flow rate of 0.5 cc/min. The inlet pressure exceeded the safety pressure and injection was started again ten times. Flow direction was from top to bottom, in contrast to Sample A, for all injection steps. The SE-SPI measurement was run with 1024 echoes in total collected with an echo time of 1800 μs. Twenty time-domain points were sampled on each echo.

The validity of SE-SPI is well established for determining mobile fluid content in porous materials (Muir and Balcom 2013). In addition, SE-SPI, CPMG and free induction decay

measurements provide a plethora of data that gives internal consistency to the conclusions gathered from this work.

Because of the chosen echo time, 1800 μs, CPMG and SE-SPI methods are unable to reliably measure ^{1}H in water with T_2 values less than 1 ms. Therefore, noise is an inherent part of MR signal acquisition and affects the uncertainty bounds (or standard deviation) of quantitative MRI measurements. The standard deviation of MR parameters such as proton density and T_2 were calculated from measurements and the propagation of the uncertainties to petrophysical properties were calculated using partial derivatives.

As the core holder was unable to exert more than 0.15 MPa to the core plug periphery, restricting the pressure of the pump to 0.10 MPa results in limited fines migration, compared to what would be expected at higher pressures.

4.3 Results and Discussion

After bulk CPMG measurements showed a noticeable shift in the T_2 distribution mode of the core plug during the flooding, from 170 to 220 ms, SE-SPI was used to investigate the difference between pseudo pore size distributions at different positions along the core. The shift in the T_2 spectra of the core inlet and outlet shows opposite trends. The pore size distribution of the inlet and outlet, inferred from T_2 distributions, are shifted to larger and smaller values respectively, as shown in Figure 4-1. This suggests that the average pore size is increased at the inlet of the core and reduced at the outlet end of the core. Throughout

the text, Samples A and B before deionized water injection were compared to after the fourth and the third deionized water injection steps respectively.

The result of each SE-SPI imaging measurement was a three-dimensional scalar volume data set in which position and T_2 were the independent variables and water content was measured at each position and T_2 value. This scalar volume data set could be visualized in different ways. For example, water content was shown as a function of T_2 at two constant positions along the core in Figure 4-1. The 3D data set could also be shown as a 2D map of position and T_2 with the help of colors showing the intensity of water content in arbitrary units. The change in T_2 mode is visible in this plot, as shown in Figure 4-2. Before flooding, the T_2 map was even at different positions along the cores confirming the homogeneity of the Berea core plugs studied (Figure 4-2a and c). However, the T_2 distribution modes followed a slopping line after core flooding (Figure 4-2b and d), suggesting structural changes in the pore space. Flow direction was from bottom to top for Sample A and from top to bottom for Sample B. In both cases, T_2 was shifted to larger values at the core plug inlet (bottom of Sample A and top of Sample B) and smaller values at the outlet ends (top of Sample A and bottom of Sample B), respectively.

The second difference between the T_2 maps before and after flooding was the disappearance of short T_2 components. The same data set was represented as T_2 distributions at different voxel locations to accentuate the disappearance of short T_2 components of Sample A in Figure 4-3. The reason behind this disappearance was not

clear. However, it may be because of the confined water associated with authigenic clay plates covering rock grains which changed structure after exposure to deionized water.

The T_2 distribution was reduced to an average T_2 value from which other physical properties of the porous medium were derived. Several T_2 averages can be defined using different averaging methods (Nechifor et al. 2014). However, it is shown that the logarithmic mean is the best average transverse relaxation time constant for predicting permeability in sandstones (Borgia et al. 1997). The logarithmic means and their standard errors of transverse relaxation time distributions of six voxels within the core plug are shown in Figure 4-4. Measurement noise propagates through Fourier transform, T_2 inversion, and other mathematical operations and adds up as the logarithmic mean T_2, T_{2LM}, uncertainty. This uncertainty is based on the standard deviation of five measurements. The maximum value of this standard deviation along the core was 5 ms, which was used as a liberal estimate to prevent over-interpretation of results. This liberal estimate of T_{2LM} uncertainty was also broad enough to partially immune interpretations based on T_{2LM} to suboptimal BRD algorithm parameters. Although the logarithmic mean T_{2LM} showed variation along the sample before core flooding, it showed a distinctive declining profile along the flow path thereafter; bottom to top for Sample A and top to bottom for Sample B, as shown in Figure 4-4. Decreasing logarithmic mean T_2 along the core was ascribed to clay particle detachment and subsequent filtration within the core plug.

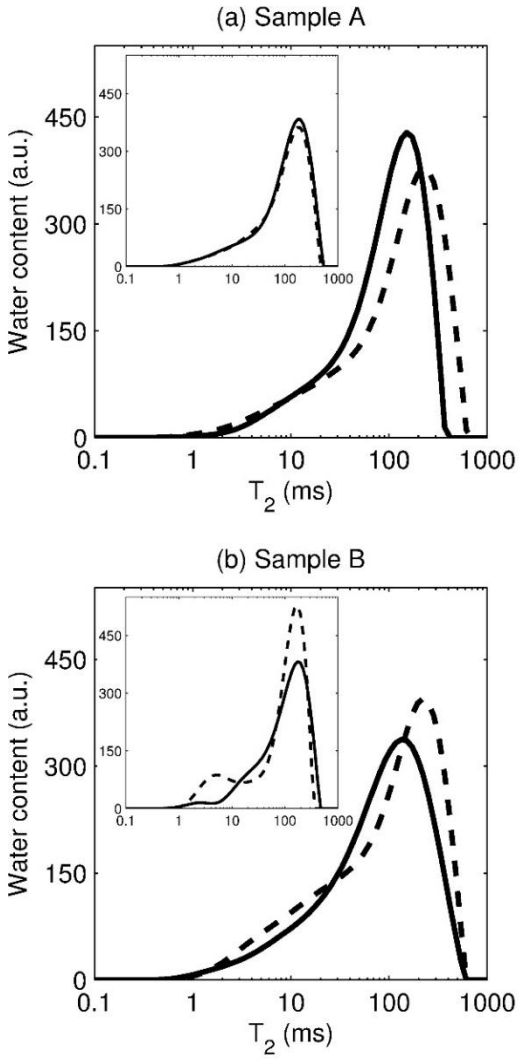

Figure 4-1 Comparing T_2 spectra of the core inlet and outlet, average of a 6.25 mm section starting 10 mm away from the ends of the core. The T_2 spectra of the inlet (dashed line) and outlet (solid line) coincide before core flooding, as shown in the insets. After core flooding, the T_2 spectra of the core inlet (dashed line) and outlet (solid line) are shifted to longer and shorter T_2 times respectively, as shown in the main figure. The changes are ascribed to fines detachment at the inlet and blockage at the outlet of the core respectively.

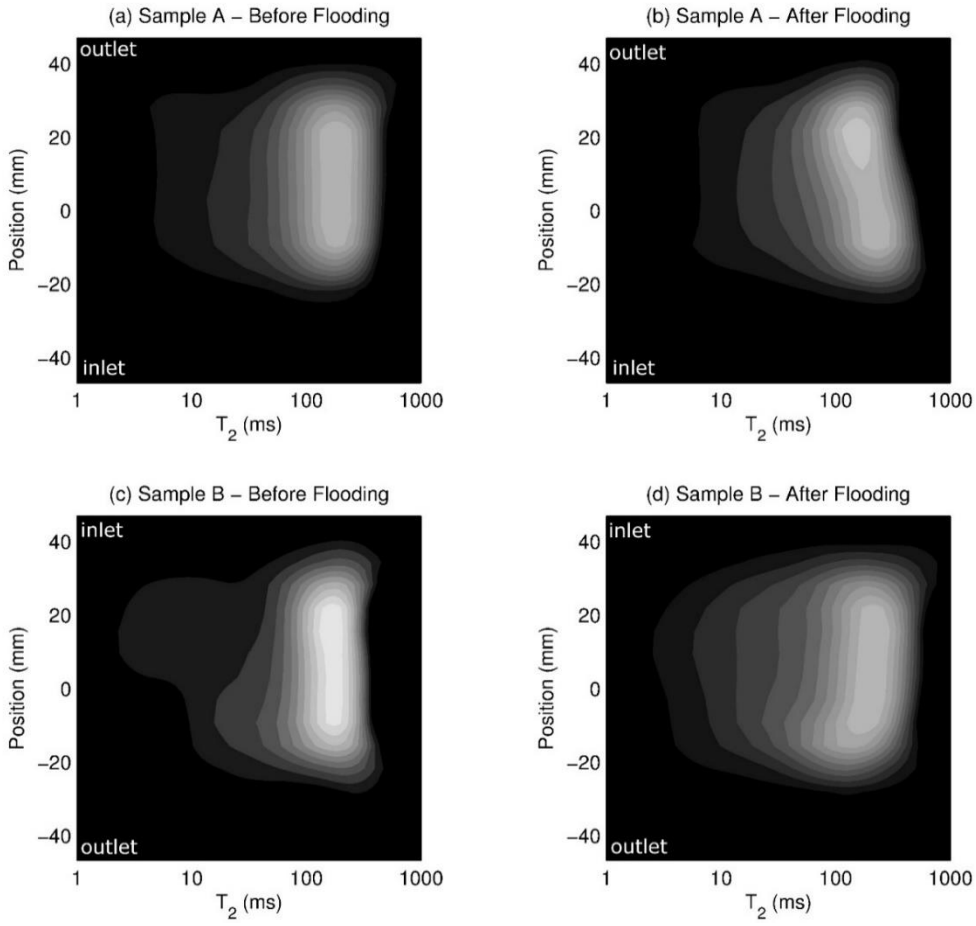

Figure 4-2 T_2 maps of the core plugs before and after flooding in grayscale. Water content values from zero to 550 in arbitrary units are linearly mapped black to white. The homogeneity of the Berea core plugs is apparent from their even T_2 map before core flooding (Left, 'a' and 'c'). The shift of T_2 distribution after flooding suggests structural change in the pore space (Right, 'b' and 'd'). Fines migration leads to longer T_2 components, larger pores, in the entrance (bottom of Sample A and top of Sample B). Shorter T_2 in the outlet end region (top of Sample A and bottom of sample B) is the result of fines filtration.

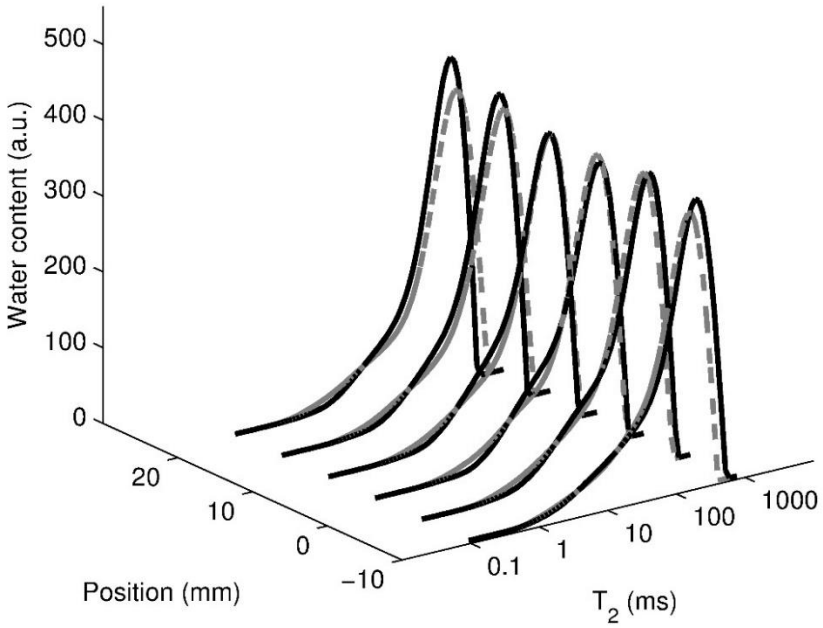

Figure 4-3 T_2 distributions at different positions along the core Sample A. Gray and black lines represent T_2 distributions before and after flooding respectively. The disappearance of short T_2 components, zero to ten milliseconds, is noticeable in this plot. The reason for this disappearance is not clear, but it may be ascribed to the confined water associated with authigenic clay plates covering rock grains; the structure of which change after exposure to deionized water.

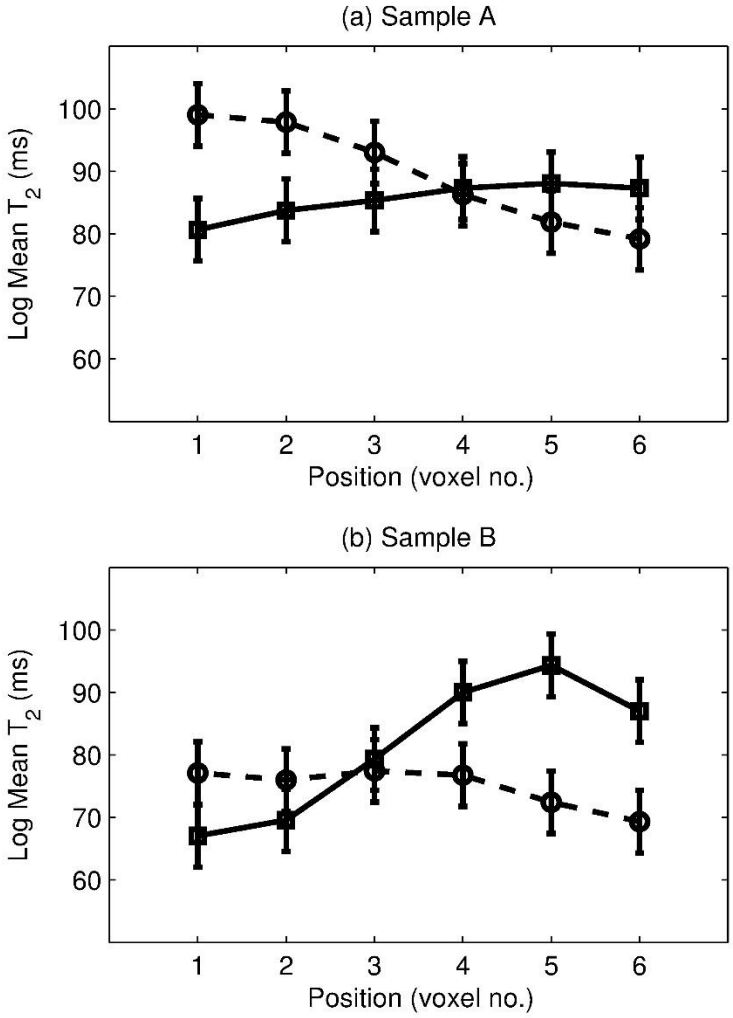

Figure 4-4 Logarithmic mean transverse relaxation time along the Berea core plugs before (square markers, solid line) and after (circle markers, dashed line) deionized water flooding. The mean T_2 profile along the core shows a distinctive declining pattern after flooding. The filtration of detached clay particles within the core leads to reduced pore size distributions along the core. Position is represented by the volume element (voxel) number starting from the inlet of the cores.

The mean T_2 permeability model (also known as SDR model) for sedimentary rocks estimates permeability as a function of logarithmic mean T_2 and porosity; it works best for samples containing water phase only (Coates et al. 1999),

$$k = a\, T_{2\mathrm{LM}}^2 \phi^4 \tag{4-1}$$

where k is permeability, T_{2LM} is logarithmic mean T_2, ϕ is porosity, and a is a proportionality parameter which depends on the rock type. Therefore, Equation (4-1) directly incorporates two parameters from SE-SPI MR experiments into the permeability estimation: T_{2LM} and ϕ. In water saturated rocks and with short echo times, T_2 is proportional to the reciprocal of the ratio of pore surface area to pore volume and is consequently proportional to the pore hydraulic radius (Coates et al. 1999). The porosity exponent, in Equation (4-1), is the result of correcting the permeability model based on the established correlations between tortuosity and porosity. The mean T_2 permeability model fits into permeability-porosity relationships relying on specific surface area which require porosity raised to a power of roughly 4 (Nelson 1994). Most of the surface area is contributed by the smallest pore sizes of T_2 distribution. However, the small pores contribute least to permeability. The porosity power of 4 serves to unweight the contribution of the small pores (Nelson 1994). In the surface area models, porosity serves a dual role, first as a measure of tortuosity and second as a measure of the pore size distribution function (Nelson 1994). Sigal (2002) provides an interesting insight into the theoretical foundations of the mean T_2 permeability model.

The mean T_2 permeability model has two shortcomings:

(1) MR measures the pore body size, while permeability is affected by the pore throat size. Equation (4-1) works because there is a strong correlation between the throat and pore size, which is the case in porous rocks (Coates et al. 1999). However, this correlation is partially disrupted in the fines migration process.

(2) The effects of the pore space topology (connectedness) is not considered in this model. Pore connectivity can change dramatically without a considerable change in porosity or pore size in processes like fines migration. Sen et al. (1990) has shown that adding the porosity exponent from formation factor measurements, which is a proxy for connectedness, leads to better permeability predictions. This is especially relevant to permeability predictions from well logs.

The proportionality parameter a, in Equation (4-1), is essentially a model fitting parameter to address the shortcomings of the mean T_2 permeability model. The combined effect of throat-to-pore size ratio and pore space topology is considered in the proportionality parameter in Equation (4-1). The proportionality parameter was employed as a model fitting parameter to match the model predictions and experimental permeability data. The initial and final permeabilities of the core plugs measured using a differential pressure gauge at the time of initial and final SE-SPI images were 7.1 mD and 3.2 mD for Sample A and 145 mD and 49.8 mD for Sample B, respectively. Permeability, as the most accessible manifestation of the effects of pore throat size and pore space topology, was

used to calculate the proportionality ratio before and after flooding: $a_r = 0.34$ for Sample A and $a_r = 0.28$ for Sample B. This value was calculated from Equation (4-1) and applied to the bulk of the cores before and after the injection of deionized water as the values of permeability, logarithmic mean T_2 , and porosity were all known. This value of the proportionality ratio was used for the bulk of the cores as permeability measured using a differential gauge was not spatially resolved. However, this average value was used for spatially resolved permeability calculations. The similarity in a_r values between samples A and B potentially demonstrates the similar changes in pore topology and geometry in Berea sandstone core plugs resulting from the water-shock experiment.

Using the ratios of proportionality parameter, logarithmic mean T_2 and ϕ, Equation (4-1) turns into

$$k_r = a_r \, T_{2\mathrm{LM}r}^2 \phi_r^4, \tag{4-2}$$

where the r index means the ratio of the property before and after flooding.

For estimating the permeability ratio along the core, the porosity ratio was required which was calculated from the first points in the CPMG data for each volume element of the core plug, as shown in Figure 4-5**.** These calculations showed that permeability had a decreasing trend along the core plugs, as shown in Figure 4-6. The average permeability calculated using this method was guaranteed to match the conventionally measured one as its value was already incorporated into the proportionality parameter. Therefore, the permeability

profile was not independent of values measured using differential pressure gauge. Independent spatially resolved measurements of permeability could be acquired using pulsed gradient MR methods as reported by Romanenko et al. (2012). Spatially resolved pulsed field gradient methods, although not used in this study, also offer excellent potential for more information on fines migration effects in rocks.

Topology (the connectedness) and geometry (shape and size) of the pores are the most important factors affecting the transport properties of porous rocks (Sahimi et al. 1990). Continuum models like Equation (4-1) cannot satisfactorily describe the connectivity of the pore space from a global standpoint (Sahimi et al. 1990). CPMG and SE-SPI experiments are only sensitive to the geometry of the pore space and do not reveal any information on the connectivity. However, other MR measurements like exchange or velocimetry (Romanenko et al. 2012) have the potential to extract information on topological effects in the laboratory. In well logging applications, the porosity exponent can significantly enhance the correlation between permeability and relaxation time (Sen et al. 1990). Therefore, although we do not have access to permeability values for correction purposes in the case of well logging, registered values of porosity exponent could be used to incorporate the effects of topology.

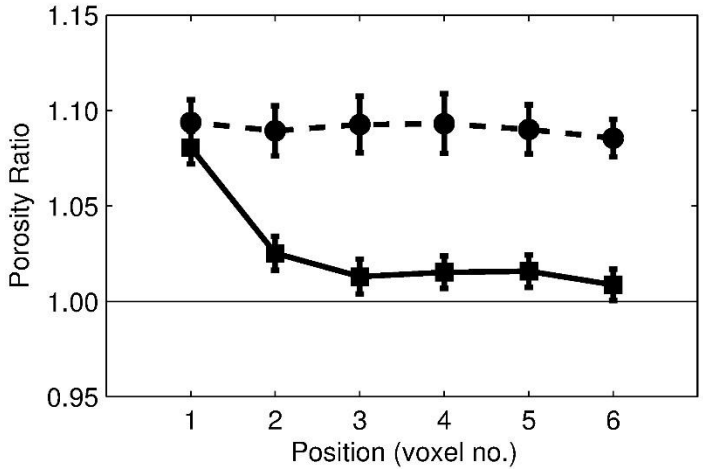

Figure 4-5 The ratio of porosities of volume elements in the core plugs Sample A (solid line) and B (dashed line) normalized to before flooding as a function of voxel number from the inlet end of the cores. Each voxel is a slab of the core 6.25 mm thick. The porosity ratio is more than one for all the measured points and decreases with distance from the inlet end. Porosity trend in Sample B is within the uncertainty range, while Sample A shows a clear declining trend along the core. Position is represented by the volume element (voxel) number starting from the inlet end of the cores.

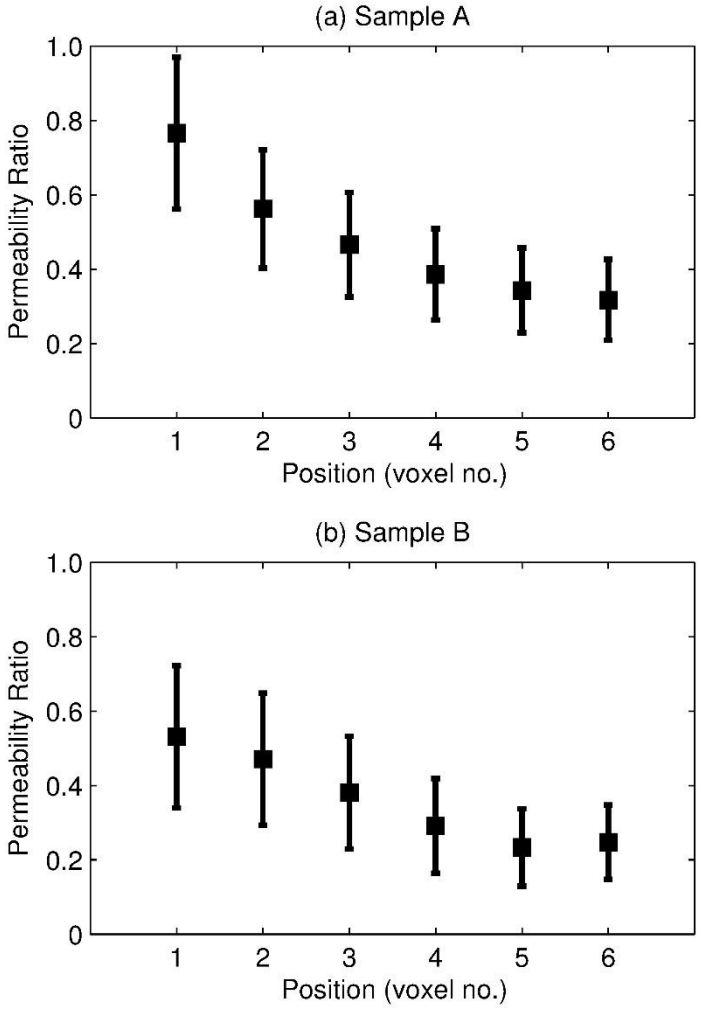

Figure 4-6 Permeability ratio along the core plug. Fines migration in the core plug causes reduced permeability because of pore throat plugging and reduced connectivity. Position is represented by the volume element (voxel) number starting from the inlet of the cores.

The flow of deionized water in sandstone cores would not cause fines migration, unless the cores were previously exposed to brines of a certain ionic strength (Khilar and Fogler 1983). Clay and quartz minerals both have negative surface charge. However, because of the presence of adsorbed ions and hence attractive forces, clay plates can cover the quartz crystals. Changes in the surface potential can lead to a repulsive force between quartz grains and the clay plates not confined by stress. This change in the surface potential is brought about by changes in the solution pH (Valdya and Fogler 1992). The sodium ions adsorbed on the clay surfaces are removed by ion-exchange after exposure to deionized water resulting in an increased pH (Carroll 1959). This changes the surface potentials resulting in repulsive forces between them and eventually their detachment (Valdya and Fogler 1992). The dislodged clay particles flow in the pore space until they are trapped in pore throats or exit the core into the effluent stream. This filtration process depends on the fines particle size distribution and the pore size distribution of rock. X-ray diffraction measurements showed three types of minerals in the fines: muscovite, clinochlore, and halite. Muscovite is the most common mica mineral, structurally similar to micaceous clays and clinochlore is a type of chlorite, one of the major groups of clays. In addition to the clays, there was also halite in all fine samples; 11% in the last sample collected, indicative of the role of ion-exchange in the formation damage process. The semi-quantitative mineral composition of the Berea core plug and its fines show that muscovite is the leading mineral initially released in the effluent stream followed by clinochlore while halite seems to be quasi-constant in the outlet stream, as shown in Table 4-2.

Clay particles are thin sheets with large surface area. Therefore, their dislocation is not only associated with increased porosity, but also significant change in transverse relaxation time as the transverse relaxation time is governed by relaxation at the pore surface. The relaxation rate, the inverse of the relaxation time, is proportional to the surface-to-volume ratio of the pores in the fast exchange regime:

$$\frac{1}{T_{2\mathrm{LM}}} = \rho \frac{S_p}{V} \qquad (4\text{-}3).$$

Table 4-2 Semi-quantitative mineral composition of the Berea core plug and collected fines as percentages for Sample A.

Mineral	**Berea Sandstone**	**Fines Sample 1[a]**	**Fines Sample 3**	**Fines Sample 6**
Quartz	89			
Feldspar (albite)	06			
Clays	05			
Muscovite	01	93	02	13
Clinochlore	04	02	73	76
Halite		05	25	11

[a] Fine samples one, three, and six were collected immediately after, after five pore volumes, and at the end of deionized water injection respectively.

In Equation (4-3), $T_{2\mathrm{LM}}$ is logarithmic mean transverse relaxation time, ρ is surface relaxivity constant, S_p is the surface area of the pore and V is the volume of the pore fluid which has access to the pore surface. Assuming equal average surface relaxivity constant for all the volume elements along the core, and using Equation (4-3) as a ratio formulation, we have

$$S_r = V_r/T_{2\mathrm{LM}r}, \tag{4-4}$$

where subscript r shows the ratio of the final value to the initial value. Accumulation of clays are expected to result in increasing values of S_r along the flow path, as shown in Figure 4-7. The surface area ratio is 0.90 and 1.1 near the inlet and the outlet of Sample A respectively. Sample B showed even larger change in surface to volume ratio along the core. Small uncertainties in the logarithmic mean T_2 resulted in very large uncertainties in the surface area ratio to the point that considering the uncertainties, the difference between two consecutive points becomes questionable. However, the difference between the first two and last two points is large enough to demonstrate a meaningful change in the surface area ratio. Increasing the number of scans in the SE-SPI experiment reduces the uncertainty associated with data. However, the measurement time is proportional to the number of scans and this results in longer acquisition time.

Each MR experiment was a signal measured as a function of time designed to reveal certain information about the nuclei present in the sample through its initial amplitude and decay rate. However, MR signal bears noise from the resistance of the coil and system electronics. This noise results in uncertainties associated with the measured amplitude and lifetime of MR signals. The uncertainty of water content of each volume element of the core was assigned the standard deviation of the last ten echo amplitudes in its decay train of the SE-SPI dataset after Fourier transform. Each registered value in the decaying signal had an uncertainty associated with it which propagates through Fourier transform, T_2 inversion,

and logarithmic mean T_2 calculation. Propagation of signal noise through these calculations showed the upper bound of logarithmic mean T_2 uncertainty to be 5 ms through repetitive measurements. The logarithmic mean T_2 uncertainty, which itself is a function of the signal noise level, is the major factor contributing to high uncertainties associated with permeability and surface area ratios provided in Figures 4-6 and 4-7. It is feasible to further reduce noise by using signal averaging, improved coil design, and electrically insulating the differential pressure meter from the pore-filling fluid.

In addition to these experimental studies, fluid-solid reaction in porous materials has extensively been studied theoretically by continuum and statistical models. Continuum models cannot accurately predict the changes in permeability in fines migration processes as they use Kozeny-Carman like equations for permeability predictions which exclude information on pore interconnectivity (Sahimi et al. 1990). Sharma and Yortsos (1986; 1987) developed the first significant statistical model for fines migration, which uses an effective medium approximation to represent the flow field in a network of interconnected pores. This predictive model estimates particle trapping as a function of time and position by a solution of non-linear PDEs. The adjustable parameters in these models are tuned so that the predictions match experimental bulk permeability as a function of time. Spatially resolved information on the pore level behavior provided by this method provides more data for matching adjustable parameters. The trend and range of permeability predictions from logarithmic mean T_2 profile of only the first step of deionized water injection (results not shown here) was correlated with the theoretical local permeability predictions by

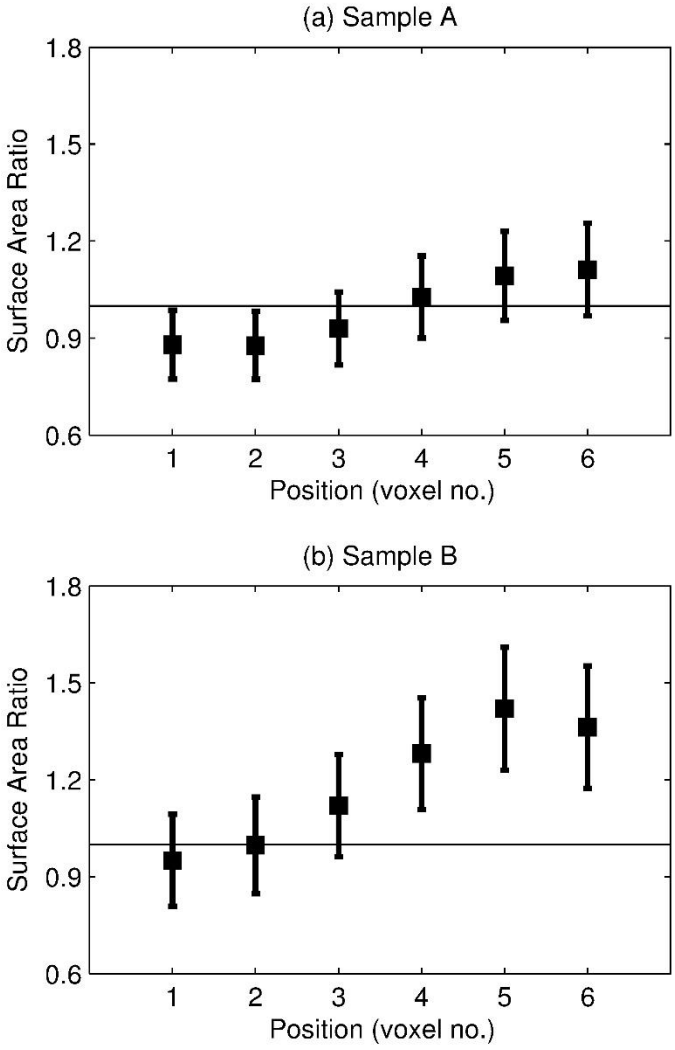

Figure 4-7 Surface area ratio profile of the sample inferred from T_2 distributions. Position is represented by the volume element (voxel) number starting from the inlet of the cores. Surface area increases with distance from the inlet of the core. Migration of clay particles which have high surface to volume ratio leads to higher surface area close to the outlet of the core plug.

Sharma and Yortsos (1987, their figure 7). The intricacies of the Sharma-Yortsos model and laboratory experiment leave the experimental-theoretical agreement of the results to a later study.

4.4 Conclusions

MRI methods based on CPMG can map T_2 distributions in porous rocks, hence showing the spatial variation of the pseudo pore size distribution. The SE-SPI imaging method was used to obtain profiles of pseudo pore size distribution along two Berea core plugs undergoing a water-shock fines migration experiment.

It was observed that the mean pseudo pore size decreased in the flow direction. In addition to the mean pseudo pore size, the surface area ratio following water shock to that of the prior brine injection step showed increasing surface area accessible to exchanging water molecules. Although the porosity profile was slightly increased, the permeability decreased along the core plugs from the inlet to the outlet direction. Reductions in the mean T_2 are consistent with decreasing T_1 values in deep bed filtration experiments by other investigators (Fordham 1993). However, the reason behind the disappearance of short T_2 components in the range of 1-5 ms is subject to further investigation.

The results of this study validate that this MRI method can demonstrate permeability impairment and can therefore be applied for testing the remedial processes or preventive measures for fines migration. In a broader perspective, this method presents a new

approach to identify, study, and especially prevent potential problems associated with impending fines migration during petroleum production.

This chapter illustrated a simple example of using MRI in monitoring core flooding studies. Currently, the compatibility of brines for water flooding projects is almost exclusively performed using aqueous thermodynamics packages. However, the sensitivity of rocks to the water injection flow rate is still an issue that is investigated experimentally. The method devised in this research can characterize the effects of fines migration in rocks spatially and quantitatively. Previously, this was limited to bulk measurements the information of which is limited to effluent analysis and differential pressure. This work is cited by six research papers since its publication.

4.5 References

Al-Abduwani, F. A. H., Farajzadeh, R., and Van den Broek, W. M. G. T. 2005. Filtration of Micron-Sized Particles in Granular Media Revealed by X-ray Computed Tomography. *Rev. Sci. Instrum.* 76 (10): 1-6. 103704. http://dx.doi.org/10.1063/1.2103467.

Al-Duailej, Y. K., Kwak, H. T., Caliskan, S. et al. 2013. Wormhole Characterisation Using NMR. International Petroleum Technology Conference, Beijing, China, 26-28 March. IPTC-17063-MS. http://dx.doi.org/10.2523/17063-MS.

Azari, M. and Leimkuhler, J. M. 1990. Formation Permeability Damage Induced by Completion Brines. *J. Pet. Technol.* 42 (4): 486-492. SPE-17149-PA. http://dx.doi.org/10.2118/17149-PA.

Borgia, G. C., Brown, R. J. S., and Fantazzini, P. 1997. Different "Average" Nuclear Magnetic Resonance Relaxation Times for Correlation with Fluid-Flow Permeability and Irreducible Water Saturation in Water-Saturated Sandstones. *J. Appl. Phys.* 82 (9): 4197-4204. http://dx.doi.org/10.1063/1.366222.

Butler, J. P., Reeds, J. A., and Dawson, S. V. 1981. Estimating Solutions of First Kind Integral Equations with Nonnegative Constraints and Optimal Smoothing. *SIAM J. Numer. Anal.* 18 (3): 381-397. http://dx.doi.org/10.1137/0718025.

Carroll, D. 1959. Ion Exchange in Clays and Other Minerals. *Geol. Soc. Am. Bull.* 70 (6): 749-779. http://dx.doi.org/10.1130/0016-7606(1959)70[749:IEICAO]2.0.CO;2.

Coates, G. R., Xiao, L., and Prammer, M. G. 1999. *NMR Logging: Principles and Applications*. Houston: Halliburton Energy Services.

Fordham, E. J., Horsfield, M. A., Hall, L. D. et al. 1993. Depth Filtration of Clay in Rock Cores Observed by One-Dimensional ^{1}H NMR Imaging. *J. Colloid Interf. Sci.* 156 (1): 253-255. http://dx.doi.org/10.1006/jcis.1993.1106.

Fordham, E. J., Roberts, T. P. L., Carpenter, T. A. et al. 1991. Dynamic NMR Imaging of Rapid Depth Filtration of Clay in Porous Media. *AIChE J.* 37 (12): 1900. http://dx.doi.org/10.1002/aic.690371214.

Heaton, N. J., Freedman, R., Karmonik, C. et al. 2002. Applications of a New-Generation NMR Wireline Logging Tool. SPE Annual Technical Conference and Exhibition, San Antonio, Texas, 29 September-2 October. SPE-77400-MS. http://dx.doi.org/10.2118/77400-MS.

Horsfield, M. A., Fordham, E. J., Hall, C. et al. 1989. ^{1}H NMR Imaging Studies of Filtration in Colloidal Suspensions. *J. Magn. Reson.* 81 (3): 593-596. http://dx.doi.org/10.1016/0022-2364(89)90098-X.

Hürlimann, M. D. 1998. Effective Gradients in Porous Media due to Susceptibility Differences. *J. Magn. Reson.* 131 (2): 232-240. http://dx.doi.org/10.1006/jmre.1998.1364.

Khilar, K. C. and Fogler, H. S. 1983. Water Sensitivity of Sandstones. *SPE J.* 23 (1): 55-64. SPE-10103-PA. http://dx.doi.org/10.2118/10103-PA.

Minh, C. C., Jaffuel, F., Poirier, Y. et al. 2011. Quantitative Estimation of Formation Damage from Multi-Depth of Investigation NMR Logs. SPWLA 52nd Annual Logging Symposium, Colorado Springs, Colorado, 14-18 May. SPWLA-2011-JJJ.

Muir, C. E. and Balcom, B. J. 2013. A Comparison of Magnetic Resonance Imaging Methods for Fluid Content Imaging in Porous Media. *Magn. Reson. Chem.* 51 (6) 321-327. http://dx.doi.org/10.1002/mrc.3947.

Muir, C. E. and Balcom, B. J. 2012. Pure Phase Encode Magnetic Resonance Imaging of Fluids in Porous Media. In *Annual Reports on NMR Spectroscopy*, Vol. 77, ed. Webb, G. A., Chap. 2, 81-113.Burlington: Academic Press. http://dx.doi.org/10.1016/B978-0-12-397020-6.00002-7.

Nelson, P. H. 1994. Permeability-Porosity Relationships in Sedimentary Rocks. *Log Analyst* 35 (3): 38-62. SPWLA-1994-v35n3a4.

Nechifor, R. E., Romanenko, K., Marcia, F. et al. 2014. Spatially Resolved Measurements of Mean Spin-Spin Relaxation Time Constants. *J. Magn. Reson.* 239: 16-22. http://dx.doi.org/10.1016/j.jmr.2013.11.012.

Petrov, O. V., Ersland, G., and Balcom, B. J. 2011. T_2 Distribution Mapping Profiles with Phase-Encode MRI. *J. Magn. Reson.* 209 (1): 39-46. http://dx.doi.org/10.1016/j.jmr.2010.12.006.

Romanenko, K., Xiao, D., Balcom, B. J. 2012. Velocity field measurements in sedimentary rock cores by magnetization prepared 3D SPRITE. *J. Magn. Reson.* 223:120-128. http://dx.doi.org/10.1016/j.jmr.2012.08.004.

Sahimi, M., Gavalas, G. R., Tsotsis, T. T. 1990. Statistical and Continuum Models of Fluid-Solid Reactions in Porous Media. *Chem. Eng. Sci.* 45: 1443-1502. http://dx.doi.org/10.1016/0009-2509(90)80001-U.

Sen, P.N., Straley, C., Kenyon, W.E. et al. 1990. Surface-to-volume ratio, charge density, nuclear magnetic relaxation, and permeability in clay-bearing sandstones. *Geophysics* 55 (1): 61-69. http://dx.doi.org/10.1190/1.1442772.

Sigal, R. 2002. Coates and SDR Permeability: Two Variations on the Same Theme. *Petrophysics* 43 (1): 38-46. SPWLA-2002-v43n1a4.

Sharma, M. M., Chamoun, H., Sita Rama Sarma, D. S. H. et al. 1992. Factors Controlling the Hydrodynamic Detachment of Particles from Surfaces. *J. Colloid Interf. Sci.* 149 (1): 121-134. http://dx.doi.org/10.1016/0021-9797(92)90398-6.

Sharma, M. M., Yortsos, Y. C. 1986. Permeability Impairment Due to Fines Migration in Sandstones. SPE Formation Damage Control Symposium, Lafayette, Louisiana, 26-27 February. SPE-14819-MS. http://dx.doi.org/10.2118/14819-MS.

Sharma, M. M., Yortsos, Y. C. 1987. Fines Migration in Porous Media. *AIChE J.* 33 (10): 1654-1662. http://dx.doi.org/10.1002/aic.690331009.

Straley, C., Rossini, D., Schwartz, L. M. et al. 1994. Chemical Shift Imaging of Particle Filtration in Sandstone Cores. *Magn. Reson. Imaging* 12 (2): 313-315. http://dx.doi.org/10.1016/0730-725X(94)91544-X.

Straley, C., Rossini, D., Schwartz, L. M. et al. 1995. Particle Filtration in Sandstone Cores: A Novel Application of Chemical Shift Magnetic Resonance Imaging Techniques. *Log Analyst* 36 (2): 42-51. SPWLA-1995-v36n2a3.

Tran, T. V., Civan, F., and Robb, I. 2010. Effect of Permeability Impairment by Suspended Particles on Invasion of Drilling Fluids. IADC/SPE Asia Pacific Drilling Technology Conference and Exhibition, Ho Chi Minh City, Vietnam, 1-3 November. SPE-133724-MS. http://dx.doi.org/10.2118/133724-MS.

Valdya, R. N. and Fogler, H. S. 1992. Fines Migration and Formation Damage: Influence of pH and Ion Exchange. *SPE Prod. Eng.* 7 (4): 325-330. SPE-19413-PA. http://dx.doi.org/10.2118/19413-PA.

Van der Zwagg, C. H., Stallmach, F., Basan, et al. 1997. New Methodology to Investigate Formation Damage using Non-Destructive Analytical Tools. SPE European Formation Damage Conference, The Hague, Netherlands, 2-3 June. SPE-38161-MS. http://dx.doi.org/10.2118/38161-MS.

Vinegar, H. J. 1986. X-ray CT and NMR Imaging of Rocks. *J. Pet. Technol.* 38 (3): 257-259. SPE-15277-PA. http://dx.doi.org/10.2118/15277-PA.

Chapter 5 – Magnetic Resonance Imaging of CO_2 Flooding in Berea Sandstone: Partial Derivatives of Fluid Saturation[2]

Core flooding experiments are useful to understand fluid displacement processes in rocks. In such laboratory experiments, magnetic resonance imaging (MRI) can accurately quantify fluid saturation. The previous chapter provided a simple example of using MRI in monitoring fines migration, a process relevant to petroleum production. In this work[3], MRI and numerical methods were employed to describe displacement phenomena in CO_2 flooding of oil-saturated Berea core plugs. In miscible and immiscible displacement of decane by CO_2, temporal and spatial derivatives of saturation were acquired with a smoothing spline interpolation and processed to compute saturation wave velocity, dispersion coefficient, and the advection-dispersion kernel.

5.1 Introduction

Unlike most carbon utilization methods, enhanced oil recovery (EOR) has the potential to permanently store four to eight percent of the carbon dioxide mitigation challenge (Mac Dowell et al. 2017). Integrated carbon capture and storage (CCS) projects, such as the Weyburn-Midale project in Canada, have demonstrated the benefits of carbon dioxide

[2] Largely based on a submission to the SPE Journal: Afrough, A., Romero-Zerón, L., Shakerian, M., Bell, C. A., Marica, F., Balcom, B. J. 2019. Magnetic Resonance Imaging of CO_2 Flooding in Berea Sandstone: Partial Derivatives of Fluid Saturation. *SPE J.* revised in response to reviews.

injection in petroleum reservoirs (Beckwith 2011). Such projects are important steps towards large-scale CO_2 injection in oil reservoirs and saline formations (Beckwith 2011). Engineering EOR-CCS projects requires sound characterization of the underlying physical and chemical phenomena at scales ranging from nanometers to kilometers.

Magnetic resonance (MR) makes available pore-, core-, and log-scale information on rock and fluid properties as well as rock/fluid interactions. At laboratory scale, MRI can determine the mechanisms of fluid displacement; provide previously unmeasurable information about rocks and rock/fluid interaction; and measure petrophysical properties faster, easier, or with higher accuracy compared to other methods (Baldwin and King 1998).

Previous investigators encountered four major limitations in applying MR methods to CO_2 flooding in the laboratory: (1) sample size, (2) difficulties in imaging realistic samples and fluids, (3) imaging methods, and (4) data processing methods; from which the second and third problems are interrelated.

The sample size in previous research was limited to diameters of 7.5 mm (Bagherzadeh et al. 2011), 15 mm (Zhao et al. 2011a), and 26 mm (Suekane et al. 2005). Standard 38-mm diameter core plugs are studied in this research using the MS-5000 core holder (Shakerian et al. 2017), a non-magnetic metallic core holder with an integrated radiofrequency (RF) probe. Material selection and design of the MS-5000 (Shakerian et al. 2017) and its successor (Shakerian et al. 2018) permit enhanced oil recovery experiments on standard

38-mm diameter core plugs. MRI instruments with high-pressure and controlled-temperature capabilities permit the incorporation of advanced magnetic resonance studies in core laboratories for petrophysics and enhanced oil recovery studies (Mitchell et al. 2013).

Previous researchers who studied CO_2 flooding by MRI mainly used multi-slice spin-echo imaging methods at high magnetic fields of 2 T (Brautaset et al. 2008; Brautaset 2009), 7 T (Suekane et al. 2005, 2006, and 2009), and 9.6 T (Zhao et al. 2011a, 2011b, 2016; Song et al. 2013, 2014; Teng et al. 2014; Hao et al. 2015; Liu et al. 2011, 2016). Slice-selective MRI methods at high magnetic fields are unfavorable for imaging fluids in realistic porous media for two reasons: (a) High static magnetic fields commonly lead to unfavorable quantitative MR measurements due to the diffusion of pore filling fluids in the internal magnetic field gradient of porous media produced by magnetic susceptibility mismatch (Mitchell et al. 2013, Fig. 7). (b) Slice-selective MRI methods commonly have echo times of more than 10 ms which leads to an attenuation that alters the predicted saturation in samples with short T_2 components. Therefore, previous investigators mainly used glass-bead or sand packs and avoided challenging fluids such as heavy oil (Suekane et al. 2005, 2006; Liu et al. 2011; Zhao et al. 2011a, 2011b; Song et al. 2012). Suekane et al. (2005, 2006), Brautaset et al. (2008), and Zhao et al. (2011b) applied MRI methods to monitor CO_2 flooding processes and observed image artifacts due to problems associated with magnetic field gradients in their work. Brautaset et al. (2008) concluded that the fast signal decay of the ^1H nuclei, in decane-saturated chalk, did not permit reproducible saturation

measurement. Appropriate MRI methods must yield a linear signal increase with saturation.

In the current work, pure phase encoding MRI methods, including 1D Double Half k-space Single Point Ramped Imaging with T_1 Enhancement (1D DHK SPRITE, Deka et al. 2006) and 1D T_2-mapping Spin Echo-Single Point Imaging (SE-SPI, Petrov et al. 2011), were used at a low magnetic field of 0.2 T to circumvent the shortcoming of previous studies. The SPRITE class of MRI methods are well-known for their superb quantitative fluid content measurement (Muir and Balcom 2013; Mitchell et al. 2013). Even in the most challenging rock samples, such as the Wallace sandstone with ubiquitous aluminum, ferric, and manganese oxides, the relative uncertainty in fluid saturation was less than 10% (Muir and Balcom 2013). MRI measurements performed in this work demonstrated that uncertainty in imaged decane saturation in Berea was within 0.02 saturation units by material balance (Afrough et al. 2018). Previous work had an error of about 10% in glass bead packs (Suekane et al. 2005, p. 5). In SE-SPI, contrary to slice-selective methods, change in T_2 is allowed, but T_2 itself is also mapped in the imaging.

There are many instances in which time and space derivatives of saturation are necessary for parameter extraction in core flooding experiments. This work demonstrates numerical smoothing spline methods that can not only compute smooth first partial derivatives of saturation, but also the second partial derivatives that could be used in partial differential equations (PDE) such as that of advection-dispersion. An extensive function library in the

MATLAB programming environment was developed and used in a previous work (Afrough et al. 2018). This function library reads MR and MRI files acquired by the instrument, corrects data phase, removes the background signal, registers images, filters k-space data, performs Fourier transformation, stores cleaned data, performs quality control, and plots and visualizes results. The software suite was used to analyze the correlation between transverse relaxation time constants and saturation to draw information from the pore-scale processes (Afrough et al. 2018). This work extends the capabilities of the previous work by the computation of partial derivatives and analysis of the advection-dispersion PDE.

The subject of the current work is quantitative fluid saturation measurement during miscible and immiscible CO_2 displacement in decane-saturated Berea sandstone to obtain information on the displacement phenomena at core-plug scale. Partial derivatives of saturation constitute a direct method and a model-free mean for interpreting experimental data. Contrary to conventional core-flooding studies, the computation of partial derivatives of in-situ fluid saturation made possible the evaluation of wave velocity, dispersion coefficient, and the fundamental solution of the advection-dispersion PDE.

The importance of interplay between thermodynamics and fluid flow in porous media is well known in fluid mechanics (Ganesan and Brenner 2000) and petroleum engineering (Orr 2007). Despite theoretical advancements in this regard (Brenner 2005), in-situ experimental data is still very limited, especially in systems in which the effect of

dispersion is significant. This study not only provides a new method of analyzing core flooding data by computing partial derivatives, but also provides a valuable experimental dataset (Afrough et al. 2019) for other researchers to develop, verify, and compare models that describe mixture flow in porous media.

The scope of this paper is limited to the following core-plug scale processes: the study of saturation as a function of time and position, and the establishment of the evolution function of the advection-dispersion PDE.

5.2 Mathematical and Experimental Methods

Experimental procedures and numerical differentiation of the experimental data with smoothing splines are presented below.

5.2.1 Numerical Differentiation

MRI measures a prepared magnetization in the sample space, such as ^{1}H density, as a function of the spatial frequency. This function is then Fourier transformed to yield ^{1}H density as a function of position. One-dimensional T_2-mapping SE-SPI measures the density of ^{1}H nuclei as a profile along a core plug. The calibration of the signal amplitude with a known sample provides a means of calculating porosity, while the division of the signal amplitude by that of a fully saturated core plug produces saturation profiles.

In this study, we outline a post-processing scheme to compute a smooth spatiotemporal saturation function $S(y,t)$, and its partial derivatives including the first partial derivative

of saturation with respect to time $\partial S/\partial t$, the first partial derivative of saturation with respect to position $\partial S/\partial y$, and the second partial derivative of saturation with respect to position $\partial^2 S/\partial y^2$, from the experimental bivariate proton density $\rho_P(y,t)$ data.

Nonparametric regression methods, such as splines, relax model assumptions (Green and Silverman 1994) and provide an exploratory framework to study partial derivatives of multivariate functions. A smoothing spline sp fitting experimental data (ζ_i, η_i) applied variational optimization methods to penalize both the error measure

$$E(sp) = \sum_i |\eta_i - sp(\zeta_i)|^2 \tag{5-1}$$

and the roughness measure

$$R(\mathcal{D}^2 sp) = \int |\mathcal{D}^2 sp(\zeta)|^2 d\zeta \tag{5-2}$$

balanced by a smoothing parameter α such that the functional

$$F(sp) = \alpha E(sp) + (1-\alpha) R(\mathcal{D}^2 sp) \tag{5-3}$$

is minimized (Green and Silverman 1994). Multivariate tensor-product splines described by de Boor (1978), implemented in the MATLAB programming language as Curve Fitting Toolbox, were applied to convert proton density data $\rho_P(y,t)$ into a smooth proton density $\rho_{PS}(y,t)$ function. Normalizing smooth proton densities, in the range of smooth background proton density $\rho_{PS}^{BK}(y,\cdot)$ and smooth saturated proton density $\rho_{PS}^{SA}(y,\cdot)$ values, determined saturation from

$$S(y,t) = \frac{\rho_{PS}(y,t) - \rho_{PS}^{BK}(y,\cdot)}{\rho_{PS}^{SA}(y,\cdot) - \rho_{PS}^{BK}(y,\cdot)} \quad (5\text{-}4)$$

in a gridded (y,t) domain. Note that $(\cdot)$ is a placeholder for time which means the background and saturated proton density profiles are constant at all times. Domains of y and t were normalized due to the difference in their orders of magnitude and a smoothing parameter of $\alpha = 0.999$ was manually chosen in all smoothing splines. Applying different smoothing parameters near $\alpha = 1$ resulted in similar partial derivative values. The gridded saturation data were fitted by another smoothing spline and its derivatives calculated the partial derivatives $\partial S/\partial y$ and $\partial S/\partial t$ as gridded data. The gridded data for partial derivative $\partial S/\partial y$ was further subjected to another smoothing spline approximation to calculate its derivative $\partial^2 S/\partial y^2$. This two-step differentiation procedure reduced noise in $\partial^2 S/\partial y^2$ and ensured that it had a continuous derivative in its domain. The heavy-oil saturation data was corrected using an experimental hydrogen index of 0.92 at 40°C measured in this work. The validity of the numerical differentiation scheme, described above, was verified by the integration of the derivatives. We emphasize the importance of a proper normalization and smoothing. Too simplistic a procedure yields erroneous derivatives.

5.2.2 Advection-Dispersion Equation and Partial Derivatives of Saturation

The common practice in measuring dispersion coefficients in laboratory core analysis involves saturating a core plug with a fluid of initial tracer composition and injecting another fluid of different tracer composition, with the same density and viscosity, at a

constant volumetric flow rate with macroscopic mean velocity v (Handy 1959). Monitoring effluent composition provides effluent flux (Brigham 1974), in contrast to in-situ saturations, which can be fit to a solution of the advection-dispersion PDE (Logan 2001),

$$\frac{\partial S}{\partial t} + v \cdot \frac{\partial S}{\partial y} = D_L \frac{\partial^2 S}{\partial y^2}, \tag{5-5}$$

to obtain the longitudinal dispersion coefficient D_L. Equation (5-5) is also known as convective-diffusion (Sahimi 1993), or convection-dispersion (Vanderborght and Vereecken 2007) in petroleum engineering and geohydrology, respectively. Saturation S in Equation (5-5) can be regarded as the normalized tracer concentration with respect to its minimum and maximum. Please note that saturation, as defined by Equation (5-4) and later in an equivalent form by Equation (5-12), is neither a volumetric phase fraction nor the average decane composition. However, it indeed has a one-to-one relationship with the total decane composition in a core-plug section, as shown in the appendix.

Many uncorrelated steps in the movement of fluid molecules are required for a porous material to obey Equation (5-5) with a constant longitudinal dispersion coefficient D_L and a Gaussian dispersion kernel (Klafter and Sokolov 2011). Bacri et al. (1990) demonstrated that if the correlation length of dispersion is not small compared to the sample length, finite-size effects can significantly affect flowing and in-situ saturations. Therefore, it is important to characterize the dispersion correlation length of a porous material and determine conditions under which Equation (5-5) is valid (Sahimi 1993, pp. 1458).

For constant D_L and a step boundary condition with $S(0, t > 0) = 0$ and $S(+\infty, t > 0) = 1$, and initial condition $S(y, 0) = 1$, the evolution function of Equation (5-5) is

$$S(y,t) = \frac{1}{2}\left\{1 - \text{erfc}\left[\frac{(y-y_0)-v(t-t_0)}{\sqrt{4D_L(t-t_0)}}\right]\right\} \tag{5-6}$$

where erfc is the complimentary error function (Logan 2015, p. 82). The starting time t_0 is the time that CO_2 is injected from the top face at $y_0 = L/2$ where L is the length of the core plug. Simplifying Equation (5-6) with the first term of its Taylor series expansion results in

$$S(y,t) \cong \frac{1}{\sqrt{4\pi D_L(t-t_0)}}[(y-y_0) - v(t-t_0)]. \tag{5-7}$$

where the inverse of slope squared is

$$\left(\frac{\partial y}{\partial S}\right)^2 = 4\pi D_L(t-t_0) \tag{5-8}$$

by which the longitudinal dispersion coefficient could be calculated. Equation (5-6) is not the same as the solution for the constant displacing fluid injection rate. However, it is a good approximation (Bacri et al. 1990; Orr 2007, pp. 15).

Direct differentiation of Equation (5-6), with respect to y, leads to the fundamental solution G of the advection-dispersion equation, Equation (5-5),

$$G(y,t) = \frac{1}{\sqrt{4\pi D_L(t-t_0)}} \exp\left\{-\frac{[(y-y_0)-v(t-t_0)]^2}{4D_L(t-t_0)}\right\}. \tag{5-9}$$

The function G is also called the kernel or Green's function of Equation (5-5) and is the solution that results from a point source of unit saturation at $y = y_0$ and $t = t_0$ (Logan 2015, pp. 82-84). Kernel functions have interesting properties; for example, Equation (5-9) has unit integral in the range of $-\infty < y < +\infty$ for $t > 0$. Logan (2015) provides a basic introduction to the kernel functions of convection-diffusion PDEs. Aris and Amundson (1957) develop kernel functions of the dispersion equation in the mixing cell and diffusion languages. A more comprehensive and advanced study of kernel functions, especially those for the diffusion equation, is covered by Duffy (2001).

Regardless of miscibility, it is possible to estimate wave velocity as a function of saturation in a displacement process. Wave velocity $(\partial y/\partial t)_S$ is the velocity at which a chosen saturation propagates (Orr 2007, p. 45) and can be evaluated from the partial derivatives of saturation with respect to position and time using the triple product rule (Willhite 1986, p. 61) by

$$v_s = \left(\frac{\partial y}{\partial t}\right)_S = -\left(\frac{\partial S}{\partial t}\right)_y \Big/ \left(\frac{\partial S}{\partial y}\right)_t. \tag{5-10}$$

The wave velocity indicates how fast a saturation propagates and is different from the velocity of liquid or vapor phases in the case of two-phase flow (Orr 2007, p. 45). The relationship between v_s, time, and position of a characteristic saturation is simply

$$y = v_s\,(t - t_0) + y_0 \tag{5-11}$$

where t_0 and y_0 are the initial time and position of the saturation at the start of the process, respectively.

Table 5-1 Physical properties of core plug samples. These rock samples are all homogeneous Berea sandstones from the Kipton formation.

Property	BP1	BA1	BA2	BA3
Diameter (mm)	38	38	38	38
Length (mm)	52	51	50	52
Porosity (fraction)	0.180	0.197	0.197	0.197
Permeability [$(\mu m)^2$]	0.0706	0.108	0.0864	0.193

Table 5-2 Physical properties of pore-filling fluids at 40 °C and ambient pressure (except for CO_2).

Sample	Dynamic viscosity (mPa.s)	Volumetric mass density (g/cm^3)
Decane	0.69	0.715
Carbon dioxide @ 6 MPa	0.018	0.149
Carbon dioxide @ 9 MPa	0.035	0.486
Heavy oil	640	0.946
H_2O brine	0.75	1.012
D_2O brine	0.90	1.124

5.2.3 Core-Plug Samples and Materials

The rock samples used in this study included four Berea sandstone core plugs of 38 mm diameter and 50 mm length with a porosity of approximately 0.20 and permeabilities in the range of $0.1 - 0.2\ (\mu m)^2$. The core plugs were drilled from a slab taken from the Kipton formation by Kocurek Industries (Caldwell, Texas, USA) and displayed identical T_2 distributions, a sign of similar pore geometry. The core plug properties are summarized

in Table 5-1. Supercritical CO_2 flooding does not affect the pore structure of Berea core plug because of the chemical resistance of quartz (Vogt et al. 2014).

Decane (≥95%, Sigma-Aldrich, St. Louis, Missouri, USA), CO_2 (99.7%, Air Liquide Canada, Montreal, Canada), and heavy crude oil (with a viscosity of 640 mPa·s at 40°C supplied by Husky Energy, Calgary) were used in the experiments. Fluorinert (3M, St. Paul, Minnesota, USA) was used as the confining fluid in the core holder, because it has no ^1H in its structure. Brine prepared in this work had a concentration of 3 wt% sodium chloride with water and deuterium oxide (99.8%, Cortecnet, Voisins-le-Bretonneux, France). All fluids, except heavy oil, were degassed before use. Table 5-2 shows the physical properties of the pore filling fluids.

5.2.4 Instrumentation

MRI measurements were performed with an Oxford Maran DRX-HF (Oxford Instruments Limited, Abingdon, UK) vertical bore permanent magnet at a static magnetic field of 0.2 T, resulting in an ^1H frequency of 8.5 MHz. This instrument is equipped with a 1KW BT01000-AlphaS RF amplifier (TOMCO Technologies, Stepney, Australia) and a shielded three-axis magnetic field gradient coil set driven by Techron 7782 gradient amplifiers (Techron, Elkhart, Indiana, USA) that provide maximum magnetic field gradients of 25 G/cm, 24 G/cm, and 33 G/cm in the x-,y-, and z-direction, respectively. The core plug was placed vertically in the magnet and the core holder such that $y = 0$ marks the centre and x- and z-directions form the radial plane of the core plug.

The free induction decay (FID), Carr-Purcell-Meiboom-Gill (CPMG), 1D DHK SPRITE (Deka et al. 2006), T_2-mapping SE-SPI (Petrov et al. 2011), and 3D π Echo Planar Imaging (π EPI) (Xiao and Balcom 2015) methods measured proton density in bulk and spatially resolved. An in-house function library in the MATLAB array programming language (MathWorks Inc., Natick, Massachusetts, USA) was developed for reading data and image files, Fourier transformation, data storage, quality control plots, registering profiles and images, data smoothing, visualization, curve fitting, and plotting. WinDXP (Oxford Instruments, Abingdon, UK) performed exponential analysis of decaying signals using the Butler-Reeds-Dawson (BRD) algorithm (Butler et al. 1981).

Core flooding experiments were performed in the MS-5000 custom-built high-pressure MRI core holder (Shakerian et al. 2017). The core holder is made of Hastelloy-C276 which is non-magnetic and has low electrical conductivity for reducing eddy currents induced by switching magnetic field gradients (Goora et al. 2013). This core holder is composed of a vessel, two closures, a body made of polyether-ether-ketone (PEEK) that encloses the solenoid RF probe, and a heat exchange jacket. Three pumps, a Quizix-6000-SS (Chandler Engineering, Tulsa), a Shimadzu LC-8A (Shimadzu, Kyoto, Japan), and a Teledyne Isco 100DX (Teledyne Isco, Lincoln, Nebraska, USA) were used for injecting oleic, aqueous, and CO_2 phases, respectively. Ashcroft K1 pressure transducers (Ashcroft, Stratford, Connecticut, USA) along with an OM-DAQ-USB-2401 USB data acquisition system (Omega Engineering, Stamford, Connecticut, USA) and several analog pressure gauges recorded and displayed pressures.

5.2.5 Experimental Methodology

A preliminary experiment PR1 studied the effect of CO_2/decane mole ratio on the range of T_1, T_2, and T_2^* at a room temperature of 20°C and a pressure of 4.2 MPa in Berea sample BP1. Table 3 shows a summary of the flooding experiments in this work. Full procedures are described below.

5.2.6 Miscible and Immiscible Drainage of Decane

The core plug was first installed in the core holder. The core holder assembly was then positioned in the magnet. Fluorinert was injected into the confining fluid port. A heat circulator set the temperature of the core holder at 40°C in the magnet. Confining pressure was held at least 4 MPa higher than the pore pressure. A primary CO_2 injection from the top of the core plug removed air. Decane was subsequently injected into the core plug to replace CO_2. A waiting period of 24 hours ensured a homogeneous temperature in the core plug and dissolution of any remaining CO_2 in the decane phase. CO_2 was injected from the top of the core plug at pressures of 6 and 9 MPa for immiscible and miscible displacements, respectively. The minimum miscibility pressure (MMP) of decane/CO_2 mixture is 8 MPa at 40° C (Liu et al. 2015) which was verified by the thermodynamics calculations described later. A series of FID, CPMG, DHK SPRITE, and SE-SPI measurements were performed during the injection of CO_2 and this process ceased when no further change was observed in sequential MRI profiles. For the immiscible flooding experiments, π EPI experiments were also performed to acquire 3D images of the displacement process.

5.2.7 Immiscible Flooding of Heavy Oil

This experiment was similar to the decane procedure outlined above. However, after removing air from the core plug, H_2O brine was injected into the core, then it was subsequently displaced with D_2O brine. The heavy oil was injected into the core plug and flow lines affected by the injection of heavy oil were replaced. CO_2 was then injected into the core plug. D_2O is invisible to MRI at the ^1H frequency, because D_2O brine does not have any ^1H nuclei in its chemical structure.

It is possible to undertake core flooding experiments at pressures and temperatures up to 35 MPa and 80 °C with the MS-5000 core holder. However, experiments at other conditions were not performed as they would not significantly contribute to the main objective of this research. Experiment F1 was performed twice and confirmed the repeatability of the measurements.

5.2.8 Imaging Parameters

One-dimensional SE-SPI images had 64 sections with a field of view of 64 mm, providing a nominal resolution of 1 mm per core plug section. A core-plug section is an imaginary disc of specific thickness within a core plug. Measurement of each property, such as saturation, is assigned to a position at the center of the respective section. For example, in the current study, 50 sections each 1 mm thick covered the full length of each core plug.

Table 5-3 Summary of the experiments performed in this research. INVREC is an abbreviation for inversion recovery magnetic resonance method used to measure T_1 distributions.

Experiment	**PR1**	**F1**	**F2**	**F3**
Core plug sample	BP1	BA1	BA2	BA3
Initial fluid saturation	Two-phase	Single-phase	Single-phase	Two-phase
Phase 1	Decane	Decane	Decane	Heavy oil
Phase 2	CO_2	-	-	D_2O brine
Interstitial water saturation	No	No	No	Yes
Displacing fluid	CO_2+decane	CO_2	CO_2	CO_2
Flow rate (cm^3/min)	-	0.04	0.04	0.04
Intrinsic Velocity (mm/day)	-	254	254	254
Back pressure (MPa)	6	9	6	9
Temperature (°C)	20	40	40	40
MMP at experimental temperature (MPa)	5.6	8	8	NA
Magnetic resonance methods	FID, CPMG, INVREC	FID, CPMG, INVREC, SE-SPI, DHK SPRITE	FID, CPMG, SE-SPI, DHK SPRITE, π EPI	FID, CPMG, INVREC, SE-SPI, DHK SPRITE, π EPI

The 90° and 180° RF pulse lengths were 17 and 34 μs, respectively. SE-SPI measurements were averaged four times to increase the signal-to-noise ratio and fulfill the requirements of phase cycling with a repetition delay of 6.8 seconds. Twenty time-domain points were acquired and averaged on each echo with an echo time $2\tau_E = 1800$ μs. One-dimensional SE-SPI measurements had the phase of their odd and even T_2-weighted profiles matched and were Fourier transformed without filtering. The background signal profile from the fluoropolymer elastomer sleeve and the RF probe frame was subtracted from the SE-SPI proton density profiles. Corrected ^{1}H density profiles were then normalized with respect to

the average of five reliable measurements before CO_2 flooding. This normalization process corrected for the effects of B_1 inhomogeneity and background signal. The 1D DHK SPRITE measurement parameters are reported in Afrough et al. (2018). Three-dimensional π EPI measurements were repeated 16 times for signal averaging and had 64 voxels, in each direction with an isotropic field of view of 90 mm. The total acquisition time was 27 minutes for each 1D SE-SPI profile; 8 or 16 minutes for a 1D DHK SPRITE profile; and 25 minutes for 3D π EPI images.

The quantitative accuracy of 1D DHK SPRITE and T_2-mapping SE-SPI has been established (Muir and Balcom 2013). Mass balance before and after miscible CO_2 flooding demonstrated that the residual saturation of 0.04 measured by MRI was within the saturation measurement uncertainty of 0.02. This accuracy, especially at such a low wetting phase saturation, was five times better than that of Suekane et al. (2005, p. 5).

5.3 Results and Discussion

Experiments performed in this work demonstrate three different dispersion/diffusion phenomena: capillary and hydrodynamic dispersion in displacement of decane by CO_2 at 6 and 9 MPa, respectively; and simultaneous diffusion of CO_2 and light hydrocarbons in and out of heavy oil, respectively. Each case is discussed below.

5.3.1 Displacement of Heavy Oil by CO_2

CO_2 was injected from the top of the core plug and CO_2 breakthrough occurred after a short period of constant injection rate. Early breakthrough indicated a short-lived period of

convection dominated by viscous fingering. Contact between CO_2 and the heavy-oil phase facilitated inter-phase transfer of light components and CO_2: diffusion of CO_2 in the oil phase and extraction of light components of oil by CO_2 (Afrough et al. 2018).

Overall, CO_2 reduced oil saturation from $S = 0.81$ to $S = 0.57$ during the experiment. The saturation and $T_{2\mathrm{LM}}$ maps of this process are shown in Figure 5-1. Increased $T_{2\mathrm{LM}}$ along the flow path, from top to bottom, indicates reduced viscosity and altered oleic phase composition (Hirasaki 2006). This analysis assumes unbiased behavior of viscosity and $T_{2\mathrm{LM}}$ in heavy oils toward the molar concentration of CO_2 and light components as demonstrated by Freitag (2018) and Yang et al. (2012).

No gas chromatography measurements were performed on the effluent gas stream to determine the evolution of light component extraction and CO_2 absorption as a function of time. Therefore, accurate prediction of diffusion coefficients for this process is not possible. More complex magnetic resonance methods such as $T_2 - D$ (Hürlimann et al. 2009) and especially its spatially-resolved variants (Vashaee et al. 2017) have the potential to semi-quantitatively monitor changes in the oil phase composition.

5.3.2 Displacement of Decane by CO_2

The intensity of proton density ρ_P profiles measured by MRI methods is proportional to the quantity of decane present in each core section. Saturation S, as described in the Numerical Differentiation subsection, is equivalent to

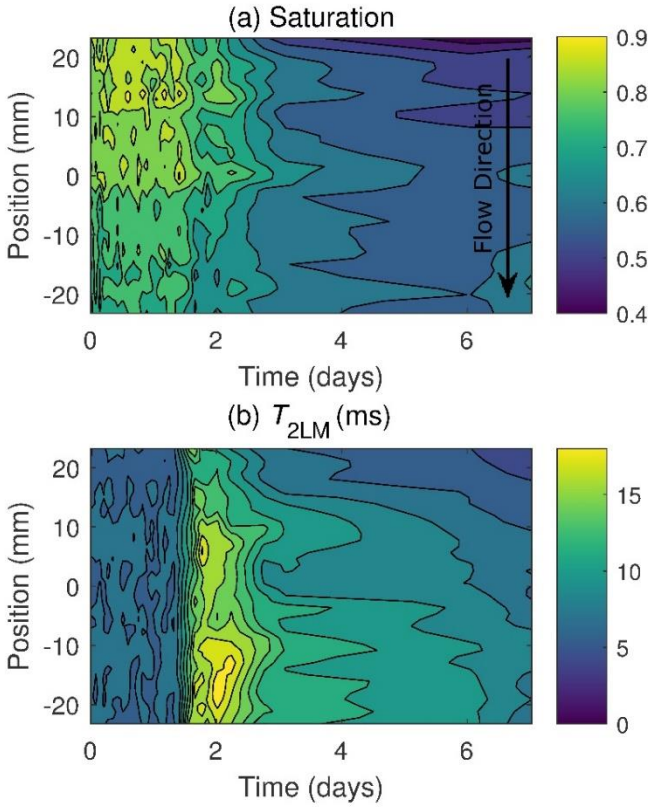

Figure 5-1 Immiscible CO_2 flooding of heavy oil in Berea at residual D_2O water saturation, at 6 MPa and 40°C; (a) Oil saturation *S* and (b) logarithmic mean T_2, T_{2LM} from 1D SE-SPI method. Changes in T_{2LM} suggest extraction of more light components from the top of the core than the bottom. The constant T_{2LM} region at the left side of (b) demonstrates the time period before CO_2 entered the core plug.

$$S = C/C_{in}, \tag{5-12}$$

where C is the total molar concentration of decane in a core-plug section as a function of position and time, and C_{in} is the initial molar concentration of decane in the same section.

Figure 5-2 shows slices of 3D images of decane saturation at discrete times measured by the π EPI method in the immiscible displacement of decane by CO_2 in Berea. The 2D slices displayed are from the center of the 3D object. The core plug center marks $y = 0$ position and y increases in the upward direction. CO_2 was injected from the top of the core plugs. The images demonstrate the sample from full decane saturation, $S = 1$, to residual saturation. The nearly linear displacement of decane by CO_2 motivates imaging the sample by 1D profiles in the y–direction using the SE-SPI method.

Smooth time-lapse saturation profiles for miscible and immiscible flooding of decane were aligned along the time axis, as shown in the contour plots of Figure 5-3a and Figure 5-4a. The saturation maps of both experiments, Figure 5-3a and Figure 5-4a, are composed of three dominant parts: full saturation on the left, residual saturation on the right, and a transition zone in the middle. Initially, at $t = 0$ days, the core plugs were saturated with decane. The residual saturation of decane from histogram analysis was respectively 0.04 and 0.25 for the miscible and immiscible displacements. Residual oil saturation, wave velocity, and the shape of the transition zone provide information on the mechanisms of flooding. The MRI method had an uncertainty of approximately 0.04 for smoothed saturations.

Thermodynamics of CO_2/decane mixtures have an important effect on the dispersion coefficient, wave velocity, and the saturation corresponding to shockwaves. Some of these effects are discussed in the next few subsections.

Displacement Front. Imaging can easily reveal the time that a wave of displacing fluid enters and exits a core plug. This is possible using saturation maps and more accurately from partial derivatives of saturation. Figure 5-3b-d and Figure 5-4b-d demonstrate partial derivatives of saturation respectively for miscible and immiscible flooding of decane-saturated Berea core plugs computed from 1D SE-SPI measurements. One-dimensional DHK SPRITE measurements lead to quantitatively similar partial derivatives. These partial derivatives are calculated by smoothing spline methods discussed in the Numerical Differentiation subsection. The computation of partial derivatives of in-situ saturation, even with robust smoothing methods applied in this study, requires high-quality saturation data such as those provided by the 1D SE-SPI and DHK SPRITE methods.

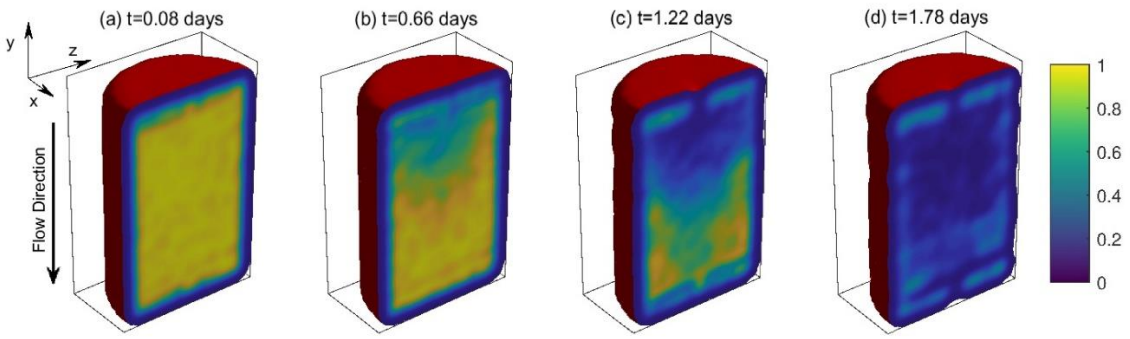

Figure 5-2 Decane saturation distribution in immiscible CO_2 flooding. Two-dimensional center slices are from 3D π EPI MRI images. Images are at times (a) 0.08, (b) 0.66, (c) 1.22, and (d) 1.78 days. The sample was initially fully saturated at $t = 0.08$ days and approaches residual saturation at $t = 1.78$ days.

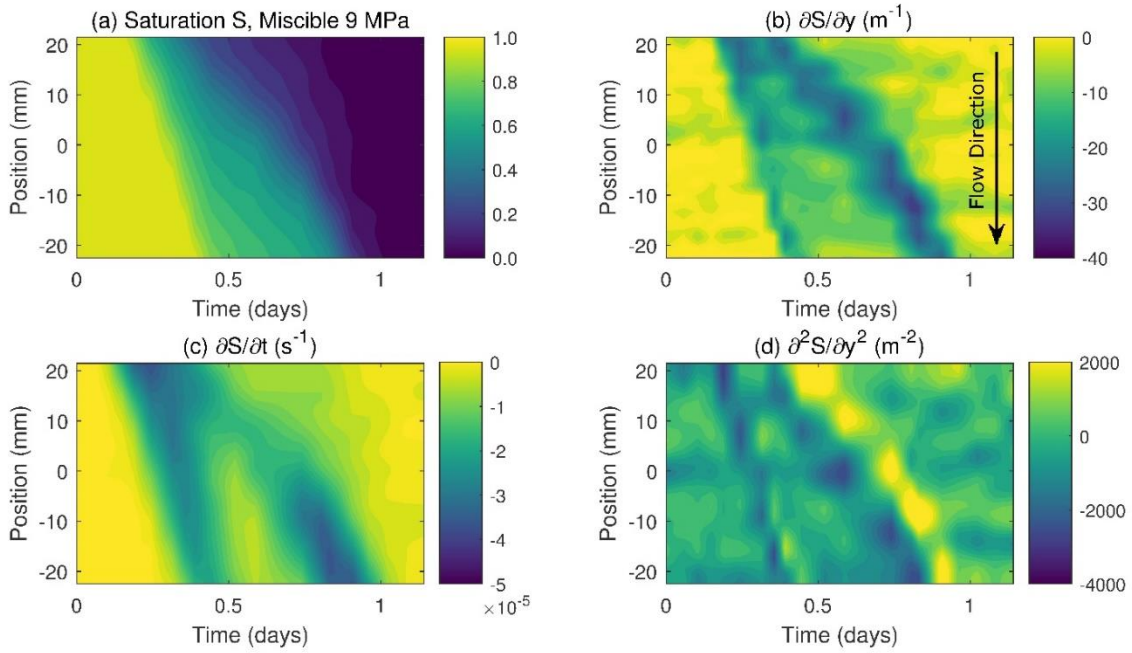

Figure 5-3 Miscible flooding of decane by CO_2 at 9 MPa and 40°C; (a) decane saturation S and (b) $\partial S/\partial y$, (c) $\partial S/\partial t$, and (d) $\partial^2 S/\partial y^2$ as a function of position y and time t from 1D SE-SPI. CO_2 injection almost completely displaced decane at the end of the experiment at $t > 1$ days. Slanted lines in the partial derivatives of saturation reveal the propagation of leading (left line) and trailing (right line) shocks.

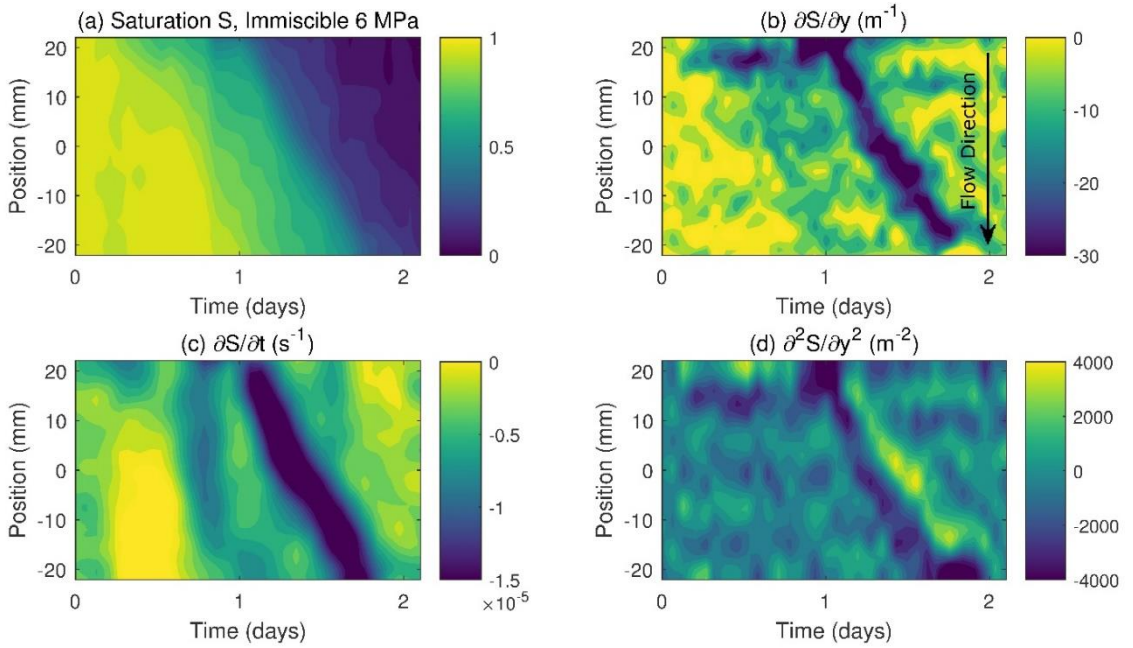

Figure 5-4 Immiscible flooding of decane by CO_2 at 6 MPa and 40°C; (a) decane saturation S and (b) $\partial S/\partial y$, (c) $\partial S/\partial t$, and (d) $\partial^2 S/\partial y^2$ as a function of position y and time t from 1D SE-SPI. The trailing shock, a slanted line, leaves an approximate residual decane saturation of $S = 0.25$.

From a thermodynamics standpoint, CO_2 flooding of decane at 6 MPa and 9 MP, both at 40°C, have fundamental differences in phase and volumetric behavior. In regards with phase behavior, at 40°C and 9 MPa, CO_2 and decane are first-contact miscible and form a single phase in all proportions. This is however not the case for CO_2 and decane at 40°C and 6 MPa at which they may form two phases; nevertheless, they may achieve multi-contact miscibility in a dynamic process such as core flooding.

Volumetric behavior of CO_2/decane mixtures at 40°C and pressures of 6 MPa and 9 MPa have fundamental differences as well. The difference between ideal and real volumes of CO_2 and decane mixtures is much more significant at 6 MPa, rather than 9 MPa. This is while the excess volume of mixing is always negative in both cases. This means that a much greater volume of CO_2 should be injected into a core plug at 6 MPa, in comparison to the 9 MPa experiment, for similar decane recovery. A comprehensive discussion on the thermodynamics of CO_2/decane mixtures at 40°C is presented in the appendix.

Dispersion Coefficient. As mentioned earlier, it is important to determine conditions under which the advection-dispersion equation, Equation (5-5), is valid with a Gaussian kernel or a single value of D_L (Sahimi 1993, p. 1458). Since the partial derivatives of saturation are accessible in this study, it is possible to directly substitute partial derivatives of saturation in the advection-dispersion equation for experiments performed at 6 MPa and 9 MPa. For the miscible experiment, at 9 MPa, partial derivatives of saturation lie on a plane in 3D scatter plot in the full range of saturation, as shown in Figure 5-5a. This indicates that dispersion and velocity values are not saturation dependent at 9 MPa and CO_2 may be considered as a tracer. In contrast, at 6 MPa, partial derivatives of saturation do not lie on a single plane, as shown in Figure 5-5b. This behavior indicates that the immiscible CO_2 flooding of decane does not follow the advection-dispersion equation with a Gaussian kernel and CO_2 cannot act as a tracer in such experiment.

The advection-dispersion PDE of Equation (5-5) is usually written in terms of composition, rather than saturation. However, Equation (5-5) written in terms of saturation is appropriate and leads to correct dispersion coefficients because it can be readily converted to a similar advection-dispersion PDE of composition z_{CO_2} by chain rule. The only difference between an advection-dispersion PDE based on z_{CO_2} and S is a term composed of multiplication of higher degree partial differentials that is negligible compared to other terms of the PDE. A one-to-one relationship between z_{CO_2} and S as shown in the appendix facilitates this treatment. Therefore, Equation (5-5) was used directly to extract velocity and dispersion coefficient from partial derivatives, or the solution of Equation (5-5) with a simple boundary and initial condition could fit to experimental data meeting the same conditions.

It is possible to estimate the longitudinal dispersion coefficient by fitting Equation (5-6) to saturation data, as shown in Figure 5-6a, or with the first term of its Taylor series expansion, as in Equation (5-8) and shown in Figure 5-6b. The dispersion coefficient was calculated to be 5.9×10^{-9} m^2/s for miscible CO_2 flooding in Berea from Figure 5-6b. For estimating parameters of Equation (5-5), fitting a plane to the miscible saturation derivatives provided the mean velocity of $v = -1.19 \times 10^{-6}$ m/s and dispersion coefficient of $D_L = 2 \times 10^{-10}$ m^2/s with lower and upper 95% confidence bounds of -2×10^{-10} and 6×10^{-10}, respectively. The dispersion coefficient calculated from surface fitting is one order of magnitude smaller than that calculated from the slope of saturation profiles. However, mean velocity is in good quantitative agreement with other methods as shown later.

Hydrodynamic dispersion as a function of Peclet number has been studied in different flow regimes as discussed by Bear (1972) and Sahimi (1993). In the miscible flooding of decane by CO_2 at Pe$=0.015 < 0.3$, diffusion dominates hydrodynamic dispersion (Sahimi 1993, p. 1460). In this flow regime, the dispersion coefficient D_L can be calculated from the diffusion coefficient D_m of decane/CO_2 at the same pressure and temperature by knowing the tortuosity factor τ of Berea (Sahimi 1993, pp. 1460) from

$$D_L = D_m/\tau. \tag{5-13}$$

The tortuosity factor is approximately equal to $\tau = 2.0$ for Berea sandstones with porosity and permeability values close to those used in this study (Attia 2005). Reverse calculation of diffusion coefficient of decane leads to $D_m = 1.2 \times 10^{-8}$ m^2/s which is consistent with reported experimental data. Evaluating the experimental data of Umezawa and Nagashima (1992), the diffusion coefficient of decane in CO_2/decane mixtures is in the range of 5×10^{-9} m^2/s $< D_m < 2.5 \times 10^{-8}$ m^2/s for the full span of compositions at 40°C and 9 MPa. The lower bound of the diffusion coefficient was confirmed by interpolation of another experimental data set (Cadogan et al. 2016) to obtain the infinite-dilution diffusion coefficient for CO_2 in decane at 40°C and 9 MPa equal to $D_m = 5.4 \times 10^{-9}$ m^2/s. Teng et al. (2014) experimentally studied the diffusion of CO_2 in decane saturated glass bead packs at 24°C and pressures from 2 to 4 MPa. The dispersion coefficients evaluated in this study are also qualitatively comparable to their results.

At a capillary number of $\mathrm{Ca} = 2.6 \times 10^{-7}$, the immiscible displacement of decane by CO_2 is governed by a quasi-static drainage mode (Sahimi 1993). Capillary pressure significantly affects saturation distribution in this flow regime. Unlike miscible fluid displacement, the immiscible flooding of decane cannot be characterized by a single value of dispersion coefficient anymore; see Figure 5-5b. Saturation distribution at the end of the drainage process mimics the capillary pressure curve which is approximately an error function of the logarithm of position (Afrough et al. 2018).

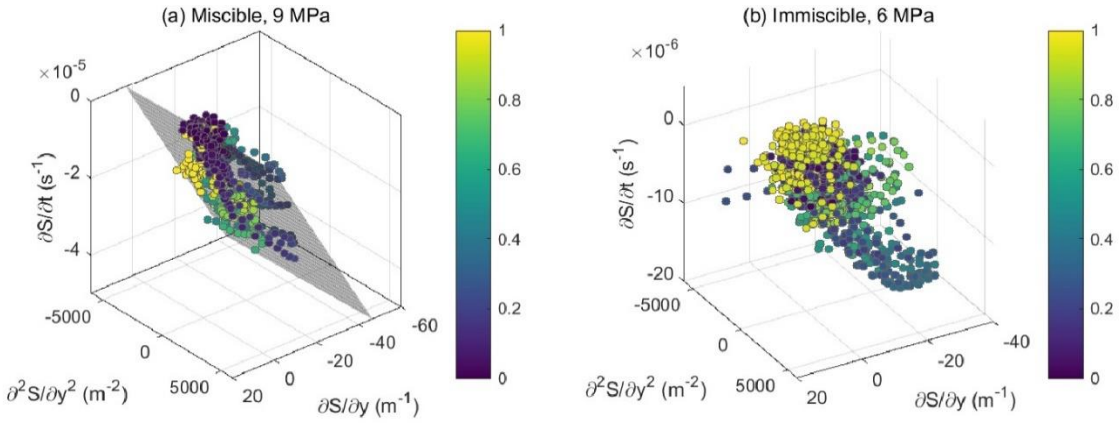

Figure 5-5 (a) Miscible 9 MPa, and (b) immiscible 6 MPa, both at 40°C, flooding of decane-saturated Berea core plugs with CO_2; correlation of partial derivatives of saturation. With a saturation-independent D_L, in (a) partial derivatives have a linear correlation. No such correlation exists for (b) due to the saturation dependent D_{Lc}.

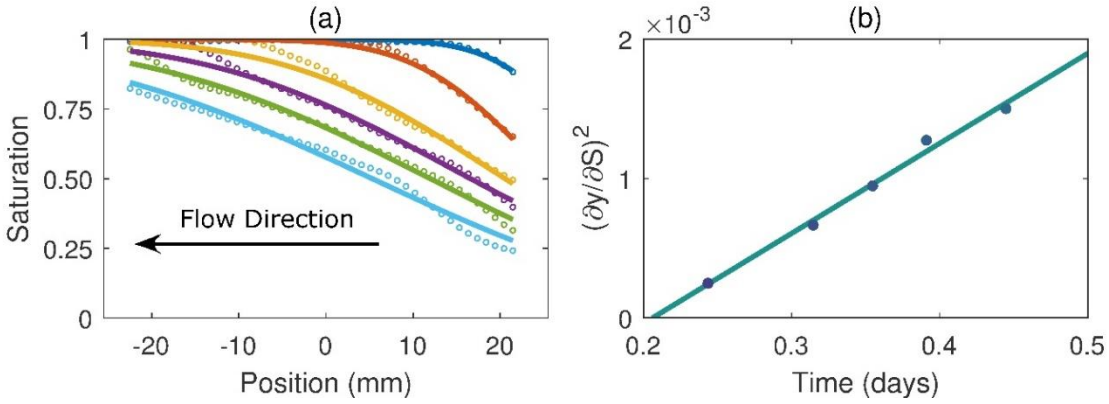

Figure 5-6 Miscible flooding of decane by CO_2 at 9 MPa and 40°C; (a) saturation S profiles ○ and their analytical fits —. Profiles from top to bottom at $t = 0.19$, 0.24, 0.32, 0.36, 0.39, and 0.44 days (b) $(\partial y/\partial S)^2$ versus time t. Data points ● are calculated from experimental data with a linear function. The dispersion coefficient was calculated from $(\partial y/\partial S)^2 = 4\pi D_L(t - t_0)$ to be $D_L = 5.9 \times 10^{-9}$ m^2/s.

Two-phase flow equations can be manipulated (Novy et al. 1989, Goodfield et al. 2001) to form an advection-dispersion equation, similar to Equation (5-5), with the saturation dependent term of capillary dispersion

$$D_{Lc}(S) = -\frac{\lambda_l \lambda_v}{\lambda_l + \lambda_v} \frac{dP_c}{dS} \tag{5-14}$$

in which $\lambda_j = k_{rj}/\mu_j$ is the phase mobility for phase j; $j = l$ for liquid and v for vapor. It is possible to obtain saturation dependent properties of rocks, such as relative permeabilities and the derivative of capillary pressure function with respect to saturation, from the correlation among saturation and its partial derivatives (Goodfield et al. 2001).

These calculations require flooding at multiple displacing flow rates (Song et al. 2014; Jiang et al. 2017), or integration of saturation data with those of pressure difference (Goodfield et al. 2001). We did not pursue the capillary dispersion coefficient as a function of saturation due to the complexity of the problem.

Wave Velocity and Shockwaves. The value of $-v_s$, from Equation (5-10), was mapped as a function of position and time for both miscible and immiscible displacements of decane by CO_2. The average decane velocity in the miscible and immiscible CO_2 flooding were -1.4×10^{-6} and -0.8×10^{-6} m/s, respectively; indicating an approximately two-fold wave velocity increase for the miscible flooding in comparison to the immiscible case. The negative sign of velocity indicates a downward flow. Figure 5-7 demonstrates the correlation of wave velocity with saturation; the solid guideline is the median saturation and dashed guidelines are 95% confidence bounds. The horizontal line demonstrates the intrinsic velocity equivalent to the pump injection rate.

For the miscible flow of CO_2 and decane in Berea core plugs, the intrinsic velocity of fluids in the pores u is obtained by correcting the Darcy velocity using porosity ϕ. Therefore, the intrinsic velocity is obtained by

$$u = q/A\phi \tag{5-15}$$

where A is the cross-sectional area of the core plug and q is the volumetric CO_2 injection rate. The intrinsic CO_2 velocity estimated from the pump flow rate using an average

porosity of 0.20 is $u = -0.75 \times 10^{-6}$ m/s from Equation (5-15). This velocity is in qualitative agreement with saturation velocities calculated from the triple product rule as a function of saturation. It is important to note that wave velocity $-v_s$, from Equation (5-10), is a direct result of measurements and no assumptions are involved in its calculation.

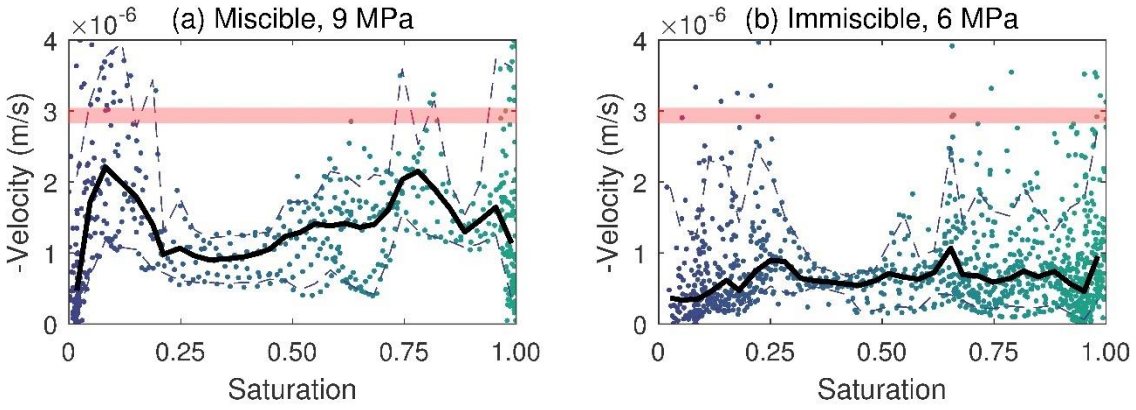

Figure 5-7 Wave velocity $v_s = (\partial y/\partial t)_S$ as a function of saturation for (a) Miscible 9 MPa, and (b) immiscible 6 MPa, both at 40°C, flooding of decane-saturated Berea core plugs with CO_2. Each data point estimates v_s for individual core plug sections at discrete times. The solid line marks the median; dashed lines mark 95% confidence bounds; and the horizontal bar is the intrinsic CO_2 velocity. Flow is downward. The generally increasing trend of velocity with saturation is due to the velocity constraint. Local extrema, indicating self-sharpening fronts, demonstrate shocks in agreement with the entropy condition.

Discrepancies between the intrinsic velocity u and velocity calculated from the triple product rule are because of the following factors: pore-flow effects, thermodynamic

effects, dispersion effects, and possible leak of CO_2 and decane from the core sleeve. With the very small flow rate used in this study, 0.04 cm^3/min, even with our best efforts, leakage is possible. However, the contribution of leakage is not more important than thermodynamics and dispersion effects. The variation of wave velocity with saturation due to thermodynamics and dynamics of shockwaves is discussed below.

Because of mixing effects, 1 cm^3 of CO_2 displaces more decane at 9 MPa than at 6 MPa. This thermodynamic effect is observed in the lower displacement velocity of decane at 6 MPa compared to 9 MPa, as shown in Figure 5-7. Diffusion and dispersion phenomena enhance the thermodynamics effect by providing interphase mass transfer of CO_2 into the liquid phase due to mixing. The intrinsic velocity is not the maximum true decane velocity in the core plug, because some portion of the porosity does not contribute to fluid flow. The combined effect of thermodynamics, topology of porous rocks, and dispersion explain the difference between decane saturation velocity in miscible and immiscible cases.

A large spread of velocity at saturations close to zero and one, in Figure 5-7, is because of division by small time derivatives at extreme saturations. However, the spread of velocity at other saturations far from zero and one is very real. Please note that the spread of velocity changes as a function of saturation. For example, in the miscible experiment, velocity has a minimal spread at approximately $S = 0.3$. This point is very well correlated with the extreme point of excess molar volume of decane and CO_2 binary mixtures at 9 MPa (see Appendix). The unbiased behavior of mixture volume to either component could be the

reason behind the small apparent uncertainty in the velocity values at this point. The transport of binary fluids that do not satisfy the law of additive volumes is governed by volume transport equations (Brenner 2005, Joseph 2010). In this work, it was recognized that the saturation wave velocity at each point is not only a function of time and position, but also a function of saturation at other locations in the core plug. A volume transport approach to convection and diffusion was not pursued further but is a direction for future research.

In Figure 5-7, the absolute value of velocity increases with saturation through most of the saturation range. This observation means that higher decane saturations, downstream, move faster than lower decane saturations, upstream. This agrees with the velocity constraint (Orr 2007, p. 51). In addition, the wave velocity at the downstream of a shock should be more than, or equal to a shock velocity. Using the entropy condition (Orr 2007, p. 52), it is easy to identify that after residual saturations of $S = 0.04$ and $S = 0.25$, at 9 and 6 MPa, respectively, there exist a shock. This shock wave, known as the trailing shock (Orr 2007, pp.53) leaves a residual decane saturation. These shock waves are identified with negative slopes. Two other shock waves exist at the flood front, at $S = 0.75$ and $S = 0.65$ for miscible and immiscible experiments, respectively.

The Fundamental Solution of the Advection-Dispersion Equation. The partial derivative of saturation with respect to position $(\partial S/\partial y)_t$ determines the fundamental solution G of the advection-dispersion equation. Knowing the partial derivatives, it is now

possible to calculate the Green's function of Equation (5-5) for both the miscible and immiscible cases. Figure 5-8a and Figure 5-8c show the wave-like movement of a point source saturation function evolving in time for the miscible and immiscible experiments, respectively. The evolution of the kernel function demonstrates a wave that moves with approximately constant velocity and spreads as it moves. This behavior agrees with the mathematics of waves applied to the convection-diffusion class of partial differential equations (Knobel 2000, pp.113-125). In some regions, the kernel function compresses as it moves toward the bottom of the core plug, as shown in Figure 5-8c. Although measurement uncertainty is an integral part of any MRI measurement, all SE-SPI, DHK SPRITE, and π EPI images confirmed the existence of regions of self-sharpening flood fronts. This effect agrees with the phenomena discussed earlier in the "Wave Velocity and Shockwaves" subsection.

Figure 5-8b and Figure 5-8d demonstrate what portion of the fundamental solution is visible in the small window of the core plug. Less than 70% of the fundamental solution, or saturation wave, is visible in the core plugs being monitored by MRI measurements. Experiments with longer core plugs and monitoring methods with a larger sensitive section can potentially show the complete limits of the fundamental solution of the advection-dispersion equation. However, this experiment demonstrated that it is still possible to observe phenomena of interest to EOR processes by CO_2 in a short core plug using appropriate MRI and data processing methods.

5.3.3 Limitations of the Current Study and Future Work.

Conventional flow equations fail to completely incorporate the effects of Korteweg stress in fluids with considerable volume change of mixing. Other methods, such as that of Brenner (2005) and Ganesan and Brenner (2000), are necessary to model systems studied in this research and explain apparent uncertainties in the computed wave velocity, as shown in Figure 5-7. The data for experiments of this work will be publicly accessible at the UNB Dataverse Research Data Repository for those interested in pursuing such studies.

Future work will benefit from a complete integration of MRI monitoring systems with existing advanced core flooding practices. In this work, not all differential pressure data was recorded during experiments, and effluent stream was not analyzed by gas chromatography or optical methods from a glass-window cell. Incorporating such steps in a similar work will further enhance our understanding of flow phenomena with complex thermodynamics behavior; especially those involving reservoir hydrocarbon mixtures.

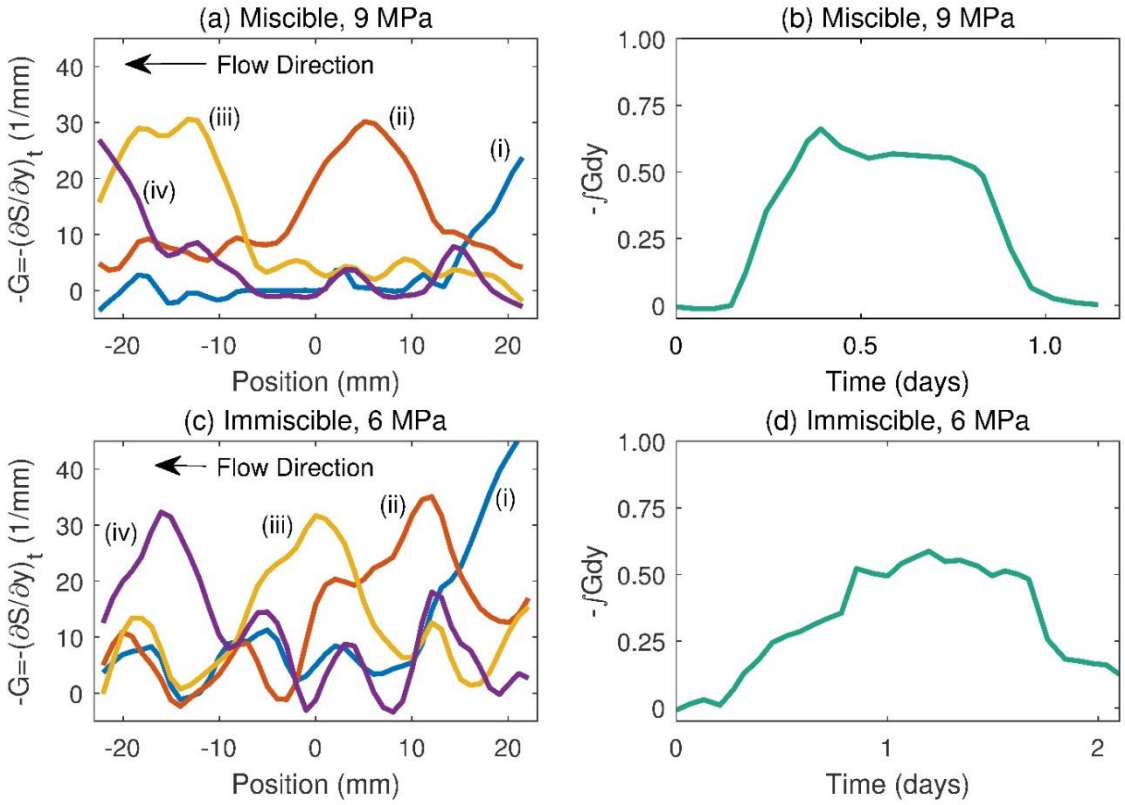

Figure 5-8 The evolution of the fundamental solution of the advection-dispersion equation as a function of position in miscible (a) and immiscible (b) displacement of decane-saturated Berea core plugs with CO_2. (i) to (iv) in (a) represent $t = 0.19$, 0.59, 0.83, and 0.91 days; (i) to (iv) in (b) represent $t = 1.07$, 1.20, 1.35, and 1.67 days. The integration of the saturation wave demonstrates the fraction of the saturation wave visible in the core plug window, (b) and (d). Self-sharpening kernel functions in (c) demonstrate the development of shockwaves.

5.4 Conclusions

Spatiotemporal evolution of saturation can demonstrate diffusion and dispersion effects in CO_2 flooding of decane and heavy-oil saturated core plugs. Appropriate magnetic resonance methods are precise enough to permit accurate evaluation of partial derivatives of saturation with respect to time and position. Such partial derivatives were shown to demonstrate the evolution of wave velocities and the advection-dispersion kernel in CO_2 displacement of decane-saturated Berea core plugs. Wave velocity as a function of saturation demonstrated the movement of leading and trailing shocks in the CO_2 displacement of decane in a 5-cm Berea core plug. Thermodynamics of decane and CO_2 mixtures show that the apparent uncertainty in the wave velocity is due to the composition-dependent excess volume of mixing. This study not only provides a new method of analyzing core flooding data by computing partial derivatives, but also provides a valuable experimental dataset for other researchers to develop, verify, and compare models that describe mixture flow in porous media.

MRI has a dual feature in providing information on microscopic and macroscopic scales respectively through its relaxation and imaging properties. Imaging was used in this chapter to study macroscopic phenomena. Relaxation is used in the next chapter to study microscopic phenomena in miscible and immiscible displacement of decane by CO_2 in Berea sandstone in the same experiment.

5.5 Appendix—Thermodynamics of Decane/CO_2 Mixtures

Thermodynamics, along with transport processes, play a significant role in the displacement of decane by CO_2 in Berea. The $P - x_{C_{10}} - y_{C_{10}}$ diagram for the vapor/liquid equilibrium of CO_2/decane mixtures at constant temperature $T = 40$°C is shown in Figure 5-9. The mixture is in the liquid-like supercritical state in its entire range of composition at 9 MPa. However, at 6 MPa, the binary mixture forms liquid and vapor phases in the range of $0 < z_{C_{10}} < 0.41$. The solid horizontal line at 6 MPa shows the tie line connecting decane mole fractions of 0.41 in the liquid phase and 0.001 in the vapor phase.

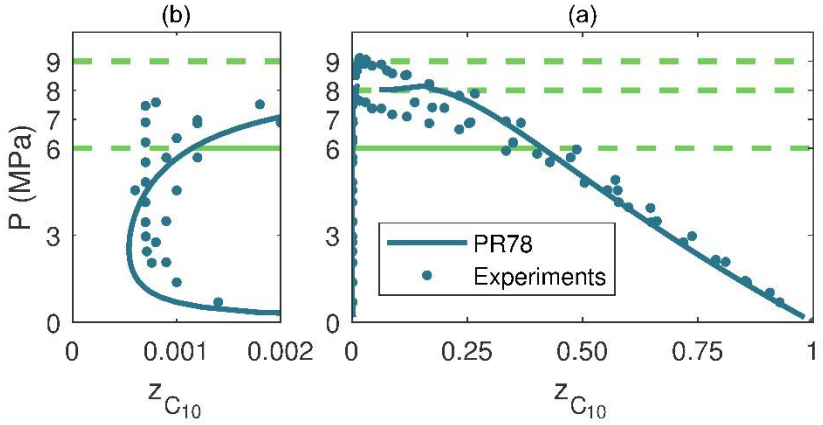

Figure 5-9 Pressure-composition $P - z_{C_{10}}$ relationship for CO_2/decane mixtures at 40°C: from the PR-EOS ─ and from experimental equilibrium data ● in (a) Full range of $z_{C_{10}}$ and (b) the dew-point region. The experimental datasets are referenced in the text and were performed at temperatures in the range of 37°C to 50°C. The solid horizontal line at $P = 6$ MPa demonstrates the vapor-liquid tie line.

The mixture critical point on the pressure-composition plot would be a tangent point at which a horizontal line touches the curve and connects two identical phase compositions (Smith et al. 2005, pp. 342). Interpolation of experimental data of Gulari et al. (1987) gives the critical pressure of 8.3 MPa and critical decane composition of approximately 0.01 at 40°C. This point is one of the many mixture critical points that lie on the critical locus between critical temperatures of CO_2 at $T_{C,CO_2} = 30.98$°C (Lemmon 2017) and decane at $T_{C,C_{10}} = 345$°C (Muzny et al. 2017). The critical pressure of the decane/CO_2 binary mixture is also in agreement with the experimental MMP of this system (Liu et al. 2015).

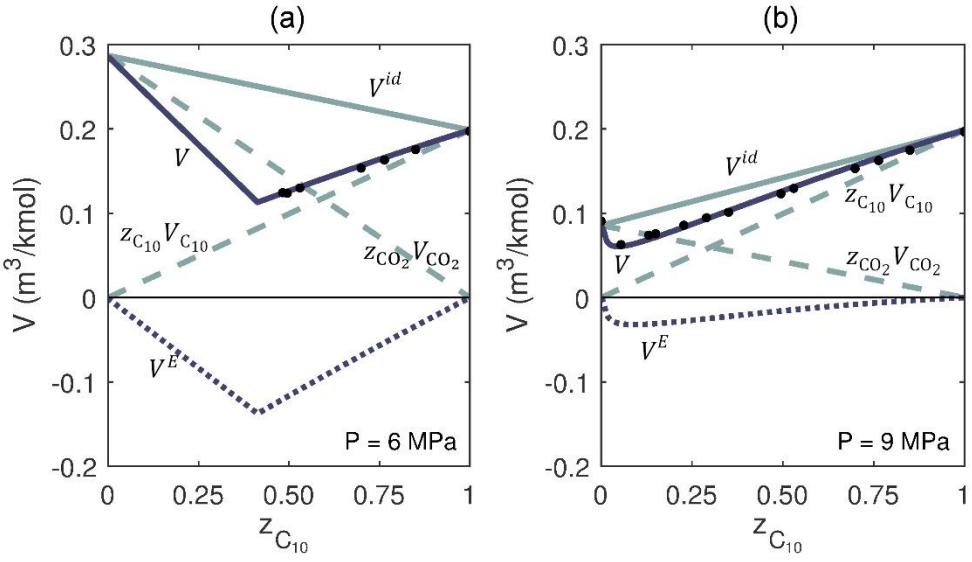

Figure 5-10 Molar volume for the contribution --- of decane and CO_2 ($z_{C_{10}}V_{C_{10}}$ and $z_{CO_2}V_{CO_2}$) to the ideal solution volume V^{id} —, the real mixture volume V —, experimental data ●, and excess molar volume V^E … at $P = 6$ MPa (a), and 9 MPa (b). Excess molar

volume indicates nonidealities in the volume change of mixing. Data from the literature referenced in the text.

Two avenues permit exploration of the volumetric behavior of decane/CO_2 mixtures in the solution thermodynamics formalism: partial molar volume of each component, and excess volume. These two approaches are interrelated. Excess molar volume V^E characterizes the non-ideal volume behavior of real solutions. It is the real solution volume V that is in excess of the ideal solution volume $V^{id} = z_{CO_2}V_{CO_2} + z_{C_{10}}V_{C_{10}}$ at the same temperature, pressure, and composition (Firoozabadi 1999, pp. 27). The molar volume of component i in the pure state at the same pressure P and temperature T are denoted by V_i; where $i = CO_2$ or C_{10}. The excess molar volume can be obtained from

$$V^E = V - V^{id}$$

which means that $V^E = 0$ for ideal solutions. Figure 5-10 shows excess molar volume, real solution volume, ideal solution volume, and the components of ideal solution volume — $z_{CO_2}V_{CO_2}$ and $z_{C_{10}}V_{C_{10}}$. There is a strong evidence of mixing effects on volume according to the large deviation of excess molar volume from zero. The two-phase region at $P = 6$ MPa is recognized by the discontinuity in the slope of molar volume in Figure 5-10a.

Excess volume V^E of the decane/CO_2 mixture has an extremum at $z^*_{C_{10}} = 0.41$ and $z^*_{C_{10}} = 0.09$ for $P = 6$ MPa and 9 MPa, respectively. These extremum points matched the intersection of excess partial molar volume of decane and CO_2 and formed triple cross

points (Yu et al. 2001). With small variation of composition by adding either decane or CO_2, volume changes equally at extremum compositions $z^*_{C_{10}}$. At these points, the binary solution behaves toward both components in an unbiased manner (Yu et al. 2001). The correlation between S, from MRI measurements, and fluid composition is shown in Figure 5-11. The saturation corresponding to the extremum points are $S^* = 0.73$ and $S^* = 0.28$ for $P = 6$ MPa and 9 MPa, respectively. In the miscible CO_2 flooding experiment, $S^* = 0.28$ corresponds to the least apparent uncertainty in the velocity as a function of saturation, in Figure 5-7a.

Vapor-liquid equilibrium and fluid density calculations were performed using the standard Peng-Robinson equation of state (Peng and Robinson, 1976) by Aspen Properties software (Aspen Technology, Bedford, Massachusetts, USA).

Thermophysical properties for binary mixtures of decane and carbon dioxide retrieved from NIST ThermoData Engine (Diky et al. 2009) were used for improved predictability of the equations. A comprehensive cross-examination of thermophysical and equilibrium properties with experiments of Reamer and Sage (1963), Cullick and Mathis (1984), Song et al. (2012), Zamoudio et al. (2011), Iwai et al. (1994), Prausnitz and Benson (1959), Adams et al. (1988), Jiménez-Gallegos (2006), Nascimento et al. (2014), Kariznovi et al. (2013), Pereira et al. (2016), Barrufet et al. (1996), Geogiadis et al. (2010), and Fele Žilnik et al. (2016) verified the accuracy of the results.

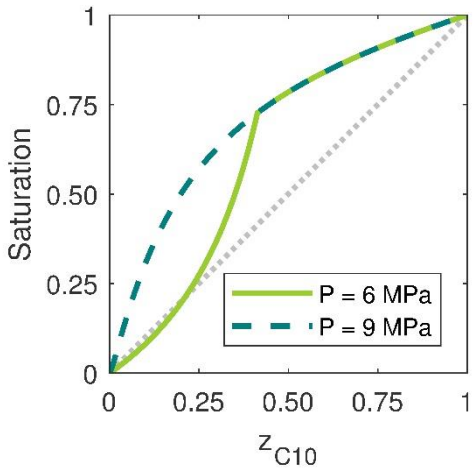

Figure 5-11 Saturation, measured by MRI methods, as a function of total decane molar composition $z_{C_{10}}$ at P = 6 MPa --- and 9 MPa —. The unit-slope is a guideline. There is an evident deviation from a linear relationship between saturation and composition. At $P = 6$ MPa, CO_2/decane mixtures form two phases in the range of $0 < z_{C_{10}} < 0.41$ which corresponds to $0 < S < 0.72$.

5.6 References

Adams, W. R., Zollweg, J. A., Streett, W. B. et al. 1988. New Apparatus for Measurement of Supercritical Fluid-Liquid Phase Equilibria. *AICHE J.* 34 (8): 1387-1391. https://doi.org/10.1002/aic.690340820.

Afrough, A., Shakerian, M., Zamiri, M. S. et al. 2018. Magnetic-Resonance Imaging of High-Pressure Carbon Dioxide Displacement: Fluid/Surface Interaction and Fluid Behavior. *SPE J.* SPE-189458-PA. https://doi.org/10.2118/189458-PA.

Aris, R. and Amundson, N. R. 1957. Some Remarks on Longitudinal Mixing or Diffusion in Fixed Beds. *AICHE J.* 3 (2): 280-282. https://doi.org/10.1002/aic.690030226.

Attia, A. M. 2005. Effects of Petrophysical Rock Properties on Tortuosity Factor. *J. Petrol. Sci. Eng.* 48 (3–4): 185-198. https://doi.org/10.1016/j.petrol.2005.06.012.

Bacri, J. -C., Rakotomalala, N., Salin, D. 1990. Anomalous Dispersion and Finite-Size Effects in Hydrodynamic Dispersion. *Phys. Fluids A-Fluid* 2 (5): 674-680. https://doi.org/ 10.1063/1.857720.

Baldwin, B. A., King, R. L. 1998. Why Would an Oil Company Use MRI? In *Spatially Resolved Magnetic Resonance: Methods, Materials, Medicine, Biology, Rheology, Geology, Ecology, Hardware*, ed. Blümler, P., Blümich, B., Botto, R., and Fukushima, E., Chap. 55, 575-601. Weinheim: Wiley-VCH Verlag GmbH.

Barrufet, M. A., Salem, S. K. E., Tantawy, M. et al. 1996. Liquid Viscosities of Carbon Dioxide + Hydrocarbons from 310 K to 403 K. *J. Chem. Eng. Data* 41 (3): 436–439. https://doi.org/10.1021/je950256y.

Bear, J. 1972. *Dynamics of Fluids in Porous Media*. New York: Dover.

Beckwith, R. 2011. Carbon Capture and Storage: A Mixed Review. *J. Pet. Technol.* 63 (5): 42-45. SPE-0511-0042-JPT. https://dx.doi.org/10.2118/0511-0042-JPT.

Brautaset, A., Ersland, G., Graue, A. et al. 2008. Using MRI to Study In-Situ Oil Recovery During CO_2 Injection in Carbonates. Oral presentation given at the International Symposium of the Society of Core Analysts, Abu Dhabi, 29 October-2 November. SCA2008-41.

Brenner, H. 2005. Kinematics of Volume Transport. *Physica A* 349 (1-2): 11-59. https://doi.org/10.1016/j.physa.2004.10.033.

Brigham, W. E. 1974. Mixing Equations in Short Laboratory Cores. *SPE J.* 14 (1): 91-99. SPE-4256-PA. https://doi.org/10.2118/4256-PA.

Butler, J. P., Reeds, J. A., and Dawson, S. V. 1981. Estimating Solutions of First Kind Integral Equations with Nonnegative Constraints and Optimal Smoothing. *SIAM J. Numer. Anal.* 18 (3): 381-397. https://doi.org/10.1137/0718025.

Cadogan, S. P., Mistry, B., Wong, Y. et al. 2016. Diffusion Coefficients of Carbon Dioxide in Eight Hydrocarbon Liquids at Temperatures between (298.15 and 423.15) K at Pressures up to 69 MPa. *J. Chem. Eng. Data* 61 (11): 3922–3932. http://doi.org/10.1021/acs.jced.6b00691.

Cullick, A. S. and Mathis, M. L. 1984. Densities and Viscosities of Mixtures of Carbon Dioxide and n-Decane from 310 to 403 K and 7 to 30 MPa. *J. Chem. Eng. Data* 29 (4): 393–396. https://doi.org/10.1021/je00038a008.

de Boor, C. 1978. *A Practical Guide to Splines.* New York: Springer-Verlag.

Deka, K., MacMillan M. B., Ouriadov, A. V. et al. 2006. Quantitative Density Profiling with Pure Phase Encoding and a Dedicated 1D Gradient. *J. Magn. Reson.* 178: 25-32. https://doi.org/10.1016/j.jmr.2005.08.009.

Diky, V., Chirico, R. D., Kazakov., A. F. et al. 2009. ThermoData Engine (TDE): Software Implementation of the Dynamic Data Evaluation Concept. 3. Binary Mixtures. *J. Chem. Inf. Model.* 49 (2): 503–517. https://doi.org/10.1021/ci800345e.

Duffy, D. G. 2001. *Green's Functions with Applications*. Boca Raton: Chapman & Hall/CRC.

Fele Žilnik, L., Grilc, M., Levec, J. et al. 2016. Phase-Equilibrium Measurements with a Novel Multi-Purpose High-Pressure View Cell: CO_2 + n-Decane and CO_2 + Toluene. Fluid Phase Equilibr. 419 (July): 31-38. https://doi.org/10.1016/j.fluid.2016.03.010.

Firoozabadi, A. 1999. *Thermodynamics of Hydrocarbon Reservoirs*. New York: McGraw-Hill.

Freitag, N. P. 2018. Similarity of the Effect of Different Dissolved Gases on Heavy-Oil Viscosity. *SPE Reserv. Eval. Eng.* 21 (3): 747-756. https://doi.org/10.2118/189456-PA. SPE-189456-PA.

Georgiadis, A., Llovell, F., Bismarck, A. et al. 2010. Interfacial Tension Measurements and Modelling of (Carbon Dioxide + n-Alkane) and (Carbon Dioxide + Water) Binary Mixtures at Elevated Pressures and Temperatures. *J. Supercrit. Fluid.* 55 (2): 743-754. https://doi.org/10.1016/j.supflu.2010.09.028.

Goodfield, M., Goodyear, S. G., Townsley, P. H. 2001. New Coreflood Interpretation Method Based on Direct Processing of In-situ Saturation Data. Oral presentation given at the SPE Annual Technical Conference and Exhibition, New Orleans, Louisiana, 30 September-3 October. SPE-71490-MS.

Goora, F. G., Han, H., Ouellette, M. et al. 2013. Investigation of Magnetic Field Gradient Waveforms in the Presence of a Metallic Vessel in Magnetic Resonance Imaging Through Simulation. *IEEE T. Magn.* 49(6): 2920-2932. https://doi.org/10.1109/TMAG.2012.2234758.

Green, P. J. and Silverman, B. W. 1994. *Nonparametric Regression and Generalized Linear Models: A Roughness Penalty Approach.* London: Chapman & Hall.

Gulari, Es., Saad, H., and Bae, Y. C. 1987. Effect of Critical Phenomena on Transport Properties in the Supercritical Region. In *Supercritical Fluids*, ACS Symposium Series, Vol. 329, Chap. 1, 2-14. Washington, DC: American Chemical Society.

Handy, L. L. 1959. An Evaluation of Diffusion Effects in Miscible Displacement. *J. Pet. Technol.* 11 (3): 61-63. SPE-1130-G. https://doi.org/10.2118/1130-G.

Hürlimann, M. D. 1998. Effective Gradients in Porous Media due to Susceptibility Differences. *J. Magn. Reson.* 131 (2): 232-240. https://dx.doi.org/10.1006/jmre.1998.1364.

Hürlimann, M.D., Freed, D.E., Zielinski, L.J. et al. 2009. Hydrocarbon Composition from NMR Diffusion and Relaxation Data. *Petrophysics* 50 (2) 116-129. SPWLA-1997-v38n2a1.

Iwai, Y., Hosotani, N., Morotomi, T. et al. 1994. High-Pressure Vapor-Liquid Equilibria for Carbon Dioxide + Linalool. *J. Chem. Eng. Data* 39 (4): 900–902. https://doi.org/10.1021/je00016a059.

Jiménez-Gallegos, R., Galicia-Luna, L. A., and Elizalde-Solis, O. 2006. Experimental Vapor−Liquid Equilibria for the Carbon Dioxide + Octane and Carbon Dioxide + Decane Systems. *J. Chem. Eng. Data* 51 (5): 1624–1628. https://doi.org/10.1021/je060111z.

Joseph, D. D. 2010. Fluid Dynamics of Mixtures of Incompressible Miscible Liquids. In Applied and Numerical Partial Differential Equations. Computational Methods in Applied Sciences, vol. 15., ed. Fitzgibbon, W., Kuznetsov, Y.A., Neittaanmäki, P. et al., pp. 127-145. Dordrecht: Springer.

Kariznovi, M., Nourozieh, H., and Abedi, J. 2013. Phase Composition and Saturated Liquid Properties in Binary and Ternary Systems Containing Carbon Dioxide, n-Decane, and n-Tetradecane. *J. Chem. Thermodyn.* 57 (February): 189-196. https://doi.org/10.1016/j.jct.2012.08.019.

Knobel, R. 2000. *An Introduction to the Mathematical Theory of Waves.* Providence: American Mathematical Society.

Lemmon E. W. 2017. Thermophysical Properties of Fluids. In *CRC Handbook of Chemistry and Physics*, 98th edition, ed. J. Rumble, Chap. 6, 6-37. Cleveland: CRC Press.

Liu, Y., Jiang, L., Tang, L. et al. 2015. Minimum Miscibility Pressure Estimation for a CO_2/n-Decane System in Porous Media by X-Ray CT. *Exp. Fluids* 56 (7): 154. http://dx.doi.org/10.1007/s00348-015-2025-4.

Logan, J. D. 2015. *Applied Partial Differential Equations*, third edition. Cham: Springer.

Mac Dowell, N., Fennell, P. S., Shah, N. et al. 2017. The Role of CO_2 Capture and Utilization in Mitigating Climate Change. *Nat. Clim. Change.* 7 (4):243-249. https://doi.org/10.1038/nclimate3231.

Meiboom, S., Gill, D. 1958. Modified Spin-Echo Method for Measuring Nuclear Relaxation Times. *Rev. Sci. Instrum.* 29 (8): 688-691. https://dx.doi.org/10.1063/1.1716296.

Mitchell, J., Chandrasekera, T. C., Holland, D. J. et al. 2013. Magnetic Resonance Imaging in Laboratory Petrophysical Core Analysis. *Phys. Rep.* 526 (3): 165-225. https://dx.doi.org/10.1016/j.physrep.2013.01.003.

Muir, C. E. and Balcom, B. J. 2012. Pure Phase Encode Magnetic Resonance Imaging of Fluids in Porous Media. In *Annual Reports on NMR Spectroscopy*, Vol. 77, ed. G. A. Webb, Chap. 2, 81-113.Burlington, Massachusetts: Academic Press.

Muir, C. E. and Balcom, B. J. 2013. A Comparison of Magnetic Resonance Imaging Methods for Fluid Content Imaging in Porous Media. *Magn. Reson. Chem.* 51 (6) 321-327. https://dx.doi.org/10.1002/mrc.3947.

Muzny, C. D., Diky, V., Kazakov, A. et al. 2017. Critical Constants of Organic Compounds. In *CRC Handbook of Chemistry and Physics*, 98th edition, ed. J. Rumble, Chap. 6, 6-69. Cleveland: CRC Press.

Nascimento, F. P., Paredes, M. L. L., Souza, K. M. et al. 2014. Vapor-Liquid Equilibrium of CO_2/Toluene, CO_2/n-Decane and CO_2/Toluene/n-Decane: Experimental Measurements and Thermodynamic Modeling. Poster presentation given at the 14th European Meeting on Supercritical Fluids, Marseille, France, 18-21 May.

Novy, R. A., Toledo, P. G., Davis, H. T. et al. 1989. Capillary Dispersion in Porous Media at Low Wetting Phase Saturations. *Chem. Eng. Sci.* 44 (9): 1785-1797. https://doi.org/10.1016/0009-2509(89)85121-8.

Orr, F. M.Jr. 2007. *Theory of Gas Injection Processes*. Holte: Tie-Line Publications.

Peng, D. Y. and Robinson, D. B. 1976. A New Two-Constant Equation of State. *Ind. Eng. Chem. Fundamen.* 15 (1): 59-64. https://doi.org/10.1021/i160057a011.

Pereira, L. M. C., Chapoy, A., Burgass, R. et al. 2016. Measurement and Modelling of High Pressure Density and Interfacial Tension of (Gas + n-Alkane) Binary Mixtures. *J. Chem. Thermodyn.* 97 (June): 55-69. https://doi.org/10.1016/j.jct.2015.12.036.

Petrov, O., Ersland, G., and Balcom, B. J. 2011. T_2 Distribution Mapping Profiles with Phase Encode MRI. *J. Magn. Reson.* 209: 39-46. https://doi.org/10.1016/j.jmr.2010.12.006.

Prausnitz, J. M. and Benson, P. R. 1959. Solubility of Liquids in Compressed Hydrogen, Nitrogen, and Carbon Dioxide. *AICHE J.* 5 (2): 161-164. https://doi.org/10.1002/aic.690050208.

Reamer, H. H. and Sage, B. H. 1963. Phase Equilibria in Hydrocarbon Systems. Volumetric and Phase Behavior of the n-Decane-CO_2 System. *J. Chem. Eng. Data* 8 (4): 508–513. http://doi.org/10.1021/je60019a010.

Romero-Zerón, L. B., Ongsurakul, S., Li, L. et al. 2009a. Visualization of Mobility-Control by Polymer Waterflooding through Unconsolidated Porous Media using Magnetic Resonance Imaging. *Pet. Sci. Technol.* 27 (17): 2046-2062. https://doi.org/10.1080/10916460802611325

Romero-Zerón, L.B., Li, L., Ongsurakul, S. et al. 2009b. Visualization of Waterflooding through Unconsolidated Porous Media using Magnetic Resonance Imaging. *Pet. Sci. Technol.* 27 (17): 1993-2009. https://doi.org/10.1080/10916460802611267.

Romero-Zerón, L. B., Ongsurakul, S., Li, L. et al. 2010a. Visualization of the Effect of Porous Media Wettability on Polymer Flooding Performance through Unconsolidated Porous Media using Magnetic Resonance Imaging. *Pet. Sci. Technol.* 28 (1): 52-67. https://doi.org/10.1080/10916460802611432.

Romero-Zerón, L. B., Ongsurakul, S., Li, L. et al. 2010b. Magnetic Resonance Imaging of Phase Trapping and in situ Permeability Modification in Unconsolidated Porous Media. *Pet. Sci. Technol.* 28 (3): 262-276. https://doi.org/10.1080/10916460802611457.

Sahimi, M. 1993. Flow Phenomena in Rocks: From Continuum Models to Fractals, Percolation, Cellular Automata, and Simulated Annealing. *Rev. Mod. Phys.* 65 (4): 1393-1545. http://dx.doi.org/10.1103/RevModPhys.65.1393.

Shakerian, M., Marica, F., Afrough, A. et al. 2017. A High-Pressure Metallic Core Holder for Magnetic Resonance Based on Hastelloy-C. *Rev. Sci. Instrum.* 88 (12): 123703. https://doi.org/10.1063/1.5013031.

Smith, J. M., Van Ness, H. C., and Abbott, M. M. 2005. *Introduction to Chemical Engineering Thermodynamics*, seventh edition. Boston: McGraw-Hill.

Song, Y., Jian, W., Zhang, Y. et al. 2012. Densities and Volumetric Characteristics of Binary System of CO_2 + Decane from (303.15 to 353.15) K and Pressures up to 19 MPa. *J. Chem. Eng. Data* 57 (12): 3399–3407. https://doi.org/10.1021/je300388b.

Song, Y., Zhu, N., Zhao, Y. et al. 2013. Magnetic Resonance Imaging Study on Near Miscible Supercritical CO_2 Flooding in Porous Media. *Phys. Fluids* 25 (5): 053301. https://dx.doi.org/ 10.1063/1.4803663.

Song, Y., Jiang, L., Liu, Y. et al. 2014. Study of the Fluid Flow Characteristics in a Porous Medium for CO_2 Geological Storage using MRI. *Magn. Reson. Imaging* 32 (5): 574-584. http://dx.doi.org/10.1016/j.mri.2014.01.021.

Suekane, T., Soukawa, S., Iwatani, S. et al. 2005. Behavior of Supercritical CO_2 Injected into Porous Media Containing Water. *Energy* 30 (11-12): 2370-2382. https://dx.doi.org/10.1016/j.energy.2003.10.026.

Suekane, T., Ishii, T., Tsushima, S. et al. 2006. Migration of CO_2 in Porous Media Filled with Water. *J. Therm. Sci. Tech. Jpn.* 1 (1): 1-11. https://dx.doi.org/10.1299/jtst.1.1.

Teng, Y., Liu, Y., Song, Y. et al. 2014. A Study on CO_2 Diffusion Coefficient in n-Decane Saturated Porous Media by MRI. *Enrgy. Proced.* 61: 603-606. https://doi.org/10.1016/j.egypro.2014.11.1180.

Umezawa, S. and Nagashima, A. 1992. Measurement of the Diffusion Coefficients of Acetone, Benzene, and Alkane in Supercritical CO_2 by the Taylor Dispersion Method. *J. Supercrit. Fluid.* 5 (4): 242-250. https://doi.org/10.1016/0896-8446(92)90014-B.

Vashaee, S., Newling, B., MacMillan, B. et al. Local Diffusion and Diffusion-T2 Distribution Measurement in Porous Media. *J. Magn. Reson.* 278 (May): 104-112. https://doi.org/10.1016/j.jmr.2017.03.014.

Vogt, S. J., Shaw, C. A., Maneval, J. E. et al. 2014. Magnetic Resonance Measurements of Flow-Path Enhancement during Supercritical CO_2 Injection in Sandstone and Carbonate Rock Cores. *J. Petrol. Sci. Eng.* 122 (October): 507-514. https://dx.doi.org/10.1016/j.petrol.2014.08.013.

Willhite. 1986. *Waterflooding*. Richardson: Society of Petroleum Engineers.

Yang, Z. Hirasaki, G.J., Appel, M. et al. 2012. Viscosity Evaluation for NMR Well Logging of Live Heavy Oils. *Petrophysics* 53 (1) 22-37. SPWLA-2012-v53n1a2.

Yu, Z., Liu, Y., Zhou, R. et al. 2001. A Principle to Correlate Extreme Values of Excess Thermodynamic Functions with Partial Molar Quantities. *Sc. China Ser. B-Chem*. 44 (3): 315-319. https://doi.org/10.1007/BF02879622.

Xiao, D., Balcom, B. J. 2015. π Echo-Planar Imaging with Concomitant Field Compensation for Porous Media MRI. *J. Magn. Reson.* 260 (November): 38-45. https://dx.doi.org/10.1016/j.jmr.2015.08.023.

Zamudio, M., Schwarz, C. E., and Knoetze, J. H. 2011. Phase Equilibria of Branched Isomers of C10-Alcohols and C10-Alkanes in Supercritical Ethane. *J. Supercrit. Fluid.* 58 (3): 330-342. https://doi.org/10.1016/j.supflu.2011.07.004.

Zhao, Y., Song, Y., Liu, Y. et al. 2011a. Visualization and Measurement of CO_2 Flooding in Porous Media Using MRI. *Ind. Eng. Chem. Res.* 50 (8): 4707-4715. https://dx.doi.org/10.1021/ie1013019.

Zhao, Y., Song, Y., Liu, Y. et al. 2011b. Visualization of CO_2 and Oil Immiscible and Miscible Flow Processes in Porous Media using NMR Micro-Imaging. *Pet. Sci.* 8 (2): 183-193. https://dx.doi.org/10.1007/s12182-011-0133-1.

Chapter 6 – Magnetic Resonance Imaging of High-Pressure Carbon Dioxide Displacement: Fluid Behavior and Fluid/Surface Interaction[3]

MRI provides a wealth of information on petroleum flooding displacement mechanisms, and in-situ pore level behavior. The previous chapter discussed macroscopic effects of dispersion during CO_2 flooding of oil-saturated rocks. This chapter[2] uses MRI monitoring of an enhanced oil recovery process, CO_2 flooding, to extract information on the pore surface/fluid interaction. Transverse relaxation time constant T_2 is used to extract such information.

This study demonstrates MRI methods that have potential for studying the mechanisms of CO_2 displacement processes in Berea core plugs during the recovery of decane and heavy oil. The correlation between fluid saturation and T_2 revealed the contrast in decane/pore-surface interaction between miscible and immiscible drainage of decane by CO_2. T_2 profiles demonstrated changes in the composition and viscosity of the heavy oil caused by the extraction of light components by CO_2.

---

[3] Largely based on: Afrough, A., Shakerian, M., Zamiri, M. S., MacMillan, B., Marica, F., Newling, B., Romero-Zerón, L., Balcom, B. J. 2017. Magnetic Resonance Imaging of High Pressure Carbon Dioxide Displacement: Fluid/Surface Interaction and Fluid Behavior. *SPE J.* 23 (3): 772-787. https://doi.org/10.2118/189458-PA.

6.1 Introduction

Carbon dioxide, a major greenhouse gas, has been injected into petroleum reservoirs, for enhanced oil recovery, for several decades (Beckwith 2011). Enhanced petroleum recovery by CO_2 flooding has the potential to be concurrent with CO_2 sequestration, mitigating its climate change impact (Orr 2009). The CO_2 used may originate from a variety of sources including gas processing plants, synthetic fuel power plant emissions, and natural CO_2 reservoirs (Beckwith 2011). The production gain from CO_2 injection into petroleum reservoirs can only be projected and realized with sound engineering estimates supported by quality laboratory data. This has led to significant research and attracted interest in an array of technologies for investigating CO_2 injection into reservoir rocks (Vinegar and Wellington 1987; Nakatsuka et al. 2010).

The fluid/surface interaction and properties of the pore-filling fluids, during CO_2 flooding, are difficult to investigate non-invasively. Magnetic Resonance (MR) and Magnetic Resonance Imaging (MRI) can provide a wealth of information on displacement mechanisms and in-situ pore level behavior, not accessible by other methods (Baldwin and King 1999). However, the application of MRI to such studies has been restricted owing to limitations of instrumentation, lack of appropriate methodologies, and lack of qualified professionals, in addition to the multifaceted nature of the method. At the same time, Nuclear Magnetic Resonance (NMR) logging has become an invaluable tool addressing challenging problems in petroleum reservoir evaluation (Coates et al. 1999), clearly demonstrating the potential benefits of magnetic resonance to the petroleum industry.

The objective of this study was to investigate the mechanisms of linear CO_2 displacement processes, both miscible and immiscible, in porous rocks by measuring fluid saturation and transverse relaxation time distributions.

MRI has been used in several CO_2 flooding experiments reported in the literature. Suekane et al. (2005; 2006; 2009) used a custom-built polyamide-imide pressure vessel at a magnetic field of 7 T. They monitored water content in glass bead packs invaded by supercritical CO_2 flow. They also showed that $1/T_1$ was correlated with CO_2 concentration dissolved in bulk water, water-saturated bead packs, and core plugs (Suekane et al. 2009). Brautaset et al. (2008) conducted water and CO_2 flooding in decane-saturated low-permeability chalk of different wettabilities at pressures more, and less, than the reported Minimum Miscibility Pressure (MMP). They did so to assess the enhanced oil recovery potential from CO_2 injection. A non-linear correlation between signal intensity and oil saturation led them to conclude that the relaxation properties of the oil-CO_2 mixture did not allow reproducible saturation predictions. Quantitative MRI methodologies were not used in this research leaving open the question of whether fluid saturation may be reliably measured.

In a series of recent publications, researchers from the Key Ocean Energy Utilization and Energy Conservation laboratory at Dalian University of Technology, China, studied CO_2 flooding of decane-saturated glass bead packs. They used a polyimide core holder with titanium end-caps capable of operating at 15 MPa and 70 °C in a 9.6 T MRI instrument

(Zhao et al. 2011). They injected CO_2 into decane-saturated bead packs at miscible (Zhao et al. 2011), near miscible (Song et al. 2013), and immiscible (Zhao et al. 2011) conditions and measured fluid saturation in two-dimensional slices employing standard Spin Echo Multi Slice (SEMS) methods. They also performed CO_2 flooding of water-saturated glass bead packs (Song et al. 2012; Song et al. 2014). In related publications, they have calculated CO_2-oleic phase diffusivity in bulk liquids and bead packs using concentration gradients inferred from saturation and T_1 profiles (Hao et al. 2015; Zhao et al. 2016). They also measured the spin echo signal intensity of decane in equilibrium with CO_2 at different pressures, temperatures, and measured the MMP of the CO_2/decane system (Song et al. 2011). This method was not investigated further for the case of more complex fluids.

Researchers who have previously used MRI to monitor CO_2 flooding processes have, to this point, encountered three major limitations: (1) employing porous samples and fluids not representative of reservoir rocks and fluids, (2) employing non-metallic MRI core holders which limit sample size, and accessible temperatures and pressures, and (3) applying inappropriate imaging and data processing methods. Problem (3) is linked to problem (1). Appropriate MRI methods will permit quantitative studies in realistic samples. These limitations and their solutions are addressed in this work as described below.

(1). The magnetic susceptibility of pore-filling fluids and rock grains differs in realistic rocks. This creates internal magnetic field gradients in the pore space when MR/MRI measurements are undertaken in real rocks, especially sandstones. Diffusion of

the pore-filling fluid in these gradients is an inherent problem in spin echo MR measurements involving porous rocks (Hürlimann 1998). Previous investigators have mainly used high static magnetic fields of 2 T (Brautaset et al. 2008), 9.6 T (Zhao et al. 2011), and 7 T (Suekane et al. 2005). Such high static magnetic fields lead to unfavorable quantitative MR measurements (Mitchell et al. 2013) that forced previous investigators to use idealized samples (glass bead packs) with a small susceptibility mismatch. In the current work, at a low static magnetic field of 0.2 T, pure phase-encoding methods were used to perform quantitative MR measurements on Berea sandstones. Phase-encoding MRI methods provide quantitative maps of fluid saturation, which are not affected by B_0 inhomogeneity, susceptibility effects, or chemical shift (Muir and Balcom 2012). In contrast to phase-encoding, common frequency-encoding methods are inherently affected by susceptibility mismatch. In addition, switched magnetic field gradients, which are usually not well characterized, can result in image artifacts in frequency-encoding MRI measurements. Such artifacts are observed and acknowledged in the works of Zhao et al. (2011), Suekane et al. (2005; 2006), and Brautaset et al. (2008). Pure phase-encoding methods like SPRITE and SE-SPI (Muir and Balcom 2012) were applied in the current work to overcome this limitation and to quantitatively image fluid saturation and T_2 distributions. π Echo Planar Imaging (π EPI, a frequency-encoding MRI method) with corrected magnetic field gradient waveforms (Xiao and Balcom 2015), was also used for fast quantitative 3D imaging of immiscible displacement of decane in this work.

The displaced oleic fluids used in previous studies have been alkanes, usually decane (Zhao et al. 2011; Brautaset et al. 2008). Alkanes heavier than decane, such as n-hexadecane and n-tetradecane, have also been used in the measurement of CO_2 diffusivity in saturated glass bead packs owing to their favorable T_1 change with CO_2 dissolution (Hao et al. 2015; Zhao et al. 2016). In contrast to the liquid alkanes used in CO_2 experiments reported in the literature to date, heavy oil samples may have transverse relaxation times as short as 5 ms. Inappropriate MRI methods such as SEMS yield inaccurate fluid saturation maps for systems with such short transverse relaxation time constants. SE-SPI has the capability to quantitatively map fluids with T_2 values as short as 2 ms. CO_2 flooding of heavy oil represents an extreme case in MRI, which is successfully demonstrated in this work.

(2). Supercritical CO_2, at pressures exceeding 7 MPa and in volumes as large as a standard 38 mm diameter core plug, is a major challenge to MRI measurement because of limitations imposed by MRI magnet bore size and high-pressure sealing systems compatible with MR measurements. Previous work has used small sample volumes of 7.5 mm (Bagherzadeh et al. 2011), 15 mm (Zhao et al. 2011), and 26 mm (Suekane et al. 2005) diameter. The capability of MRI instruments to image standard 38 mm diameter core plugs at high pressure would permit the incorporation of MRI into standard laboratory core analysis/flooding programs. The current study highlights new high-pressure capabilities in MRI instrumentation. The core holder used in the current study can test 38 mm diameter standard core plugs at high pressure.

Most commercially available MRI compatible core holders are non-metallic and have the radio frequency (RF) probe, which excites and detects the signal, outside the high-pressure vessel (Gao et al. 2005; Han et al. 2011). Non-metallic core holders have unfavorable failure mechanisms at high pressure. Metallic core holders provide a safer alternative with broader operating conditions and easier temperature regulation. Han et al. (2011) demonstrated the possibility of MRI measurements inside metallic vessels. Ouellette et al. (2016) built a prototype core holder from high strength Nitronic. However, the core holder developed by Ouellette et al. (2016) was not used for high pressure measurements. The current study features a high pressure non-magnetic metallic core holder capable of, and tested for, withstanding a maximum pressure of 35 MPa and temperatures up to 80 °C (Shakerian et al. 2017; Li et al. 2016). It includes an RF probe located inside the metallic core holder. Incorporation of the RF probe inside the vessel enhances the signal-to-noise ratio (SNR) according to the principle of reciprocity (Hoult and Richards 1976).

(3). Previous MRI studies of CO_2 flooding have principally used ^1H SEMS proton density images to map liquid phase content. For instance, only two papers have reported images of average longitudinal relaxation time constants (Suekane et al. 2009; Hao et al. 2015) in CO_2 flooding experiments. More sophisticated MR measurement, data processing, and interpretation methods are necessary to acquire quantitative relaxation time constants. Quantitative spatially and temporally resolved distributions of relaxation time constants in addition to proton density, measured by the SE-SPI method, yield information about the surface/fluid interaction and properties of the pore-filling fluids. The current work employs

the SE-SPI method with pre-equalized magnetic field gradients (Vashaee et al. 2015). The application of pre-equalized magnetic field gradient waveforms reduced the first echo time to 1.8 ms, making SE-SPI with pre-equalized magnetic gradients capable of measuring short-lived echoes. This work expands the capabilities of the associated MRI data processing framework developed by Afrough et al. (2016) for investigating fluid/rock interactions in porous rocks. An extensive function library developed in-house was used for data processing, including: reading MR and MRI data and image files, phase correction, removal of background signal, filtering, Fourier transformation, image registration, uncertainty calculation, data storage, statistical analysis, and data visualization. Spatial and time resolved data obtained by this method can potentially serve as solutions to Partial Differential Equations (PDE) modelling fluid flow in porous rocks in inverse problems.

This study demonstrates MRI methods that have potential for studying the mechanisms of linear CO_2 displacement processes in Berea core plugs during the recovery of decane and heavy oil. It also addresses the interaction between decane and the pore surface. The SE-SPI method is particularly sensitive to the changes in fluid properties or pore surface/fluid interactions.

6.2 Materials and Methods

Each MR experiment involves a spectrometer registering a time-varying electric signal received by an RF coil. The signal is normally in the form of $I_{0i}\exp(-t/\tau_i)$ or a summation of such terms in which I_{0i} is an initial amplitude, τ_i is an exponential decay

constant, and t is measurement time. MR experiments can be designed to extract ^{1}H density, relaxation time constants T_1, T_2, and T_2^*, and diffusion coefficient D from the initial amplitude or decay constant of the signal or a series of signals. Properties of the fluids (Hürlimann et al. 2009) and porous medium (Kleinberg 1999), such as ^{1}H density, pore size, diffusivity, velocity, and viscosity, can be measured or inferred from these MR properties. Fluid saturation is proportional to the ^{1}H density while pore size, permeability, and viscosity are correlated with T_1 and T_2.

6.2.1 Core Plug Samples and Materials

The three Berea core plugs employed were 50 mm long and 38 mm in diameter, with permeabilities ranging from 100 to 200 mD and porosities ranging from 19 to 20%. These core plugs were drilled from slabs taken from the Kipton formation by Kocurek Industries (Caldwell, Texas, US), and, as expected, they had uniform properties and similar T_2 distributions. The pore structure of Berea was unaffected by exposure to supercritical CO_2 with no measurable changes in two-dimensional MR relaxation measurements (Vogt et al. 2014). The chemical resistance of quartz to supercritical CO_2 is the main reason for consistency in the pore structure of Berea upon exposure to CO_2. Decane (≥95%, Sigma-Aldrich Co., St. Louis, MO), CO_2 (99.7%, Air Liquide Canada Inc., Montreal, QC), and heavy crude oil (with a viscosity of 640 mPa.s at 40°C supplied by Husky Energy, Calgary, AB) were employed in these experiments. Fluorinert (3M, St. Paul, MN) was used as the confining fluid in the core holder. A solution of sodium chloride with a concentration of 3 wt% was prepared from degassed deionized water and deuterium oxide (99.8%, Cortecnet,

Voisins-le-Bretonneux, France). Liquids, except for the heavy oil, were degassed and liquid containers were capped throughout the experiments.

6.2.2 Instrumentation

MRI measurements were performed with an Oxford Maran DRX-HF (Oxford Instruments, Abingdon, UK) vertical bore permanent magnet operating at ^{1}H frequency of 8.5 MHz. This unit includes a 1 KW BT01000-AlphaS RF amplifier (TOMCO Technologies, Sydney, Australia) and a shielded three-axis magnetic field gradient coil set driven by Techron 7782 (Techron, Elkhart, IN) gradient amplifiers providing maximum magnetic field gradients of 26 G/cm, 24 G/cm, and 33 G/cm in x-, y-, and z- directions, respectively. In the MRI magnet, the core plug center marks the $y = 0$ position and y increases in the axial upward direction. x and z directions form the radial plane of the core plug.

The MS-5000, a custom-built MR/MRI compatible core holder, was employed to facilitate MR/MRI measurements of high-pressure processes (Shakerian et al. 2017; Li et al. 2016). This core holder was made of Hastelloy-C276, which is non-magnetic and has low electrical conductivity to reduce eddy currents induced by switching magnetic field gradients. This core holder also features an integrated solenoid RF probe.

The following methods were employed for bulk and spatially resolved measurements of proton density, T_2 distribution, T_1, and T_2-weighted proton density: free induction decay (FID), Carr-Purcell-Meiboom-Gill (CPMG), inversion recovery (INVREC), single point ramped imaging with T_1 enhancement (SPRITE), SE-SPI, and π EPI. The WinDXP

software package (Oxford Instruments, Abingdon, UK) was employed to extract T_2 distributions from the exponentially decaying signals employing the BRD algorithm (Butler et al. 1981). An extensive function library developed in-house written in the Matlab (Mathworks, Natick, Massachusetts, US) array programming language was employed for data processing. Quizix-6000-SS (Chandler Engineering, Tulsa, OK) and Shimadzu LC-8A (Shimadzu, Kyoto, Japan) pumps were employed for pumping aqueous and oleic phases. A Teledyne ISCO 100DX (Teledyne ISCO, Lincoln, NE) pump equipped with heating jackets was used for injecting CO_2. Pressures were read from analog pressure gauges and Ashcroft K1 pressure transducers (Ashcroft, Stratford, CT) in conjunction with an OM-DAQ-USB-2401 USB data acquisition system (Omega Engineering Inc., Stamford, CT). High pressure Swagelok (Swagelok, Solon, OH) and HiP (High Pressure Equipment Co, Erie, PA) flow lines and connectors transmitted the fluids from pumps to the core holder. A Julabo F25 heating circulator (Julabo, Seelbach, Germany) was used for temperature control of the pump and core holder heating jacket.

6.2.3 Experimental Methodology

In preliminary work, the effect of CO_2/decane mole ratio on the range of T_1, T_2, and T_2^* for ^1H in a Berea core plug was studied. INVREC, CPMG, and FID measurements reported T_1, T_2, and T_2^* time constants respectively. T_1 had a long lifetime component of approximately 1500 ms, on average, which had a decreasing trend with increasing CO_2/decane mole ratio. The logarithmic mean T_2 (T_{2LM}) decreased from 165 ms to 90 ms with increasing CO_2 mole fractions ranging from zero to 0.95, while T_2^* decreased from

0.98 ms to 0.70 ms. The proximity of the Omega data acquisition system to the MRI system introduced electrical noise in the MR signal. This condition was mitigated by distancing the data acquisition unit from the magnet. The pressure transducers were also electrically insulated from the core holder by employing high pressure electrically insulating PEEK connections.

6.2.3.1 Miscible and Immiscible Drainage of Decane

The Berea core plug was first installed in the core holder. The core holder assembly was tested for leaks and positioned in the magnet thereafter. Fluorinert injected into the confining port at the bottom of the core holder exerted pressure on the sleeve. Confining pressure was always held at least 4 MPa higher than the pore pressure. Nitrogen was used to set the dome pressure of the back-pressure regulator. CO_2 was injected into the flow lines leading to the core plug to remove air. Decane was subsequently injected into the core plug to replace CO_2. FID and CPMG methods were employed to monitor the filling process. Temperature equilibration was achieved in approximately 24 hours, with dissolution of any residual CO_2 in the decane phase. CO_2 was then injected from the top of the core holder at a rate of 0.04 cc/min at 40 °C and experimental pressures of 9 MPa and 6 MPa for miscible and immiscible displacements, respectively. The MMP of the decane/CO_2 system is 8.0 MPa at 40 °C (Liu et al. 2015). The reported miscibility pressure of the CO_2/decane mixture was confirmed by a $P - x_{CO_2} - y_{CO_2}$ phase diagram at constant temperature of 40°C. The phase diagram was calculated employing Peng-Robinson equation of state in Aspen Properties software (Aspen Technology, Bedford, MA). A series

of FID, CPMG, SPRITE, and SE-SPI measurements were undertaken during injection. CO_2 injection ceased after no change was observed in sequential measurements. Core plugs were removed from the core holder and weighed immediately thereafter.

In the case of immiscible CO_2 flooding, 3D π EPI MRI measurements (Xiao and Balcom 2015) were also performed throughout the experiment. The core plug was flushed with high pressure supercritical CO_2 at 10 cc/min, after no change was observed in sequential image profiles, to measure the background signal.

6.2.4 Immiscible Flooding of Heavy Oil

The procedure followed for immiscible CO_2 flooding of heavy oil was similar to that employed in immiscible CO_2 flooding of decane, with a few differences. In this case, the CO_2 injection stage for the removal of air from the lines and core plug was followed by the injection of H_2O and then D_2O brine. Heavy oil was then injected into the core plug. The flow lines affected by injection of the heavy oil were replaced and CO_2 was injected into the core plug. A series of FID, CPMG, SPRITE, and π EPI measurements were performed during CO_2 injection. Oil recovery was monitored as a function of time.

Introduction of D_2O brine into the CO_2 flooding of heavy oil had three objectives: (1) demonstrating the capability of the laboratory method to measure realistic core plugs with three phases present, (2) covering the Berea pore surface with wetting phase, D_2O, to significantly reduce surface relaxation for heavy oil, and (3) D_2O, unlike H_2O, is MRI invisible at ^1H Larmor frequency, so only the oil phase is visible in MR measurements.

6.2.5 Imaging Methods

The spin echo class of MR methods can measure the transverse relaxation time, which has been related to pore size, surface to volume ratio, permeability, and capillary pressure (Coates et al. 1999). The CPMG method is the classic spin echo experiment widely used in NMR logging. It consists of a 90° RF pulse followed by a train of 180° pulses that rotate the net magnetic moment of the sample hydrogen nuclei in the Larmor frequency rotating frame of reference. The spacing between the 90° and the first 180° pulse, τ, is half the echo time and the spacing between the 180° pulses is 2τ, the inter-echo spacing. Echoes of declining amplitude will form between the 180° pulses. The transverse relaxation time, T_2, is determined from this decay. The initial amplitude is proportional to porosity. The time constant T_2 is proportional to the pore size in water saturated porous rocks (Coates et al. 1999). The CPMG method compensates for the effects of magnetic field inhomogeneity and corrects the effect of imperfect 180° pulses (Coates et al. 1999).

The SE-SPI method with pre-equalized magnetic gradient waveforms is a pure phase encoding CPMG based MRI method (Petrov et al. 2011). This method was utilized in this research to measure the spatially resolved T_2 distribution during CO_2 flooding of oil saturated core plugs. The SE-SPI method is similar to CPMG with two major differences: (1) the period between the 90° RF pulse and the first 180° pulse is τ_0, which may be different from τ, and (2) it includes pulsed magnetic field gradients between the 90° and the first 180° RF pulse to spatially resolve the T_2 distribution. The oil saturation and the T_2 distribution are two independent properties measured by SE-SPI at each linear volume

element of the core plug. The signal intensity, spatially resolved, after the *n*th echo in an SE-SPI imaging method is given by

$$Signal = M_0 \exp\left(\frac{-2\tau_0}{T_2}\right) \exp\left(\frac{-(n-1)2\tau}{T_2}\right) \quad (6\text{-}1)$$

where M_0 is the initial magnetization. Further information on the SE-SPI and SPRITE methods is provided by Muir and Balcom (2012).

6.2.6 Imaging Parameters

The RF probe was used with 50% amplifier power, 40% receiver gain (54 dB), and 80 μs deadtime. A 125 KHz digital filter with dwell time of 8 μs and a filter dead time of 26 μs was used in all but the π EPI images. SPRITE images had 64 pixels and a field of view of 100 mm. An RF pulse length of 2 μs, equivalent to a 10.6° flip angle, with an encoding time of 146 μs, was employed in the SPRITE images. The encoding time of 146 μs minimized background signal from the PEEK RF probe support as the PEEK FID has a local minimum at this point (Shakerian et al. 2017). SPRITE measurements were repeated 128 or 64 times with a repetition delay of 5 s with 4 phase cycling steps. 1D SPRITE profiles were Fourier transformed after applying a flat top window low-pass filter with a full width at half maximum of 0.15 mm^{-1} in k-space. The background profile from the polymeric sleeve and the PEEK frame of the RF probe was subtracted from the SPRITE proton density profiles. Corrected ^1H density profiles were normalized with respect to the average of five reliable measurements before CO_2 flooding. π EPI measurements were

repeated 16 times for signal averaging. The nominal π EPI image resolution was 1.4 mm with an echo time of 3 ms. π EPI images were 64 pixels with an isotropic 3D field of view of 90 mm.

SE-SPI images were 64 pixels with a field of view of 100 mm. The 90° and 180° RF pulse lengths were 17 μs and 34 μs respectively. SE-SPI measurements were repeated four times to increase the SNR with a repetition delay of 6.8 s. Signal from all 20 time-domain points on the echo peaks, generated with an echo time, 2τ, of 1800 μs, were averaged in SE-SPI measurements. The 1536 T_2 weighted images, acquired in the SE-SPI measurements, were pruned to reduce the number of T_2 weighted images to 512. 1D SE-SPI measurements had the phase of their odd and even T_2 weighted profiles matched and were Fourier transformed after applying the same flat top window low-pass filter previously employed in analyzing SPRITE measurements. The normalization process corrected for the effects of B_1 inhomogeneity and background signal. The T_2 weighted images were inverted to spatial T_2 distributions with a fixed regularization parameter of 5 in the BRD algorithm and T_{2LM} was calculated from the T_2 distributions.

6.2.7 Validity and Reliability

The validity of the FID, CPMG, SPRITE, and SE-SPI measurements is well established for determining mobile fluid content in porous materials (Muir and Balcom 2013, and Mitchell et al. 2013). In addition, they provide a plethora of data that may be checked for internal consistency. MR, and especially MRI, provide considerable experimental data

from a limited number of representative samples or experiments. These data include, but are not limited to, space and time resolved measurements of fluid content, apparent transverse (T_2^*), transverse (T_2) and longitudinal (T_1) relaxation time constants, and diffusivity D. A major advantage of MRI methods is that these magnetic resonance data complement each other. The reliability of the MR methods employed was established by frequent measurements prior to CO_2 injection into the core plugs which all gave consistent and reasonable T_2 and proton density values.

6.3 Results and Discussion

All MRI experiments were performed at ^{1}H frequency. Therefore, CO_2 and the fluorinated oil used as the confining fluid were MRI invisible at ^{1}H Larmor frequency as they have no hydrogen atoms in their chemical structure.

6.3.1 Fluid Saturation Measurement

The normalized 1D SPRITE profiles were corrected for small B_1 inhomogeneities and gave a measure of molar decane saturation S.

$$S = C/C_i, \tag{6-2}$$

where C is the molar concentration of decane in a core plug section as a function of position y and time t in the core plugs, and C_i is the initial molar concentration of decane in the same section. C and S are therefore proportional to proton density from either SPRITE or

SE-SPI profiles, or π EPI images. $S = 1$ corresponds to a fully decane-saturated section within the core plug, and $S = 0$ corresponds to a section with no decane present.

The processed SPRITE profiles for miscible and immiscible flooding of decane were aligned along the time axis, as shown in the contour plots of Figure 6-1. These maps show S as a function of position y and time t in the core plugs. The core plug center marks the $y = 0$ position and y increases in the upward direction. CO_2 was injected from the top of the core plug. Grayscale values from black to white represent saturation values from zero to one. This map provides oil saturation at any time and position within the core plug during the experiments.

One-dimensional SPRITE measurements, although on a core plug section scale, provide evidence of displacement mechanisms. The saturation maps of the miscible and immiscible injection experiments, as shown in Figure 6-1, have three dominant parts: full saturation, on the left; residual saturation, on the right; and a transition zone, in the middle. Residual oil saturation, flood-front velocity, and the shape of transition zone provide information on the mechanisms of flooding processes.

6.3.2 T_2 Distribution Measurement

CO_2 affects the dispersion forces between decane molecules in the oleic phase at high pressure (Yang et al. 2012). The injection of CO_2 into a decane-saturated core plug also alters decane-pore surface interactions by changing the polarity of the oleic phase (de Gennes 1985; Yang et al. 2012). These surface effects are usually investigated in static

control experiments. SE-SPI produces spatially resolved T_2 distributions which reflect fluid-surface interaction or fluid behavior (Kleinberg 1999) in dynamic processes. SE-SPI is one of the few MRI methods that has such a sensitivity to surface interaction and fluid properties. This method is, unlike conventional laboratory methods, non-invasive and measures average physical properties for a large number of pores. The SPRITE method, although of superior capability in measuring fluid content does not provide T_2 values. It was expected that saturation and T_2 together could provide more insights into the displacement mechanisms through the T_2 sensitivity to fluid-surface interactions. One-dimensional SE-SPI measurements were performed to quantitatively measure T_2 distributions as a function of position and time. T_2 values, from SE-SPI measurements, are related to petrophysical or fluid properties of interest to petroleum engineers (Coates et al. 1999).

The transverse relaxation rate $1/T_2$ in porous rocks is primarily affected by three processes: (1) bulk fluid relaxation, (2) surface relaxation, and (3) diffusion in magnetic field gradients. These three processes act in parallel in the fast-exchange regime and their rates add to determine the transverse relaxation rate (Kleinberg 1999). Low static magnetic fields induce minimal internal magnetic field gradients G_i in the pore space (Hürlimann 1998). Employing short echo times and a low static magnetic field, 0.2 T, ensures that diffusion in internal magnetic field gradients is negligible for experiments performed in this study. In the fast-exchange regime, the total relaxation rate of water in the pore space is a simple volumetric average rate (Dunn et al. 2002),

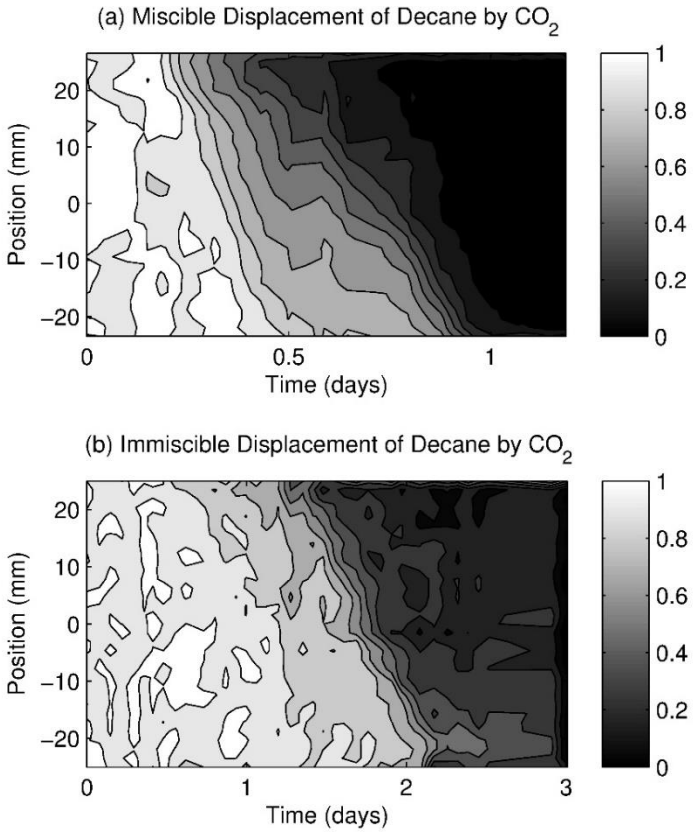

Figure 6-1 Decane saturation S as a function of position y and time t for (a) miscible and (b) immiscible displacement of decane by CO_2. The core plug center marks the $y = 0$ position and y increases in the axial upward direction. x and z directions form the radial plane of the core plug and gravity is in the $-y$ direction. CO_2 was injected from the top of the core plugs. Grayscale values from black to white represent saturation values from zero to one. Hydrodynamic dispersion effects are observed as saturation contour lines in the transition zone of the miscible flooding (a). Immiscible displacement is dominated by capillary dispersion with capillary end effects at late time data (b). 3D π EPI measurements confirmed 1D decane saturation values in (b).

$$\frac{1}{T_2} = \left(1 - \frac{\delta S_p}{V_p}\right)\frac{1}{T_{2b}} + \frac{\delta S_p}{V_p}\frac{1}{T_{2s}} + D\frac{(\gamma G_i t_E)^2}{12}, \quad (6\text{-}3)$$

where δ is the thickness of the bound layer, V_p is the pore-fluid volume, S_p is the wetted surface area, T_{2b} is the transverse relaxation time constant of the pore-filling fluid in bulk, and T_{2s} is the transverse relaxation time of the bound fluid layer.

In the fast-exchange regime, it is assumed that the diffusion of the pore-filling fluid is fast enough that all its molecules relax at the pore surface (Brownstein and Tarr 1979). Water was totally absent from the Berea core plugs during the CO_2 flooding of decane-saturated core plugs. In the absence of water in the core plug, decane preferentially wets the rock surface in the presence of CO_2. This is in agreement with the experimental work of Li and Fan (2015) on hydrophilic and hydrophobic capillary tubes. Our Berea core plugs are water wet and composed of 89% quartz (Afrough et al. 2017). In the absence of water, according to Li and Fan (2015), decane wets the Berea pore surface in liquid, gas, and supercritical states of CO_2. Consequently, the fast-exchange model is valid for the transverse relaxation of decane in Berea sandstone. For decane in the sandstone, at low magnetic fields, $T_{2s} \ll T_{2b}$ such that

$$\frac{1}{T_2} = \frac{\delta S_p}{V_p}\frac{1}{T_{2s}}. \quad (6\text{-}4)$$

It is important to note that Equation (6-4) is only valid if water is not present in the core plugs. Water can significantly modify the decane/CO_2 configuration in pores. This

discussion, including the displacement mechanisms below does not apply to experiments where water saturation exists in core plugs.

However, the heavy oil diffusivity is not high enough that all its protons relax at the surface. The heavy oil bulk transverse relaxation time was measured to be 8 ms at 40 °C. For heavy oil in a Berea core plug and at low magnetic fields, bulk processes are the main contributor to the transverse relaxation mechanisms (Coates et al. 1999). Therefore,

$$\frac{1}{T_2} = \frac{1}{T_{2b}}, \tag{6-5}$$

where T_{2b} is the bulk heavy oil transverse relaxation time constant.

The data processing method used in analyzing SE-SPI measurements was previously discussed in the Imaging Methods subsection of Materials and Methods. The first T_2-weighted profile, with a decay time of 1.80 ms, was regarded as a proton density profile for the SE-SPI measurements. All T_2-weighted profiles were subjected to the same process as SPRITE profiles to obtain molar decane saturation S. Each 1D SE-SPI imaging measurement results in a three-dimensional scalar volume data set in which position and T_2 are independent variables and oil content is measured at each position and T_2 value as incremental saturation. Such a 3D scalar volume data set can be shown as a function of position and T_2 in a T_2-map.

T_2-maps can reveal information on the mechanisms involved in displacement processes in porous rocks. T_2-maps of the miscible and immiscible flooding of decane and immiscible flooding of heavy oil by CO_2 at discrete time points are shown in Figure 6-2 through 6-4, respectively. The T_2-maps were uniform before flooding, as shown in Figure 6-2a, Figure 6-3a, and Figure 6-4a. After flooding, CO_2 injection reduced the oil saturation and altered the T_2 distribution. In a T_2 distribution, the summation of incremental saturation over all T_2 times is the same as saturation.

It is easier to consider an average T_2 value, rather than a distribution, from which other physical properties of the porous medium could be derived. Several T_2 averages can be defined employing different averaging methods (Nechifor et al. 2014). The logarithmic mean is the best average transverse relaxation time constant for predicting petrophysical properties (Borgia et al. 1997). T_{2LM} is shown with a solid white line in each T_2-map, as shown in Figure 6-2 through 6-4. SE-SPI provides both S and T_{2LM} for each section in the core plug as a function of position and time. Saturation and T_{2LM} for the miscible and immiscible flooding of decane and immiscible flooding of heavy oil by CO_2 were calculated from SE-SPI measurements and are shown as a function of time and position in Figure 6-5 through 6-7.

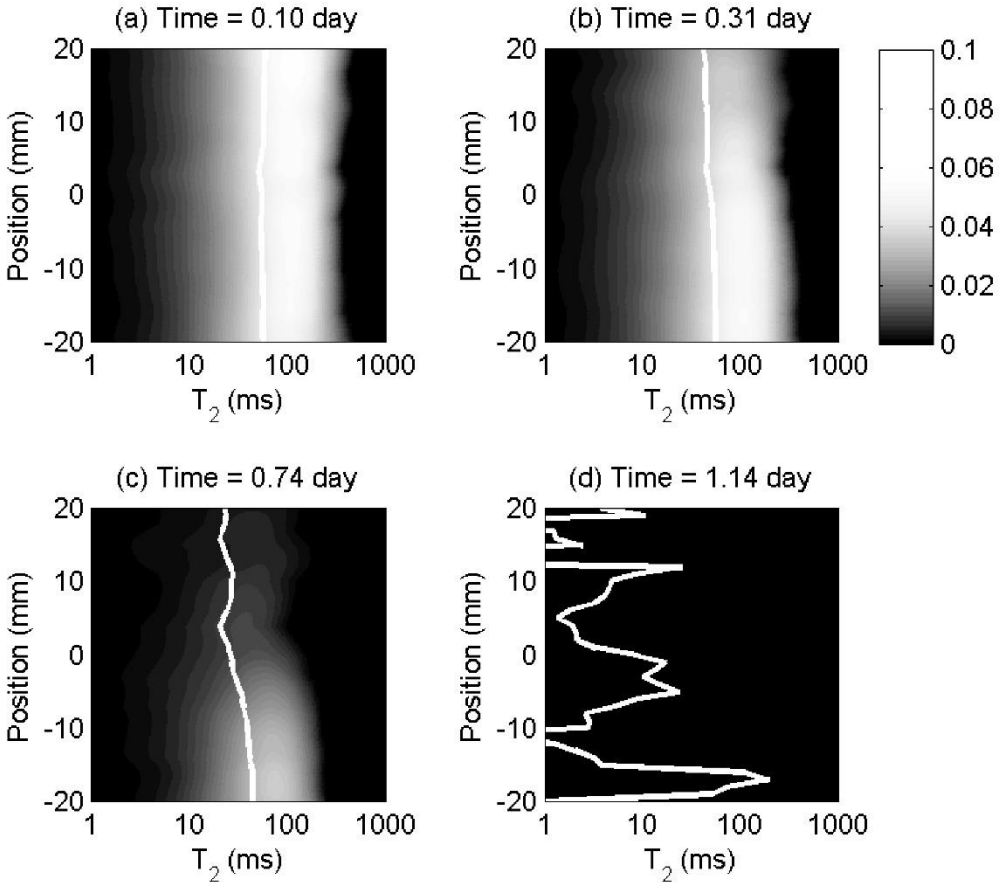

Figure 6-2 T_2 maps of miscible flooding at four discrete time points at (a) 0.10 days, (b) 0.31 days, (c) 0.74 days, and (d) 1.14 days. Incremental saturation is shown as a function of position and T_2 in each T_2 map. The incremental saturation values from zero to 0.1 are mapped from black to white. Fading T_2 distributions show decane saturations close to zero at times 0.74 days and 1.14 days. T_{2LM} is superimposed on the T_2 map as a solid white line. The summation of incremental saturation over all T_2 values in each pixel position is equal to the decane saturation of the respective core plug pixel.

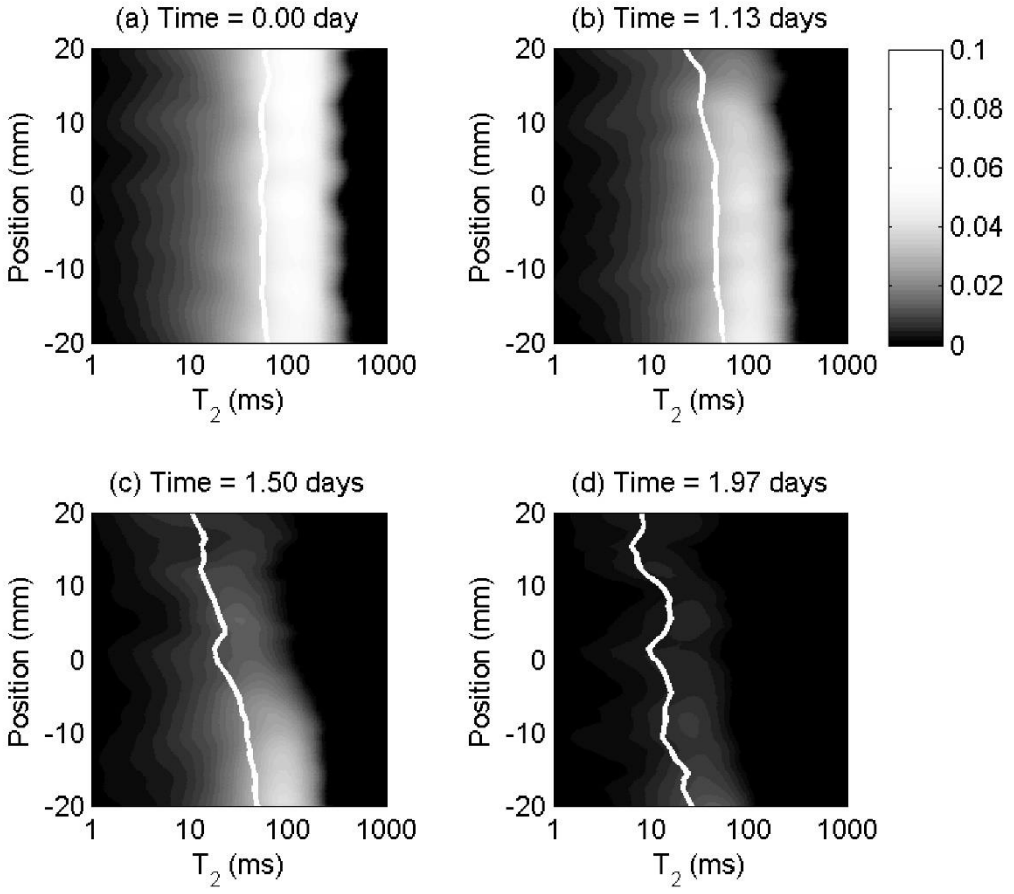

Figure 6-3 T_2 maps of immiscible flooding at four time points (a) 0.00 day, (b) 1.13 days, (c) 1.50 days, and (d) 1.97 days. Incremental saturation is shown as a function of position and T_2 in each T_2 map. The incremental saturation values from zero to 0.1 are mapped from black to white. Fading T_2 distributions show decane saturations close to zero at times 1.50 days and 1.97s day. T_{2LM} is superimposed on the T_2 map as a solid white line. The plotting and processing parameters with these T_2 maps are the same as those for the miscible injection case, Figure 6-2.

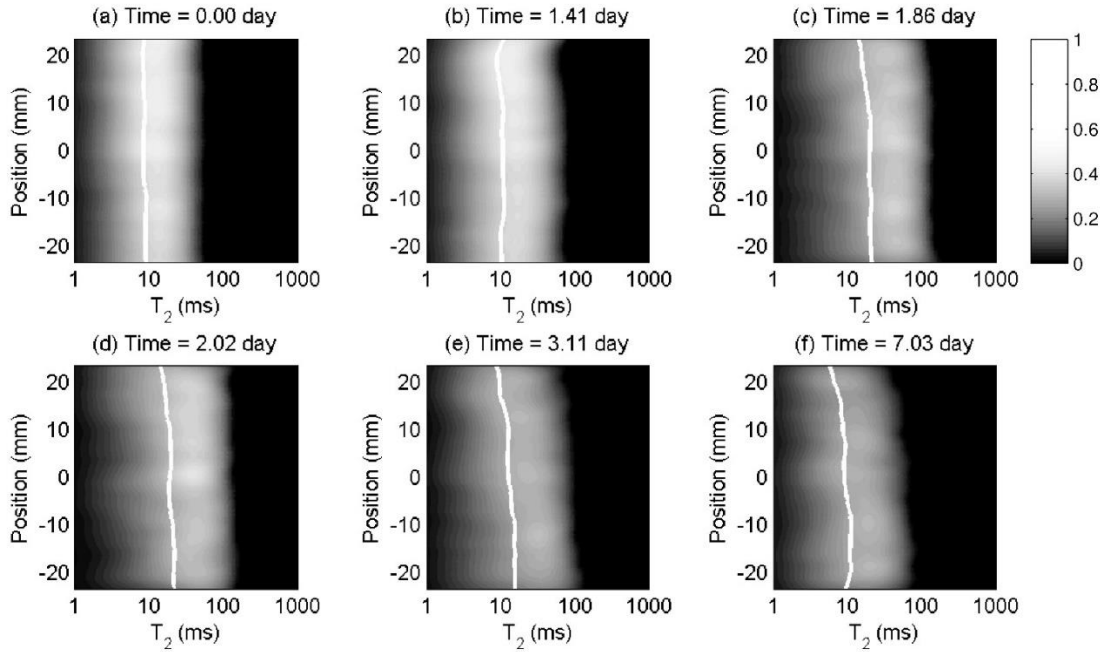

Figure 6-4 T_2 maps of heavy oil at six time points during the CO_2 flooding (a) 0.00 day, (b) 1.41 days, (c) 1.86 days, (d) 2.02 days, (e) 3.11 days, and (f) 7.03 days. Incremental saturation is shown as a function of position and T_2 in each T_2 map. The incremental saturation values from zero to 0.1 are mapped from black to white. T_{2LM} is superimposed on the T_2 map as a solid white line. T_2 first shifted to longer times and then shifted back to short T_2 times. The plotting and processing parameters of these T_2 maps are the same as those for the miscible and immiscible injection cases, Figure 6-2 and Figure 6-3.

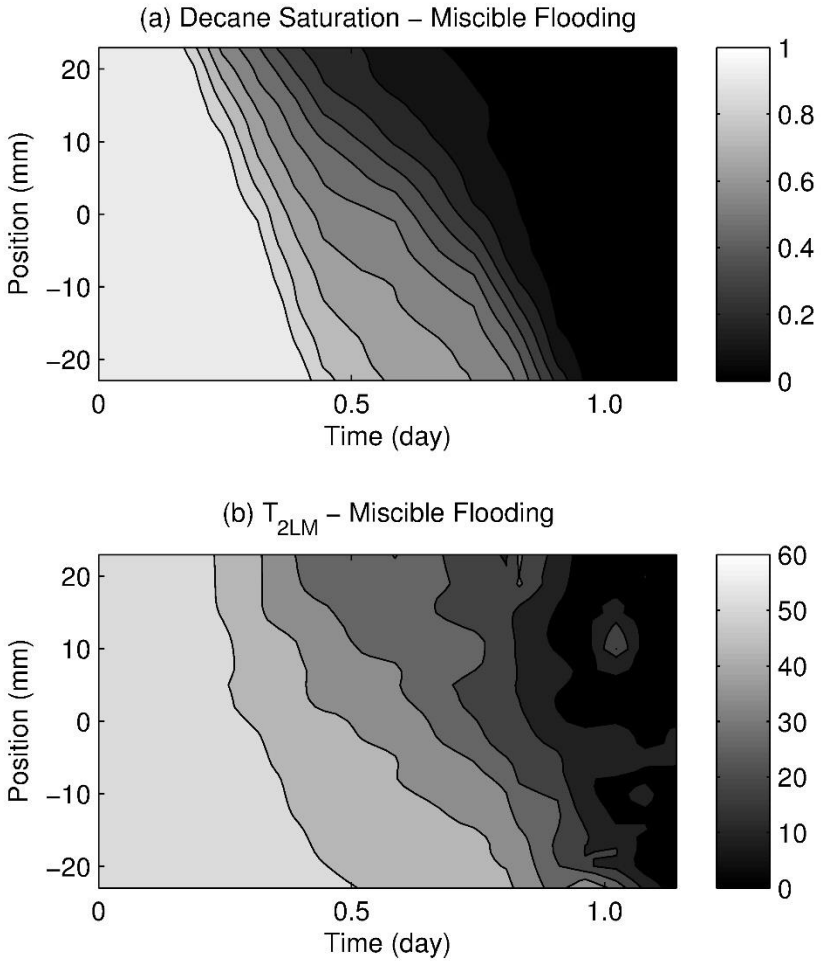

Figure 6-5 (a) Decane saturation S and (b) logarithmic mean transverse relaxation time T_{2LM} as functions of position y and time t for miscible displacement of decane. CO_2 was injected from the top of the core plug. Grayscale values from black to white represent S values from zero to one and T_{2LM} values from 0 ms to 60 ms respectively. Hydrodynamic dispersion is the dominant phenomenon in this miscible flooding process.

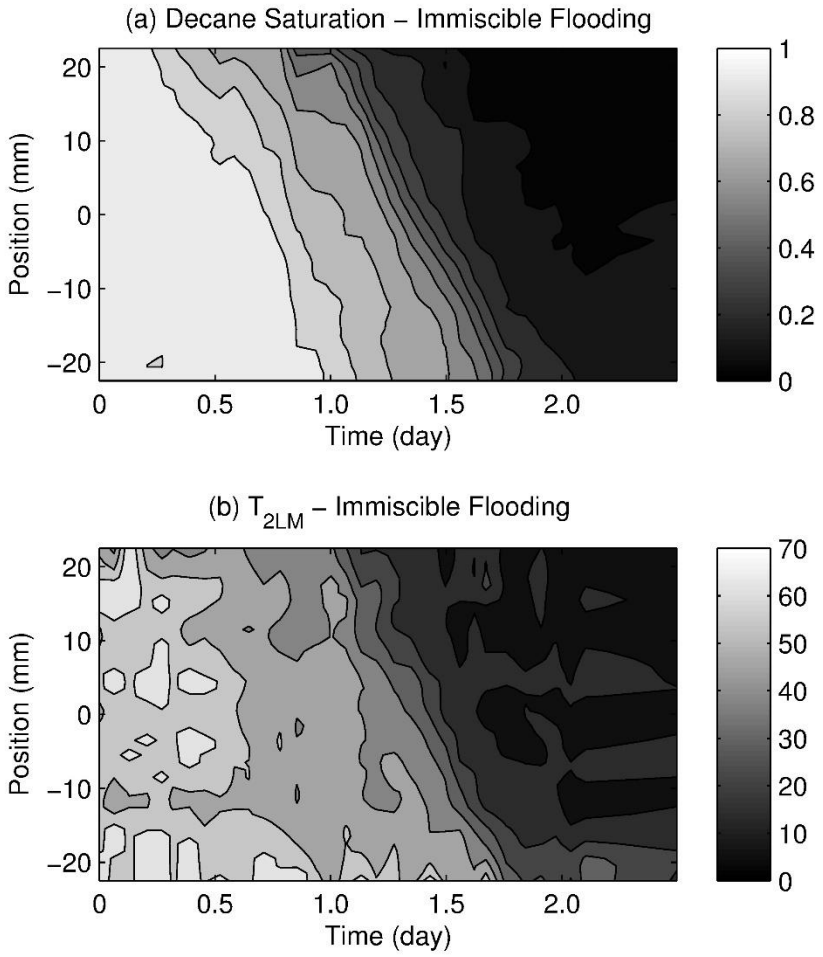

Figure 6-6 (a) Decane saturation S and (b) logarithmic mean transverse relaxation time T_{2LM} as functions of position y and time t for immiscible displacement of decane. CO_2 was injected from the top of the core plug. Colors from black to white represent S values from zero to one and T_{2LM} values from 0 ms to 70 ms respectively. At a capillary number of 2.6×10^{-7}, the displacement is in quasi-static drainage mode and is dominated by interfacial forces. 3D π EPI measurements confirmed 1D decane saturation values in (a).

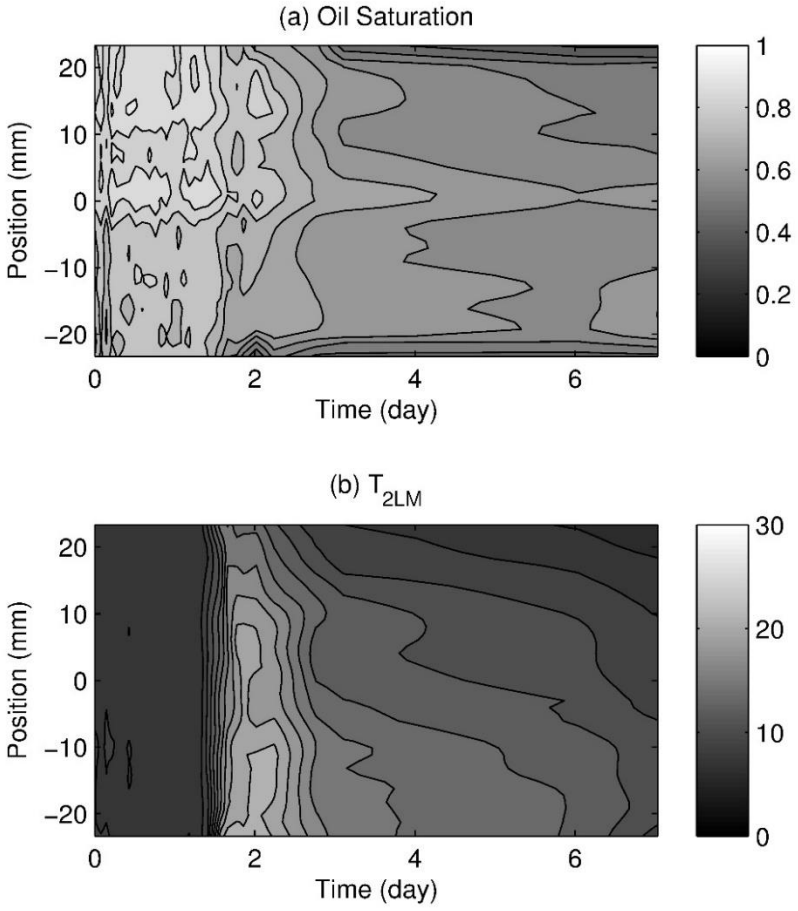

Figure 6-7 (a) Oil saturation S and (b) logarithmic mean transverse relaxation time T_{2LM} as functions of position y and time t for CO_2 displacement of heavy oil. CO_2 was injected from the top of the core plug. Grayscale values from black to white represent S values from zero to one and T_{2LM} values from zero to 30 ms, respectively. Changes in T_{2LM} suggest extraction of more light components from the top of the core than the bottom. T_{2LM} also suggests viscosity change along the core plug during the experiment. The short T_{2LM} region at left in (b) is due to heavy oil unexposed to CO_2 during the first 36 hours of the experiment.

The saturation map from the SE-SPI method is well correlated with the saturation map calculated from SPRITE measurements for CO_2 displacement of decane. Small differences between the two maps result from the inability of SE-SPI to measure signals with a T_2 lifetime of less than 2 ms (Vashaee et al. 2015) and the effects of uncertainty in the binning process for contouring. The uncertainty in reported saturation was 0.02 based on the noise level. T_{2LM} uncertainty for the miscible and immiscible CO_2 flooding of decane was 2.9 ms and 5.1 ms, respectively. T_{2LM} uncertainty for the CO_2 flooding of heavy oil was 0.21 ms. Low decane saturations result in low SNR and T_2 distribution measurement with high uncertainty. Therefore, T_{2LM} uncertainty is higher than 2.9 ms at saturations less than $S = 0.12$ for miscible CO_2 flooding, as demonstrated in Figure 6-2d. All uncertainty values are reported as combined standard uncertainty, u_c (Taylor and Kuyatt 1994), for each measurement result v. Therefore, u_c defines an interval $v - u_c$ to $v + u_c$ about the measurement result v within which the value of the measurand estimated by v is believed to lie with a level of confidence of approximately 68 percent (Taylor and Kuyatt 1994).

6.3.3 Displacement Mechanisms

There is a correlation between T_{2LM} and saturation in each flooding experiment, as shown in Figure 6-8, that bears information about the dominant displacement mechanisms in each case. In the CO_2 flooding of decane, T_{2LM} is linearly correlated with S for the saturation range of 0.2 to 1. However, the $T_{2LM} - S$ correlation clearly deviates from the linear

relationship at low decane saturations. The $T_{2LM} - S$ correlation can demonstrate the interaction between decane and pore surface, as shown in the following subsections.

Three cases are demonstrated in this work: miscible CO_2 flooding of decane, immiscible CO_2 flooding of decane, and immiscible CO_2 flooding of heavy oil. Hydrodynamic dispersion, almost completely controlled by diffusion, was the dominant displacement phenomenon in the miscible CO_2 injection in the decane-saturated Berea core plug. In immiscible CO_2 flooding of the decane-saturated Berea core plug, convection with a significant influence of capillary dispersion was the dominant displacement phenomenon. CO_2 flooding of the heavy-oil-saturated Berea core plug was dominated by three mechanisms in different stages of the experiment: (a) a short-lived early period dominated by convection significantly influenced by viscous fingering, followed by (b) diffusion of CO_2 in the oil phase, and later (c) extraction of light components from the oil phase by CO_2.

6.3.4 Miscible CO_2 Flooding of Decane

Almost no decane remained in the core plug as residual saturation, shown as black, in the late time profiles of Figure 6-1a. The residual decane saturation was calculated to be 0.04 from a histogram analysis of saturation values. Material balance before and after CO_2 flooding confirmed that the residual saturation was within the MRI saturation measurement uncertainty of 0.02.

Miscible and immiscible displacements in porous rocks are well studied (Dullien 1992). If two fluids mix in all proportions, their miscible displacement is called first-contact miscible that can lead to near ideal recovery factors when injecting sufficient miscible phase. However, the mobility of the miscible displacing phase is usually higher than the displaced phase and this results in instabilities in the displacement front. Hydrodynamic dispersion is the major phenomenon affecting the design of miscible displacement processes (Bear 1972). Dispersion is usually measured in the laboratory by injecting a displacing fluid into a core plug and analyzing the effluent fluid composition as a function of time. Dispersion coefficient values may be translated into field values for simulations in different heterogeneous, stratified, or fractured scales in the case of field applications (Sahimi 1993). Non-invasive time and spatially resolved measurements provide superior knowledge assisting the study of such processes.

Hydrodynamic dispersion, almost completely controlled by diffusion, is the dominant mass transfer phenomenon in miscible injection processes with a Peclet number of less than 0.3 (Sahimi 1993). The Peclet number, the ratio of advection to diffusion transport, was 0.015 in this case. For $Pe < 0.3$, advection is so slow that diffusion controls dispersion almost completely. The effect of hydrodynamic dispersion is shown as approximately straight saturation contour lines of varying slopes in the lower half of the core plug, as shown in Figure 6-1a. Saturation data in the upper half of the core plug are affected by entrance effects of the short core plug at small Peclet numbers.

The solution to the 1D convection-dispersion PDE of displaced fluid content with a step boundary condition, such as the one applied in this experiment, is the summation of two terms including error functions of position and time (Orr 2005). The transition zone of such a front can be approximated by a first order polynomial that is the first term in the Taylor series expansion of the solution of the PDE. The dispersion coefficient can be calculated from the slope of these straight saturation lines. The result of such calculations will be presented in a future work. We should emphasize that data processing of this type requires quantitative saturation maps. The methodologies used in this research can uniquely measure fluid saturation with high accuracy in a wide variety of samples.

T_2-maps of the miscible flooding, Figure 6-2a-d, indicate a correlation between decane saturation and T_2 distribution. This correlation can be clearly seen in Figure 6-5. The nature of this correlation between decane saturation and T_2 can potentially demonstrate the interaction between decane, as the pore filling fluid, and pore surfaces.

At 9 MPa and 40 °C, the CO_2/decane mixture forms a single-phase fluid. Therefore, the wetted pore surface area S_p is expected to be constant and equal to the pore surface area $\hat{S}_p$. The molar density of decane in the bound layer ρ_s, however, is expected to change with saturation. If T_{2s} is constant, it is expected that $1/T_2$ will be linearly correlated with inverse saturation $1/S$,

$$\frac{1}{T_2} = \frac{\rho_S}{\rho_B}\left(\frac{\delta \hat{S}_p}{\tilde{V}_p T_{2S}}\right)\frac{1}{S}, \tag{6-6}$$

with a slope of $(\rho_s/\rho_B)\cdot\left(\delta\hat{S}_p/\tilde{V}_p T_{2s}\right)$, where $\tilde{V}_p$ is the pore volume, and ρ_B is the bulk molar density of decane. Equation (6-6) is derived in the current work assuming $\delta\hat{S}_p/\tilde{V}_p \ll 1$. A change in the slope of a $1/T_{2LM} - 1/S$ plot demonstrates a change in the interaction between pore-surface and decane molecules, if other parameters are constant. Bulk longitudinal relaxation rate measurements as a function of CO_2 concentration in water-saturated bead packs measured by Suekane et al. (2009) support this model. The correlation between $1/T_{2LM}$ and $1/S$ for the miscible flooding of decane with CO_2 in Berea is shown in Figure 6-9a, in which the average relaxation rate $1/T_{2LM}$ is shown as a function of decane saturation ranging from 1.00 to 0.05. The black solid line is a smoothing spline fitted to the averages of logarithmically binned data. Figure 6-9b shows the derivative

$$d(1/T_{2LM})/d(1/S) = (\rho_s/\rho_B)\cdot\left(\delta\hat{S}_p/\tilde{V}_p T_{2s}\right) \tag{6-7}$$

indicating a reduction in the molar density of decane in the bound layer ρ_s with decreasing decane saturation S. The slope of Figure 6-9a is directly proportional to (ρ_s/ρ_B), the ratio of molar densities of decane in the surface bound layer and bulk decane. The slope of the $1/T_{2LM} - 1/S$ plot, in contrast to a $T_{2LM} - S$ plot, conveniently shows the (ρ_s/ρ_B) change through its slope, because the second grouped term in the right-hand side of Equation (6-7), $\delta\hat{S}_p/\tilde{V}_p T_{2s}$, is expected to be constant.

T_{2s} is assumed not to change significantly as the mixture composition does not strongly affect surface relaxation mechanisms, including homonuclear dipole-dipole coupling,

cross-relaxation by other nuclear spins, relaxation by paramagnetic ions, and relaxation by free electrons (Kleinberg 1999). $\hat{S}_p$ and $\tilde{V}_p$ are physical properties of the rock and are considered constant. The bulk density of decane ρ_B is a function of temperature and pressure and can be assumed constant. Therefore, with $\delta\hat{S}_p/\tilde{V}_p T_{2s}$ being constant, the derivative $d(1/T_{2LM})/d(1/S)$ demonstrates the changes in the molar density of decane in the bound layer, as shown in Figure 6-9b. The uncertainty in the calculation of the derivative can be as high as 25%.

6.3.5 Immiscible CO_2 Flooding of Decane

Immiscible displacement, although phenomenologically different, bears some similarity to miscible flooding. The saturation of the wetting phase in immiscible displacement obeys a convection-diffusion equation. The dispersion coefficient of this equation is a function of the derivative of the capillary pressure with respect to the wetting phase saturation (Sahimi 1993).

Immiscible flooding showed a residual saturation profile in the core plug dominated by capillary-gravity equilibrium, as shown in Figure 6-1b. The flooded sections had an average residual decane saturation of 0.25, supposedly a mixture of the wetting fluid covering pore surfaces and fully saturated pores. The immiscible flooding experiment ended with the injection of CO_2 at high flow rate and high pressure, miscible with decane, through the core plug. Under these conditions the background signal was measured, which is shown as a black vertical line at day three in Figure 6-1b.

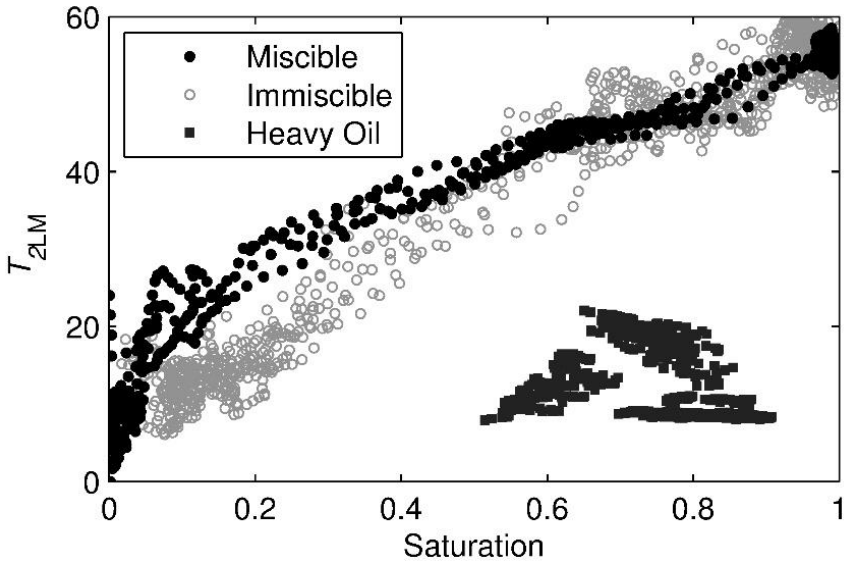

Figure 6-8 The $T_{2LM} - S$ cross plot for (●) miscible drainage of decane by CO_2, (○) immiscible drainage of decane by CO_2, and (■) displacement of heavy oil by CO_2. Saturation and logarithmic mean transverse magnetization T_{2LM} data from SE-SPI method were measured at all sections 1 mm thick along the axis of core plugs. This cross plot doesn't show much difference between the miscible and immiscible cases early in the flooding process. However, the slope and residual saturation of these two processes are different indicating a major difference between miscible and immiscible flooding. CO_2 flooding of heavy oil is shown as a triangle in the cross plot. Uncertainty in the immiscible flooding data is higher than that of the miscible case. This is the result of more noise in MRI measurements which propagates through T_{2LM} calculations.

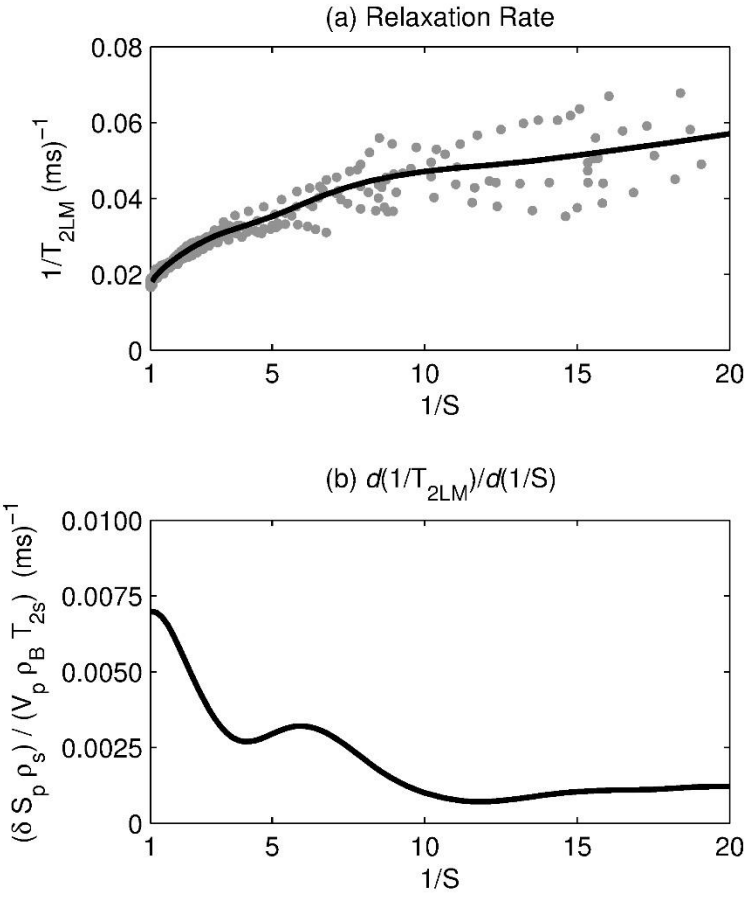

Figure 6-9 (a) $1/T_{2LM}$ versus $1/S$ for miscible CO_2 displacement of decane in Berea. $S - T_{2LM}$ pairs measured for each core plug pixel employing SE-SPI are shown as circles. A smoothing spline was fitted to the binned data points (solid line). The spline was employed for calculating the derivative $d(1/T_{2LM})/d(1/S) = (\rho_s/\rho_B) \cdot \left(\delta\hat{S}_p/\tilde{V}_p T_{2s}\right)$ (b). $d(1/T_{2LM})/d(1/S)$ is directly proportional to $\rho_s$and demonstrates changes in the density of decane molecules at the pore surface as a function of saturation.

Each image section consists of tens of thousands of pore bodies as 0.1 cm^3 of Berea sandstone contains approximately 10-20,000 pore bodies and pore throats (Patzek 2001). Immiscible displacement proceeds by step-wise invasion of the displacing fluid in quasi-static drainage mode. Pores drain in cascading events, draining multiple geometrically defined pore clusters in each step (Berg et al. 2013). This leaves some wetting fluid in the extreme corners and roughness of the pore surface as thin layers spanning many pores (Green and Willhite 1998; Berg et al. 2013). Such a process can be modeled with an ordinary percolation statistical model (Lenormand 1990). The capillary number, the ratio between viscous and capillary forces, represents the relative effect of capillarity. At the capillary number calculated for this experiment, 2.6×10^{-7}, the displacement follows a quasi-static drainage mode. The flow rate is so small that the interface between the displacing and displaced fluid advances in one pore cluster at a time (Sahimi 1993). The saturation distribution is profoundly affected by the capillary pressure in this drainage mode. The saturation distribution in the core plug at the end of such a process mimics the capillary pressure curve, which is an error function of the logarithm of position (Kosugi 1996). Figure 6-6b shows this effect as the capillary end effect after day two.

T_2-maps of the immiscible flooding, Figure 6-3a-d, indicate a correlation between decane saturation and T_2 distribution. This correlation is clearly observed in Figure 6-6. At 6 MPa and 40 °C, the CO_2/decane mixture forms two phases: a decane-rich liquid phase, and a CO_2-rich vapor phase. The decane-rich liquid phase preferentially wets the pore surface. We postulate that the wetted surface area S_p is constant during the immiscible CO_2

displacement of decane. However, the volume of the pore filling fluid V_p , in Equation (6-4), does change. V_p is linearly correlated with saturation, assuming a constant density of ^{1}H in the liquid phase: $V_p = S \times \tilde{V}_p$, where $\tilde{V}_p$ is the pore volume. This is a valid assumption, if pressure is constant along the core plug. In the immiscible displacement of decane by CO_2 in Berea, it is expected that $1/T_2$ is linearly correlated with $1/S$,

$$\frac{1}{T_2} = \frac{S_p}{\hat{S}_p}\left(\frac{\delta \hat{S}_p}{\tilde{V}_p T_{2s}}\right)\frac{1}{S}, \tag{6-8}$$

with a slope of $\left(S_p/\hat{S}_p\right) \cdot \left(\delta \hat{S}_p/\tilde{V}_p T_{2s}\right)$. Changes in the wetted surface area S_p can be calculated from the slope if T_{2s} and δ are constant. Any change in the derivative $d(1/T_{2LM})/d(1/S)$ in the immiscible flooding experiment is the result of changes in the surface area wetted by decane. T_{2s} and δ do not change with mixture composition and $\tilde{V}_p$ is a petrophysical property. The bound layer thickness δ is no more than 100 nm thick (Israelachvili 1991) and is expected to be one to two orders of magnitudes less than the wetting liquid thickness. Therefore, the $\delta \hat{S}_p/\tilde{V}_p T_{2s}$ term in Equation (6-8) is expected to be constant.

The correlation between $1/T_{2LM}$ and $1/S$ during immiscible flooding of decane by CO_2 is shown in Figure 6-10a, in which the relaxation rate, $1/T_{2LM}$, is shown as a function of decane saturation ranging from 1.00 to 0.10. The black solid line is a smoothing spline fitted on the averages of logarithmically binned data. Figure 6-10b shows the derivative

$$d(1/T_{2LM})/d(1/S) = \left(S_p/\hat{S}_p\right) \times \left(\delta\hat{S}_p/\tilde{V}_p T_{2s}\right) \quad (6\text{-}9)$$

indicating a reduction in the wetted surface area S_p with decreasing decane saturation below the residual decane saturation S_{or}. The derivative demonstrates a considerable change beyond the average residual decane saturation of 0.25. The cause of the change in the value of derivative within the 0.25-1.00 saturation range is unclear. Different processing methods, with and without smoothing, employing different fitting functions resulted in identical trends and similar quantitative results. The uncertainty in the T_{2LM} values is higher in immiscible flooding, because of greater noise that propagates through the T_2 inversion algorithm. The uncertainty in the derivative can be as high as 30%.

6.3.6 Extraction of Light Components from Heavy Oil

The transverse relaxation rate of heavy oil in Berea is expected to be dominated by heavy oil bulk relaxation time constant, $T_{2b} = 8$ ms. Assuming equal quantities of heavy oil available for surface relaxation and bulk relaxation, the average relaxation of heavy oil will be: $1/T_2 = 1/T_{2b} + 1/T_{2s}$. The relaxation rate of heavy oil is $1/T_{2b} = 0.13$ ms^{-1}. The surface relaxation is related to the pore size distribution of the Berea core plugs. Similar homogeneous Berea core plugs from the same slab were used in this research. Assuming a similar pore size distribution provides the same surface relaxation effect, the surface relaxation of heavy oil in Berea is approximately the same as that of decane in Berea, 0.02 ms^{-1}, or of the same order of magnitude. Then, $1/T_{2b}$ dominates the relaxation rate, $1/T_2$. Therefore, for the relaxation of heavy oil used in this study in Berea, $T_2 = T_{2b}$. In addition,

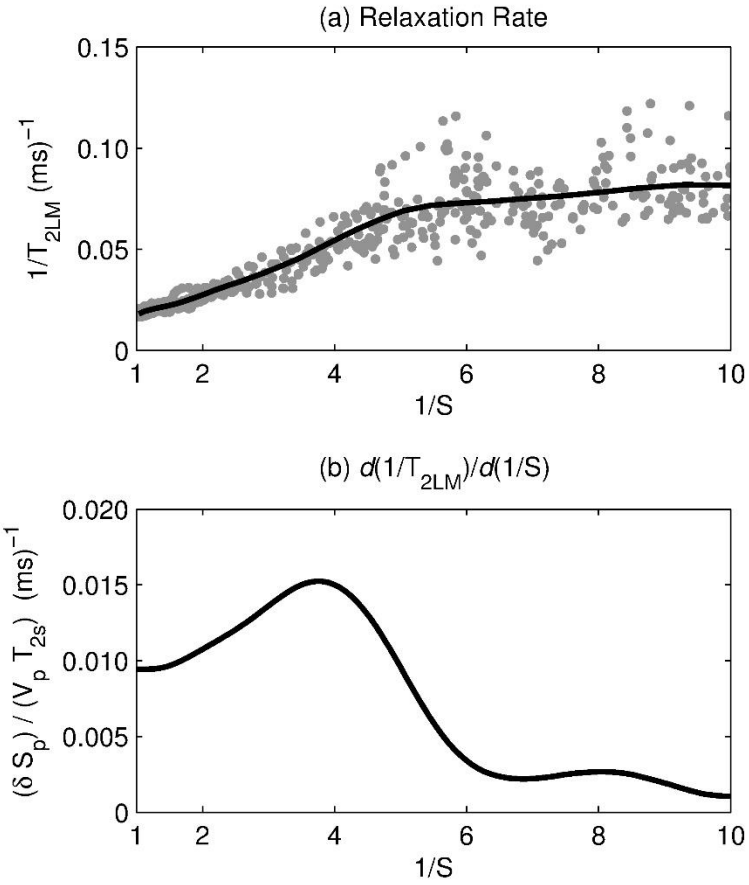

Figure 6-10 $1/T_{2LM}$ versus $1/S$ for immiscible CO_2 displacement of decane in Berea. $S - T_{2LM}$ pairs measured for each core plug pixel employing SE-SPI are shown as circles. The core plug had an average residual decane saturation of 0.25 ($1/S = 4$). A smoothing spline was fitted to the binned data points (solid line). The spline was employed for calculating the derivative $d(1/T_{2LM})/d(1/S) = \left(S_p/\hat{S}_p\right) \times \left(\delta\hat{S}_p/\tilde{V}_p T_{2s}\right)$ (b). $d(1/T_{2LM})/d(1/S)$ is directly proportional to S_p and demonstrates changes in the pore surface area wetted by decane as a function of saturation.

the injection of D_2O brine into Berea and subsequent heavy oil injection makes water the primary wetting phase, because Berea is a water wet rock type. Therefore, we expect even a smaller contribution from surface relaxation as stated above.

The exposure of heavy oil to CO_2 is expected to increase oil mobility which manifests as longer T_2 relaxation values (Yang et al. 2012). Figure 6-4 shows SE-SPI T_2-maps of the heavy oil CO_2 displacement experiment at different flooding times. First, the T_2 distribution of heavy oil shifted to longer values, as shown in Figure 6-4a-c. With time, however, T_2 shifted to shorter times, as shown in Figure 6-4d-f. It is well established that the transverse relaxation time distribution is correlated with hydrocarbon composition and properties (Hürlimann et al. 2009). Hydrocarbon viscosity is related to T_{2LM} (Hirasaki 2006) by

$$\frac{1}{T_{2LM}} = \frac{\eta^{0.9}}{1.2} \tag{6-10}$$

where η is the oil viscosity in mPa.s and T_{2LM} is in seconds. This correlation requires deoxygenated oils as oxygen alters the relaxation time constant of oils. Deoxygenation of oils (Mutina and Hürlimann 2005) involves repeated freeze-thaw cycles not followed in this work. The viscosity of the heavy oil sample predicted from T_{2LM} is not accurate as the deoxygenation procedure was not followed. However, it is expected that the viscosity is still correlated with T_{2LM}. The shift in T_2 distributions of the heavy oil to shorter times is ascribed to the dissolution of light components in the CO_2 phase and their extraction from

the liquid phase. At the end of the process, after six days of injecting CO_2 at 0.04 cm^3/min, the oil T_2 in the Berea core plug was reduced to approximately its initial value.

Figure 6-7 shows S and T_{2LM} calculated from the SE-SPI images as a function of position and time for CO_2 flooding of heavy oil. CO_2 displaced heavy oil and extracted its components from $S = 0.81$ to $S = 0.57$ by the end of the experiment. Figure 6-7 demonstrates that the injection of CO_2 into the D_2O brine and heavy oil saturated Berea core plug affects the viscosity of the heavy oil at all positions along the core plug. CO_2 is more likely to displace the well connected D_2O fluid system with a viscosity of 1.5 mPa.s rather than the heavy oil with a viscosity of 640 mPa.s. Increased CO_2-heavy oil contact within the core plug affected heavy oil mobility quite rapidly. T_{2LM} increased along the flow path after CO_2 entered the core plug. $1/T_{2LM} - 1/S$ plots, although removing the spatial information from the data, can clearly demonstrate the difference between the processes involved in the CO_2 displacement of heavy oil and decane, as shown in Figure 6-11. The triangle shape scatter plot of Figure 6-11 shows different stages of contact between CO_2 and the heavy oil. Different sections within the core plug show almost the same T_{2LM} with a scattered saturation before the CO_2 invasion of the core plug, as shown in Figure 6-11 marked by 'a'. This variation in saturation is because of capillary effects in the vertical core plug. CO_2 removed some heavy oil from the core plug by viscous force, from 'a' to 'b', and, at the same time, increased the mobility of the heavy oil by contacting it, as shown in Figure 6-11 marked by 'b'. Further CO_2 injection extracts the recoverable light components from the heavy oil phase and reduces the T_{2LM} and S, as shown in Figure

6-11 marked by ‘c’. These processes are also demonstrated in the $T_{2LM} - S$ plot of Figure 6-8.

The viscosity of the oil is inversely correlated with its T_{2LM}. Therefore, the viscosity of the heavy oil at the end of CO_2 flooding is expected to be close to its initial value or even higher, owing to the fact that light components in the heavy oil have been removed by mass transfer to the CO_2 phase. The diffusion of CO_2 in the heavy oil phase and the extraction or vaporization of light components from the heavy oil into the CO_2 phase are two distinct processes that take place at different rates. The rate of these two processes can be calculated from in-situ saturation and T_2 distribution data. The result of such calculations will be presented in a future work.

6.4 Conclusions

MRI provides a wealth of information on displacement mechanisms and in-situ pore level behavior. Similar information is difficult or impossible to achieve using other methods. In miscible and immiscible flooding experiments, CO_2 displaced decane and heavy oil from Berea sandstone core plugs and the processes were monitored by MRI methods. Hydrodynamic dispersion, almost completely controlled by diffusion, was the dominant displacement phenomenon in the miscible CO_2 injection in the decane-saturated Berea core plug. In immiscible CO_2 flooding of the decane-saturated Berea core plug, convection with a significant influence of capillary dispersion was the dominant displacement phenomenon. CO_2 flooding of the heavy-oil-saturated Berea core plug was dominated by three

mechanisms in different stages of the experiment: (a) a short-lived early period dominated by convection significantly influenced by viscous fingering, followed by (b) diffusion of CO_2 in the oil phase, and later (c) extraction of light components from the oil phase by CO_2.

$1/T_{2LM} - 1/S$ plots computed from SE-SPI images provided information about the mechanisms of the different displacement processes at the pore scale that are summarized as follows.

(1) The density of decane in the pore surface bound layer decreased during the miscible drainage of decane by CO_2.

(2) In immiscible displacement of decane by CO_2, the pore surface area wetted by decane monotonically decreased at saturations less than 0.25 (residual saturation). This behavior potentially demonstrates the development of a non-continuous wetting film on the pore surface.

(3) CO_2 flooding of heavy oil shows an initial increase in T_{2LM} caused by increased fluid mobility. Later, T_{2LM} decreased consistent with the extraction of light components from the heavy oil that enriched the displacing CO_2 phase.

These conclusions are consistent with theories of miscible and immiscible flow phenomena in porous rocks (Sahimi 1993; Green and Willhite 1998; Orr 2007). MRI methods used in

the current study demonstrate their potential in studying the mechanisms involved in processes significantly affected by changes in fluid properties and pore/fluid interaction.

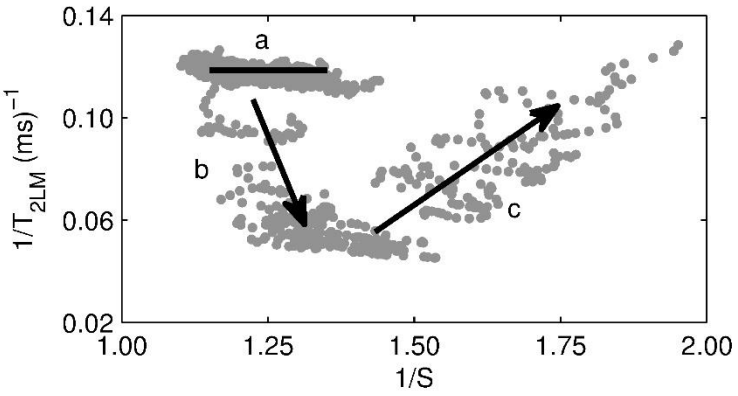

Figure 6-11 $1/T_{2LM}$ versus $1/S$ for CO_2 displacement of heavy oil in Berea. $T_{2LM} - S$ pairs measured for core plug pixels employing SE-SPI are shown as discrete data points. Initially, there was an inhomogeneous oil concentration with the same T_{2LM} along the core plug, due to capillary end effect, as shown in region 'a'. Oil T_{2LM} increased and oil saturation decreased with CO_2 entering the core plug, as shown in region 'b'. Oil T_{2LM} was then reduced and oil saturation was reduced further after a few days, as shown in region 'c'. The increase in T_{2LM}, in region 'b', is attributed to the increased mobility of heavy oil in contact with CO_2. The reduction in concentration and T_{2LM} of heavy crude oil, as shown in region 'c', is ascribed to the vaporization of light components from the heavy crude oil. The significant difference between this figure and Figure 6-9 and Figure 6-10 demonstrates the contrast between the mechanisms involved in the displacement of decane and heavy oil by CO_2, in the absence and presence of water phase, respectively.

This chapter is the first piece of research that systematically studied the effect of T_2 to interface fluid properties. The combination of high-quality experiments, richness in data, and derivation of mathematical equations for both miscible and immiscible cases makes the results of this work useful to both NMR logging interpretation and laboratory studies of fluids in porous media.

Chapters 5 and 6 demonstrate the richness information that MRI monitoring of core-flooding processes provide, on both pore and core-plug scales. In contrast to Chapters 4-6, the next chapter is a fundamental research on the MR relaxation in porous media. It was during the experimental research work of Chapters 4-6 that the author noticed the existence of small peaks in short relaxation time constants of the T_2 distributions in rocks and recognized that such features are the result of non-ground eigenvalues.

6.5 References

Afrough, A., Shakerian, M., Zamiri, M. S., MacMillan, B., Marica, F., Newling, B., Romero-Zerón, L., Balcom, B. J. 2017. Magnetic Resonance Imaging of High Pressure Carbon Dioxide Displacement: Fluid/Surface Interaction and Fluid Behavior. *SPE J.* 23 (3): 772-787. https://doi.org/10.2118/189458-PA.

Andrew, M., Bijeljic, B., Blunt, M. J. 2014. Pore-Scale Imaging of Trapped Supercritical Carbon Dioxide in Sandstones and Carbonates. *Int. J. Greenh. Gas Control* 22:1-14. http://dx.doi.org/10.1016/j.ijggc.2013.12.018.

Bagherzadeh, S. A., Moudrakovski, I. L., Ripmeester, J. A. et al. 2011. Magnetic Resonance Imaging of Gas Hydrate Formation in a Bed of Silica Sand Particles. *Energ. Fuel* 25 (7):3083-3092. http://dx.doi.org/10.1021/ef200399a.

Baldwin, B. A., King, R. L. 1998. Why Would an Oil Company Use MRI? In *Spatially Resolved Magnetic Resonance: Methods, Materials, Medicine, Biology, Rheology, Geology, Ecology, Hardware*, ed. Blümler, P., Blümich, B., Botto, R., and Fukushima,

E., Chap. 55, 575-601. Weinheim: Wiley-VCH Verlag GmbH. http://dx.doi.org/10.1002/9783527611843.ch55.

Bear, J. 1992. *Dynamics of Fluids in Porous Media*. New York: Dover Publications. PP439

Beckwith, R. 2011. Carbon Capture and Storage: A Mixed Review. *J. Pet. Technol.* 63 (5): 42-45. SPE-0511-0042-JPT. http://dx.doi.org/10.2118/0511-0042-JPT.

Berg, S., Oedai, S., Ott, H. 2013. Displacement and Mass Transfer between Saturated and Unsaturated CO_2-Brine Systems in Sandstone. *Int. J. Greenh. Gas Control* 12: 478-492. http://dx.doi.org/10.1016/j.ijggc.2011.04.005.

Berg, S., Ott, H., Klapp, S. A. et al. 2013. Real-Time 3D Imaging of Haines Jumps in Porous Media Flow. *P. Natl. Acad. Sci. USA* 110 (10): 3755-3759. http://dx.doi.org/10.1073/pnas.1221373110.

Brautaset, A., Ersland, G., Graue, A. et al. 2008. Using MRI to Study In-Situ Oil Recovery During CO_2 Injection in Carbonates. International Symposium of the Society of Core Analysts, Abu Dhabi, UAE, 29 October-2 November. SCA2008-41.

Brigham, W. E., 1974. Mixing Equations in Short Laboratory Cores. *SPE J.* 14(1):91-99. https://doi.org/10.2118/4256-PA.

Brownstein, K. R., Tarr, C. E. 1979. Importance of Classical Diffusion in NMR Studies of Water in Biological Cells. *Phys. Rev. A* 19 (6): 2446-2453. http://dx.doi.org/10.1103/PhysRevA.19.2446.

Coates, G. R., Xiao, L., and Prammer, M. G. 1999. *NMR Logging: Principles and Applications*. Houston: Halliburton Energy Services.

de Gennes, P. G. 1985. Wetting: statics and dynamics. *Rev. Mod. Phys.* 57 (3):827-863. http://dx.doi.org/10.1103/RevModPhys.57.827.

Dunn, K. -J. Bergman, D. J., LaTorraca, G. A. 2002. *Nuclear Magnetic Resonance: Petrophysical and Logging Applications*. Oxford: Elsevier Science, pp. 77.

Dullien, F. A. L. 1992. *Porous Media: Fluid Transport and Pore Structure*. 2nd Ed. San Diego: Academic Press.

Fischer, S., Zemke, K., Liebscher, A. et al. 2011. Petrophysical and Petrochemical Effects of Long-Term CO_2-Exposure Experiments on Brine-Saturated Reservoir Sandstone. *Energy Procedia* 4: 4487-4494. http://dx.doi.org/10.1016/j.egypro.2011.02.404.

Gao, S., House, W., Chapman, W. G. 2006. Detecting Gas Hydrate Behavior in Crude Oil using NMR. *J. Phys. Chem. B* 110 (13): 6549-6552. http://dx.doi.org/10.1021/jp055039a.

Gist, G. A., Thompson, A. H., Katz, A. J., Higgins, R. L. 1990. Hydrodynamic Dispersion and Pore Geometry in Consolidated Rock. *Phys. Fluids A-Fluid* 2 (9): 1533-1544. http://dx.doi.org/10.1063/1.857602.

Green, D. W., Willhite, G.P. 1998. *Enhanced Oil Recovery*. Richardson: Society of Petroleum Engineers. pp. 25.

Goodfield, M., Goodyear, S. G., Townsley, P. H. 2001. New Coreflood Interpretation Method Based on Direct Processing of In-situ Saturation Data. SPE Annual Technical Conference and Exhibition, New Orleans, Louisiana, 30 September-3 October. SPE-71490-MS. http://dx.doi.org/10.2118/71490-MS.

Han, H., Ouellette, M., MacMillan, B. et al. 2011. High Pressure Magnetic Resonance Imaging with Metallic Vessels. *J. Magn. Reson.* 213 (1): 90-97. http://dx.doi.org/10.1016/j.jmr.2011.09.001.

Hao, M., Song, Y., Su, B. et al. 2015. Diffusion of CO_2 in n-Hexadecane Determined from NMR Relaxometry Measurements. *Phys. Lett. A* 379 (18-19): 1197-1201. http://dx.doi.org/10.1016/j.physleta.2015.02.026.

Hirasaki, G. J. 2005. NMR Applications in Petroleum Reservoir Studies In *NMR Imaging in Chemical Engineering*, ed. Stapf, S., Han, S.-I., Chap. 3, 321-339. Weinheim: Wiley-VCH Verlag GmbH. http://dx.doi.org/10.1002/3527607560.ch3f.

Hoult, D. I., Richards, R. E. 1976. The Signal-to-Noise Ratio of the Nuclear Magnetic Resonance Experiment. *J. Magn. Reson.* 24 (1):71-85. http://dx.doi.org/10.1016/0022-2364(76)90233-X.

Hürlimann, M. D. 1998. Effective Gradients in Porous Media due to Susceptibility Differences. *J. Magn. Reson.* 131 (2): 232-240. http://dx.doi.org/10.1006/jmre.1998.1364.

Hürlimann, M. D., Freed, D. E., Zielinski, L. J. et al. 2009. Hydrocarbon Composition from NMR Diffusion and Relaxation Data. Petrophysics 50 (2) 116-129. SPWLA-1997-v38n2a1.

Israelachvili, J.N. 1991. *Intermolecular and Surface Forces*. Amsterdam: Academic Press. PP 123

Jiang, L., Liu, Y., Song, Y. et al. 2015. Application of X-Ray CT Investigation of CO_2–Brine Flow in Porous Media. *Exp. Fluids* 56 (5):91. http://dx.doi.org/10.1007/s00348-015-1959-x.

Kleinberg, R. L. 1999. Nuclear Magnetic Resonance. In *Methods in the Physics of Porous Media*, ed. Wong, P., Chap. 9, 337-385. San Diego: Academic Press. http://dx.doi.org/10.1016/S0076-695X(08)60420-2.

Kosugi, K. 1996. Lognormal Distribution Model for Unsaturated Soil Hydraulic Properties. *Water Resour. Res.* 32 (9): 2697-2703. http://dx.doi.org/10.1029/96WR01776.

Lenormand, R. 1990. Liquids in Porous Media. *J. Phys.-Condens. Mat.* 2: SA79-SA88. http://dx.doi.org/10.1088/0953-8984/2/S/008

Li, M., Xiao, D., Shakerian, M. et al. 2016. Magnetic Resonance Imaging of Core Flooding in a Metal Core Holder. International Symposium of the Society of Core Analysts, Snowmass, Colorado, 21-26 August. SCA2016-019.

Li, X., Fan, X. 2015. Effect of CO_2 on Contact Angle in Oil-Wet and Water-Wet Pores. *Int. J. Greenh. Gas Control* 36: 106-113. http://dx.doi.org/10.1016/j.ijggc.2015.02.017.

Liu, Y., Jiang, L., Tang, L. et al. 2015. Minimum Miscibility Pressure Estimation for a CO_2/n-Decane System in Porous Media by X-Ray CT. *Exp. Fluids* 56 (7):154. http://dx.doi.org/10.1007/s00348-015-2025-4.

Liu, Y., Zhao, Y., Zhao et al. 2011. Magnetic Resonance Imaging of CO_2 Miscible and Immiscible Displacement in Oil-Saturated Glass Beads Pack. *Magn. Reson. Imaging* 29 (9): 1110-1118. http://dx.doi.org/10.1016/j.mri.2011.05.009.

Måloy, K.J., Furuberg, L., Feder, J. et al. 1992. Dynamics of Slow Drainage in Porous Media. *Phys. Rev. Lett.* 68 (14): 2161-2164. https://doi.org/10.1103/PhysRevLett.68.2161.

Meiboom, S., Gill, D. 1958. Modified Spin-Echo Method for Measuring Nuclear Relaxation Times. *Rev. Sci. Instrum.* 29(8): 688-691. http://dx.doi.org/10.1063/1.1716296.

Mitchell, J., Chandrasekera, T. C., Holland, D. J. et al. 2013. Magnetic Resonance Imaging in Laboratory Petrophysical Core Analysis. *Phys. Rep.* 526 (3): 165-225. http://dx.doi.org/10.1016/j.physrep.2013.01.003.

Muir, C. E. and Balcom, B. J. 2013. A Comparison of Magnetic Resonance Imaging Methods for Fluid Content Imaging in Porous Media. *Magn. Reson. Chem.* 51 (6) 321-327. http://dx.doi.org/10.1002/mrc.3947.

Muir, C. E. and Balcom, B. J. 2012. Pure Phase Encode Magnetic Resonance Imaging of Fluids in Porous Media. In *Annual Reports on NMR Spectroscopy*, Vol. 77, ed. Webb, G.A., Chap. 2, 81-113.Burlington: Academic Press. http://dx.doi.org/10.1016/B978-0-12-397020-6.00002-7.

Mutina, A. R., Hürlimann, M. D. 2005. Effect of Oxygen on the NMR Relaxation Properties of Crude Oils. *Appl. Magn. Reson.* 29 (3): 503-513. http://dx.doi.org/10.1007/BF03167180.

Nakatsuka, Y., Xue, Z., Garcia, H. et al. 2010. Experimental Study on CO_2 Monitoring and Quantification of Stored CO_2 in Saline Formations using Resistivity Measurements. *Int. J. Greenh. Gas Control* 4 (2): 209-216. http://dx.doi.org/10.1016/j.ijggc.2010.01.001.

Ouellette, M., Li, M., Liao, G. et al. 2016. Rock Core Analysis: Metallic Core Holders for Magnetic Resonance Imaging Under Reservoir Conditions. In *Mobile NMR and MRI - Developments and Applications*, ed. Johns, M. L., Fridjonsson, E. O., Vogt, S. J., Haber, A., Chap. 10, 290-309. Cambridge: Royal Society of Chemistry. http://dx.doi.org/10.1039/9781782628095-00290.

Orr, F. M. Jr. 2007. *Theory of Gas Injection Processes*. Holte: Tie-Line Publications. pp. 15, 76.

Orr, F. M. Jr. 2009. Onshore Geologic Storage of CO_2. *Science* 325 (5948): 1656-1658. http://dx.doi.org/10.1126/science.1175677.

Patzek, T. W. 2001. Verification of a Complete Pore Network Simulator of Drainage and Imbibition. *SPE J.* 6 (2): 144-156. SPE-71310-PA. http://dx.doi.org/10.2118/71310-PA.

Sahimi, M. 1993. Flow Phenomena in Rocks: From Continuum Models to Fractals, Percolation, Cellular Automata, and Simulated Annealing. *Rev. Mod. Phys.* 65 (4):1393-1545. http://dx.doi.org/10.1103/RevModPhys.65.1393.

Shakerian, M., Marica, F., Afrough, A., Goora, F. G., Li, M., Vashaee, S., Balcom, B. J. 2017. A High-Pressure Metallic Core Holder for Magnetic Resonance Based on Hastelloy-C. Review of Scientific Instruments 88 (12): 123703. https://doi.org/10.1063/1.5013031.

Song, Y., Jiang, L., Liu, Y. et al. 2012. An Experimental Study on CO_2/Water Displacement in Porous Media using High-Resolution Magnetic Resonance Imaging. *Int. J. Greenh. Gas Control* 10: 501-509. http://dx.doi.org/10.1016/j.ijggc.2012.07.017.

Song, Y.C., Zhu, N.J., Liu, Y. et al. 2011. Magnetic Resonance Imaging Study on the Miscibility of a CO_2/n-Decane System. *Chinese Phys. Lett.* 28 (9): 096401-1-14. http://dx.doi.org/10.1088/0256-307X/28/9/096401.

Song, Y., Zhu, N., Zhao, Y. et al. 2013. Magnetic Resonance Imaging Study on Near Miscible Supercritical CO_2 Flooding in Porous Media. *Phys. Fluids* 25 (5): 053301. http://dx.doi.org/ 10.1063/1.4803663.

Song, Y., Jiang, L., Liu, Y. et al. 2014. Study of the Fluid Flow Characteristics in a Porous Medium for CO_2 Geological Storage using MRI. *Magn. Reson. Imaging* 32 (5): 574-584. http://dx.doi.org/10.1016/j.mri.2014.01.021.

Suekane, T., Soukawa, S., Iwatani, S. et al. 2005. Behavior of Supercritical CO_2 Injected into Porous Media Containing Water. *Energy* 30 (11-12): 2370-2382. http://dx.doi.org/10.1016/j.energy.2003.10.026.

Suekane, T., Ishii, T., Tsushima, S. et al. 2006. Migration of CO_2 in Porous Media Filled with Water. *J. Therm. Sci. Tech. Jpn.* 1 (1): 1-11. http://dx.doi.org/10.1299/jtst.1.1.

Suekane, T., Furukawa, N., Tsushima, S. et al. 2009. Application of MRI in the Measurement of Two-Phase Flow of Supercritical CO_2 and Water in Porous Rocks. *J. Por. Media* 12 (2): 143-154. http://dx.doi.org/10.1615/JPorMedia.v12.i2.40.

Taylor, B. N., Kuyatt, C. E. 1994. *NIST Technical Note 1297: Guidelines for Evaluating and Expressing the Uncertainty of NIST Measurement Results*. Gaithersburg: National Institute of Standards and Technology. pp. 3.

Vashaee, S., Goora, F., Britton, M. M. et al. 2015. Mapping B_1-Induced Eddy Current Effects Near Metallic Structures in MR Images: A Comparison of Simulation and Experiment. *J. Magn. Reson.* 250: 17-24. http://dx.doi.org/10.1016/j.jmr.2014.10.016.

Vinegar, H. J., Wellington, S.L. 1987. Tomographic Imaging of Three-Phase Flow Experiments. *Rev. Sci. Instrum.* 58 (1): 96-107. http://dx.doi.org/10.1063/1.1139522.

Vogt, S. J., Shaw, C. A., Maneval, J. E. et al. 2014. Magnetic Resonance Measurements of Flow-Path Enhancement during Supercritical CO_2 Injection in Sandstone and Carbonate Rock Cores. *J. Petrol. Sci. Eng.* 122: 507-514. http://dx.doi.org/10.1016/j.petrol.2014.08.013.

Xiao, D., Balcom, B. J. 2015. π Echo-Planar Imaging with Concomitant Field Compensation for Porous Media MRI. *J. Magn. Reson.* 260: 38-45. http://dx.doi.org/10.1016/j.jmr.2015.08.023.

Yang, Z., Li, M., Peng, B. et al. 2012. Dispersion Property of CO_2 in Oil. 1. Volume Expansion of CO_2 + Alkane at near Critical and Supercritical Condition of CO_2. *J. Chem. Eng. Data* 57 (3):882-889. http://dx.doi.org/10.1021/je201114g.

Yang, Z. Hirasaki, G. J., Appel, M. et al. 2012. Viscosity Evaluation for NMR Well Logging of Live Heavy Oils. *Petrophysics* 53 (1) 22-37. SPWLA-2012-v53n1a2.

Zhao, Y., Song, Y., Liu, Y. et al. 2011. Visualization and Measurement of CO_2 Flooding in Porous Media Using MRI. *Ind. Eng. Chem. Res.* 50 (8): 4707-4715. http://dx.doi.org/10.1021/ie1013019.

Zhao, Y., Chen, J., Yang, M. et al. 2016. A Rapid Method for the Measurement and Estimation of CO_2 Diffusivity in Liquid Hydrocarbon-Saturated Porous Media using MRI. *Magn. Reson. Imaging* 34 (4): 437-441. http://dx.doi.org/10.1016/j.mri.2015.12.024.

Zhao, Y., Song, Y., Liu, Y. et al. 2011. Visualization of CO_2 and Oil Immiscible and Miscible Flow Processes in Porous Media using NMR Micro-Imaging. *Pet. Sci.* 8 (2): 183-193. http://dx.doi.org/10.1007/s12182-011-0133-1.

Chapter 7 – Non-Ground Eigenstates in Magnetic Resonance Relaxation of Porous Media: Absolute Measurement of Pore Size[4]

Geometric and topologic properties of porous materials have an immense effect on their macroscopic properties. Topologic properties describe pore connectivity and affect many rock properties such as tortuosity and dispersion coefficient and may be investigated using MR propagator and time-dependent diffusion methods. Geometric properties of porous media describe size and characterize the dominant pore size or investigate bimodal versus unimodal pore size distributions. This chapter is focused on describing geometric features of pore space in rocks.

The pore size distribution of Berea sandstones is unimodal and almost log-normal. Assuming a fast-exchange regime for relaxation, where there is a one-to-one correlation between the T_2 distribution and pore size, the T_2 distribution of Berea is supposed to be unimodal as well. However, in the measurements of the previous chapters, the author always observed a T_2 mode of smaller magnitude in the range of 0.5-20 ms in addition to the dominant peak of several hundred milliseconds. Investigating the reason behind this

[4] Largely based on a paper accepted for publication in the journal Physical Review Applied: Afrough, A., Vashaee, S., Romero-Zeron, L., Balcom, B. J. 2019. Nonground Eigenstates in Magnetic Resonance of Porous Media – Absolute Measurement of Pore Size. *Phys. Rev. Appl.*

bimodal distribution lead to the finding that non-ground eigenstates of the magnetization evolution equation contribute to the relaxation process.

Magnetization evolution due to translational motion of spins in magnetic fields is governed by the Bloch-Torrey equations. In confined geometries, magnetization of such systems is often expressed as a series of eigenstates, the eigenvalues of which are related to the characteristic confinement length. In this work, we highlight the importance of non-ground eigenvalues and their contribution to the relaxation of initially homogeneous magnetization by longitudinal and transverse ^{1}H relaxation processes in porous materials. We show that a simple magnetic resonance relaxation measurement can reliably characterize confinement size in fluid occupied porous materials. Pore sizes calculated from the eigenvalues are shown to agree with independent X-ray microtomography and electron microscopy measurements in rock samples.

7.1 Introduction

Confined fluids are ubiquitous in nature and in technological materials. Water in cytosol, geological formations, soil, cement, and wood are but a few examples. Diffusion of spins in porous materials, with an eigenfunction expansion and diffusion propagator, provides information on the surface-to-volume ratio (Seevers 1966), pore size (Song 2000; Song, Ryu, and Sen 2000), periodicity (Callaghan et al. 1991; Callaghan et al. 1992), and length scales (Song, Ryu, and Sen 2000) of fluid confinements. The evolution of magnetization

$\boldsymbol{M}(\boldsymbol{r}, t)$ in a fluid with scalar self-diffusivity D is governed by the Bloch-Torrey equations (Torrey 1956):

$$\left(\frac{\partial}{\partial t} - D\nabla^2 + \frac{1}{T_{2b}}\right) M_+(\boldsymbol{r}, t) = 0 \tag{7-1}$$

in the transverse plane, where $M_+ = M_x + iM_y$, and

$$\left(\frac{\partial}{\partial t} - D\nabla^2 + \frac{1}{T_{1b}}\right) M_z(\boldsymbol{r}, t) = \frac{M_0}{T_{1b}} \tag{7-2}$$

in the direction of the static magnetic field. In the above equations, M_0 is the equilibrium magnetization of confined fluid with bulk longitudinal and transverse relaxation time constants T_{1b} and T_{2b}, respectively. T_1 and T_2 are the exponential decay constants of M_z and M_+ to M_0 and 0, respectively.

Due to enhanced magnetization relaxation at wetted surfaces by homonuclear dipole-dipole coupling, cross-relaxation by other nuclear spins, relaxation by free electrons and paramagnetic ions (Kleinberg 1999), Equations (7-1) and (7-2) are subject to Fourier boundary conditions

$$(D\hat{n} \cdot \nabla + \rho_2)\, M_+(\boldsymbol{r}, t) = 0, \tag{7-3}$$

and

$$(D\hat{n} \cdot \nabla + \rho_1)\, M_z(\boldsymbol{r}, t) = 0, \tag{7-4}$$

where ρ_1 and ρ_2 are longitudinal and transverse surface relaxivities, respectively. In general, self diffusivity will be a tensor and ρ_1 and ρ_2 may be heterogenous; however, they are treated as constant scalars here.

Simple magnetic resonance experiments in porous media typically commence with a homogeneous magnetization such as $M_z(\boldsymbol{r},t) = -M_0$ or $M_+(\boldsymbol{r},t) = M_0$. Previous attempts to extract the system geometry and parameters of magnetic resonance relaxation in porous media from Equations (7-1) and (7-2), largely the work of Y. -Q. Song and coworkers (Song 2000; Song, Ryu, and Sen 2000), have been focused on creating an inhomogeneous magnetization by employing internal magnetic field gradients to significantly accentuate the non-ground eigenstates. Recent efforts (Song, Zielinski, and Ryu 2008; Song et al. 2014; Johnson and Schwartz 2014) have been directed at diffusive coupling between different environments and provided compelling evidence (for example see Song et al. 2014, Fig. 1) that non-ground eigenstates contribute to 1D and 2D magnetic resonance relaxation data. Other researchers (Keating 2014; Müller-Petke et al. 2015; Costabel et al. 2018) have also recognized the contribution of non-ground eigenvalues to magnetic resonance relaxation in porous media. However, these researchers have not fully explored the opportunities this phenomenon provides; for example, in characterizing complex pore geometries in natural samples.

The objective of this letter is to clearly demonstrate that non-ground eigenstates contribute to longitudinal and transverse ^{1}H magnetic resonance relaxation measurements with

homogeneous magnetization in porous materials. We also show for the first time that a straightforward 2D relaxation measurement of T_1 and T_2 may be processed to yield an absolute confinement size. It is shown in this work that while the ground eigenstate dominates the diffusion of spins, it is perfectly feasible to observe non-ground eigenstates with a much-reduced intensity; the first, and in some cases even the second, non-ground eigenvalue may be observed in relaxation data. The distinctive pattern of such eigenvalues makes it possible to recognize them in porous materials, even with multiple pore sizes.

The existence of non-ground eigenstates in magnetic resonance measurements of homogeneous magnetization permits the design of new porous media measurement methods. These ideas will also permit reprocessing of a very large body of extant magnetic resonance measurements.

The importance of non-ground eigenstates is demonstrated through two examples using the $T_1 - T_2$ relaxation correlation method. Two-dimensional magnetic resonance relaxation methods dramatically improved our understanding of complex diffusion dynamics and exchange in porous media. The $T_1 - T_2$ magnetic resonance relaxation correlation experiment (Lee et al. 1993; and Song et al. 2002) provides rich information on pore fluid dynamics. The $T_1 - T_2$ method is analyzed by two-dimensional multi-exponential analysis (Callaghan et al. 2007) and can simultaneously characterize multiple eigenvalues of the system. Similar ideas may also be applied to 1D relaxation data.

7.2 Methods and Materials

Radiofrequency (RF) pulses applied at the Larmor frequency $f = \frac{\gamma}{2\pi} B_0$ of ^{1}H rotates the sample magnetization vector into the transverse plane where it may be observed by inducing a voltage in the probe. The $T_1 - T_2$ method is composed of a T_1 encoding segment and a T_2 encoding segment;

$$\underbrace{\left[\pi - \tau_1 - \frac{\pi}{2}\right]}_{T_1 \text{ encoding}} \underbrace{[-(\tau_i - \pi - \tau_i)_N]}_{T_2 \text{ encoding}}. \tag{7-5}$$

The T_1 encoding commences with a 180° pulse followed by a waiting period τ_1 and a 90° pulse. T_2 information is imparted by the second segment with 180° pulses, with a time spacing of $2\tau_i$, and a phase shift of 90° compared to other rf pulses. Spin echoes form between refocusing 180° pulses in the second segment at $\tau_2 = 2k\tau_i$ with $1 < k \leq N$, where τ_2 is time beginning in the second segment.

By varying the τ_1 encoding period *P* times and keeping τ_i and *N* constant, the measurement of Equation (7-5) acquires time-domain relaxation correlation information as a $P \times N$ matrix $m_+(\tau_1, \tau_2)$ where only spin echoes are acquired by the rf coil. The magnetization m_+ acquired by the RF coil is equal to

$$m_+(\tau_1, \tau_2) = \int_{\boldsymbol{r}} M_+(\boldsymbol{r}, \tau_1, \tau_2)\, d\boldsymbol{r}, \tag{7-6}$$

$$= \sum_{q=0}^{\infty} \sum_{p=0}^{\infty} I\left(T_{1,p}, T_{2,q}\right) e^{-\tau_1/T_{1,p}} e^{-\tau_2/T_{2,q}},$$

where the deviation of signal from equilibrium is normalized in the longitudinal direction. An regularized inverse two-dimensional Fredholm integral of the first kind transforms the measured signal $m_+(\tau_1, \tau_2)$ into a 2D relaxation correlation function $I(T_{1,p}, T_{2,q})$ from which eigenvalues of magnetic resonance relaxation may be identified (Venkataramanan, Song, and Hürlimann 2002). The inversion algorithm of Venkataramanan, Song, and Hürlimann (2002) was employed in this work. Increasing the regularization parameter α penalizes the complexity of the solution; therefore, large α leads to smooth solutions whereas small α leads to a discretized result (Venkataramanan, Song, and Hürlimann 2002). Equation (7-6) assumes the rf coil is uniformly sensitive within the sample space.

Brownstein-Tarr numbers

$$\mathrm{BT}_i = \frac{\rho_i l}{D} \tag{7-7}$$

represent the ratio of magnetization relaxation rate at domain boundaries to the rate of mass diffusivity in a confined geometry with characteristic length l. Equation (7-7) in magnetic resonance relaxation of porous materials is analogous to the Damköhler number of the second kind in chemical reaction engineering that describes the effect of surface reaction kinetics on the overall diffusion-reaction process (Bird, Stewart, and Lightfoot, 2002, p. 551). i equals 1 or 2 for longitudinal and transverse relaxation, respectively. ρ_i is analogous to the surface reactivity and l is analogous to the diffusion length in chemical reaction engineering. BT_i set the diffusion or surface relaxation dependence of relaxation time

constants represented in $I(T_{1,p}, T_{2,q})$. In simple geometries, and for arbitrary BT_i values, the eigenvalues of magnetization evolution in a confined environment are

$$T_{i,n} = \frac{l^2}{4D\,\xi_{n,i}^2}, \tag{7-8}$$

where $\xi_{n,i}$ are functions of confinement geometry, diffusion coefficient, eigenvalue number n, and BT_i. In a planar pore geometry (Brownstein and Tarr 1979), $\xi_{n,i}$ are the positive roots of

$$2\xi_{n,i} \tan \xi_{n,i} = \mathrm{BT}_i. \tag{7-9}$$

Equations (7-7) to (7-9), adopted from the work of Brownstein and Tarr(1979), are valid for planar geometries for both ground $n = 0$ and non-ground $n > 0$ eigenvalues and for longitudinal $i = 1$ and transverse $i = 2$ relaxation processes. A correct combination of pore size l, longitudinal surface relaxivity ρ_1, and transverse surface relaxivity ρ_2 leads to a cluster of eigenvalue peaks that, through the Brownstein-Tarr theory, matches experimental peak locations in $T_1 - T_2$ experiments. At $\mathrm{BT}_i \to 0$ or $\mathrm{BT}_i \to \infty$, the ratio of eigenvalues of the diffusion-relaxation PDEs is simplified. However, complete numerical solution of Equations (7-7) to (7-9) should be used for predicting pore size due to their non-linearity.

In natural porous media, pore size is a distribution and not a single number. It is common practice in applied science and engineering however not to use the distributions of pore

size, but rather a parameter describing its central tendency. Once the mean pore size is determined, the data can likely be further processed to yield the standard deviation of pore size. The effect of pore shape does not significantly affect eigenvalues, and their intensities, of the magnetic resonance relaxation in porous media; this is especially true for $BT_i \ll 100$ (Brownstein and Tarr, 1979, Figure 1 and 2). Diffusion-relaxation in porous media is usually in the intermediate-diffusion region, where $1 < BT_i < 10$ and the effect of pore shape is not significant.

Two geological samples, Berea sandstone and Indiana limestone, with different pore geometries and constitutive minerals demonstrate the distinctive pattern of eigenvalues in simple longitudinal and transverse ^{1}H magnetic resonance relaxation measurements. We show that simple magnetic resonance relaxation measurements can measure the absolute value of the confinement size. The new confinement size measurement method was verified in three glass bead packs of different, but uniform, bead size (results not reported). In natural porous materials, the new method predicted correct values of pore size compared to ground truth measurements of SEM microscopy and X-ray CT imaging, even in the carbonate sample with a bimodal pore size distribution.

The Berea sample used in this study was an Upper Devonian sandstone from the Kipton formation, a grain-supported rock with quartz, feldspar, and micaceous clay minerals that has a porosity of 0.20. The pore size mode from microscopy was 26 μm with a pore size distribution that was log-normal.

The Indiana limestone sample has a grain-dominated fabric, made up of fossil fragments and oolites, with calcite cement. Indiana limestone features small calcite crystals lining the pore surface and intraparticle porosity in some grains. The limestone sample features a bimodal pore size distribution in backscattered electron microscopy images with a porosity of 0.15. The large and small pore modes are 50 μm and 10.1 μm, respectively; both from electron microscopy.

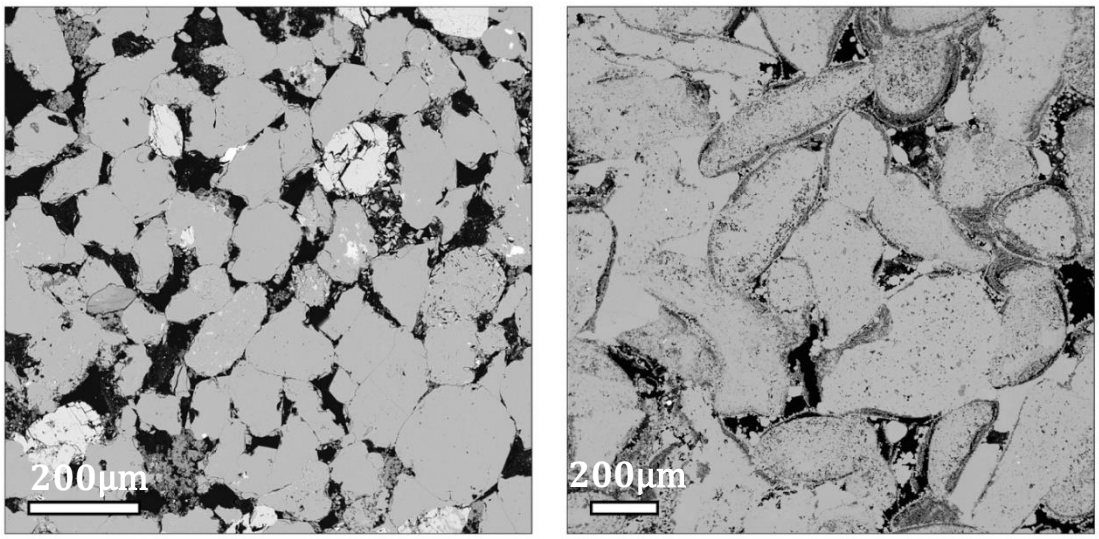

Figure 7-1 Backscattered electron scanning microscopy images of resin-impregnated Berea sandstone (left) and Indiana limestone (right) with polished surfaces. Resin-filled pore space is black; in the sandstone sample, quartz is medium gray, feldspar is light gray, and clay is dark gray. Virtually all the limestone is composed of calcite.

$T_1 - T_2$ measurements were performed with a B_0 static magnetic field of 0.05 T and 90° RF pulse lengths of 27 μs. Measurements were undertaken at ambient temperature of 24 °C. τ_1 was varied logarithmically $P = 56$ times, in the range of 0.1 ms to 15 s, and $N = 8125$ echoes were acquired with $\tau_i = 125$ μs or 300 μs. Each measurement was repeated four times for signal averaging and phase cycling with a repetition delay of 20 s. The measurement time for sandstone and limestone samples was 106 minutes and 156 minutes. The inverse integral transform method of (Venkataramanan, Song, and Hürlimann 2002) converted $m_+(\tau_1, \tau_2)$ to $I(T_{1,p}, T_{2,q})$ with $T_{i,p}$ in the range of 1 μs to 10 s in 512 logarithmic steps. Logarithmic variation of the regularization parameter from 100000 down to 0.01 reduced blurring in $I(T_{1,p}, T_{2,q})$ while maintaining the main features of $I(T_{1,p}, T_{2,q})$. The regularization parameter was not reduced beyond 0.01 for normalized m_+ matrices. The signal-to-noise ratio (SNR) of $m_+(\tau_1, \tau_2)$ was 168 and 123 for the Berea sandstone and Indiana limestone samples. Two-dimensional microscopy or 3D microtomography images were corrected by a median filter, binarized with adaptive thresholding (Bradley and Roth 2007) and reduced to skeletons (Lee, Kashyap, and Chu 1994). The value of the distance transform at each skeleton voxel was regarded as its respective pore radius. After binning, pore size probabilities were corrected according to their volumetric contribution.

7.3 Results and Discussion

The regularization parameter α employed in the inverse Fredholm integral transformation of the 2D relaxation correlation function $I(T_{1,p}, T_{2,q})$ can cause significant blurring of eigenvalues. However, a proper choice of the regularization parameter will demonstrate multi-modal features of $I(T_{1,p}, T_{2,q})$. Such 2D relaxation correlation functions for Berea sandstone and Indiana limestone at $B_0 = 0.05\,\mathrm{T}$ are shown in Figure 7-2. The regularization parameter for the multiexponential analysis of relaxation measurements were varied over seven orders of magnitude, with three examples shown in Figure 7-2. Eigenvalues of magnetization relaxation are labeled as Epq; where E determines the environment, and p and q are eigenstate numbers respectively for $T_{1,p}$ and $T_{2,q}$; Ppq represents water in pores of Berea sandstone, and Lpq and Spq represent water in large and small pores of Indiana limestone, respectively. Only the gross features of $I(T_{1,p}, T_{2,q})$ are observed with large regularization parameters. However, with a decrease in the regularization parameter, low-intensity non-ground eigenvalues of the diffusion-relaxation system, such as $P11$, $P22$, $L11$, and $S11$ emerge. To the best of our knowledge, this is the first attempt to systematically examine the variation of the regularization term to aid interpretation in magnetic resonance relaxation analysis. $N0q$ are diffusion-relaxation eigenvalues related to ^{1}H that do not experience the effect of pore walls and demonstrate bulk-like behavior in the T_1 domain.

Pearling or peak splitting is another important feature of variation of the regularization parameter in Figure 7-2. This is a common feature of algorithms employed in multiexponential analysis (Borgia, Brown, and Fantazzini, 1998); in such cases a single broad peak may break into smaller peaks, as observed in the case of $P00$ at $\alpha = 0.1$ for the Berea sandstone in Figure 7-2. Pearling does not affect the detection of ground and non-ground eigenvalues. It only affects the ground eigenvalue peak at small regularization parameters. The T_1, T_2, and intensity of the ground eigenvalue peak are detected at a large regularization parameter, for example at $\alpha = 1000$ in Figure 7-2. Even at small regularization parameters, pearling does not change the position of the peak.

Peaks of small amplitude that sometimes appear in erroneous positions in $T_1 - T_2$ data are different from pearling effects. However, they do not affect our analysis. They may be caused by SNR problems. In laboratory measurements where SNR is usually greater than 100, random peaks rarely appear, and they have very low intensities. The intensity of non-ground eigenvalues is greater than any possible random peaks at SNR > 100. Therefore, at least the first non-ground eigenvalue will not be buried in noise. The $I(T_{1,p}, T_{2,q})$ data, in Figure 7-2, are shown in $\log_{10}$-scale of intensity and the range of -4 and -2 for two main reasons: (a) filtering any insignificant low-intensity peaks with $\log_{10} I(T_{1,p}, T_{2,q}) < -4$, while at the same time (b) enhancing the visibility of low-intensity features by using a logarithmic intensity scale.

The procedure for the detection of ground and non-ground eigenvalues begins as follows. For normalized time-domain data, the 2D inversion method of Venkataramanan, Song, and Hürlimann (2002) with a regularization parameter of $\alpha = 1000$ provides sufficient smoothing to only show ground eigenvalues. At $\alpha = 1000$, if there is only one peak, like the Berea sandstone shown in Figure 7-2, the pore size distribution is unimodal. If two peaks exist at $\alpha = 1000$, the pore size distribution is bimodal and the ratio between the integral intensity of peaks is the ratio between their volumetric contribution to porosity. This is the case for the Indiana limestone sample shown in Figure 7-2.

The Brownstein-Tarr theory provides guidelines to distinguish non-ground eigenvalue peaks relative to the ground peak. A correct combination of l, ρ_1, and ρ_2 leads to a cluster of peaks that, through the Brownstein-Tarr theory, matches experimental peak locations in $T_1 - T_2$ experiments. At small regularization parameters, such as that of $\alpha = 0.1$, non-ground eigenvalues emerge as peaks with shorter characteristic times and smaller intensities relative to the ground eigenvalues. The characteristic time of the first non-ground eigenvalue is approximately 0.1 of that of the ground eigenvalue and its intensity is $2 - 10\%$ of that of the ground eigenvalue. The non-ground eigenvalues should also meet the condition of $T_2 \leq T_1$ and usually fall on or close to the linear diagonal line of the $T_1 - T_2$ correlation plot. These guidelines aid selection of a physically sensible peak as the non-ground eigenvalue to be tested with an optimization algorithm based on the Brownstein-Tarr theory. If experimental peaks are not chosen correctly, theory does not match with experimental results and one would know that the chosen non-ground eigenvalue peak is

not detected correctly. This process can be repeated until a cluster of eigenvalues that satisfactorily matches theory is found.

A direct search optimization method (Kolda, Lewis, and Torczon, 2003) varied $\log_{10} l/\mu\text{m}$, $\log_{10} \rho_1/(\mu\text{m}/s)$, and $\log_{10} \rho_2/(\mu\text{m}/s)$ and solved Equations (7-7) to (7-9), for the planar geometry, to match the time constants of eigenvalues detected in $I(T_{1,p}, T_{2,q})$. Input parameters were all constrained in the range of 10^{-2} to 10^{-8} and had starting values of 10^{-6}, 10^{-4}, and 10^{-4}. Eigenvalues calculated from Equation (7-9) were corrected for bulk relaxation of two mass-percent NaCl solution at $B_0 = 0.02$ T, $T_{1b} = 3.07$ s and $T_{2b} = 2.80$ s. Within the objective function of the optimization method, the roots of $x \cdot \tan x - \text{BT}_i$ were computed employing a combination of bisection, secant, and inverse quadratic interpolation methods in the ranges of $(0, \pi/2 - \varepsilon)$, $(\pi, 3\pi/2 - \varepsilon)$, and $(2\pi, 5\pi/2 - \varepsilon)$ respectively for the ground, the first non-ground, and the second non-ground eigenvalues with $\varepsilon = 1 \times 10^{-16}$.

The optimization method correctly matched the measured eigenvalues with liberal constraints for l, ρ_1, and ρ_2. For Berea sandstone, this work predicted a 22.1 μm pore size; whereas the pore size from scanning electron microscopy and X-ray microtomography had modes of 26 μm and 39 μm, respectively. Berea sandstone had estimated surface relaxivity constants of $\rho_1 = 138\,\mu\text{m/s}$ and $\rho_2 = 237\,\mu\text{m/s}$. The predicted pore size agrees with previously published results for surface-area-to-volume ratio of Berea sandstone (Hürlimann et al. 1994). Surface relaxivities of Berea sandstone calculated in this work are

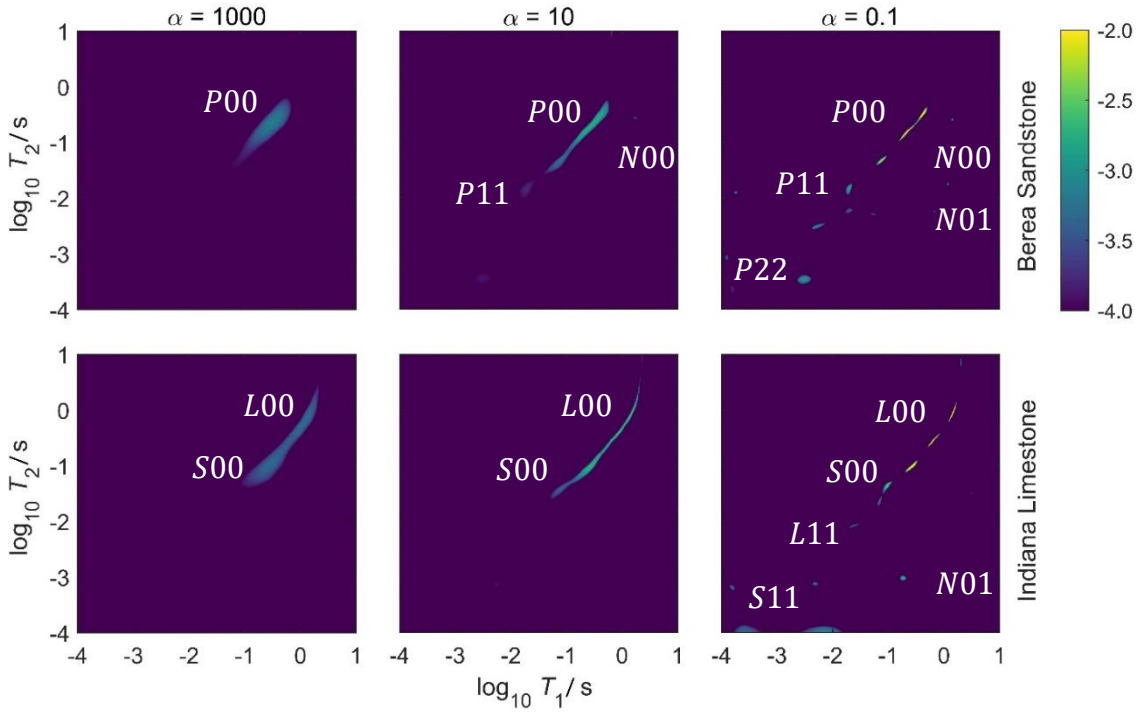

Figure 7-2 Two-dimensional relaxation correlation functions $I(T_{1,p}, T_{2,q})$ for brine-saturated Berea sandstone (top) and Indiana limestone (bottom) at $B_0 = 0.05$ T and regularization parameters of $\alpha = 1000$, 10, and 0.1. Intensity range of 10^{-4} to 10^{-2} is mapped to purple (black) to yellow (white), respectively, using a logarithmic scale to reveal small eigenvalues. Only ground eigenvalues are visible at $\alpha = 1000$. Non-ground eigenvalues emerge at $\alpha = 10$ and 0.1. Wide ground-state peaks split at small regularization parameters (Borgia, Brown, and Fantazzini, 1998). $P00$, $P11$, and $P22$ are the first three eigenvalues of magnetization relaxation in Berea sandstone. In the case of Indiana limestone Spq and Lpq respectively represents eigenvalues of small and large pores. $N0q$ mark signal that demonstrate bulk-like features in the T_1 domain.

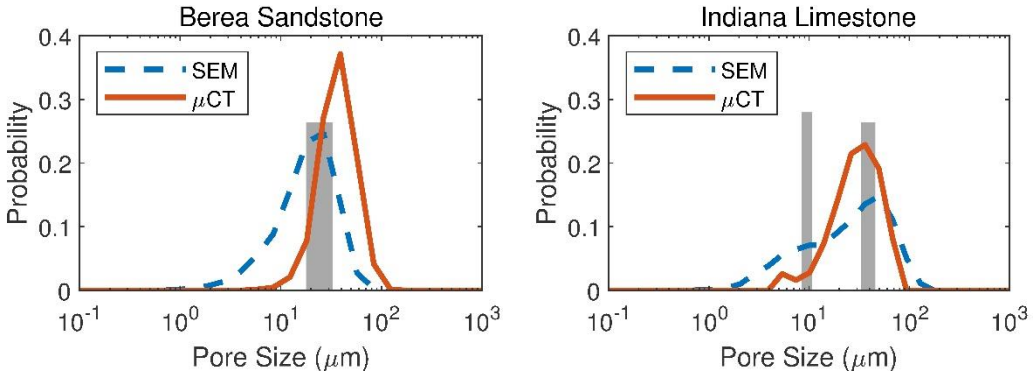

Figure 7-3 Volumetric probability of pore diameter from scanning electron microscopy (---) and X-ray micro-tomography (—) for Berea sandstone (left) and Indiana limestone (right). The pore size from magnetic resonance relaxation by a direct search algorithm is shown as a gray rectangle. A pore diameter of 22.1 μm was computed for Berea sandstone and pore diameters of the large and small pores in Indian limestone were estimated to be 39.6 μm and 10.0 μm. The width of the rectangle shows the estimated size by varying the input parameters and the heights demonstrate relative pore size population.

less than a factor of 10 different from those reported in the literature (Hürlimann et al. 1994; Luo, Paulsen, and Song 2015). With samples used in this study, Equations (7-7) to (7-9), demonstrated a greater sensitivity to the pore size as opposed to surface relaxivities.

For Indiana limestone, the analytical method presented in this work estimated pore sizes of 10.0 μm and 39.6 μm for small and large pores, respectively. The pore sizes from processed scanning electron microscopy images were 10.1 μm and 50 μm for small and large pores, respectively. Indiana limestone had estimated surface relaxivity constants of

$\rho_1 = 64\ \mu m/s$ and $\rho_2 = 204\ \mu m/s$ for small pores and $\rho_1 = 60\ \mu m/s$ and $\rho_2 = 195\ \mu m/s$ for large pores. Surface relaxivities of large and small pores are satisfactorily similar although they are acquired with two separate sets of eigenvalues. These results agree with previously published results for Indiana limestone pore size (Freire-Gormaly et al. 2015; Ji et al. 2012) and surface relaxivity of Indiana limestone is within the expected surface relaxivity range for sedimentary rocks (Hürlimann et al. 1994).

In all cases studied in this research, observed intensities of the non-ground relaxation eigenvalues were slightly larger than those estimated. Brownstein and Tarr calculated the intensity of non-ground eigenvalues for planar, cylindrical, and spherical geometries and realized that the contribution of non-ground eigenvalues is larger for cylindrical and spherical geometries with the same BT_i values (Brownstein and Tarr, 1979). The majority of the discrepancy between estimated and measured intensities of non-ground eigenvalues is due to the simple planar geometry assumed in this work.

7.4 Non-Ground Eigenvalues in 1D Data

Observation of non-ground eigenvalues of magnetic resonance relaxation is also possible in T_2 or T_1 distributions measured by CPMG and inversion recovery methods with importance in petroleum laboratory measurements (Mitchell et al. 2013), well-logging (Coates et al. 1999), and industrial measurement and control (Mitchell et al. 2014). It is usually assumed that non-ground eigenstates are not observed in T_1 and T_2 distributions and that these distributions are direct proxies for pore size. Here, we demonstrate that this

is not the case and estimate pore size for unimodal-pore-size Berea sandstone from a single T_2 distribution, as shown in Figure 7-4. Using an optimization method similar to the one described earlier, but only for the T_2 distribution, the pore diameter of Berea sandstone was estimated to be 33.9 μm, with a distribution in the range of 17 μm to 66 μm with ρ_2 on the order of hundreds of micrometers per second.

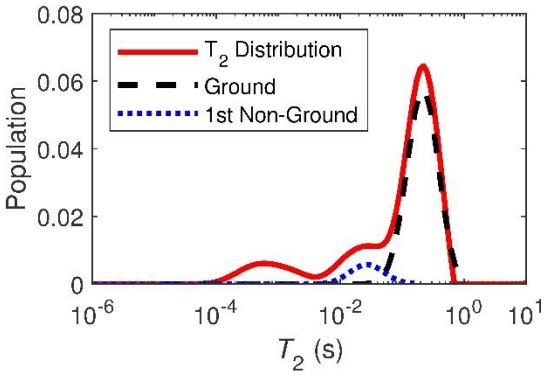

Figure 7-4 T_2 distribution of Berea sandstone and its estimated ground and non-ground eigenvalues. The T_2 distribution (–) was measured using the CPMG method with an inter-echo spacing of 300 μs. Varying l and ρ_2 and using a planar geometry for solving eigenvalues of the relaxation-diffusion equation lead to estimated (– –) contributions to the T_2 distribution by the dominant ground eigenvalues and a smaller non-ground eigenvalue peak.

7.5 Conclusion

In summary, for the first time we show how uniform magnetization in natural porous media may result in non-ground eigenvalues detected by 2D magnetic resonance relaxation measurements. It is also shown that the distinctive pattern of these eigenvalues makes possible identification of multiple pore sizes; with the possibility of further processing to yield the standard deviation of pore size. In the future, we are going to apply this method and its variants to a variety of rocks and other porous materials of technological importance such as wood and cement.

This short piece will be followed by an extended manuscript in the future. The extended manuscript will feature experiments on Bentheimer, another well-known rock type, in addition to Berea sandstone and Indiana limestone. The extended manuscript will discuss T_1, T_2, and $T_1 - T_2$ measurement features in three magnetic fields corresponding to ^{1}H frequencies of 2, 8.5 and 100 MHz. It will be shown that the T_1/T_2 ratio is a function of the static magnetic field due to magnetic field dependent surface relaxivities. The extended manuscript will finish with MRI examples of spatially resolved $T_1 - T_2$ measurement.in rocks to determine the thickness of liquid films wetting rock pore surfaces.

7.6 References

Bird, R. B., Stewart, W. E., and Lightfoot, E. N. 2002. *Transport Phenomena*, 2nd Ed. New York: John Wiley & Sons.

Borgia, G. C., Brown, R. J. S., and Fantazzini, P. 1998. Uniform-Penalty Inversion of Multiexponential Decay Data. *J. Magn. Reson.* 132 (1): 65-77. https://doi.org/10.1006/jmre.1998.1387.

Bradley, D. and Roth, G. 2007. Adaptive Thresholding Using the Integral Image, *J. Graph. Tools* 12 (2): 13-21. https://doi.org/10.1080/2151237X.2007.10129236.

Brownstein, K. R., and Tarr, C. E. 1979. Importance of Classical Diffusion in NMR Studies of Water in Biological Cells. *Phys. Rev. A* 19 (6): 2446-2453. https://doi.org/10.1103/PhysRevA.19.2446.

Callaghan, P. T., Coy, A., Halpin, T. P. J., et al. 1992. Diffusion in Porous Systems and the Influence of Pore Morphology in Pulsed Gradient Spin-Echo Nuclear Magnetic Resonance Studies. *J. Chem. Phys.* 97 (1): 651-662. https://doi.org/10.1063/1.463979.

Callaghan, P. T., Arns, C. H., Galvosas, et al. 2007. Recent Fourier and Laplace Perspectives for Multidimensional NMR in Porous Media. *Magn. Reson. Imaging* 25 (4): 441-444. https://doi.org/10.1016/j.mri.2007.01.114.

Callaghan, P. T., Coy, A., MacGowan, D., et al. 1991. Diffraction-like Effects in NMR Diffusion Studies of Fluids in Porous Solids. *Nature* 351:467–469. https://doi.org/10.1038/351467a0.

Coates, G., Xiao, L., and Prammer, M. 1999. *NMR Logging: Principles and Applications*. Houston: Haliburton Energy Services.

Costabel, S., Weidner, C., Müller-Petke, M., et al. 2018. Hydraulic Characterisation of Iron-Oxide-Coated Sand and Gravel Based on Nuclear Magnetic Resonance Relaxation Mode Analyses. *Hydrol. Earth Syst. Sci.* 22 (3): 1713-1729. https://doi.org/10.5194/hess-22-1713-2018.

Freire-Gormaly, M., Ellis, J. S., MacLean, H. L., et al. 2015. Pore Structure Characterization of Indiana Limestone and Pink Dolomite from Pore Network Reconstructions. *Oil Gas Sci. Technol.* 71 (3): 33. https://doi.org/10.2516/ogst/2015004.

Hürlimann, M. D., Helmer, K. G., Latour, L. L., et al. 1994. Restricted Diffusion in Sedimentary Rocks: Determination of Surface-Area-to-Volume Ratio and Surface Relaxivity. *J. Magn. Reson. Ser. A* 111 (2): 169-178. https://doi.org/10.1006/jmra.1994.1243.

Ji, Y., Baud, P., Vajdova, V. et al. 2012. Characterization of Pore Geometry of Indiana Limestone in Relation to Mechanical Compaction. *Oil Gas Sci. Technol.* 67 (5): 753-775. https://doi.org/10.2516/ogst/2012051.

Johnson, D. L. and Schwartz, L. M. 2014. Analytic Theory of Two-Dimensional NMR in Systems with Coupled Macro- and Micropores. *Phys. Rev. E* 90 (3): 032407. https://doi.org/10.1103/PhysRevE.90.032407.

Keating, K. 2014. A Laboratory Study to Determine the Effect of Surface Area and Bead Diameter on NMR Relaxation Rates of Glass Bead Packs. *Near Surf. Geophys*. 12 (2): 243-254. https://doi.org/10.3997/1873-0604.2013064.

Kleinberg, R.L. 1999. Nuclear Magnetic Resonance. In *Methods in the Physics of Porous Media*, ed. Wong, P., Chap. 9, 337-385. San Diego: Academic Press. http://dx.doi.org/10.1016/S0076-695X(08)60420-2.

Kolda, T. G., Lewis, R. M., and Torczon, V. 2003. Optimization by Direct Search: New Perspectives on Some Classical and Modern Methods. *SIAM Rev.* 45 (3): 385-482. https://doi.org/10.1137/S003614450242889.

Lee, J. H., Labadie, C., Springer, C. S. et al. 1993. Two-Dimensional Inverse Laplace Transform NMR: Altered Relaxation Times Allow Detection of Exchange Correlation. *J. Am. Chem. Soc.* 115 (17): 7761–7764. https://doi.org/10.1021/ja00070a022.

Lee, T. C., Kashyap, R. L., and Chu, C. N. 1994. Building Skeleton Models via 3-D Medial Surface Axis Thinning Algorithms. *CVGIP-Graph. Model. Im.* 56 (6): 462-478. https://doi.org/10.1006/cgip.1994.1042.

Luo, Z. X., Paulsen, J., and Song, Y. Q. 2015. Robust Determination of Surface Relaxivity from Nuclear Magnetic Resonance DT_2 Measurements. *J. Mag. Res.* 259: 146-152. https://doi.org/10.1016/j.jmr.2015.08.002.

Mitchell, J., Chandrasekera, T. C., Holland, D. J., et al. 2013. Magnetic Resonance Imaging in Laboratory Petrophysical Core Analysis. *Phys. Rep.* 526 (3): 165-225. https://doi.org/10.1016/j.physrep.2013.01.003.

Mitchell, J., Gladden, L. F., Chandrasekera, T. C., et al. 2014. Low-Field Permanent Magnets for Industrial Process and Quality Control. *Prog. Nucl. Mag. Res. Sp.* 76: 1-60. https://doi.org/10.1016/j.pnmrs.2013.09.001.

Müller-Petke, M., Dlugosch, R., Lehmann-Horn, J., et al. 2015. Nuclear Magnetic Resonance Average Pore-Size Estimations Outside the Fast-Diffusion Regime. *Geophysics* 80 (3): 195-206. https://doi.org/10.1190/geo2014-0167.1.

Seevers, D. O. 1966. A Nuclear Magnetic Method for Determining the Permeability of Sandstones. Oral Presentation given at the Society of Petrophysicists and Well-Log Analysts 7th Annual Logging Symposium, Tulsa, 9-11 May 1996. SPWLA-1966-L.

Song, Y. Q., Carneiro, G., Schwartz, L. M., et al. 2014. Experimental Identification of Diffusive Coupling Using 2D NMR. *Phys. Rev. Lett.* 113 (23): 235503.

Song, Y. Q., Venkataramanan, L., Hürlimann, M. D., et al. 2002. T_1-T_2 correlation Spectra Obtained Using a Fast Two-Dimensional Laplace Inversion. *J. Magn. Reson.* 154 (2): 261-68. https://doi.org/10.1006/jmre.2001.2474.

Song, Y. Q., Ryu, S., and Sen, P. N. 2000. Determining Multiple Length Scales in Rocks. *Nature* 406 (6792):178–81. https://doi.org/10.1038/35018057.

Song, Y. Q., Zielinski, L., and Ryu, S. 2008. Two-Dimensional NMR of Diffusion Systems. *Phy. Rev. Lett.* 100 (24): 20-23. https://doi.org/10.1103/PhysRevLett.100.248002.

Song, Y. Q. 2000. Detection of the High Eigenmodes of Spin Diffusion in Porous Media. *Phys. Rev. Lett.* 85 (18): 3878–81. https://doi.org/10.1103/PhysRevLett.85.3878.

Torrey, H. C. 1956. Bloch Equations with Diffusion Terms. *Phys. Rev.* 104 (3): 563–65. https://doi.org/10.1103/PhysRev.104.563.

Venkataramanan, L., Song, Y. Q., and Hürlimann, M. D. 2002. Solving Fredholm Integrals of the First Kind with Tensor Product Structure in 2 and 2.5 Dimensions. *IEEE T. Signal Proces.* 50 (5): 1017-1026. https://doi.org/10.1109/78.995059.

Chapter 8 – Conclusions and Future Work

Secondary recovery or Enhanced Oil Recovery (EOR) fluids are designed to alter the relative effect of viscous forces, capillary forces, and rock wettability among others for improved oil displacement. This is possible by strongly influencing solid-solid, solid-fluid, or fluid-fluid interfaces. Magnetic Resonance Imaging (MRI) is one of the most capable technologies extant to probe the interaction between fluids and the pore surface of rocks. The Spin Echo – Single Point Imaging (SE-SPI) MRI method was employed to map fluid saturation and T_{2LM}, the logarithmic mean T_2, in core plugs undergoing processes affecting fluid/pore surface interactions. T_{2LM} is inversely proportional to the pore surface area in contact with the pore-filling fluid.

8.1 Conclusions

Fines migration is a costly and catastrophic problem in oilfields (Crowe et al. 1992). Careful waterflooding program development with sensitivity analysis of formation rocks to water injection rate and water composition can reduce fines migration problems in the field; especially in reservoir sectors with high oil production rates where production loss would be a major problem.

Experiments on fines migration are usually limited to the monitoring of effluents and differential pressure. The experimental method of this work provides much more information per experiment undertaken for flow-rate sensitivity of fines migration. In this research, changes in T_{2LM} demonstrated changes in pore surface area as a result of fines

migration in water-shock experiments. Permeability was mapped along two core plugs based on the mean T_{2LM} permeability model. This research outcome is significant because spatially resolved porosity and permeability profiles may aid petroleum engineers in better estimating the effects of fines migration and provide accurate insights to avoid this problem. This is a new look at an old and important problem in petroleum production.

CO_2 has been injected into petroleum reservoirs to enhance oil production for a few decades (Beckwith 2011). In addition, carbon dioxide injection into oil reservoirs is a practical step before largescale CO_2 injection into aquifers. CO_2 is significantly soluble in water and hydrocarbon mixtures; causing considerable changes in the partial molar volume of the mixture components. Flow of mixing fluids follows the volume transport equations described by Brenner (2005).

In this work, CO_2 flooding of decane saturated Berea core plugs were performed at high pressure, at miscible and immiscible conditions, in an MRI-compatible core holder with an integrated radiofrequency probe. It was shown that in absence of water, the density of decane in the pore surface bound layer decreased during the miscible drainage of decane by CO_2. However, there is qualitative evidence that, under immiscible conditions and above the residual oil saturation, the wetted surface area in contact with decane is constant. Below the residual saturation, under immiscible conditions, we postulate that a non-continuous wetting film forms on the pore surface.

CO_2 flooding of a heavy oil saturated Berea core plug with interstitial water phase present was also imaged by the SE-SPI method to demonstrate the capability of MRI methodologies employed in determining the mechanisms of hydrocarbon recovery.

MR relaxation data is not usually translated into parameters that chemical or petroleum engineers and scientists are familiar with. However, in chapters 4 and 6, MR parameters such as proton density and T_{2LM}, and their correlation, were translated into parameters such as porosity, saturation, surface area, and density familiar to petroleum and chemical engineers.

At the core-plug scale, the CO_2 flooding research demonstrated that it is possible to observe leading and trailing shocks in displacement of decane by CO_2 in a Berea sample with a length of only 5 cm. Self-sharpening fronts were observed and the measured wave velocity agreed with the thermodynamics of CO_2/decane mixtures at miscible and immiscible conditions.

Transport phenomena coupled with thermodynamics effects manifests in many real-world processes. One of the recent areas of progress in this regard is the role of Korteweg stress in fluid dynamics. Korteweg stress, or simply put as concentration variation, occurs in many chemical, petroleum, or hydrogeological engineering processes such as: plug flow reactors, saltwater intrusion in coastal aquifers, or separation of oxygen isotopes. Recent progress in this regard has incorporated the effects of volume change of mixing in diffusion processes in fluids. Howard Brenner (2005) was the leading scholar on the topic and his

work has already been applied to experimental studies where excess volume of a mixture is a strong function of composition. The experimental results and insights obtained from the miscible and immiscible CO_2 flooding of decane work provides invaluable experimental data useful to validate the current equations that describe flow in porous media and demonstrate the significance of the correction terms introduced by these new methods. Successful application of the new volume transport equations to this data set also verifies the accuracy of experimental methods used in this study.

In the last study within this research, it was shown that non-ground eigenstates contribute to the relaxation of initially-homogeneous magnetization in natural porous media. This is probably the most significant contribution of this research. This finding may have far-reaching implications in quantitative magnetic resonance and its applications such as petroleum well-logging, monitoring of aquifers, and industrial quality control. Industrial applications of magnetic resonance in porous media are usually limited to CPMG, and inversion recovery relaxometry by low-field permanent magnets. Previously, it was necessary to have a foreknowledge of surface relaxivity to be able to convert the T_1 or T_2 distributions to the pore size distribution. The analysis method developed in this work eliminates this restriction. Therefore, it is now possible to find the approximate pore size in porous media using simple relaxation MR methods.

8.2 Recommendations for Future Work

The recommendations for future work, based on the experiments performed in this study, are discussed below.

8.2.1 Fines migration

Previous fines migration studies relied solely on bulk permeability measurements to quantify fines migration effects. The method devised in this research can quantify porosity, permeability, and surface area ratio along the core. The following recommendations are offered to advance industrial applications of this project.

(1) High pressure experiments on injection rate sensitivity of fines migration.

Two phenomena can trigger fines migration: high shear rates at the pore surface and chemical incompatibility of the injected water and reservoir brine. Knowledge of electrolyte thermodynamics of reservoir brines has advanced sufficiently to eliminate the chemical incompatibility of the injected water. The major issue is the sensitivity of fines migration to high shear rates in water injection processes or at the oil production wells. This fines migration analysis method can replace traditional laboratory methods. A simple experiment is proposed to investigate the effect of rate sensitivity in Berea. A pump can be set to inject brine into a Berea core plug in a ramp mode. The brine injection rate will start at 0.01 cc/min and will increase in ten steps to 10 cc/min. Throughout the injection, the differential pressure will be monitored and T_2 distributions will be measured along the core

plug employing the SE-SPI method. The effects of fines migration may be quantified as a function of flow rate.

(2) Application in exploration and production environments.

It would be beneficial to offer such fines migration studies to petroleum companies as a service. More fines migration experiments are required to be performed on different samples and different pressures to ensure the industrial applicability of the method. The methodology developed in this study can be complemented with velocity mapping and be provided to petroleum corporations by H2 Laboratories, an NMR core analysis company in Fredericton.

(3) Matching fines migration models with experiments.

In this project, it was realized that models that predict fines migration in porous rocks only predict the permeability profile in the first step of the fines migration experiment. If flow is stopped and started again, the permeability profile would be different from fines migration models' prediction. It would be interesting to see the difference between predictions of the models and experimental results. To date, these models have only had to match bulk permeability values. The MRI method devised in this study provides the opportunity to validate mathematical models.

8.2.2 CO_2 Flooding

In experiments performed in this research, it was observed that common equations of fluid flow cannot fully describe concentration shocks in fluid flow in rocks. It is recommended that volume conservation equation of Brenner (2005) be applied for the CO_2/decane experiment performed in this work to fully understand the effects of volume change and thermodynamics on such complex flow systems. Such quality quantitative information is very limited, especially in porous materials. The experimental data acquired in this research are being published so that other research groups focused on such studies can use them. It is hoped that this work contributes to our understanding of transport processes where thermodynamics effects are significant.

8.2.3 Non-Ground Eigenstates in Magnetic Resonance of Porous Media

It is suggested that more experiments be performed on a variety of natural porous media, including different types of rocks, wood, cement, soil, glass bead packs, and sand. The computer program developed in this study still needs minor input by the user to function. If made fully automatic, it could be widely applied for automatic processing of 1D and 2D data and be applied to well logging data for testing purposes.

Non-ground eigenstates in magnetic resonance of porous media could be also observed in $T_2 - T_2$, $T_2 - D$, or other MR experiments. It is suggested that features of these experimental methods data be investigated for that purpose.

It is recommended to commercialize this pore sizing method when the mathematical methods required for its automatic function reach maturity. Local company Green Imaging Technologies can play an important role in this endeavor. It is also recommended to investigate other possible benefits non-ground eigenmodes may have in MR measurements.

8.3 References

Beckwith, R. 2011. Carbon Capture and Storage: A Mixed Review. *J. Pet. Technol.* 63 (5): 42-45. SPE-0511-0042-JPT. http://dx.doi.org/10.2118/0511-0042-JPT.

Brenner, H. 2005. Kinematics of Volume Transport. *Physica A* 349 (1-2): 11-59. https://doi.org/10.1016/j.physa.2004.10.033.

Crowe, C., Masmonteil, J., and Thomas, R. 1992. Trends in Matrix Acidizing. *Oilfield Review* 4 (4).

Appendix A – Exponential Capillary Pressure Functions in Sedimentary Rocks[5]

Capillary pressure is defined as the difference between the wet and non-wet phase pressures in porous materials. It is a property specific to the combination of rock and fluids under investigation. The distribution of fluids in oil reservoirs and their flow path is largely determined by capillary pressure and it is one of the most important inputs in reservoir simulation software programs used to predict future productions.

Exponential capillary pressure functions in rocks has been an ongoing work of the author before joining UNB MRI Research Centre. However, the quality of fluid saturation data provided by MRI in rock centrifugation experiments provided compelling verification data to put exponential capillary pressure functions to test.

The Brooks-Corey power-law capillary pressure model is commonly imposed on core analysis data without verifying the validity of its underlying assumptions. The Brooks-Corey model, originally developed to model the pressure head during the drainage of soil, is only valid at low wetting phase saturations. However, such models are often applied in petroleum production simulations and may lead to erroneous recovery factors when the

[5] Largely based on a reviewed conference proceeding. Published as: Afrough, A., Bahari Moghaddam, M., Romero-Zerón, L., Balcom, B. J. 2018. Exponential Capillary Pressure Functions in Sedimentary Rocks. International Symposium of the Society of Core Analysts, Trondheim, Norway, 27-30 August.

saturation range of interest is far from the end points. We demonstrate that exponential models work much better for capillary pressure compared to the Brooks-Corey model over a wide saturation range.

Mercury injection porosimetry, petrographic image analysis, and magnetic resonance studies suggest that the pore and throat size distribution in many rocks are log-normally distributed. This fact was previously employed to calculate the capillary pressure function as a function of saturation for pore size distributions described by a truncated log-normal distribution. Employing a Taylor series expansion, we simplify the random fractal capillary pressure model of Hunt to $P_c = \exp(a - bS)$, where S is the wetting phase saturation, and a and b characteristic of the porous medium.

An extensive dataset of seventeen centrifuge capillary pressure measurements were used in this research to demonstrate the merit of the new method. For both sandstones and carbonates, the logarithm of capillary pressure showed a linear relationship with saturation as observed by magnetic resonance imaging centrifuge capillary pressure measurements over a wide saturation range. This work demonstrates that: (a) in semi-log plots of capillary pressure as a function of saturation, capillary pressure will vary linearly over a wide saturation range, (b) such a plot as described in (a) will show the uni- or bimodal pore size distribution of the rock, (c) the exponential capillary pressure function simplifies analytical models that use the capillary pressure function, for example oil recovery models for fractured reservoirs.

Introduction

Empirical correlations help establish functional relationships between capillary pressure P_c and wetting phase saturation S_w in natural porous materials. The Brooks-Corey capillary pressure model (Brooks and Corey, 1964), the most well-known such equation, reduces the functional relationship between capillary pressure and effective saturation S_{we} to the bubbling pressure P_b and pore-size-distribution index λ according to

$$P_c(S_{we}) = P_b S_{we}^{-1/\lambda} \tag{A-1}$$

where P_b is a measure of the maximum pore size which forms a continuous flow network and λ characterizes the pore size distribution. Effective saturation normalizes the wetting phase saturation S_w in the range of end-point saturations (residual wetting phase saturation S_{wr} and residual non-wetting phase saturation S_{nwr}) such that

$$S_{we} = \frac{S_w - S_{wr}}{(1 - S_{nwr}) - S_{wr}}. \tag{A-2}$$

For primary drainage, with $S_{nwr} = 0$, Equation (A-2) reduces to

$$S_{we} = \frac{S_w - S_{wr}}{1 - S_{wr}}. \tag{A-3}$$

Brooks and Corey (1964) developed the above relationship for $S_w > S_{wr}$, although saturations less than S_{wr} can exist. This is because S_{wr}, as calculated with the method outlined in, is an interpolation of irreducible wetting-phase saturation rather than the lowest saturation measured during an experiment. They also acknowledged the effect of hysteresis

on capillary pressure values. Other assumptions inherent in this empirical model are that the porous material is isotropic and is undergoing through drainage (Brooks and Corey, 1964).

Wells and Amaefule (1985) and Lekia and Evans (1990) demonstrated that the Brooks-Corey capillary pressure model fails for tight gas sand samples. Lekia and Evans (1990) circumvented the shortcomings of the Brooks-Corey model by explicitly using the wetting-phase saturation, in contrast with the effective saturation. Later, recognition of the applicability of fractal theories to sandstones by Katz and Thompson (1987) led to the development of power-law analytical equations for capillary pressure for low wetting phase saturations by Toledo et al. (1994). Yang et al. (2015) provides the analytical derivation of Brooks-Corey capillary pressure function according to the mathematics of fractals. Novy et al. (1989) had previously demonstrated that capillary pressure is a power-law function of saturation at low wetting phase saturations by modeling fluid flow in networks and considering the effect of disjoining pressure. The most recent advance in modeling relative permeability and capillary pressure in porous materials, developed by Hunt (2004a), will be reviewed and examined in this work.

The main goal of this work is to demonstrate that exponential capillary pressure functions are superior to the model of Brooks-Cory over a wider wetting-phase saturation range. In this paper we show first that the capillary pressure model of Hunt is approximately exponential, even for $D < 3$. This is confirmed with an extensive experimental data set

taken from the literature. Secondly, the effect of bimodal pore size distributions on P_c will be discussed. Finally, we present the application of such models in analytical solutions of gravity drainage in fractured reservoirs.

Theory

Hunt (2004a) investigated random fractal models of porous materials applicable to soil systems. They applied critical path analysis in the form of continuum percolation to predict relative permeability. Assuming a finite-range power-law distribution of pore radii, from r_0 to r_m, the probability density function for pore radii of a random fractal porous material would be $W(r) \propto r^{-1-D}$. The fractal dimension D of such system of porosity ϕ is (Hunt, 2004a, p. 45)

$$D = 3 - \frac{\log(1-\phi)}{\log\left(\frac{d_m}{d_0}\right)}. \tag{A-4}$$

The pressure required to remove the wetting phase from a pore of size r is $P_c = B/r$, where B is a constant. With a non-wetting entry pressure of $P_{cA} = B/r_m$, the wetting phase saturation is (Hunt, 2004b)

$$S_w = \left(\frac{3-D}{r_m^{3-D}}\right)\int_{r_0}^{B/P_c} r^{2-D}\mathrm{d}r = 1 - \left(\frac{1}{\phi}\right)\left[1 - \left(\frac{P_c}{P_{cA}}\right)^{D-3}\right]. \tag{A-5}$$

Only with a porosity of unity, Equation (A-5) is identical to the Brooks-Corey model. Solution of Equation (A-5) for capillary pressure in terms of saturation gives (Hunt, 2004b)

$$P_c = P_{cA}\left[\frac{1}{1-\phi(1-S_w)}\right]^{\frac{1}{3-D}}. \quad \text{(A-6)}$$

This equation is valid for $D < 3$ whereas values more than 3 are non-physical. For $D = 3$, the integral of Equation (A-5) is equal to

$$P_c = P_{cA}\exp\left[-(1-S_w)\ln\left(\frac{r_m}{r_0}\right)\right]. \quad \text{(A-7)}$$

We recognize that Equation (A-6) can be simplified by a Taylor series expansion. Equation (A-6) simplifies to

$$\log P_c = \log P_{cA} + \frac{\phi}{3-D}(1-S_w). \quad \text{(A-8)}$$

which is equivalent to

$$P_c = P_{cA}\ \exp\left[\frac{\phi}{3-D}\ (1-S_w)\ \right]. \quad \text{(A-9)}$$

In the next section, experimental data is tested against this model.

Results and Discussions

We first present the verification of the exponential capillary pressure function, Equation (A-9), with experimental data. Deviation from this behavior and possible applications in analytical fluid flow models follows.

Exponential Capillary Pressure vs. Experimental Data

Figure A-1 demonstrates a typical oil/water primary drainage capillary pressure in a sandstone core plug as a function of the wetting phase saturation in a semi-log plot. In the saturation range of $(0.23, 0.75)$, the exponential capillary pressure function fits experimental data, shown by filled circles, with a coefficient of determination of $R^2 = 0.993$. The range of validity of this descriptive behavior is marked with vertical dashed lines. For $S_w > 0.75$, experimental capillary pressure data, shown as open squares □, deviate from the exponential P_c. Deviation from the exponential capillary pressure at high and low saturations is due to fluid flow dominated by the effect of macropores (Hunt 2004) and surface films (Toledo et al. 1994; Novy et al. 1989), respectively.

Equation (A-9) was tested with 17 centrifuge capillary pressure measurements on consolidated rock core plugs, with water permeabilities in the range of 0.0014 to 0.69 $(\mu m)^2$ and porosities in the range of 0.14 to 0.48. The experimental datasets are found in the literature in Brooks and Corey (1964), Cano Barrita et al. (2008), Chen and Balcom (2005), Fernø et al. (2009), Nørgaard et al. (1999), Green et al. (2008), and Baldwin and Yamanashi (1991). Six datasets represent displacement of water by oil; the others are air/water centrifuge experiments. All, but two datasets, (Brooks and Corey 1964; Green et al. 2008), were measured employing saturation profile measurements by either magnetic resonance or nuclear tracer imaging.

All seventeen capillary pressure datasets employed in this study are shown in Figure A-2. The $P_c - S_w$ relationship is plotted in semi-log and log-log graphs in Figures A-2a and b,

respectively. Color lines represent descriptive fits to experimental data points in each dataset. Both sandstones and carbonates are represented in this graph. Data points are not differentiated according to the datasets or the displacing fluid due to the sheer amount of data.

The exponential capillary pressure function, Equation (A-9), only fits a segment of the $P_c - S_w$ experimental data points; the largest and smallest such range are $\Delta S_w = 0.6$ and 0.3, respectively. The average coefficient of determination for the fitted segments is above 0.90 for all data sets, except for four data sets of Baldwin and Yamanashi (1991) in which saturation had high uncertainty due to less-quantitative MRI methods. The coefficient of determination was in the range of 0.65 to 0.85 for exponential fits to appropriate segments of data from Baldwin and Yamanashi (1991). Figure A-2 demonstrates the advantages of centrifuge capillary pressure methods based on saturation profile measurement over the traditional centrifuge method by providing more data points.

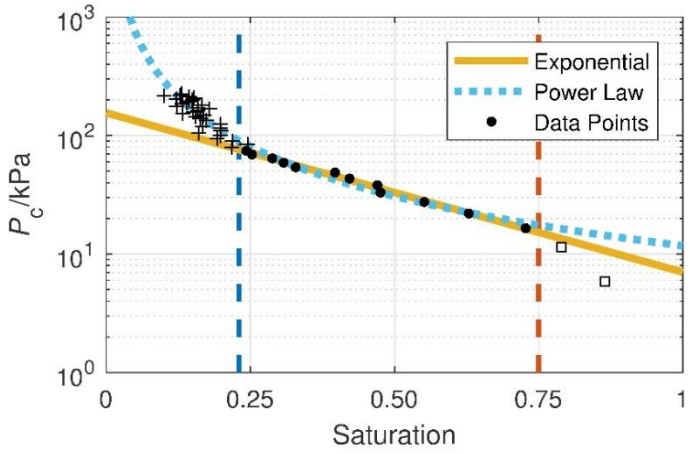

Figure A-1 A typical oil/water drainage capillary pressure as a function of the wetting phase saturation in a semi-log plot. The exponential capillary pressure function of $\log_{10} P_c/\text{kPa} = -1.344\, S_w + 2.191$ fits experimental data ● in the saturation range of $(0.23, 0.75)$, shown by the vertical lines, with $R^2 = 0.993$. Deviation from this exponential function is because of film flow + and macropores □ at low and high saturations, respectively. The Brooks-Corey capillary pressure function … of $P_c/\text{kPa} = 11.75\, S_w^{-1.389}$ were obtained by a descriptive fit to experimental data ● and +. It appears that the line … fits data well, however, the deviation of data from the fitted line … in the range of $(0.23, 0.75)$ demonstrates an obvious trend that is far from random. Data from (Cano Barrita, 2008).

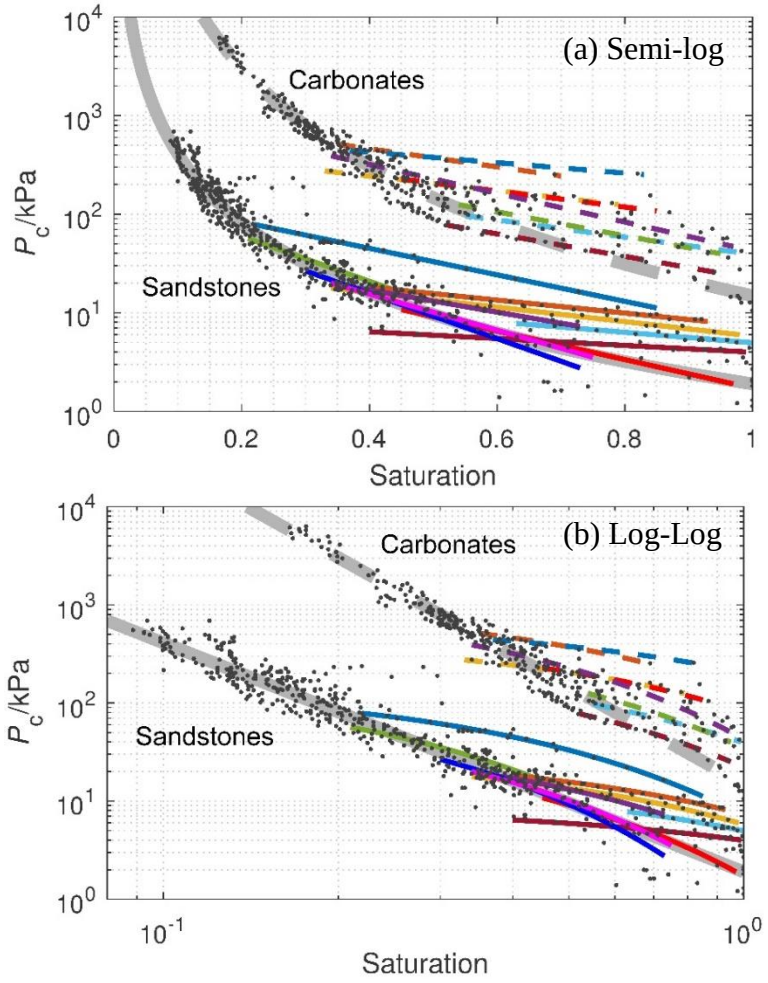

Figure A-2 Seventeen experimental datasets of drainage capillary pressure by centrifuge methods shown by ●. Colored lines represent descriptive fits of exponential capillary pressure functions in the range of their validity to sandstone ─ and carbonate --- samples. (a) is the $P_c - S_w$ relationship in a semi-log graph and (b) is the same data in the log-log form. All $P_c - S_w$ data at low wetting phase saturations collapse to power-law relationships, one for sandstones and one for carbonates shown by gray lines, representing the conditions at which film flow dominates. The exponential capillary pressure function fits experimental data down to a saturation on the power-law line.

All capillary pressure data collapse to a power law relationship at low wetting phase saturations. These power law relationships are shown by straight gray lines of $P_c/\text{kPa} = 1.9\, S_w^{-2.33}$ for sandstones and $P_c/\text{kPa} = 14.86\, S_w^{-3.3}$ for carbonates in Figure A-2b. This agrees with thin film models at low wetting phase saturation, when the disjoining contribution dominates the capillary contribution (Toledo et al. 1994). From the data collapse, the fractal dimension of sandstone and carbonate rocks probed by the thin liquid films of water is 2.57 and 2.70, respectively; in agreement with common fractal dimensions measured by Thompson and Katz (1987) and Toledo et al. (1994) for sedimentary rocks.

According to Figure A-2, in most cases, the Brooks-Corey capillary pressure model under predicts capillary pressure, if fitted to low-saturation $P_c(S_w)$ data. Another consequence of inappropriate use of the Brooks-Corey model is that it over-predicts the term $(-dP_c/dS_w)$ and hence the capillary pressure dispersion. Any errors in the capillary dispersion term results in erroneous prediction of two-phase transition zones in a displacement process. However, note that the Brooks-Corey model correctly predicts P_c in the low wetting phase saturation regime.

Deviation from the Exponential Capillary Pressure Model

In the previous subsection, it was demonstrated that capillary pressure in consolidated rocks can be described by an exponential relationship over a wide saturation range. Therefore, semi-log plots of $P_c(S_w)$ can be employed for quality control of experimental data. Deviations from this simple relationship can occur because of structural pores, at high

saturations, and film flow, at low saturations. An example of these effects is demonstrated in Figure A-1. Film flow capillary pressure can be estimated by the Brooks-Corey equation with appropriate parameters.

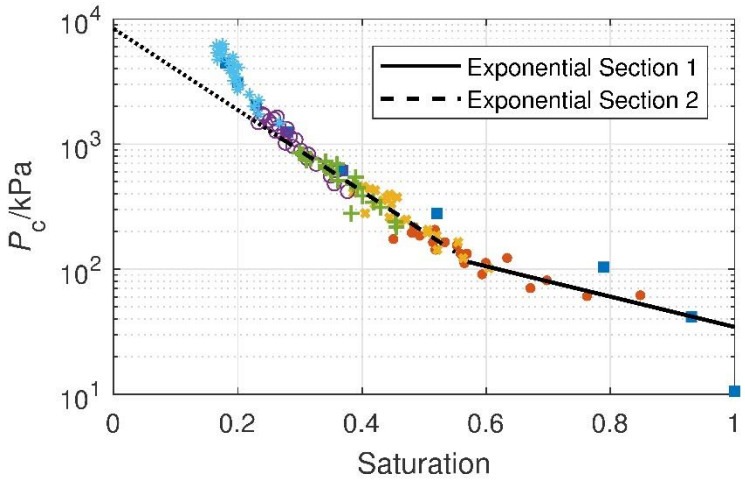

Figure A-3 Air/water capillary pressure for carbonate sample E13. Data from a porous plate experiment ■ and a centrifuge capillary pressure measurement of rotation speeds 2800 ●, 4000 ×, 5600 +, 7900 ○, and 15000 * revolutions per minute agree each other. Two exponential capillary pressure functions of $\log_{10} P_c/\text{kPa} = -1.213\, S_w + 2.751$ (—) and $\log_{10} P_c/\text{kPa} = -3.248\, S_w + 3.922$ (---) fit the experimental data in the saturation ranges of $(0.57, 0.94)$ and $(0.27, 0.55)$ with $R^2 = 0.90$ and 0.93, respectively. Deviation from the exponential function (…) is likely because of film flow at low saturations. Data from (Baldwin and Yamanashi 1991).

Deviation from the simple exponential function, however, is not limited to the effects described earlier. Hunt and Gee (2002), Satyanaga et al. (2013), and Zhou et al. (2017)

previously showed that capillary pressure in soil samples with a bimodal pore size distribution possesses bi-exponential behavior. Such an effect was also observed in this research; notably for sample E13, a carbonate core plug.

Figure A-3 demonstrates the biexponential capillary pressure function $P_c(S_w)$ which follows $\log_{10} P_c/\text{kPa} = -1.213\, S_w + 2.751$ in the saturation range of $(0.57, 0.94)$ and $\log_{10} P_c/\text{kPa} = -3.248\, S_w + 3.922$ in the saturation range of $(0.27, 0.55)$. At low saturations, capillary pressure data deviate from the exponential fit due to film flow. This bi-exponential feature is likely due to heterogeneities in the carbonate rock sample E13.

Application in Analytical Solutions of Oil Recovery from Fractured Reservoirs

Consider gravity drainage in a one-dimensional matrix block occupied by oil, as the wetting phase, and gas. At any point in the matrix, the flow rate of the oil phase can be estimated by (Firoozabadi and Ishimoto, 1994)

$$q = \frac{kk_{ro}}{\mu_o}\left(\Delta\rho g - \frac{dP_c}{dz}\right). \tag{A-10}$$

The absolute value of the derivative of capillary pressure with respect to time $(-dP_c/dS_w)$ simplifies dP_c/dz to

$$\frac{dP_c}{dz} = \frac{dP_c}{dS}\frac{dS_w}{dz} \tag{A-11}$$

where dP_c/dS_w is an exponential function; if the exponential capillary pressure model applies. The critical path analysis in random fractals also results in exponential relative

permeability functions which further simplifies Equation (A-10) to yield an exponential recovery factor in time like those previously calculated numerically (Pirker et al. 2007) and employed in the emerging fractured reservoir simulation methodology of Mittermeir and Heinemann (2015).

Conclusions

The capillary pressure model of Hunt developed for random fractals with truncated log-normal pore size distributions was simplified to an exponential function by employing a Taylor series expansion. This exponential function was shown to fit experimental data very well. Deviations from the exponential capillary pressure behavior are attributed to the effects of structural pores and film flow at high and low wetting phase saturations, respectively. The possibility of bi-exponential capillary pressure functions was demonstrated for a carbonate core plug. Exponential capillary pressure functions, along with their relative permeability counterparts, can simplify oil recovery factors in analytical solutions of flow equations for gravity drainage in fractured reservoirs among many others.

References

Baldwin, B. A., Yamanashi, W. S. 1991. Capillary-Pressure Determinations from NMR Images of Centrifuged Core Plugs: Berea Sandstone. *The Log Analyst* 32 (5): 550-556, SPWLA-1991-v32n5a6.

Brooks, R. H., Corey, A. T. 1964. *Hydrology Papers: Hydraulic Properties of Porous Media*, Fort Collins: Colorado State University.

Cano Barrita, P. F. de J., Balcom, B. J., McAloon, M. J., et al. 2008. Capillary pressure measurement on cores by MRI. *J. Petrol. Technol.* 60 (8): 63-66. https://doi.org/10.2118/0808-0063-JPT.

Chen, Q., Balcom, B. J. 2005. Measurement of Rock-Core Capillary Pressure Curves using a Single-Speed Centrifuge and One-Dimensional Magnetic-Resonance Imaging. *J. Chem. Phys.* 122 (21): 214720. https://doi.org/10.1063/1.1924547.

Firoozabadi, A., Ishimoto, K. 1994. Reinfiltration in Fractured Porous Media: Part 1- One Dimensional Model. *SPE Advanced Technology Series* 2 (2): 35-44. https://doi.org/10.2118/21796-PA.

Fernø, M. A., Bull, Ø., Sukka, P. O., et al. 2009. Capillary Pressures by Fluid Saturation Profile Measurements During Centrifuge Rotation. *Transport Porous Med.* 80 (2): 253-267. https://doi.org/10.1007/s11242-009-9355-8.

Green, D. P., Gardner, J., Balcom, B. J., et al. 2008. Comparison Study of Capillary Pressure Curves Obtained Using Traditional Centrifuge and Magnetic Resonance Imaging Techniques. Oral presentation given at the SPE/DOE Improved Oil Recovery Symposium, Tulsa, Oklahoma, 19-23 April. SPE-110518.

Hunt, A. G. 2004. *Percolation Theory for Flow in Porous Media*, Heidelberg: Springer-Verlag.

Hunt, A. G. 2004. An Explicit Derivation of an Exponential Dependence of the Hydraulic Conductivity on Relative Saturation. *Adv. Water Resour.* 27 (2): 197-201. https://doi.org/10.1016/j.advwatres.2003.11.005.

Hunt, A. G., Gee, G. W. 2002. Application of Critical Path Analysis to Fractal Porous Media: Comparison with Examples from the Hanford Site. *Adv. Water Resour.* 25 (2): 129-146. https://doi.org/10.1016/S0309-1708(01)00057-4.

Lekia, S. D. L., Evans, R. D. 1990. A Water-Gas Relative Permeability Relationship for Tight Gas Sand Reservoirs. *J. Energy Resour. Technol.* 112 (4): 239-245. https://doi.org/10.1115/1.2905766.

Mittermeir, G. M. 2015. Material-Balance Method for Dual-Porosity Reservoirs with Recovery Curves to Model the Matrix/Fracture Transfer. *SPE Reservoir Evaluation and Engineering* 18, 2, 171-186. https://doi.org/10.2118/174082-PA.

Novy, R. A., Toledo, P. G., Davis, H. T., et al. 1989. Capillary Dispersion in Porous Media at Low Wetting Phase Saturations. *Chem. Eng. Sci.* 44 (9): 1785-1797. https://doi.org/10.1016/0009-2509(89)85121-8.

Nørgaard, J. V., Olsen, D., Reffstrup, J., et al. 1999. Capillary-Pressure Curves for Low-Permeability Chalk Obtained by Nuclear Magnetic Resonance Imaging of Core-Saturation Profiles. *SPE Reserv. Eval. Eng.* 2 (2): 141-148. https://doi.org/10.2118/55985-PA.

Pirker, B., Mittermeir, G. M., Heinemann, Z. E. 2007. Numerically Derived Type Curves for Assessing Matrix Recovery Factors. Oral presentation given at the

EUROPEC/EAGE Conference and Exhibition, London, U.K., 11-14 June. SPE-107074-MS.

Satyanaga, A., Rahardjo, H., Leong, E. -C., et al. 2013. Water Characteristic Curve of Soil with Bimodal Grain-Size Distribution. *Comput. Geotech.* 48 (March): 51-61. https://doi.org/10.1016/j.compgeo.2012.09.008.

Thompson, A. H., Katz, A. J., Krohn, C. E. 1987. The Microgeometry and Transport Properties of Sedimentary Rock. *Adv. Phys.* (36) 5: 625-694. https://doi.org/10.1080/00018738700101062.

Toledo, P. G., Novy, R. A., Davis, H. T., et al. 1994. Capillary Pressure, Water Relative Permeability, Electrical Conductivity and Capillary Dispersion Coefficient of Fractal Porous Media at Low Wetting Phase Saturations. *SPE Advanced Technology Series* (2) 1: 136-141. https://doi.org/10.2118/23675-PA.

Wells, J. D., Amaefule, J. O. 1985. Capillary Pressure and Permeability Relationships in Tight Gas Sands. Oral presentation given at the SPE/DOE Low Permeability Gas Reservoirs Symposium, Denver, Colorado, 19-22 March. SPE-13879-MS.

Yang, Y., He, C., Lin, F. 2015. Comments on "Reply to comments on "Analytical Derivation of Brooks-Corey Type Capillary Pressure Models Using Fractal Geometry and Evaluation of Rock Heterogeneity"" *J. Petrol. Sci. Eng.* 133: 713-715. https://doi.org/10.1016/j.petrol.2015.07.006.

Zhou, H., Mooney, S. J., Peng, X. 2017. Bimodal Soil Pore Structure Investigated by a Combined Soil Water Retention Curve and X-Ray Computed Tomography Approach. *Soil Sci. Soc. Am. J.* 81 (6): 1270-1278. https://doi.org/10.2136/sssaj2016.10.0338.

Appendix B – Fast Measurement of 180° RF Pulse Length

This appendix assists researchers with guidelines to ensure that a radio frequency (RF) probe used in MR measurements of long duration core flooding experiments demonstrates a consistent behavior. The stability of the 180° RF pulse length is a robust method to monitor the behavior of an RF probe. A fast method to measure the 180° RF pulse length by only four FID measurements is proposed in this appendix. Regular measurement of the 180° RF pulse length ensures that the measured data are quantitative. This method significantly reduces the measurement time of 180° RF pulse length which is necessary for quantitative MR and MRI analysis.

Several processes may interfere with the quantitative nature of magnetic resonance imaging (MRI) measurements during long core flooding experiments.

(1) During the course of core flooding experiments, new fluids are injected into a core plug saturated with the initial pore-filling fluids. New fluids in the pore space of rocks may change the electrical characteristics of the RF probe circuit (Webb, 2011). This possible detuning of the RF probe requires constant monitoring of the MRI system to ensure that the RF probe is on resonance. This effect has been observed in brine injection into deionized-water saturated Berea core plugs in fines migration experiments.

(2) The tuning of RF coils often changes in MRI measurements of long duration core flooding experiments. This happens even in long duration static experiments. The

main reason for this is not clear. However, it may be associated with mechanical vibration of gradients that affect the RF coil and circuit.

(3) Inconsistency in the power delivered by the RF amplifier can interfere with the quantitative nature of MRI measurements. It has been observed that the power delivered by the RF amplifier can change during a week-long experiment. These inconsistencies may be the result of high duty cycle effects.

Frequent measurement of the 90° and 180° RF pulse lengths is a simple qualitative method to ensure that none of the above processes interfere with the quantitative nature of MRI measurements. However, the measurement of 90° RF pulse length is a long process in systems with long T_1s. A new method based on the phase of the measured signal was devised in this research to measure the 180° RF pulse length. With a good first estimate, it is possible to measure the 180° RF pulse length with only four free induction decay (FID) measurements.

Usually, measuring 90° and 180° RF pulse lengths involves running a series of FIDs and measuring the signal magnitude as a function of the RF pulse length. The 90° and 180° RF pulse lengths have the maximum and minimum magnitudes respectively, as shown in Figure B-1. In this example, the 90° and 180° RF pulse lengths were 28.35 and 56.70 μs as measured employing .AutoP90, the automatic script provided by the RINMR software, with 25 FID measurements and a good first estimate of the 90° RF pulse length. In a typical core flooding experiment, such a measurement would require 9 minutes.

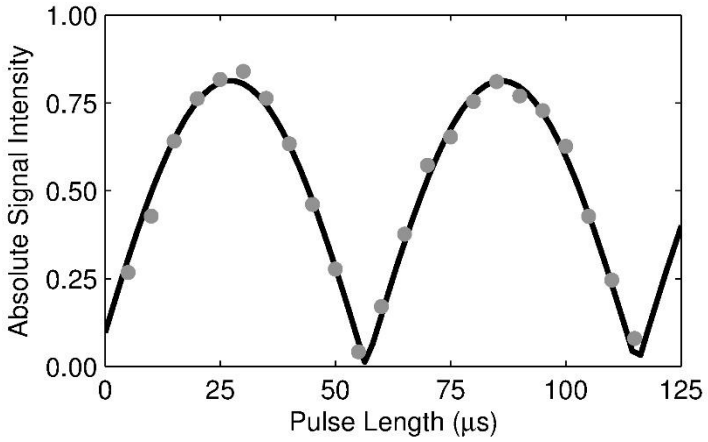

Figure B-1 FID signal magnitude as a function of RF pulse length in an experiment to measure the 90° and 180° RF pulse lengths. FID measurements are shown as gray circles on top of a theoretical fit.

The new method to measure the 180° pulse length employs the phase of the FID data, θ. The phase θ of the magnetization in the transverse plane is not constant in FID experiments with varying flip angles. It oscillates between θ and $\pi + \theta$ with increasing duration of the RF pulse. This phase was employed to translate the FID signal magnitude into a signed number, as shown in Figure B-2.

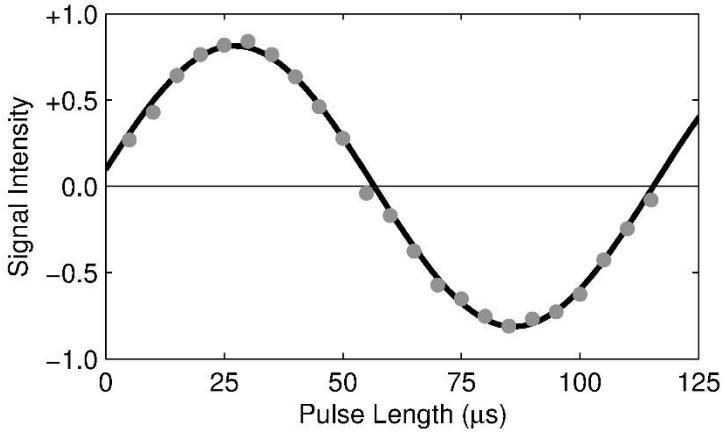

Figure B-2 The signed FID signal intensity as a function of RF pulse length in an experiment to measure the 90° and 180° RF pulse lengths. FID measurements are shown as gray circles on top of a sine function fitted to the data.

The signed FID signal intensity is a sinusoidal function of the pulse length with a period equivalent to a 360° flip angle. Therefore, the signal intensity of the FID signal reaches zero with a 180° pulse length. With a good first estimate of the 180° pulse length, it is possible to measure the FID at two pulse lengths less than and larger than the 180° pulse length and fit a straight line to these points to obtain the 180° RF pulse length at the intersection with zero intensity, as shown in Figure B-3.

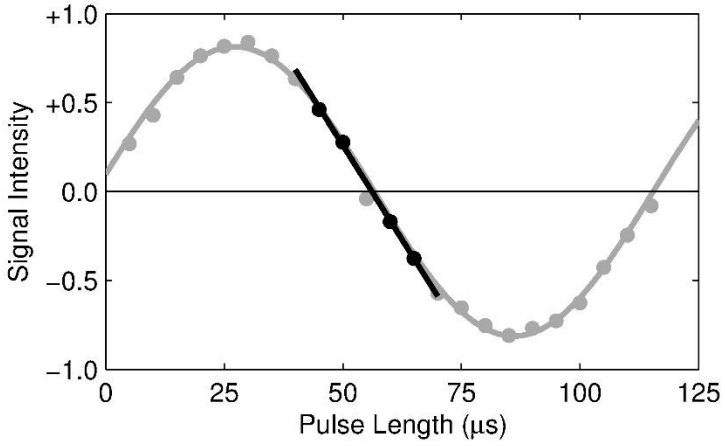

Figure B-3 The first term of the Taylor series expansion of the sine function at $\theta=\pi$ is a linear function. Four FID points are measured around $\theta = \pi$, two shorter and two longer than π. The linear function fitted to these four experimental points shows the 180° RF pulse length at its intersection with zero signal intensity.

This process measures the 180° pulse length with only four FID measurements in 16% of the time required to measure 180° pulse length employing the .AutoP90 script provided by RINMR software program.

In summary, three precautionary measures should be taken to provide information that validate the quantitative nature of MRI experiments in core flooding experiments:

(1) Regular measurements of the resonance frequency. This can be done employing the Wobble script in RINMR software,

(2) Regular measurements of the 180° pulse length employing the method described above, and

(3) Measuring the voltage of the sinusoidal RF wave function from crest to trough using the peak-to-peak measure feature of a digital oscilloscope.

References

Webb. A. 2011. Dielectric Materials in Magnetic Resonance. *Concept. Magn. Reson. A* 38A (4): 148-184. http://dx.doi.org/10.1002/cmr.a.20219.

Curriculum Vitae

Candidate's full name: Armin Afrough

Universities attended: Petroleum University of Technology

Bachelor of Science in in Petroleum Engineering

2007-2011

Patents:

Afrough, A., Romero-Zerón, L., Balcom, B. J. US Provisional Patent (US62/779,714): "Method and System for Determining Confinement Size in Porous Media" filed December 14, 2018.

Publications:

Afrough, A., Romero-Zerón, L., Shakerian, M., Bell, C. A., Marica, F., Balcom, B. J. 2019. Magnetic Resonance Imaging of CO_2 Flooding in Berea Sandstone: Partial Derivatives of Fluid Saturation. Submitted to *SPE J*. Revised in response to reviews.

Afrough, A., Vashaee, S., Romero-Zerón, L., Balcom, B. J. 2019. Non-Ground Eigenstates in Magnetic Resonance Relaxation of Porous Media - Absolute Measurement of Pore Size. *Phys. Rev. Appl.* Accepted for publication.

Afrough, A., Shakerian, M., Zamiri, M. S., MacMillan, B., Marica, F., Newling, B., Romero-Zerón, L., Balcom, B. J. 2018. Magnetic Resonance Imaging of High-Pressure

Carbon Dioxide Displacement – Fluid Behavior and Fluid/Surface Interaction. *SPE J.* 23 (3): 772-787. https://doi.org/10.2118/189458-PA. SPE-189458-PA.

Afrough, A., Bahari Moghaddam, M., Romero-Zerón, L., Balcom, B. J. 2018. Exponential Capillary Pressure Functions in Sedimentary Rocks. International Symposium of the Society of Core Analysts, Trondheim, Norway, 27-30 August. SCA2018-012. 9 pages.

Shakerian, M., Afrough, A., Vashaee, S., Marica, F., Romero-Zerón, L., Balcom, B. J. 2018. Monitoring Gas Hydrate Formation with Magnetic Resonance Imaging in a Metallic Core Holder. International Symposium of the Society of Core Analysts, Trondheim, Norway, 27-30 August. SCA2018-025. 13 pages.

Afrough, A., Zamiri, M. S., Romero-Zerón, L., and Balcom, B. J. 2017. Magnetic Resonance Imaging of Fines Migration in Berea Sandstone. *SPE J.* 22 (5): 1385-1392. https://doi.org/10.2118/186089-PA. SPE-186089-PA.

Shakerian, M., Marica, F., Afrough, A., Goora, F. G., Li, M., Vashaee, S., Balcom, B.J. 2017. A High-Pressure Metallic Core Holder for Magnetic Resonance Based on Hastelloy-C. Review of Scientific Instruments 88 (12). Article number 123703. https://doi.org/10.1063/1.5013031.

Li, M., Xiao, D., Shakerian, M., Afrough, A., Goora, F., Marica, F., Romero-Zerón, L., and Balcom, B.J. 2016. Magnetic Resonance Imaging of Core Flooding in a Metal Core Holder. International Symposium of the Society of Core Analysts, Snowmass, Colorado, 21-26 August. SCA2016-019. 12 pages.

Kazemzadeh, E., Salehi, A., Sheikhzakariai, S. J., Afrough, A. 2014. Qualitative Characterization of Core Sample Porosity Using MRI Images. *J. Earth Space Phys.* 40 (1): 57-67. https://dx.doi.org/10.22059/jesphys.2014.36696.

Conference Presentations:

Shakerian, M., Afrough, A., Vashaee, S., Marica, F., Romero-Zerón, L., Balcom, B. J. 2018. Monitoring Gas Hydrate Formation with Magnetic Resonance Imaging in a Metallic Core Holder. International Symposium of the Society of Core Analysts, Trondheim, Norway, 27-30 August. Oral Presentation.

Afrough, A., Bahari Moghaddam, M., Romero-Zerón, L., Balcom, B. J. 2018. Exponential Capillary Pressure Functions in Sedimentary Rocks. International Symposium of the Society of Core Analysts, Trondheim, Norway, 27-30 August. Oral Presentation.

Afrough, A., Romero-Zerón, L., Balcom, B. J. 2017. Experimental Evidence of Both Fast and Slow Diffusion Regimes in a Sandstone Core Plug by 2D NMR Relaxometry and Diffusometry Correlation. International Conference on Magnetic Resonance Microscopy, Halifax, Canada, 13-17 August 2017. Poster.

Afrough, A., Shakerian, M., Zamiri, M. S., MacMillan, B., Marica, F., Newling, B., Romero-Zerón, L., Balcom, B. J. 2017. MRI of High Pressure Carbon Dioxide Displacement: Fluid/Surface Interaction and Fluid Behavior. International Conference on Magnetic Resonance Microscopy, Halifax, Canada, 13-17 August 2017. Oral Presentation.

Li, M., Xiao, D., Shakerian, M., Afrough, A., Goora, F., Marica, F., Romero-Zerón, L., and Balcom, B.J. 2016. Magnetic Resonance Imaging of Core Flooding in a Metal Core Holder. International Symposium of the Society of Core Analysts, Snowmass, Colorado, 21-26 August. SCA2016-019. Oral Presentation.

Afrough, A., Romero-Zerón, L., Balcom B. 2015. MRI of Fines Migration in Berea Sandstone. International Conference on Magnetic Resonance Microscopy, Munich, Germany, 6-8 August 2015. Poster.

Afrough, A. 2010. Mathematical Modeling of Stereographic Projection" Proceedings of the 27th Symposium on Geoscience, Tehran, Iran, February 2010. Poster.

Afrough, A. 2010. Optimizing Separator Pressures Using Genetic Algorithm" Proceedings of the 8th National Iranian Chemical Engineering Student Congress, Kermanshah, Iran, May 2010. Poster.